Dissertation

submitted to the

Combined Faculties of the Natural Sciences and Mathematics

of the Ruperto–Carola–University of Heidelberg, Germany

for the degree of

Doctor of Natural Sciences

Put forward by

B.Sc. Xiao-Fan Xu

born in: Liaoning (P.R.China)

Oral examination: July 23rd, 2014

Manipulating Quantum Entanglement with Atomic Ensembles and with Atoms in Optical Superlattices

*** Towards Scalable Quantum Information Processing ***

Referees: Prof. Dr. Jian-Wei Pan
Prof. Dr. Matthias Weidemüller

Zusammenfassung

Manipulation von Quantenverschränkung mit atomaren Ensemblen und mit Atomen in optischen Übergittern

Die Quanteninformatik bietet vielversprechende Möglichkeiten für die Entwicklung sicherer und effizienter neuer Arten, um Informationen zu übertragen und zu verarbeiten. Außerordenliche Anstrengungen wurden und werden in dieser Richtung unternommen, jedoch ist die Realisierung einer skalierbaren Struktur noch immer eine beträchtliche Herausforderung. Unter den möglichen Kandidaten gelten Photonen als gute Überbringer und neutrale Atome als gute Speicher. In dieser Dissertation werden Quellen für die Verschränkung von Photonen mit Materie, die die Vorteile beider Systeme ausnutzen, eingesetzt, um die für skalierbare Quantennetzwerke notwendigen Techniken der Teleportation und des effizienten Verschränkungsaustauschs zwischen zwei atomaren Quantenspeichernknoten vorzuführen. Weiterhin werden diese Verschränkungsquellen weiterentwickelt und eine aktiv vorwärtsgesteuerte Einweg-Quantenberechnung mit stationären Quantenspeichern vorgestellt, die für die Skalierbarkeit eines Quantencomputers benötigt wird. Um ein anderes Merkmal der Skalierbarkeit, die einfache Erweiterbarkeit, zu erfüllen, werden ultrakalte Atome in einem zwei-dimensionalen optischen Übergitter untersucht und ein Experiment zur Herstellung von Vierteilchenverschränkung wird entwickelt. Mit Hilfe der Photonen-Materie Verschränkungsquellen, eingesetzt als Quantenspeicher und als Knoten in Quantennetzwerken, ist die Verwirklichung von großflächigen Quantennetzwerken absehbar. Währenddessen könnten große verschränkte Zustände in optischen Übergittern durch die Anwendung von kontrollierten Wechselwirkungen hergestellt werden, die dabei behilflich sein könnten, Quantenprozessoren zu bauen, die die klassischen Gegenstücke an Leistung übertreffen.

Abstract

Manipulating Quantum Entanglement with Atomic Ensembles and with Atoms in Optical Superlattices

Quantum information science possesses promising potentialities for developing new secure and efficient ways to transfer and process information. Prodigious efforts have been and are being devoted, however, a scalable architecture is still a considerable challenge. Among the potential candidates, photons are assumed to be good carriers, and neutral atoms good hosts. In this thesis, photon-matter entanglement sources, which exploit the advantages of both, are employed to demonstrate a teleportation between two atomic-ensemble quantum memory nodes and an efficient entanglement swapping, which are essential for scalable quantum networks. Later, the entanglement source is further developed, and an active feedforward one-way quantum computation is presented with stationary quantum memories, which are necessary for scalable quantum computers. To fulfil another feature of scalability, the ease of integration, ultracold atoms in two-dimensional optical superlattices are studied and an experiment is designed to generate four-qubit entangled states. With the help of the photon-matter entanglement sources, serving as quantum memories and nodes of quantum networks, realization of large-scale quantum networks is foreseeable. Meanwhile, by applying controllable interactions, large entangled states could be generated in optical superlattices, which might help to construct quantum processors that outperform the classical counterparts.

Contents

Abstract **v**

List of Figures **xiii**

List of Tables **xvii**

Abbreviations **xix**

Physical Constants **xxi**

Introduction **1**

1 Entanglement and Quantum Memory with Cold Atomic Ensembles **9**
- 1.1 Theory of Atomic-Ensemble-Based Quantum Memory . . . 9
  - 1.1.1 Creation of a Collective Excitation . . . 10
  - 1.1.2 Retrieval of the Stored Collective Excitation . . . 14
  - 1.1.3 Non-classical Correlation . . . 16
  - 1.1.4 Quantum Memory Storage Lifetime . . . 17
    - 1.1.4.1 Inhomogeneity of Magnetic Field-Induced Dephasing . . . 17
    - 1.1.4.2 Thermal Atomic Motion-Induced Dephasing . . . 20
    - 1.1.4.3 Loss of Atoms in Collection Mode . . . 21
- 1.2 Quantum Repeater with Cold Atomic Ensembles . . . 23
  - 1.2.1 The DLCZ Protocol . . . 23
  - 1.2.2 Robust Scheme Resistant to Phase Noise . . . 24
- 1.3 Experimental Setup for Atomic-Ensemble-Based Quantum Memory . . . 26
  - 1.3.1 Preparing Atomic Ensemble in a Magneto-Optical Trap . . . 27

1.3.2 Memory Built-in Atom-Photon Entanglement Source 27
1.3.3 Bell-State Analyzer 31

2 Quantum Teleportation between Atomic-Ensemble Quantum Memories 33
2.1 Scheme of the Experiment 33
2.2 Spin-Wave State Preparation 36
2.3 Spin-Wave State Teleportation 38
2.3.1 Quantum Teleportation with Short Fiber 38
2.3.2 Quantum Teleportation with Long Fiber 39
2.3.3 Heralded Quantum Teleportation 40
2.4 Discussion 42

3 Efficient Entanglement Swapping Based on Delayed Choice 45
3.1 Scheme of the Experiment 46
3.2 Results of the Experiment 48
3.3 Discussion 50

4 One-Way Quantum Computing with Photon-Matter Hyperentanglement 51
4.1 Introduction to One-Way Quantum Computing 52
4.2 Cluster State Preparation 53
4.3 Cluster State Characterization 55
4.4 Results of the One-Way Quantum Computing 58
4.4.1 Single-Qubit Rotations 58
4.4.2 Two-Qubit Controlled-Phase Gate 62
4.4.3 Grover's Searching Algorithm 65
4.5 Discussion 65

5 Preparing a Two-Dimensional Ultracold Quantum Gas 69
5.1 Theory of Three-Dimensional Bose-Einstein Condensates 70
5.1.1 Quantum Statistics 70
5.1.2 Non-interacting Bosons in a Harmonic Trap 71
5.1.3 Weakly Interacting Bose Gas 72

5.2 Theory of Two-Dimensional Bose Fluids 73
    5.2.1 Effective Two-Body Interaction 74
    5.2.2 Berezinskii-Kosterlitz-Thouless Transition 74
    5.2.3 Two-Dimensional Bose Gas in a Harmonic Trap 76
5.3 Experimental Realization of a Two-Dimensional Degenerate Bose Gas . . 77
    5.3.1 Vacuum System 78
    5.3.2 Diode Laser System 78
    5.3.3 Absorption Imaging 81
        5.3.3.1 Absorption Imaging of a Three-Dimensional Atomic Cloud 81
        5.3.3.2 Absorption Imaging of a Two-Dimensional Atomic Cloud 82
    5.3.4 Real-Time Control System 83
    5.3.5 Magneto-Optical Trap and Optical Molasses 83
    5.3.6 Magnetic Trap and Magnetic Transport 84
        5.3.6.1 Magnetic Trapping 85
        5.3.6.2 Magnetic Transport 86
    5.3.7 Transfer to a Dipole Trap 87
        5.3.7.1 Optical Dipole Potential 87
        5.3.7.2 Experimental Setup for the Optical Dipole Trap 88
    5.3.8 Achieving a Bose-Einstein Condensate 90
    5.3.9 Achieving a Two-Dimensional Superfluid 90
        5.3.9.1 Loading Atoms into a One-Dimensional Optical Lattice . 90
        5.3.9.2 Making and Probing Two-Dimensional Superfluid 94

6 Quantum Gases in Two-Dimensional Optical Lattices 97
6.1 Single Particle in a Periodic Potential 97
    6.1.1 Bloch Bands 97
    6.1.2 Wannier Functions 98
    6.1.3 Tight Binding Approximation 99
6.2 Bose-Hubbard Model and the Superfluid to Mott Insulator Transition . . 100
    6.2.1 Bose-Hubbard Hamiltonian 101
    6.2.2 Superfluid to Mott Insulator Transition 102
        6.2.2.1 Superfluid Ground State 103

6.2.2.2 Mott Insulator Ground State . . . 103
6.2.2.3 Quantum Phase Transition . . . 104
6.2.2.4 Mott Insulator at Finite Temperature . . . 105
6.3 Experimental Observation of Superfluid to Mott Insulator Transition . . . 106
6.3.1 Forming a Lattice Potential . . . 106
6.3.2 Calibration of the Lattice Depth . . . 107
6.3.3 Achieving the Mott Insulator Regime . . . 110
6.3.3.1 Investigation of the Lattice Band Population . . . 110
6.3.3.2 Deep Lattice Condition . . . 111
6.3.3.3 Observation of the Quantum Phase Transition . . . 114

7 Creating Entanglement in Two-Dimensional Optical Superlattices 117
7.1 Superlattice Band Struncture . . . 117
7.2 Bose-Hubbard Model for Superlattices . . . 121
7.2.1 Double-Well Bose-Hubbard Model . . . 121
7.2.1.1 Single Particle in a Double Well . . . 122
7.2.1.2 Two Particles in a Double Well . . . 122
7.2.1.3 Superexchange in a Double Well . . . 123
7.2.2 Ring-Exchange in an Optical Plaquette . . . 124
7.3 Realizing an Optical Superlattice . . . 127
7.3.1 Relative Phase Control . . . 128
7.3.2 Suppressing Air Refraction Effect . . . 129
7.3.3 Loading Condensates into Superlattices . . . 130
7.4 Experimental Plan of the Four-Qubit Entanglement Generation . . . 132
7.4.1 Removing Defects . . . 133
7.4.2 State Preparation . . . 134
7.4.3 State Evolution . . . 137
7.4.4 State Detection . . . 137
7.4.5 In Situ Imaging System Design . . . 139
7.4.6 Discussion . . . 141

Conclusion and Outlook 143

A Hyperfine Structure for Rubidium 87 **147**

B Characterization of Quantum States and Quantum Processes **149**

B.1 Characterization of a Quantum State 149

B.2 Characterization of a Quantum Process 152

C Laser Beam Intensity Stabilization **155**

D Modified Edlén Equation **159**

List of Publications **161**

Acknowledgements **163**

Bibliography **165**

List of Figures

1.1 An illustration of the interaction between atomic ensemble and light. . . . 11
1.2 A schematic view of write and read processes. 14
1.3 Energy shift and storage lifetime as a function of the magnetic field for clock states. 20
1.4 Storage lifetime τ_{th} as a function of the detection angle θ. 22
1.5 Entanglement generation and swapping in the DLCZ protocol. 23
1.6 Creation of remote atom-atom entanglement with the improved protocol. 25
1.7 Entanglement connection with the improved protocol. 26
1.8 An illustration of the configuration of MOT. 28
1.9 The Λ-type system of Rubidium 87 for write and read. 29
1.10 An schematic view of the atom-photon entanglement source. 30
1.11 Three types of the Bell-state analyzers. 31

2.1 Experimental setup for quantum teleportation between two remote atomic ensembles. 35
2.2 Time sequence for quantum teleportation between atomic ensembles. . . . 36
2.3 Tomography results of the prepared atomic states. 37
2.4 Measured process matrix χ for the teleportation with short fiber. 39
2.5 Measured process matrix χ for the teleportation with long fiber. 40
2.6 Heralding efficiency as a function of the excitation probability. 42

3.1 A sketch of the entanglement swapping scheme. 46
3.2 Experimental setup for the efficient entanglement swapping. 47
3.3 Time sequence for the efficient entanglement swapping. 48
3.4 Visibility measurements on pairs of entangled photons of ensemble A. . . 49
3.5 Demonstration of enhancement with the feedback technique. 49

4.1 A typical cluster state configuration. 52
4.2 Experimental setup for the one-way quantum computing with photon-matter hyperentanglement. 54
4.3 Measured lower bound of fidelity of the cluster state. 56
4.4 Averaged retrieval efficiency oscillation of $|\pm\rangle$ states. 57
4.5 Quantum state tomography of the cluster state. 57
4.6 Single-qubit rotations. 59
4.7 Fidelities of the single-qubit rotations. 61
4.8 Bloch sphere representation of arbitrary single-qubit rotations. 61
4.9 Two-qubit C-Phase gate. 64
4.10 Grover's searching algorithm. 66

5.1 A typical experimental time sequence. 77
5.2 An illustration of the vacuum system. 78
5.3 An illustration of the diode laser system. 79
5.4 Frequencies of the laser beams. 80
5.5 A schematic view of the real-time control system. 84
5.6 Magnetic field generated by anti-Helmholtz coils. 86
5.7 Magnetic transport system. 87
5.8 Optical dipole trap setup. 89
5.9 Evaporation in the dipole trap to achieve a BEC. 91
5.10 Characteristics of the BEC trap. 92
5.11 Realization of the pancake lattice. 93
5.12 Pancake lattice periodicity. 94
5.13 Loading atoms into a single layer. 94
5.14 Characterizing the two-dimensional quantum gas. 95

6.1 Energy bands of the one-dimensional optical lattices. 98
6.2 Probability density of the Bloch wave function in the lowest band. 99
6.3 Wannier function and probability density. 100
6.4 Bose-Hubbard parameters. 102
6.5 Distribution of atoms in the superfluid phase and the Mott insulator phase. 103
6.6 Two-dimensional Bose-Hubbard model phase diagram. 104

6.7 Density and variance in the deep Mott insulator. 106
6.8 Realization of the short wavelength optical lattice. 107
6.9 Kapitza-Dirac effect of the short lattice pulse. 108
6.10 Lattice depth calibration by the Kapitza-Dirac effect. 108
6.11 Lattice depth calibration by the band excitation. 109
6.12 Investigating the band population. 111
6.13 Evaluation of the deep lattice condition. 112
6.14 Collapse and revival of the residual superfluid. 113
6.15 Interference pattern for different lattice depths. 114
6.16 Restoring the phase coherence. 115
6.17 Visibility versus lattice depth. 115

7.1 Band structure of shallow superlattices. 119
7.2 Band structure of deep superlattices. 120
7.3 A schematic view of optical plaquettes. 125
7.4 Eigenstates of the lattice gauge Hamiltonian. 126
7.5 Suppressing superexchange with a magnetic field gradient. 127
7.6 Superlattice potential and the relative phase. 127
7.7 Phase control via the laser frequency tuning. 128
7.8 A schematic view of the relative phase control. 129
7.9 Superlattice phase with the environment change. 130
7.10 Realization of the optical superlattice. 131
7.11 Observation of the quantum phase transition with long lattice. 131
7.12 Interference pattern of the condensates in superlattices. 133
7.13 Filtering sequence for plaquettes. 135
7.14 State preparation by tilting the lattice. 136
7.15 State detection process. 138
7.16 Loss of fidelity due to limited optical resolution. 138
7.17 High-resolution imaging system. 140
7.18 Spin-dependent optical lattice. 141

A.1 Rubidium 87 hyperfine structure. 147

C.1 A schematic view of the feedback loop. 155

C.2 Bode diagrams of the feedback loop. 156
C.3 Intensity noise suppression. 156
C.4 PI controller modification. 157

List of Tables

1.1 Storage lifetime (μs) for different ground-state pairs. 19

2.1 Teleportation fidelities with short fiber. 39

2.2 Teleportation fidelities with long fiber. 40

4.1 Reduced density matrices and fidelities. 58

4.2 Reconstructed process matrices of Pauli error correction operations. . . . 62

4.3 Simulation of the single-qubit rotations. 63

Abbreviations

AOM	**A**cousto-**O**ptic **M**odulator
BEC	**B**ose-**E**instein **C**ondensate
BKT	**B**erezinskii-**K**osterlitz-**T**houless
BS	non-polarizing **B**eam **S**plitter
BSA	**B**ell-**S**tate **A**nalyzer
BSM	**B**ell-**S**tate **M**easurement
C-Phase	**C**ontrolled-**Phase**
CCD	**C**harge-**C**oupled **D**evice
Dark SPOT	**Dark SP**ontaneous-force **O**ptical **T**rap
DM	**D**ichroic **M**irror
DP-Lock	**D**igital optical **P**hase **Lock** loop
EIT	**E**lectromagnetically **I**ndued **T**ransparency
EOM	**E**lectro-**O**ptic **M**odulator
fast-PD	**fast P**hoto**D**iode
FPGA	**F**ield-**P**rogrammable **G**ate **A**rray
HWP	**H**alf-**W**ave **P**late
KD	**K**apitz-**D**irac
LDA	**L**ocal **D**ensity **A**pproximation
LRO	**L**ong-**R**ange **O**rder
MOT	**M**agneto-**O**ptical **T**rap
PBS	**P**olarizing **B**eam **S**plitter

PIEZO	**PIEZO**electric ceramics
POL	**POL**arizer
PPLN	**P**eriodically **P**oled **L**ithium **N**iobate
PVC	**P**umping **V**apor **C**ell
QWP	**Q**uarter-**W**ave **P**late
SPDC	**S**pontaneous **P**arametric **D**own-**C**onversion
TOF	**T**ime-**O**f-**F**light
TSP	**T**itanium **S**ublimation **P**ump
TTL	**T**ransistor-**T**ransistor **L**ogic
UHV	**U**ltra-**H**igh **V**acuum
VCO	**V**oltage-**C**ontrolled **O**scillator

Physical Constants

Universal Constants [1,2]

Speed of Light in Vacuum	c	$=$	$2.997\ 924\ 58 \times 10^{8}$ m/s (exact)
Vacuum Permeability	μ_0	$=$	$4\pi \times 10^{-7}$ N/A^2 (exact)
Vacuum Permittivity	ϵ_0	$=$	$(\mu_0 c^2)^{-1}$ (exact)
		$=$	$8.854\ 187\ 817... \times 10^{-12}$ F/m
Planck Constant	h	$=$	$6.626\ 069\ 57(29) \times 10^{-34}$ J $\cdot$ s
Reduced Planck Constant	$\hbar$	$=$	$1.054\ 571\ 726(47) \times 10^{-34}$ J $\cdot$ s
Elementary Charge	e	$=$	$1.602\ 176\ 565(35) \times 10^{-19}$ C
Bohr Magneton	μ_{B}	$=$	$9.274\ 009\ 68(20) \times 10^{-24}$ J/T
		$=$	$h \times 1.399\ 624\ 555(31)$ MHz/G
Bohr Radius	a_0	$=$	$0.529\ 177\ 210\ 92(17) \times 10^{-10}$ m
Boltzmann Constant	k_{B}	$=$	$1.380\ 6488(13) \times 10^{-23}$ J/K
Standard Acceleration of Gravity	g	$=$	$9.806\ 65$ m/s^2 (exact)

Rubidium 87 Properties [3]

Atomic Mass	m	$=$	$1.443\ 160\ 648(72) \times 10^{-25}$ kg
Frequency (D-2)	ω_0	$=$	$2\pi \times 384.230\ 484\ 4685(62)$ THz
Natural Line Width (D-2)	Γ	$=$	$2\pi \times 6.0666(18)$ MHz
Frequency (D-1)	ω_0	$=$	$2\pi \times 377.107\ 463\ 380(11)$ THz
Natural Line Width (D-1)	Γ	$=$	$2\pi \times 5.7500(56)$ MHz

To my family,
and my teachers.

Introduction

QUANTUM INFORMATION SCIENCE, in which the quantum effects are employed to process information, possesses promising potentialities for developing new secure and efficient ways to transfer information and novel computational techniques of unprecedented speed. Over the past few decades, prodigious efforts have been devoted, both from physicists and from information scientists, to the field by considering various materials, such as photons, trapped atoms either ionized or neutral, nuclear magnetic resonance, quantum dots, superconductors, and so on. Especially, scalable quantum networks and quantum computers are very promising by exploiting photons as carriers to transmit information, benefitting from its high speed and low decoherence, and trapped neutral atoms for information processing and storage, benefitting from its controllable interactions. In this thesis, I present the work of how quantum networks and quantum computers could benefit by manipulating photon-matter entanglement and entanglement of ultracold bosons.

Quantum Information Science

In the study of the quantum information science, quantum communication and quantum computation are two subfields which are widely investigated. The former holds the promise of achieving secure information transfer that will not be intercepted by an unauthorized party [4], while the latter has great potential for solving complex problems that cannot be settled efficiently by classical computational systems [5].

In analogy with "bit" which is the unit of classical information, "quantum bit", or "qubit" for short, is defined as the unit of quantum information. It refers to a state in the simplest possible quantum system that can be described by a two-dimensional Hilbert space, such as electron spins and photon polarizations. The most attractive feature of the "qubit" is that it can also exist in a continuum of intermediate states or superpositions. Under special conditions, this unique feature will introduce a new resource, quantum entanglement, which exhibits correlations that have no classical parallel. With the help of such a resource, an unknown quantum state can be conveyed from one place to another through quantum teleportation [6,7].

The Birth of Quantum Information Science

Born around 1900, "quantum physics" has left, and is leaving, a trail of footprints in the process of human's reforming the world. It has had unsurpassed success in explaining many phenomena — from the structure of elementary particles to the physics of the early universe, and also led to a great number of technological applications like lasers and semiconductors [8].

In spite of the great progress that has been made by the aid of quantum mechanics in the first several decades of the twentieth century, to manifest whether quantum mechanics can be considered complete was still a tremendous challenge until the end of the century. In the "May 15, 1935" issue of Physical Review, Albert Einstein co-authored a paper with his two research associates, Boris Podolsky and Nathan Rosen, generally referred to as "EPR", introduced an idea of pairs of particles strongly correlated over large distances [9]. They explained the correlations by applying a hidden-variable theory, considering quantum mechanics as a statistical theory, in which the probabilities of the possible events are fixed by nonobservable properties. In the same year, Schrödinger realized that such correlated systems are extremely non-classical and coined the term "entanglement" for these correlations which is recognized as the essential characteristic of quantum mechanics today [10, 11]. A debate over the interpretation of the quantum theory began, however, only with Gedankenexperiments. It was John Bell in 1964 who derived the famous inequality from the local deterministic hidden-variable theory which is inconsistent with quantum-mechanical predictions for a range of parameters chosen [12]. From then on, along with technological progress, more and more experiments were performed to suggest that a local realistic explanation of nature is inappropriate [13–19].

The story did not come to the end, on the contrary, it was just a beginning. The intensive studies of fundamentals of quantum theory finally gave rise to a new field, "quantum information science", in which the distinctive quantum properties like uncertainty principle, interference, and entanglement are employed. Especially, quantum teleportation, first proposed by Charles H. Bennet and his colleagues [6], has been researched a lot, by which people can transmit a qubit exactly from one place to another without interacting with the media in between. Nowadays, it is widely accepted that quantum teleportation is not only a critical ingredient of quantum infromation science, but also a versatile tool to help us investigating the fundamentals of quantum theory [20].

The most frequently used scientific objects for studying teleportation are photons, and just recently, teleportation between single ions has been reported [21–23]. In this thesis, I will present a realization of quantum teleportation between two atomic-ensemble quantum memory nodes with the aid of photon-matter entanglement.

Quantum Communication and Quantum Network

In the last few decades, the development of science and technology necessitates a truly secure way to communicate. In particular, the most widely used algorithm for public-key cryptography, RSA [24], would be broken easily by a functional quantum computer with Shor's algorithm [25]. Fortunately, by taking advantage of quantum properties, quantum communication will help us in this respect by means of quantum cryptography [4]. In addition, it enables the establishment of a quantum network, a secure network capable of utilizing quantum principles.

One important quantum cryptographic task is quantum key distribution, that is, to share a secret random bit string between two communication terminals traditionally referred to as Alice (the sender) and Bob (the receiver). Different from classical key agreement, the quantum counterpart allows the existence of eavesdroppers (Eve) while the security is kept. The beautiful idea of quantum cryptography was first sketched in the 1970s by Stephen Wiesner [4, 26], and then developed by Charles H. Bennet and Gilles Brassard in 1984 (the protocol is known as BB84) [27]. In this BB84 protocol, two pairs of conjugate states are employed, which are commonly encoded in the photon polarizations. Thanks to the no cloning theorem [28], any interception made by Eve will introduce errors and thus can be detected by both of the terminals. Moreover, a further action named "privacy amplification" can be performed to assure a given level of security, by which Eve's information on the string is obliterated at the cost of decreasing the length of the distilled key [29]. The first demonstration of quantum cryptography was performed by a group of scientists of IBM [29]. Later, an enhanced protocol, named "decoy-state", has been researched to guarantee the unconditional security for longer transmission distance [30,31]. Meanwhile, an alternative protocol was proposed by Artur Ekert in 1991 (Ekert91), where entangled photon pairs are used [32]. The up-to-date results are presented by a European collaboration [33, 34].

Despite of the great progress in the realization of quantum communication, researchers became aware of the fact that in practice the noisy channels severely limit the transmission distance by introducing decoherence and losses, which makes the building of a large-scale quantum network extremely challenging. In a seminal paper published in 1998, Hans J. Briegel and his fellows presented a solution to establish entanglement between two remote sites by employing the so-called quantum repeater [35], of which the scheme is composed of the creation of entangled pairs between every neighbouring sites, the entanglement swapping [36], and the entanglement purification [37]. However, since the purification procedure is probabilistic, quantum memory, a way to store the qubits while performing the protocol, is necessary in order to ensure the polynomial scaling in the communication efficiency. The first consideration of the realization of quantum repeater was to store the information of the photonic states into the atomic states by achieving strong coupling between atoms and photons with high-finesse cavities [38], which is a quite challenging technique. Just a few years later, Lu-Ming Duan and his partners got around the problem and proposed a new scheme (DLCZ protocol) by employing atomic ensembles and linear optics, which, in addition, has built-in entanglement purification and is resilient to photon loss noise [39]. Following this idea, tremendous achievements have been made including an improved protocol based on the two-photon Hong-Ou-Mandel-type interference which relaxes the long distance stability requirements by about 7 orders of magnitude [40, 41], and the first demonstration of a quantum repeater node [42]. Unfortunately, due to the probabilistic characteristic of the entangled photon source used in the former experiment, the efficiency of entanglement swapping is quite limited. In this thesis, I will study and present a mew method to implement an efficient entanglement swapping by using photon-matter entanglement, where an enhanced factor of 257 is observed.

Quantum Computation and Quantum Computer

Computing might be one of the things we do the most in everyday life. The history of computing can be traced back thousands of years when the concept of numbers arose — not the abstractions. And the earliest known tool for use in computation, the abacus, was invented in Babylon around 2400 BC. Nowadays, most of the computational tasks are performed by electronic computers, and networks are established to allow computers to exchange data. About half a century after quantum mechanics was formulated, scientists realized that by taking advantage of the quantum principles, new kind of computation with qualitatively new algorithms could be conceived [43]. The first proposal of such a quantum computer was put forward by David Deutsch in 1985 [44], who afterwards also introduced the universal quantum gates, which, together with the quantum "unit wires", can be used for constructing quantum computers [45]. Following this idea, tens of quantum algorithms were proposed, and two of the best-known ones are Shor's algorithm for prime factorization [25] and Grover's algorithm for searching an unsorted database [46]. Both algorithms provide significant speedup over their classical counterparts.

With the development of quantum computation theory, researchers studied several promising physical systems to implement the quantum computer including photons, trapped atoms, nuclear magnetic resonance, quantum dots, superconductors, just to name a few, by following the rules that a quantum computer has to possess the abilities to control the quantum systems, to measure them, and to preserve the isolation from the environment at the same time [47]. Analogous to the classical computer, most of the experiments to implement quantum computation are based on sequences of unitary quantum logic gates which process the qubits [48]. In 2001, a breakthrough known as the "one-way quantum computer" proposed by Robert Raussendorf and Hans J. Briegel showed an entirely different model which is scalable [49, 50]. In this one-way architecture, a specific highly entangled state which is called cluster state is served as the computational system, and the computation proceeds by a sequence of single-qubit measurements with feedforward of previous outcomes. One-way quantum computation indeed has changed our understanding of quantum computation since there is no analogue in classical physics, and there have been already a number of experimental demonstrations reported in the last decade [48, 51–56]. Unfortunately, the probabilistic character of photon sources and entangling operations make the realization of an efficient optical quantum computation fail without the use of quantum memories. In this thesis, I will present the realization of an optical one-way quantum computation with stationary quantum memory involved.

Cold and Ultracold Neutral Atoms

Cold and ultracold neutral atoms are promising candidates for realizing quantum information processing. Unlike the ions who have strong Coulomb interaction, neutral atoms have relatively weak coupling with the environment, and typically interact only on-site via short-ranged collisional interactions. In addition, by taking advantage of Feshbach resonances, the interaction in ultracold quantum gases can be tuned [57].

In the early twentieth century, scientists found that identical particles are governed by two different quantum statistics, either Bose-Einstein statistics or Fermi-Dirac statistics. Bosons have integer spin and obey the former statistics, while fermions have half-integer spin and obey the latter statistics. It was Albert Einstein who realized that by cooling the identical bosonic atoms down to a temperature close to the absolute zero while keeping the density large enough, a new kind of matter, the so-called Bose-Einstein condensate (BEC) would be formed. Inspired by this idea, great efforts were put forth to cool atoms in the following decades. Finally, by making use of laser cooling and evaporative cooling technique, the BEC of a dilute gas of alkali atoms was observed in 1995 [58]. For a number of years, studies regarding this coherent matter wave were mainly focused on the existence of the coherence, until the year 1998 when Dieter Jaksch and his colleagues proposed that a quantum phase transition from the superfluid to the Mott insulator phase could be achieved by loading a BEC into an optical lattice and increasing the potential depth [59]. The dynamics can be easily described by a Bose-Hubbard model, in which the on-site interaction U and the tunneling matrix element J can be tuned by varying the optical lattice depth and by making use of Feshbach resonances.

During the study of quantum properties of neutral atoms, several proposals were put forward to apply neutral atoms to quantum information science. The improved DLCZ protocol mentioned in the last section is one of the examples. In this thesis, I will study the quantum information science by using the atomic-ensemble quantum memory developed from the protocol [60]. Another remarkable idea is to load a BEC into an optical lattice where each single atom represents a qubit, which makes the creation of a large entangled state feasible [61]. Following the idea, a great success was made where multi-particle entangled states were generated through controlled collisions [62]. However, the experiment is based on a spin-dependent monochromatic lattice which has limited tunability. In this respect, optical superlattices are more competent which can tune the barriers within and between the double wells irrelevant to the spins, and introduce many complex interactions to favor the manipulation of the atoms. By utilizing the tunability of the optical superlattices, two-qubit entangled states have been reported [63, 64]. In this thesis, I will study a two-dimensional system [65] where the ultracold atoms are loaded into an optical superlattice, with the hope of reaching a large entangled state for quantum information processing.

The Objective of This Work

The aim of this thesis is to achieve quantum information processing by manipulating photon-matter entanglement and entanglement of ultracold bosons, which could help to realize scalable quantum networks and quantum computers. The thesis is organized as follows:

- In Chapter 1, some useful concepts of quantum information science are reviewed, and theoretical analysis of atomic-ensemble quantum memory is given, especially focusing on the generation of photon-matter entanglement. The basic elements of the experimental setups are also explained.

- In Chapter 2, a teleportation between two atomic-ensemble quantum memory nodes is reported.
- In Chapter 3, an efficient entanglement swapping is demonstrated with the help of a delayed choice method.
- In Chapter 4, the realization of an optical one-way quantum computation is presented, in which the stationary quantum memory is involved.
- In Chapter 5, a two-dimensional degenerate Bose gas is prepared and analyzed, aiming for optical lattice loading.
- In Chapter 6, theoretical models of quantum gases in optical lattices are reviewed. The system is characterized experimentally, and the quantum phase transition from superfluid to Mott insulator is confirmed.
- In Chapter 7, a quantum gas in an two-dimensional optical superlattice is studied, and an experimental plan to generate four-qubit entanglement is proposed.

Chapter 1

Entanglement and Quantum Memory with Cold Atomic Ensembles

Quantum entanglement serves as an essential part of quantum information science, especially to achieve a quantum network and a quantum computer. Quantum systems, that once become entangled with each other, will remain entangled until either when a measurement is performed or when they decohere via interactions with environment. So far, a number of entanglement sources have been studied, including entangled photons produced by spontaneous parametric down-conversion [66], entangled ions prepared in Paul traps [67,68], entangled atoms in a cavity [69], entangled microwave photons from quantum dots [70], entanglement between light and atomic ensembles [60,71], and so on. In this chapter I will first review the theory of atomic-ensemble-based quantum memory by considering the interactions between light and atoms. Then, with the help of this, I will explain how to generate entanglement between a single photon and an atomic ensemble, which is one of the central elements for the experiments presented in this thesis. In addition, the current schemes to create remote entanglement are discussed. In the third section, the experimental parameters are illustrated.

1.1 Theory of Atomic-Ensemble-Based Quantum Memory

Atomic ensembles are regarded as good candidates to realize quantum memories, in which a quantum state of light can be stored for a controlled period of time and then retrieved on demand. So far, different types of configurations have been studied, including quantum nondemolition Faraday interaction [72,73], Raman and electromagnetically induced transparency (EIT) type [39, 74, 75], photon echo approach [76–78], and so on. In this thesis, the Raman-type configuration is employed which can be illustrated by a Λ-type three-level atomic system. To store a quantum state, one has to apply a write process in which the quantum state will be imprinted on a collective excitation of an atomic ensemble heralded by the simultaneous generation of a Stokes photon (or an anti-Stokes photon depending on the structure of the atomic system). Later, a read process is executed on demand to retrieve the quantum state from the stored collective excitation and encode it to the corresponding anti-Stokes photon (or Stokes photon). In the remaining part of the section, I will review the basic theory of the interactions between the light and the atomic ensembles mainly based on the references [79–81].

1.1.1 Creation of a Collective Excitation

In Raman-type atomic ensemble quantum memories, the write process is described as the creation, as well as the storage, of a collective excitation state, and the spontaneous emission of a single photon specifying the information of the state, due to the interaction between the atomic ensemble and a weak off-resonant classical light pulse.

Considering a Λ-type three-level atomic system depicted in Fig. 1.1, in which the two ground states are represented as $|g\rangle$ and $|s\rangle$, respectively, and $|e\rangle$ represents the excited state. At the very beginning, all the atoms in the atomic ensemble are prepared in the lowest-energy ground state $|g\rangle$ by optical pumping and the state of the atomic ensemble is described as $|0_{\mathrm{a}}\rangle \equiv \otimes_j |g\rangle_j$. The weak classical write light, which couples the transition $|g\rangle \rightarrow |e\rangle$ with a detuning Δ, can be described as

$$\mathbf{E}_{\mathrm{W}}(\mathbf{r},t) = E_{\mathrm{W}}(\mathbf{r},t)\hat{\epsilon}_{\mathrm{W}} e^{i(\mathbf{k}_{\mathrm{W}}\cdot\mathbf{r}-\omega_{\mathrm{W}}t)} + \mathrm{H.c.}, \tag{1.1}$$

where the envelope $E_{\mathrm{W}}(\mathbf{r},t)$ varies much slower than the optical angular frequency ω_{W}, and $\hat{\epsilon}_{\mathrm{W}}$ is the polarization unit vector. The spontaneously emitted Stokes field, which couples the transition $|e\rangle \rightarrow |s\rangle$, has to be represented in terms of a set of quantized harmonic oscillator modes

$$\mathbf{E}_{\mathrm{S}}(\mathbf{r},t) = \sum_{j,\alpha} \sqrt{\frac{\hbar\omega_j}{2\epsilon_0 V}}\hat{\epsilon}_{\alpha} \left[\hat{a}_{j,\alpha} e^{i(\mathbf{k}_j\cdot\mathbf{r}-\omega_j t)} + \mathrm{H.c.}\right], \tag{1.2}$$

where $\hat{\epsilon}_{\alpha}$ and ω_j are the polarization and the angular frequency of the Stokes light field of the mode $\{j,\alpha\}$, respectively, and $\hat{a}_{j,\alpha}$ is the corresponding annihilation operator. Thus, the total Hamiltonian for N atoms at position $\mathbf{r}_j$ interacting with the light in the interaction picture is formulated as

$$\begin{aligned} H =& \hbar\Delta\sum_{j}^{N}\sigma_{ee}^{j} - \hbar\sum_{j}^{N}\left[\Omega_{\mathrm{W}}(\mathbf{r}_j,t)e^{i\mathbf{k}_{\mathrm{W}}\cdot\mathbf{r}_j}\sigma_{eg}^{j} + \mathrm{H.c.}\right] \\ & - \hbar\sum_{j}^{N}\sum_{j',\alpha}\left[g_{j',\alpha}\hat{a}_{j',\alpha}e^{i(\mathbf{k}_{j'}\cdot\mathbf{r}_j - \Delta\omega_{j'}t)}\sigma_{es}^{j} + \mathrm{H.c.}\right], \end{aligned} \tag{1.3}$$

where $\Delta = \omega_{eg} - \omega_{\mathrm{W}}$ and $\Delta\omega_{j'} = \omega_{j'} - \omega_{\mathrm{W}} + \omega_{sg}$ with $\omega_{eg} = \omega_e - \omega_g$ and $\omega_{sg} = \omega_s - \omega_g$ represent the detunings, $\sigma_{lm}^{j} = |l\rangle_j\langle m|$ $(l, m = g, e, s)$ are the transition operators of the j-th atom, $\Omega_{\mathrm{W}}(\mathbf{r}_j,t) = \mathbf{d}_{eg}\cdot\hat{\epsilon}_{\mathrm{W}}E_{\mathrm{W}}(\mathbf{r}_j,t)/\hbar$ is the Rabi frequency of the write light, and $g_{j',\alpha} = \sqrt{\hbar\omega_{j'}/(2\epsilon_0 V)}\,(\mathbf{d}_{es}\cdot\hat{\epsilon}_{\alpha})/\hbar$ is the coupling constant of the Stokes field of the mode $\{j', \alpha\}$ which is also known as the "single-photon Rabi frequency". In Eq. 1.3, the terms in the first line come from the interaction between the atoms and the classical write light, while the terms in the second line come from the interaction between the atoms and the quantized Stokes field.

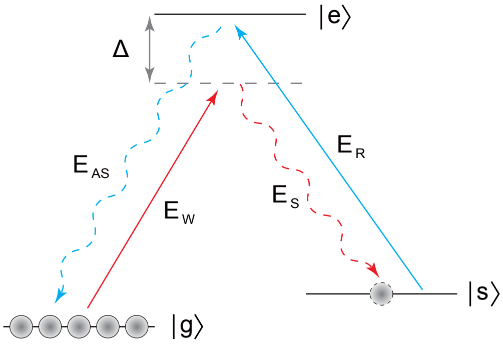

FIGURE 1.1: An illustration of the interaction between atomic ensemble and light. When a weak off-resonant classical write light is applied to the atomic ensemble, a collective excitation is created via the spontaneous Raman process along with the emission of a Stokes photon. Later, the EIT-based read process helps to convert the information of the collective excitation into a corresponding anti-Stokes photon by shining a strong resonant light pulse to the atomic ensemble.

When the Rabi frequency of the write light Ω_{W} and the line width of the excited state $|e\rangle$ are small compared to the detuning Δ, one can adiabatically eliminate the excited state and derive a Hamiltonian of light-atom interaction for two-level atomic systems

$$H = -\hbar\sum_{j}^{N}\left[\sigma_{sg}^{j}\frac{\Omega_{\mathrm{W}}(\mathbf{r}_j,t)e^{i\mathbf{k}_{\mathrm{W}}\cdot\mathbf{r}_j}}{\Delta}\sum_{j',\alpha}g_{j',\alpha}^{*}\hat{a}_{j',\alpha}^{\dagger}e^{-i(\mathbf{k}_{j'}\cdot\mathbf{r}_j - \Delta\omega_{j'}t)} + \mathrm{H.c.}\right], \tag{1.4}$$

where the AC Stark shifts are neglected. This Hamiltonian characterizes the dynamics of the spontaneous emission from the pseudo excited state $|g\rangle$ to the pseudo ground state $|s\rangle$, and the line width of the pseudo excited state is $\Gamma' = \Omega_{\mathrm{W}}^2\Gamma/\Delta^2$ where Γ is the decay rate of $|e\rangle \rightarrow |s\rangle$.

The Hamiltonian has been investigated in the last few decades [79, 82, 83], and throughout this thesis the process is confined within the spontaneous emission regime by limiting the interaction time $T < 1/\Gamma'$ (say, the pulse duration of the write). As a result of solving the Schrödinger equation with perturbation theory to the first-order, the final state of the system is

$$|\psi\rangle = \left[1 - i\int_{0}^{T} H(\tau)d\tau\right]|\text{vac}\rangle + o(p), \tag{1.5}$$

with $|\text{vac}\rangle = |0_\text{a}\rangle|0_\text{p}\rangle$, where $|0_\text{p}\rangle$ is the photon vacuum state. By assuming the Rabi frequency $\Omega_\text{W}(\mathbf{r}_j)$ is time independent, one obtains

$$|\psi\rangle = |0_\text{a}\rangle|0_\text{p}\rangle + \sum_{j}^{N} e^{i\mathbf{k}_\text{W}\cdot\mathbf{r}_j}|g...s_j...g\rangle|\gamma\rangle_j + o(p), \tag{1.6}$$

where $|\gamma\rangle_j$ describes the spontaneously emitted Stokes photon from the j-th atom with the expression

$$|\gamma\rangle_j = -i\frac{\Omega_\text{W}(\mathbf{r}_j)}{\Delta}\int_{0}^{T} d\tau \sum_{j',\alpha} g^{*}_{j',\alpha}\hat{a}^{\dagger}_{j',\alpha}e^{-i(\mathbf{k}_{j'}\cdot\mathbf{r}_j - \Delta\omega_{j'}\tau)}|0_\text{p}\rangle. \tag{1.7}$$

To further analyze the state, we restrict the detection of the Stokes field to a small solid angle along the axial direction as depicted in Fig. 1.2. In the far-zone approximation, by applying Weisskopf-Wigner theory [84], one could simplify the spatial wave function of a photon emitted by an atom from the quantized harmonic oscillator expression to

$$E(\mathbf{r}-\mathbf{r}_0) = \frac{\omega^2 d}{4\pi\epsilon_0 c^2|\mathbf{r}-\mathbf{r}_0|}e^{i\mathbf{k}\cdot(\mathbf{r}-\mathbf{r}_0)}, \tag{1.8}$$

where ω is the atomic transition frequency, d is the electric-dipole transition matrix element, $\mathbf{r}$ and $\mathbf{r}_0$ are the position of the observation point and the position of the atom, respectively, and $\mathbf{k}$ is the wave vector which is parallel to $\mathbf{r}-\mathbf{r}_0$. Thus, the Stokes field emitted from the j-th atom takes the form of

$$\begin{aligned} E^{j}_\text{S}(\mathbf{r}-\mathbf{r}_j) =& \frac{\varepsilon_\text{S}}{|\mathbf{r}-\mathbf{r}_j|}e^{i\mathbf{k}_\text{S}\cdot(\mathbf{r}-\mathbf{r}_j)} \\ =& \frac{\varepsilon_\text{S}}{\sqrt{(x-x_j)^2+(y-y_j)^2+(z-z_j)^2}} \\ & \times \exp\left[ik_\text{S}\sqrt{(x-x_j)^2+(y-y_j)^2+(z-z_j)^2}\right], \end{aligned} \tag{1.9}$$

where ε_S represents the constant that is proportional to the dipole matrix element. By expanding the square root term in Taylor series to the second-order and taking the assumption $z^2 \gg x^2, y^2 \gg x_j^2, y_j^2, z_j^2$, one derives

$$\begin{aligned} E_{\mathrm{S}}^j(\mathbf{r}-\mathbf{r}_j) \simeq & \frac{\varepsilon_{\mathrm{S}}}{\sqrt{(x-x_j)^2+(y-y_j)^2+(z-z_j)^2}} \\ & \times \exp\left\{ ik_{\mathrm{S}} \left[(z-z_j) + \frac{(y-y_j)^2}{2(z-z_j)} + \frac{(x-x_j)^2}{2(z-z_j)} - \frac{(y-y_j)^2(x-x_j)^2}{4(z-z_j)^3} \right] \right\} \\ \simeq & \frac{\varepsilon_{\mathrm{S}}}{z} \exp\left\{ ik_{\mathrm{S}} \left[(z-z_j) + \frac{y^2+x^2}{2z} \right] \right\} \\ \simeq & c_{\mathrm{S}}(\mathbf{r}) e^{-i\mathbf{k}_{\mathrm{S}}\cdot\mathbf{r}_j}, \end{aligned} \tag{1.10}$$

with the coefficient $c_{\mathrm{S}}(\mathbf{r}) = \varepsilon_{\mathrm{S}}/z \exp[ik_{\mathrm{S}}(2z^2+y^2+x^2)/(2z)]$, and the wave vector $\mathbf{k}_{\mathrm{S}} \simeq k_{\mathrm{S}}\hat{z}$ due to the assumption of a small detection solid angle. Therefore, the detected Stokes field can be regarded as a single mode and the state can be approximated by

$$|\gamma\rangle_j = \sqrt{p}\hat{a}_{\mathrm{S}}^\dagger e^{-i\mathbf{k}_S\cdot\mathbf{r}_j}|0_{\mathrm{p}}\rangle, \tag{1.11}$$

where $p = T\Gamma' d\Omega \ll 1$ is the probability for one of the atoms to scatter one Stokes photon into the detection solid angle $d\Omega$, and $\hat{a}_{\mathrm{S}}^\dagger$ is the single-mode creation operator. Substituting Eq. 1.11 into Eq. 1.6, one gets

$$|\psi\rangle = \left[1 + \sqrt{p} \left(\sum_j^N e^{i\Delta\mathbf{k}\cdot\mathbf{r}_j} \sigma_{sg}^j \right) \hat{a}_{\mathrm{S}}^\dagger \right] |\mathrm{vac}\rangle + o(p), \tag{1.12}$$

with $\Delta\mathbf{k} = \mathbf{k}_{\mathrm{W}} - \mathbf{k}_{\mathrm{S}}$. In addition, we could define a collective state operator

$$\hat{S}^\dagger = \frac{1}{\sqrt{N}} \sum_j^N e^{i\Delta\mathbf{k}\cdot\mathbf{r}_j} \sigma_{sg}^j, \tag{1.13}$$

with $1/\sqrt{N}$ for normalization and $[\hat{S}, \hat{S}^\dagger] = \sum_j^N (|g\rangle_j\langle g| - |s\rangle_j\langle s|)/N \simeq 1$ for weak interaction, which helps to simplify the form of the final state

$$|\psi\rangle = \left(1 + \sqrt{\chi}\hat{S}^\dagger\hat{a}_{\mathrm{S}}^\dagger\right)|\mathrm{vac}\rangle + o(\chi), \tag{1.14}$$

where $\chi = Np$ is the probability to detect one Stokes photon in the write process. The probability χ has to be much smaller than 1 in order to ensure the whole process is maintained within the spontaneous regime, as well as to suppress higher order excitations which will induce noise in the system.

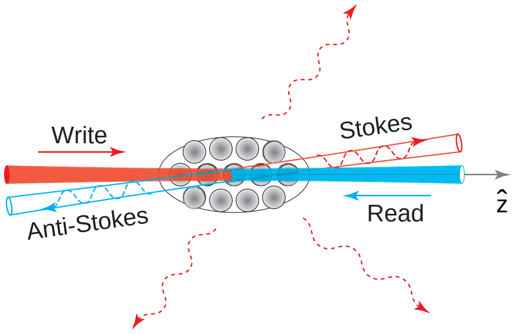

FIGURE 1.2: A schematic view of write and read processes. The write light and the read light counter-propagate along the z-axis. In the write process, the atomic ensemble scatters Stokes photons in all directions for the short interaction time. However, the Stokes field can be treated as a single mode when the detection solid angle is small and paraxial, that is, the angle between the detection direction and the z-axis is small. In the read process, only the anti-Stokes field whose propagation direction satisfies the phase matching condition will get enhanced.

The analysis above indicates that the detection of a single Stokes photon will result in a collective excitation state of the atomic ensemble expressed as

$$\hat{S}^{\dagger}|0_{\mathrm{a}}\rangle = \frac{1}{\sqrt{N}}\sum_{j}^{N} e^{i\Delta\mathbf{k}\cdot\mathbf{r}_j}|g...s_j...g\rangle, \tag{1.15}$$

which is also know as a spin-wave state [85]. Note that the discussion above is limited to the case of $t = 0$ which does not include the evolution of the spin-wave. Furthermore, Eq. 1.12 implies that there is no collective enhancement during the write process due to the lack of constructive interference in any of the directions. This can be understood in the way that the scattering photons emitted from different atoms relate to different states and all the N terms in the sum part of Eq. 1.12 are orthogonal to each other, thus no interference appears. Another important feature which has to be mentioned is the single-mode condition. In practice, to ensure high retrieval efficiency in the case that the single-mode fiber is used to couple the retrieved photon, the Fresnel number $F \equiv A/(\lambda L)$ should be kept around 1 [82,86].

1.1.2 Retrieval of the Stored Collective Excitation

In the read process, a strong resonant classical light pulse is applied to the atomic ensemble which will convert the collective excitation state (Eq. 1.15) to an anti-Stokes photon $\mathbf{E}_{\mathrm{AS}}$ while leaving an atomic vacuum state $|0_{\mathrm{a}}\rangle$. Since the read beam is strong, the emitted anti-Stokes photon will not be absorbed due to the EIT [87].

Now we focus on the situation that the read light and the write light counter-propagate as shown in Fig. 1.2. The wave vector of the read light is given by $\mathbf{k}_{\mathrm{R}} = -k_{\mathrm{R}}\hat{z}$, and the spatial wave function of the anti-Stokes field is

$$\begin{aligned} E_{\mathrm{AS}}(\mathbf{r}'-\mathbf{r}_j) =& \frac{1}{\sqrt{N}} \sum_j^N e^{i\Delta\mathbf{k}\cdot\mathbf{r}_j} e^{i\mathbf{k}_{\mathrm{R}}\cdot\mathbf{r}_j} \frac{\varepsilon_{\mathrm{AS}}}{|\mathbf{r}'-\mathbf{r}_j|} e^{i\mathbf{k}_{\mathrm{AS}}\cdot(\mathbf{r}'-\mathbf{r}_j)} \\ =& \frac{1}{\sqrt{N}} \sum_j^N e^{i(\mathbf{k}_{\mathrm{W}}-\mathbf{k}_{\mathrm{S}}+\mathbf{k}_{\mathrm{R}}-\mathbf{k}_{\mathrm{AS}})\cdot\mathbf{r}_j} \frac{\varepsilon_{\mathrm{AS}}}{|\mathbf{r}'-\mathbf{r}_j|} e^{i\mathbf{k}_{\mathrm{AS}}\cdot\mathbf{r}'}, \end{aligned} \tag{1.16}$$

in which the phase from the collective excitation state and from the read light are also included. If the phase of all the fields match, i.e., $\mathbf{k}_{\mathrm{W}} - \mathbf{k}_{\mathrm{S}} + \mathbf{k}_{\mathrm{R}} - \mathbf{k}_{\mathrm{AS}} = 0$, the term containing $\mathbf{r}_j$ vanishes yielding constructive interference. In other words, the anti-Stokes photon appears more likely on the detection surface where the phase matching condition holds. With the phase matching condition and the paraxial approximation, the anti-Stokes field is then

$$\begin{aligned} E_{\mathrm{AS}}(\mathbf{r}'-\mathbf{r}_j) \simeq& \frac{1}{\sqrt{N}} \sum_j^N \frac{\varepsilon_{\mathrm{AS}}}{|z'|} \exp\left[ik_{\mathrm{AS}}\left(|z'| + \frac{y'^2+x'^2}{2|z'|}\right)\right] \\ =& \sqrt{N} c_{\mathrm{AS}}(\mathbf{r}'), \end{aligned} \tag{1.17}$$

with the coefficient $c_{\mathrm{AS}}(\mathbf{r}') = \varepsilon_{\mathrm{AS}}/|z'| \exp[ik_{\mathrm{AS}}(2z'^2 + y'^2 + x'^2)/(2|z'|)]$, and the wave vector $\mathbf{k}_{\mathrm{AS}} \simeq -k_{\mathrm{AS}}\hat{z}$. It can be seen clearly that the intensity of the phase-matched anti-Stokes field gets an enhancement by a factor of N, the number of atoms.

Assuming γ is the emission rate for a single particle, the emission rate of the phase-matched anti-Stokes field could be then estimated as $NNd\Omega\gamma\xi_\alpha$, where $d\Omega \simeq \lambda^2/A$ is the small detection solid angle estimated by the Gaussian beam profile of the anti-Stokes field, and ξ_α is the branching ratio of the transition relating to a chosen polarization. In a similar way, the emission rate for the field other than the phase-matched one is described as $N(4\pi - d\Omega)\gamma$. Thus, the retrieval efficiency can be estimated as

$$\begin{aligned} \eta \sim& \frac{NNd\Omega\gamma\xi_\alpha}{NNd\Omega\gamma\xi_\alpha + N(4\pi - d\Omega)\gamma} \\ \simeq& 1 - \frac{1}{\mathrm{od}\xi_\alpha/6 + 1}, \end{aligned} \tag{1.18}$$

where $\mathrm{od} = \rho\sigma L = 3N\lambda^2/(2\pi A)$ is the optical depth for Rubidium 87 measured via the cycling transition $|F = 2, m_F = +2\rangle \to |F' = 3, m'_F = +3\rangle$ with the cross section $\sigma = 3\lambda^2/(2\pi)$ [3]. When the atomic ensemble is optically thick, the retrieval efficiency is expected to be close to unity. And after the read process, the Stokes and anti-Stokes state can be expressed as

$$|\psi\rangle = \left(1 + \sqrt{\chi}\hat{a}^\dagger_{\mathrm{AS}}\hat{a}^\dagger_{\mathrm{S}}\right)|\mathrm{vac}\rangle + o(\chi). \tag{1.19}$$

A more detailed analysis can be done with dark-state polariton theory which yields the same results [88].

1.1.3 Non-classical Correlation

To distinguish between classical and quantum behaviours of the light, the second-order coherence correlation has to be analyzed. This requires the application of the second-order perturbation theory to the Stokes and anti-Stokes state which yields

$$\begin{aligned}|\psi\rangle =& \left[1+\sqrt{\chi}\hat{a}^{\dagger}_{\mathrm{AS}}\hat{a}^{\dagger}_{\mathrm{S}}+\frac{\chi}{2}\hat{a}^{\dagger 2}_{\mathrm{AS}}\hat{a}^{\dagger 2}_{\mathrm{S}}\right]|\mathrm{vac}\rangle + o(\chi^{3/2}) \\ =& |0_{\mathrm{S}}0_{\mathrm{AS}}\rangle + \sqrt{\chi}|1_{\mathrm{S}}1_{\mathrm{AS}}\rangle + \chi|2_{\mathrm{S}}2_{\mathrm{AS}}\rangle + o(\chi^{3/2}), \end{aligned} \tag{1.20}$$

with $|n_{\mathrm{S}}n_{\mathrm{AS}}\rangle$ $(n=0,1,2)$ the photon number states [89].

For further analysis, the following functions are introduced [90, 91], including the second-order cross-correlation function for Stokes and anti-Stokes photons

$$g^{(2)}_{\mathrm{S,AS}} = \frac{\langle a^{\dagger}_{\mathrm{AS}}a^{\dagger}_{\mathrm{S}}a_{\mathrm{S}}a_{\mathrm{AS}}\rangle}{\langle a^{\dagger}_{\mathrm{S}}a_{\mathrm{S}}\rangle\langle a^{\dagger}_{\mathrm{AS}}a_{\mathrm{AS}}\rangle}, \tag{1.21}$$

the second-order self-correlation functions

$$g^{(2)}_{\mathrm{S}} = \frac{\langle a^{\dagger}_{\mathrm{S}}a^{\dagger}_{\mathrm{S}}a_{\mathrm{S}}a_{\mathrm{S}}\rangle}{\langle a^{\dagger}_{\mathrm{S}}a_{\mathrm{S}}\rangle^2}, \tag{1.22}$$

$$g^{(2)}_{\mathrm{AS}} = \frac{\langle a^{\dagger}_{\mathrm{AS}}a^{\dagger}_{\mathrm{AS}}a_{\mathrm{AS}}a_{\mathrm{AS}}\rangle}{\langle a^{\dagger}_{\mathrm{AS}}a_{\mathrm{AS}}\rangle^2}, \tag{1.23}$$

and the Cauchy-Schwarz inequality

$$g^{(2)}_{\mathrm{S}}g^{(2)}_{\mathrm{AS}} \geq \left[g^{(2)}_{\mathrm{S,AS}}\right]^2. \tag{1.24}$$

The inequality should hold for any classical light, however, would be violated for quantum coherence. In the case of the Stokes and anti-Stokes state described in Eq. 1.20 with $\chi \ll 1$ to keep the process within the spontaneous regime, the second-order self-correlation functions catch the values $g^{(2)}_{\mathrm{S}} = g^{(2)}_{\mathrm{AS}} \simeq 2\chi^2/(\chi^2+4\chi^3+4\chi^4) \simeq 2$, and the second-order cross-correlation function $g^{(2)}_{\mathrm{S,AS}} \simeq (\chi+4\chi^2)/(\chi^2+4\chi^3+4\chi^4) \simeq 1/\chi$. This implies the failure of satisfying the inequality, a direct evidence for the presence of quantum correlation between the Stokes and the anti-Stokes photon.

1.1.4 Quantum Memory Storage Lifetime

The quantum memory storage lifetime is a critical parameter which affects the performance of the system, such as the communication distance for a quantum repeater, and the number of operation steps for a quantum computer [92]. It is defined as the time interval after which the retrieval efficiency drops to $1/e$ of the original value. There are several decoherence mechanisms that limit the storage lifetime, such as spin-wave dephasing induced by inhomogeneity of the magnetic field and thermal atomic motion, and loss of atoms in the collection mode induced by thermal atomic motion and gravity. After all these problems are attacked, a memory of 16 s is reported by using an optical lattice to localize the atoms, a constant magnetic field to compensate the differential Stark shift, and the dynamic decoupling microwave pulses [93].

1.1.4.1 Inhomogeneity of Magnetic Field-Induced Dephasing

The most investigated mechanism is spin-wave dephasing induced by inhomogeneity of the magnetic field over the whole illuminated region of the atomic ensemble. When a residual magnetic field exists, the spin-wave state (Eq. 1.15) evolves with an additional phase

$$\hat{S}^{\dagger}(t)|0_{\mathrm{a}}\rangle = \frac{1}{\sqrt{N}} \sum_{j}^{N} e^{i\Delta\mathbf{k}\cdot\mathbf{r}_j} e^{-i(\omega_{sg}+\Delta\omega_j)t} |g...s_j...g\rangle, \tag{1.25}$$

where $\Delta\omega_j = (E_s^j - E_g^j - E_{sg})/\hbar$ is induced by the Zeeman effect with E_{sg} the energy difference between the two ground states without the residual magnetic field. Thus, the anti-Stokes field evolves to

$$E_{\mathrm{AS}}(\mathbf{r}' - \mathbf{r}_j, t) \simeq \frac{1}{\sqrt{N}} \sum_{j}^{N} c_{\mathrm{AS}}(\mathbf{r}') e^{-i(\omega_{sg}+\Delta\omega_j)t} \tag{1.26}$$

and the retrieval efficiency is estimated as

$$\begin{aligned} \eta(t) \sim & \frac{\frac{1}{N} f_N d\Omega\gamma}{\frac{1}{N} f_N d\Omega\gamma + (4\pi - d\Omega)\gamma} \\ \simeq & 1 - \frac{1}{1 + \frac{1}{4\pi N} f_N d\Omega}, \end{aligned} \tag{1.27}$$

where $f_N = |\sum_j^N \exp[-i(\omega_{sg}+\Delta\omega_j)t]|^2$ results from the interference and the branching ratio is neglected for simplicity. The factor f_N can be expanded as

$$\begin{aligned} f_N =& \left| \sum_j^N e^{-i(\omega_{sg}+\Delta\omega_j)t} \right|^2 \\ =& N + \sum_{j\neq j'}^N \cos(\Delta\omega_j t - \Delta\omega_{j'} t) \\ =& N + N(N-1)\,\overline{\cos(\Delta\omega_j t - \Delta\omega_{j'} t)} \\ =& N^2\,\overline{\cos(\Delta\omega_j t - \Delta\omega_{j'} t)}, \end{aligned} \tag{1.28}$$

where $\overline{\cos(\Delta\omega_j t - \Delta\omega_{j'} t)}$ represents the arithmetic mean.

A homogeneous residual magnetic field does not influence the retrieval efficiency, since the arithmetic mean is equal to unity which results in $f_N = N^2$. However, the retrieval efficiency will be affected by a magnetic field which is inhomogeneous since the phase of each atom evolves differently and the arithmetic mean is no longer one. According to the central limit theorem, for large N, one can assume the energy shift of each atom, $\Delta E_{sg}^j = E_s^j - E_g^j - E_{sg}$, obeys the normal distribution

$$f(\Delta E_{sg}) = \frac{1}{\sigma_{\rm sd}\sqrt{2\pi}} e^{-\frac{\Delta E_{sg}{}^2}{2\sigma_{\rm sd}^2}}, \tag{1.29}$$

where $\sigma_{\rm sd}$ represents the standard deviation and the mean is set to zero. The arithmetic mean can then be calculated with the distribution function

$$\begin{aligned} \overline{\cos(\Delta\omega_j t - \Delta\omega_{j'} t)} =& \int_{-\infty}^{+\infty}\int_{-\infty}^{+\infty} f(x)f(y)\,\cos\left(\frac{xt}{\hbar} - \frac{yt}{\hbar}\right) dxdy \\ =& e^{-\frac{\sigma_{\rm sd}^2 t^2}{\hbar^2}}. \end{aligned} \tag{1.30}$$

If the optical depth is small (on the order of ones) so that $Nd\Omega \exp(-\sigma_{\rm sd}^2 t^2/\hbar^2)/(4\pi) < 1$, the retrieval efficiency is estimated as

$$\begin{aligned} \eta(t) \sim& 1 - \frac{1}{1 + \frac{Nd\Omega}{4\pi} e^{-\frac{\sigma_{\rm sd}^2 t^2}{\hbar^2}}} \\ \simeq& 1 - \left(1 - \frac{Nd\Omega}{4\pi} e^{-\frac{\sigma_{\rm sd}^2 t^2}{\hbar^2}}\right) \\ =& \frac{Nd\Omega}{4\pi} e^{-\frac{\sigma_{\rm sd}^2 t^2}{\hbar^2}}. \end{aligned} \tag{1.31}$$

Consequently, the storage lifetime limited by inhomogeneity of the magnetic field is

$$\tau_{\text{inh}} = \frac{\hbar}{\sigma_{\text{sd}}}. \tag{1.32}$$

In the experiments, the ground states are normally chosen from the hyperfine level $|5^2S_{1/2}, F=1\rangle$ and $|5^2S_{1/2}, F=2\rangle$ of Rubidium 87. By considering only the first-order Zeeman shift, the storage lifetime for each pair is calculated and shown in Tab. 1.1, under the condition of 5 mG standard deviation of the magnetic field which is a typical inhomogeneity value in our lab over a distance of 1 mm. This explains to some extent the reason of the short lifetime measured in the paper [92] which is about 14 μs, where $|F=2, m_F=+2\rangle$ and $|F=1, m_F=0\rangle$ are used as the ground states.

TABLE 1.1: Storage lifetime (μs) for different ground-state pairs.

$F=2$ $F=1$	$m_F=-2$	$m_F=-1$	$m_F=0$	$m_F=+1$	$m_F=+2$
$m_F=-1$	15.2	22.7	45.5	$+\infty$	
$m_F=0$	22.7	45.5	$+\infty$	45.5	22.7
$m_F=+1$		$+\infty$	45.5	22.7	15.2

Taking a closer look at Tab. 1.1, one finds three pairs, the so-called "clock states", which provide infinitely long lifetime, $(|F=2, m_F=-1\rangle, |F=1, m_F=+1\rangle)$, $(|F=2, m_F=0\rangle, |F=1, m_F=0\rangle)$, and $(|F=2, m_F=+1\rangle, |F=1, m_F=-1\rangle)$. However, it is no longer true after considering higher-order effects. For the ground-state manifold of Rubidium 87 atoms, the energy shift can be estimated by using the Breit-Rabi formula [94]

$$E = -\frac{\Delta E_{\text{hfs}}}{2(2I+1)} + \mu_{\text{B}} g_I m_F B \pm \frac{\Delta E_{\text{hfs}}}{2}\sqrt{1 + \frac{4m_F x}{2I+1} + x^2}, \tag{1.33}$$

where μ_{B} is the Bohr magneton, $x = \mu_{\text{B}} B(g_J - g_I)/\Delta E_{\text{hfs}}$ is referred to as the field strength parameter with g_J and g_I the Landé factors, and the ± sign is negative for $F=1$ and positive for $F=2$. Note that, when $m_F=-2$ the square root is an exact square which is interpreted as $1-x$. Fig. 1.3(a) shows the relation between energy shift ΔE_{sg} and the applied magnetic field B for clock states. When the slope of the relation curve goes to zero, the standard deviation of the energy shift will vanish according to the error propagation function [95], thus with the Gaussian distribution assumption one gets infinitely long lifetime at these points. Fig. 1.3(b) presents the storage lifetime τ_{inh} as a function of the magnetic field with 5 mG standard deviation. And the infinitely long storage lifetime for $(|F=2, m_F=-1\rangle, |F=1, m_F=+1\rangle)$, $(|F=2, m_F=0\rangle, |F=1, m_F=0\rangle)$, and $(|F=2, m_F=+1\rangle, |F=1, m_F=-1\rangle)$ will appear at -3.22892 G, 0 G, and 3.22892 G, respectively.

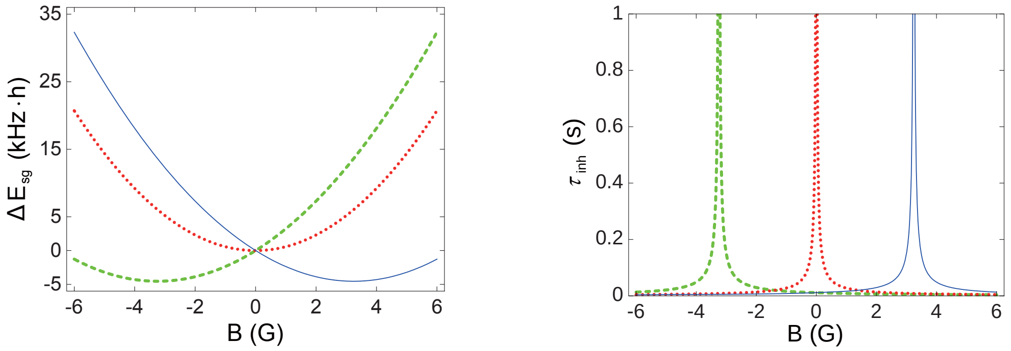

(a) Energy shift (b) Storage lifetime

Figure 1.3: Energy shift and storage lifetime as a function of the magnetic field for clock states. The green dashed line represents the result of ($|F=2, m_F=-1\rangle, |F=1, m_F=+1\rangle$), the red dotted line ($|F=2, m_F=0\rangle, |F=1, m_F=0\rangle$), and the blue solid line ($|F=2, m_F=+1\rangle, |F=1, m_F=-1\rangle$). (a) shows the energy shift ΔE_{sg} as a function of magnetic field. (b) shows the storage lifetime τ_{inh} as a function of the magnetic field with the standard deviation 5 mG. It implies that the storage lifetime could reach the order of seconds if certain magnetic field is applied.

1.1.4.2 Thermal Atomic Motion-Induced Dephasing

Thermal atomic motion is another reason which results in spin-wave dephasing, thus limits the storage lifetime. Since the temperature of the atomic ensemble is finite, the momentum of each atom obeys the Maxwell-Boltzmann distribution. After a time of t, the j-th atom moves to $\mathbf{r}_j + \Delta\mathbf{r}_j(t)$, and the spin-wave state evolves to

$$\hat{S}^{\dagger}(t)|0_{\text{a}}\rangle = \frac{1}{\sqrt{N}}\sum_j^N e^{i\Delta\mathbf{k}\cdot\mathbf{r}_j} e^{i\Delta\mathbf{k}\cdot\Delta\mathbf{r}_j(t)}|g...s_j...g\rangle. \tag{1.34}$$

The collection mode of the retrieved anti-Stokes photon was set to be the one in ideal case, therefore the phase induced by thermal motion will be passed to the anti-Stokes field

$$E_{\text{AS}}(\mathbf{r}' - \mathbf{r}_j, t) \simeq \frac{1}{\sqrt{N}}\sum_j^N c_{\text{AS}}(\mathbf{r}')e^{i\Delta\mathbf{k}\cdot\Delta\mathbf{r}_j(t)}. \tag{1.35}$$

And the retrieval efficiency is estimated as

$$\eta(t) \sim 1 - \frac{1}{1 + f_N^{\text{th}}\frac{d\Omega}{4\pi N}}, \tag{1.36}$$

where the interference factor $f_N^{\text{th}} = |\sum_j^N e^{i\Delta\mathbf{k}\cdot\Delta\mathbf{r}_j(t)}|^2$ which can be expanded as

$$f_N^{\text{th}} = N^2\,\overline{\cos(\Delta\mathbf{k}\cdot\Delta\mathbf{r}_j(t) - \Delta\mathbf{k}\cdot\Delta\mathbf{r}_{j'}(t))}. \tag{1.37}$$

Considering only the motion along the spin-wave direction which is the main contribution, the scalar product can be reduced. The velocity distribution along the direction of the wave vector of the spin-wave has a normal distribution form

$$f_{\mathrm{vel}}(v) = \frac{1}{v_{\mathrm{sd}}\sqrt{2\pi}} e^{-\frac{v^2}{2v_{\mathrm{sd}}^2}}, \tag{1.38}$$

with $v_{\mathrm{sd}} = \sqrt{k_{\mathrm{B}}T/m}$ and k_{B} the Boltzmann constant. Then the retrieval efficiency can be calculated as

$$\begin{aligned} \eta(t) \sim& 1 - \frac{1}{1 + \frac{Nd\Omega}{4\pi} e^{-\Delta k^2 v_{\mathrm{sd}}^2 t^2}} \\ \simeq& \frac{Nd\Omega}{4\pi} e^{-\Delta k^2 v_{\mathrm{sd}}^2 t^2}, \end{aligned} \tag{1.39}$$

with $\Delta k = |\mathbf{k}_{\mathrm{W}} - \mathbf{k}_{\mathrm{S}}|$. And the storage lifetime limited by the thermal motion is

$$\tau_{\mathrm{th}} = \frac{1}{\Delta k v_{\mathrm{sd}}}. \tag{1.40}$$

The wave vector of the spin-wave Δk implies the existence of a wavelength of the spin-wave in the form of $\lambda_{\mathrm{sw}} = 2\pi/\Delta k$. And the decoherence mechanism due to the thermal motion can be safely neglected as long as the thermal motion is small compared to λ_{sw}.

For our experimental parameters where the energy difference between two ground states is $h \times 6.8$ GHz and the D-1 transition is employed, the wave vector of the spin-wave can be estimated as $\Delta k \simeq k_{\mathrm{W}}\theta$ when the detection angle between $\mathbf{k}_{\mathrm{W}}$ and $\mathbf{k}_{\mathrm{S}}$ is small. Then the storage lifetime is inversely proportional to the angle θ. For a given temperature of 100 μK, the relation between the storage lifetime τ_{th} and the angle θ is depicted in Fig. 1.4. The maximal storage lifetime of 71.4 ms appears when the angle goes to zero, at which the wavelength of the spin-wave is equal to 43.9 mm. When the angle is 3°, the storage lifetime is 24.7 μs which is one of the reasons limiting the storage performance in the paper [92]. In order to weaken the mechanism, further confinement is suggested, for example, an optical lattice [96].

1.1.4.3 Loss of Atoms in Collection Mode

Apart from the spin-wave dephasing mechanism, loss of atoms also plays an important role which limits the storage lifetime. Since the mode of the anti-Stokes photon collection is fixed, any motion, which forces the atoms to fly out of the collection area, will affect the retrieval efficiency by decreasing the number of effective atoms. As discussed above, when the optical depth is small, the retrieval efficiency scales as the number of atoms in the collection mode. For this reason, the storage lifetime due to the loss of atoms could

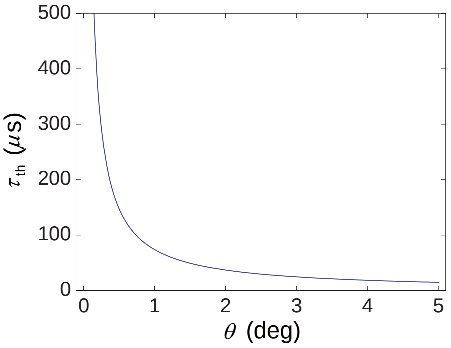

FIGURE 1.4: Storage lifetime τ_{th} as a function of the detection angle θ.

be estimated as the time interval after which the effective number of atoms drops to $1/e$ of the initial value.

There are two main reasons, gravitational motion and thermal atomic motion, which are responsible for loss of atoms. In practice, all the fields including write, read, Stokes, and anti-Stokes are either emitted or collected with single-mode fibers that approximate to the fundamental Gaussian mode. Therefore, the retrieval efficiency can be estimated as the ratio of overlapping the fundamental Gaussian mode of the expected anti-Stokes field and the one of the actual field due to the motion of atoms. For the ease of alignment, the anti-Stokes field propagates perpendicular to the direction of the gravity in most of the experiments. And the effect induced by the motion along the propagating direction of the field can be ignored since it is much smaller than the Rayleigh length of the mode. As a result, the retrieval efficiency and the storage lifetime can be expressed as

$$\eta(t) \sim \frac{N d\Omega}{4\pi} e^{-\frac{g^2 t^4}{4\mathrm{w}_0^2}}, \tag{1.41}$$

$$\tau_{\mathrm{grav}} = \sqrt{\frac{2\mathrm{w}_0}{g}}, \tag{1.42}$$

with g the standard gravity, and w_0 the beam waist. In our experiments, the anti-Stokes field has a waist of 100 μm, which yields the storage lifetime 4.5 ms. It is intuitive that one would benefit if the collection modes are arranged along the direction of the gravity.

For thermal atomic motion-induced loss, by assuming the expansion of the atomic cloud obeys the Maxwell-Boltzmann distribution, one could get the retrieval efficiency and the storage lifetime

$$\eta(t) \sim \frac{N d\Omega}{4\pi} \frac{\mathrm{w}_0^2}{\mathrm{w}_0^2 + v_{\mathrm{prob}}^2 t^2}, \tag{1.43}$$

$$\tau_{\mathrm{thloss}} = \frac{\sqrt{e-1}\,\mathrm{w}_0}{v_{\mathrm{prob}}}, \tag{1.44}$$

with $v_{\text{prob}} = \sqrt{2k_{\text{B}}T/m}$ the most probable speed. With our experimental parameter, the temperature of 100 μK, the storage lifetime due to thermal atomic motion is being 0.9 ms.

1.2 Quantum Repeater with Cold Atomic Ensembles

Generation of entanglement is a crucial part of quantum information science. The write and read process provides an effective way to realize a quantum interface between the photonic qubits and the stationary qubits. By applying the knowledge of the quantum memory, I will present the generation of entanglement based on the single-photon interference DLCZ protocol [39], and on an improved protocol employing two-photon interference [60]. The entanglement swapping [36] to extend the quantum communication distance and the atom-atom entanglement are also discussed.

1.2.1 The DLCZ Protocol

In the DLCZ protocol, two distant ensembles (A and B) are excited by two write pulses simultaneously, as shown in Fig. 1.5(a). The forward-scattered Stokes photons are collected and guided to two single photon detectors (D_1 and D_2) via a non-polarizing beam splitter (BS) to erase the path information. A click in either D_1 or D_2 states that the system of ensembles is in the entangled state

$$\begin{aligned}|\psi_{\text{a}}\rangle =&\frac{1}{\sqrt{2}}\left(\hat{S}_A^\dagger + e^{i\phi}\hat{S}_B^\dagger\right)|0_{\text{a}}\rangle_A|0_{\text{a}}\rangle_B \\ =&\frac{1}{\sqrt{2}}\left[\left(\hat{S}_A^\dagger|0_{\text{a}}\rangle_A\right)|0_{\text{a}}\rangle_B + e^{i\phi}|0_{\text{a}}\rangle_A\left(\hat{S}_B^\dagger|0_{\text{a}}\rangle_B\right)\right],\end{aligned} \tag{1.45}$$

where the phase ϕ accounts for the phase difference between the two channels.

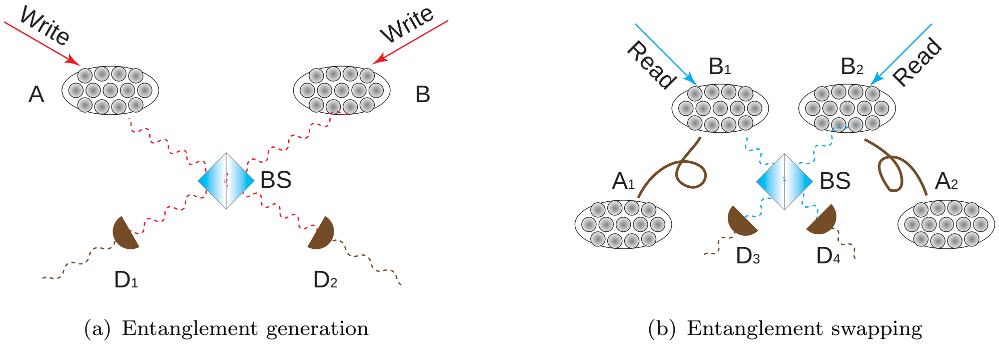

(a) Entanglement generation

(b) Entanglement swapping

FIGURE 1.5: Entanglement generation and swapping in the DLCZ protocol.

After the entanglement is established, one can simply extend it by performing entanglement swapping as depicted in Fig. 1.5(b). As a first condition, entanglement has been generated between ensemble A_1 and B_1, and between ensemble A_2 and B_2, respectively, before the application of entanglement swapping. Read pulses are applied to the ensemble B_1 and B_2 to convert the atomic excitations into photons which are detected by single-photon detectors D_3 and D_4 after interfering at a BS. The entanglement between A_1 and A_2 will be then established after a click is recorded either in D_3 or D_4.

The feasibility of the protocol relies on the phase stability. However, the single-photon Mach-Zehnder interference is involved both in the generation and swapping procedures, which is sensitive to the fluctuations of the beam path length. To make the protocol work, the phase has to be stabilized at the level of $\lambda/10$, with $\lambda \sim 1\ \mu$m typically, over a time scale of a few tens of second [97], which is rather difficult to achieve even with up-to-date technology.

1.2.2 Robust Scheme Resistant to Phase Noise

The phase fluctuations prohibit the practical use of the DLCZ protocol. To get around the problem, Bo Zhao and his colleagues proposed the idea of taking two-photon Hong-Ou-Mandel-type interference instead [97]. The basic element of the improved protocol is to locally create entanglement between the spacial mode of the spin-wave and the polarization of the signal photon as shown in Fig. 1.6. Take site A as an example, two atomic ensembles labelled as “top” and “bottom” are illuminated by write pulses. With a small probability, one scattered Stokes photon either from the top or the bottom ensemble will pass through a polarizing beam splitter (PBS) possessing the vertical polarization (V) or horizontal polarization (H), respectively. The whole system of site A can be expressed as

$$|\psi\rangle_A = \frac{1}{\sqrt{2}}\left(\hat{S}^\dagger_{A,\mathrm{t}}\hat{a}^\dagger_{A,\mathrm{t},V} + e^{i\phi_{A,HV}}\hat{S}^\dagger_{A,\mathrm{b}}\hat{a}^\dagger_{A,\mathrm{b},H}\right)|\mathrm{vac}\rangle_A, \tag{1.46}$$

where $\phi_{A,HV}$ denotes the phase difference induced by the beam path difference between H and V, and the subscript “t” (“b”) denotes top (bottom). Note that the phase different $\phi_{A,HV}$ can be easily compensated since the generation of entanglement in the improved protocol is local.

In a second stage, these local atom-photon entangled states are later converted into remote atom-atom entanglement by use of two-photon interference. As depicted in Fig. 1.6, after the atom-photon entanglement is prepared in both sites and the phase difference is compensated properly, the two scattered photons are sent to a Bell-state analyzer (BSA) type-I consisting of a PBS± (transmits positively polarized photons

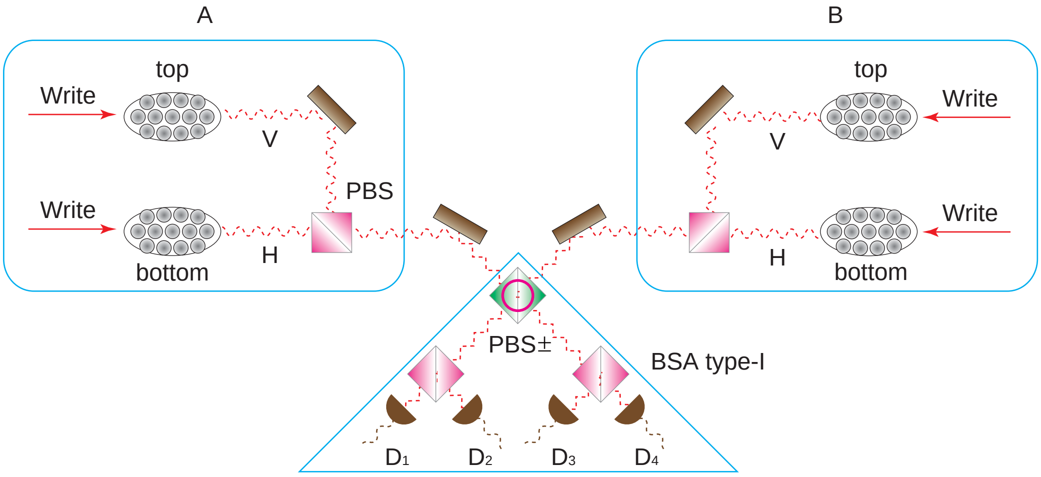

FIGURE 1.6: Creation of remote atom-atom entanglement with the improved protocol.

$|+\rangle = 1/\sqrt{2}(|H\rangle + |V\rangle)$, while reflects negatively polarized photons $|-\rangle = 1/\sqrt{2}(|H\rangle - |V\rangle)$), two PBSs, and four single-photon detectors. The BSA will project the photons into a Bell state and thus leave the ensembles entangled in a corresponding way. For instance, a detected coincidence between D_1 and D_4 heralds that the two sites are entangled in the state

$$\begin{aligned}|\psi\rangle_{AB} =& \frac{1}{\sqrt{3}} e^{i(\phi_A+\phi_B)} \left(\hat{S}^\dagger_{A,\mathrm{t}}\hat{S}^\dagger_{B,\mathrm{t}} + \hat{S}^\dagger_{A,\mathrm{b}}\hat{S}^\dagger_{B,\mathrm{b}}\right) |0_\mathrm{a}\rangle_A |0_\mathrm{a}\rangle_B \\ &+ \frac{1}{2\sqrt{3}} e^{i2\phi_A} \left(\hat{S}^\dagger_{A,\mathrm{t}}\hat{S}^\dagger_{A,\mathrm{t}} - \hat{S}^\dagger_{A,\mathrm{b}}\hat{S}^\dagger_{A,\mathrm{b}}\right) |0_\mathrm{a}\rangle_A |0_\mathrm{a}\rangle_A \\ &+ \frac{1}{2\sqrt{3}} e^{i2\phi_B} \left(\hat{S}^\dagger_{B,\mathrm{t}}\hat{S}^\dagger_{B,\mathrm{t}} - \hat{S}^\dagger_{B,\mathrm{b}}\hat{S}^\dagger_{B,\mathrm{b}}\right) |0_\mathrm{a}\rangle_B |0_\mathrm{a}\rangle_B, \end{aligned} \tag{1.47}$$

where ϕ_A (ϕ_B) represents the phase that the photon acquires during the propagation from site A (B) to the BSA. The first term is the expected maximally entangled state where the propagation phase is the global phase of the state, thus has no effect to the system. However, second-order excitations of site A and site B contribute to the second term and the third term, respectively, which limit the further use of the state. Fortunately, the unexpected two-photon excitation terms can be automatically washed out by a carefully designed BSA in the entanglement swapping step [97]. The only requirement from the two-photon interference is to keep the two photons coherent before they meet at the BSA, which implies that the phase fluctuations are within one tenth of the coherence length (on the order of 10 m for Rubidium atomic ensembles). Thus the improved protocol relaxes the stability requirements by 7 orders of magnitude.

The entanglement swapping used to extend the atom-atom entanglement is similar to the DLCZ protocol as shown in Fig. 1.7. Two pairs of the entangled atomic ensembles are prepared, say A_1-B_1 and A_2-B_2. The retrieved photons from B_1 and B_2 are sent to the BSA type-II which results in an entanglement between A_1 and A_2 when coincidence count between D_1 and D_3, D_1 and D_4, D_2 and D_3, or D_2 and D_4 is registered. Note that no expected coincidence would be registered if the two photons come from one site due to the PBS. The connection method can be cascaded to arbitrarily extend the communication distance.

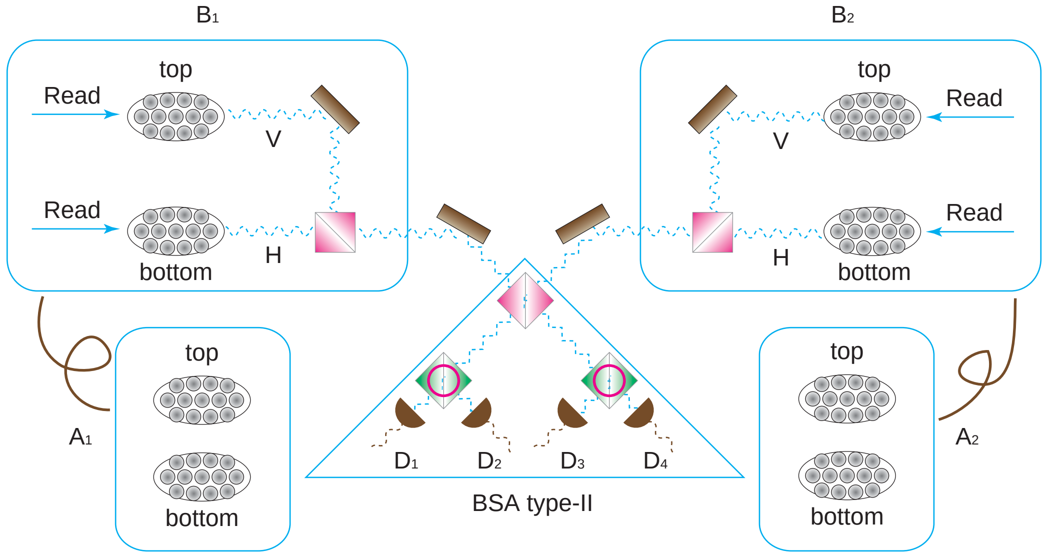

FIGURE 1.7: Entanglement connection with the improved protocol.

Compared with the DLCZ protocol, the improved protocol is insensitive to the fluctuations of path length. However, the success probability is on the order of $\chi^2\eta_{\mathrm{d}}^2$ with χ the excitation probability and η_{d} the detection efficiency, which is much less than the success probability of the DLCZ protocol ($\sim \chi\eta_{\mathrm{d}}$). In practice, although the excitation probability is small, the repetition rate of the excitation process can be quite large which remedies the negative effects.

1.3 Experimental Setup for Atomic-Ensemble-Based Quantum Memory

The atomic-ensemble-based quantum memory is the essential element throughout the first four chapters. It is based on cold Rubidium 87 atoms which are localized in the so-called magneto-optical trap (MOT) [98]. In this thesis, a double-path scheme [60] is used to generate atom-photon entanglement, so that a single atomic ensemble is adequate instead of two presented in the last section. And a double-MOT setup is built in order to generate atom-atom entanglement.

1.3.1 Preparing Atomic Ensemble in a Magneto-Optical Trap

As one of the most useful technology, MOT has been utilized widely in the study of cold and ultra-cold quantum gases [99,100]. Generally speaking, MOT makes use of Doppler cooling as well as radiation pressure to push the atoms towards center. When an atom moves towards a properly red-detuned laser beam, it will absorb a photon, thus receives a momentum kick, due to the Doppler effect and then spontaneously emit a photon to an arbitrary direction. On average, it provides a friction force towards the opposite direction which slows down the atoms. When a magnetic quadrupole field is applied, atoms moving away from the center will have a higher probability to be kicked since the Zeeman shift drives the atomic resonance closer to the laser frequency. Typically, the atoms can be cooled down to the Doppler cooling limit $T_{\mathrm{D}} = \hbar\Gamma/(2k_{\mathrm{B}})$ [101], which is around 146 μK for Rubidium 87.

In practice, a MOT requires “cooler”, “repumper”, and magnetic quadrupole field. And the basic construction is illustrated in Fig. 1.8.

Cooler which is responsible for the damping force, is composed of three orthogonal pairs of counter-propagating laser beams with circular polarization. It is red-detuned by 17 MHz from the cycling transition of the D-2 line, i.e., $|5^2S_{1/2}, F = 2\rangle \rightarrow |5^2P_{3/2}, F' = 3\rangle$, and is stabilized by the Pound-Drever-Hall frequency modulation (FM) method [102]. And it has an intensity of 10 mW/cm^2 for each beam which is provided by a Toptica DLX110 laser.

Repumper is used to assist in keeping the cooling mechanism functional by exciting the atoms out of the “dark” state. It is tuned on resonance with the $|F = 1\rangle \rightarrow |F' = 2\rangle$ transition of the D-2 line and FM-locked. And it shines to the atomic ensemble through six directions as well. A Topica taperred amplifier (BoosTa) together with a homemade laser system are responsible for it.

Magnetic quadrupole field is composed of two coils in an anti-Helmholtz configuration winded around the cell. Each coil has 19 windings with a diameter of about 6 cm. The typical working current is 5 A which corresponds to a gradient of 10 G/cm.

For a more detailed description, please refer to the thesis [103].

1.3.2 Memory Built-in Atom-Photon Entanglement Source

An atom-photon entanglement source (or photon-matter entanglement source) is essential to the study of quantum information science due to its ability to store information.

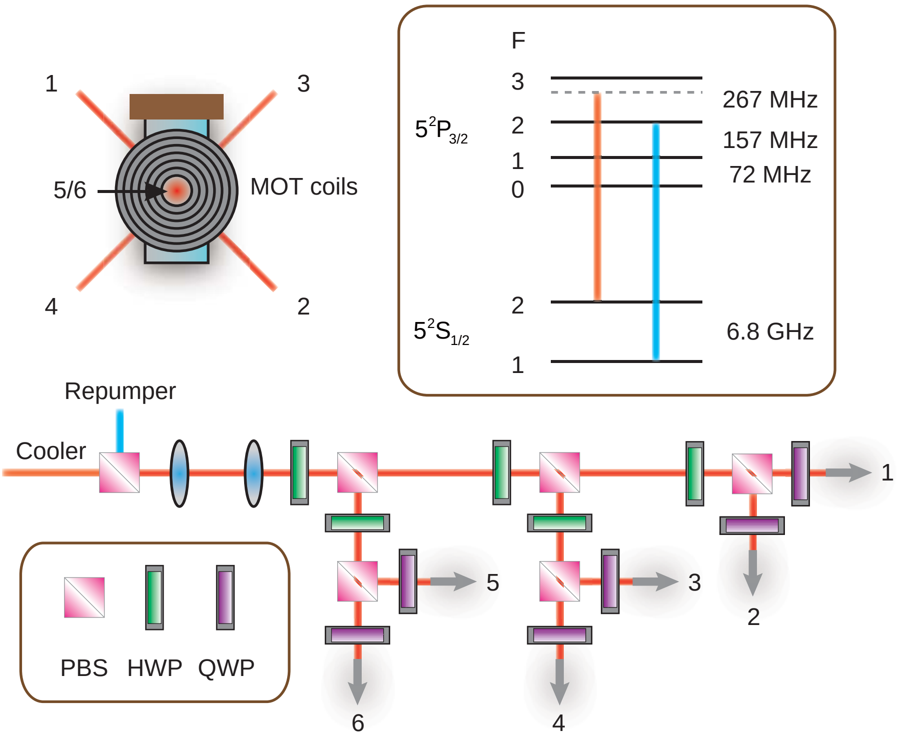

FIGURE 1.8: An illustration of the configuration of MOT. The cooler beam and the repumper beam are merged together via a PBS. After a telescope system to enlarge the beam waist, they are delivered into six ports with balanced cooler power. The frequencies of the cooler light and the repumper light are also depicted. HWP represents for half-wave plate, and QWP represents for quarter-wave plate.

In the past decade, a few methods of generating atom-photon entanglement have been developed including for example spin excitations to different magnetic sublevels [104,105] which is suffering from the different excitation efficiencies, and dual-species mixture [106] which is suffering from the low efficiency of frequency mixing. The atom-photon entanglement source in this thesis takes the idea from the paper [60] where a double-path scheme is applied. However, it is modified according to specific purposes, for example, the qubits are encoded into spatial modes in Chapter 4. Here the basic configuration will be illustrated.

The configuration of the atomic energy levels used for write and read is illustrated in Fig. 1.9. Two hyperfine ground states $|a\rangle = |5^2S_{1/2}, F = 2\rangle$ and $|b\rangle = |5^2S_{1/2}, F = 1\rangle$, and the excited state $|e\rangle = |5^2P_{1/2}, F = 2\rangle$ form a Λ-type system. The Rubidium 87 atoms are prepared initially in the state $|a, m_F = 0\rangle$ with the help of a π-pump beam. The write light is normally red-detuned by 15 MHz to the $F = 2 \rightarrow F' = 2$ transition of the D-1 line ($5^2S_{1/2} \rightarrow 5^2P_{1/2}$). The read light is tuned on resonance with the $F = 1 \rightarrow F' = 2$ transition of the D-1 line. Both of them can be switched on or off by a transistor-transistor logic (TTL) signal coming from a field-programmable gate array (FPGA) module.

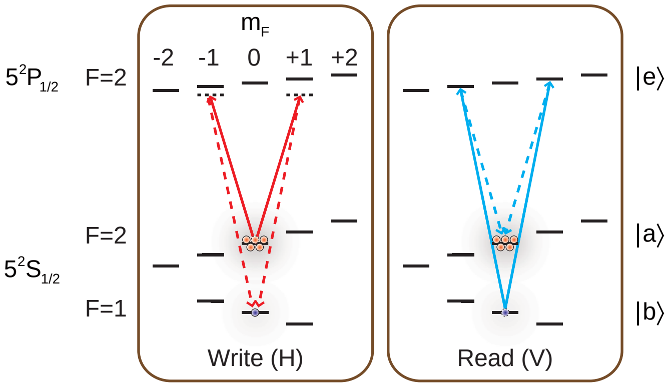

FIGURE 1.9: The Λ-type system of Rubidium 87 for write and read. The clock state $(|F=2, m_F=0\rangle, |F=1, m_F=0\rangle)$ is taken to achieve long lifetime. The write light is horizontally polarized in most of the case, and the scattered anti-Stokes signal photon is chosen to be orthogonally polarized. The read light is vertically polarized correspondingly, and the emitted idler photon has to be horizontally polarized under the condition of collective enhancement [89, 96]. The degeneracy is lifted when a magnetic bias field is applied.

The atom-photon entanglement source is illustrated in Fig. 1.10. The write pulse is chosen to be 50 ns long and 1 μW strong with a beam waist of 240 μm. The anti-Stokes signal photon is collected in two spatial modes with a beam waist of around 100 μm marked as "AS$_l$" and "AS$_r$", where the subscripts "l" and "r" denote left and right, respectively. The angle between the collection mode and the write beam is around 0.5° to 3° depending on the purpose. Later, the spatial mode information is converted to the polarizations through a PBS. Since the excitation probabilities are equal $\chi_l = \chi_r = \chi$, the atom-photon entanglement can be then described as

$$|\psi\rangle \sim \sqrt{\chi}\left(\hat{S}_l^\dagger \hat{a}_{\mathrm{AS},H}^\dagger + e^{i\phi_{\mathrm{AS}}}\hat{S}_r^\dagger \hat{a}_{\mathrm{AS},V}^\dagger\right)|\mathrm{vac}\rangle, \tag{1.48}$$

where ϕ_{AS} is the phase difference between two collection modes. According to the phase matching condition, the read light, which is counter-propagating with the write, will convert the spin-wave state into a corresponding Stokes idler photon with related wave vector. Thus the signal-idler state can be expressed as

$$|\psi\rangle_{\mathrm{AS,S}} = \frac{1}{\sqrt{2}}\left(|H\rangle_{\mathrm{AS}}|H\rangle_{\mathrm{S}} + e^{i\phi_{\mathrm{AS}}+\phi_{\mathrm{S}}}|V\rangle_{\mathrm{AS}}|V\rangle_{\mathrm{S}}\right). \tag{1.49}$$

To stabilize the phase $\phi_{\mathrm{AS}} + \phi_{\mathrm{S}}$, a positive polarized ($|+\rangle$) light named "locking beam" is applied into this Mach-Zehnder interferometer. The interference is detected and serves as a feedback signal to lock the phase by the aid of a moving mirror with piezoelectric ceramics (PIEZO). The phase information can be transferred to polarization information by simply rewriting the state in the basis $\{|+\rangle, |-\rangle\}$

$$|\psi\rangle_{\mathrm{AS,S}} = \frac{1}{2\sqrt{2}}\left[\left(1+e^{i\phi}\right)(|+\rangle|+\rangle + |-\rangle|-\rangle) + \left(1-e^{i\phi}\right)(|+\rangle|-\rangle + |-\rangle|+\rangle)\right], \tag{1.50}$$

where $\phi = \phi_{\text{AS}} + \phi_{\text{S}}$ represents the phase and the subscripts are neglected for simplicity. It can be readily seen that the phase can be compensated to zero by maximizing $|1 + e^{i\phi}|^2/|1 - e^{i\phi}|^2$ which is the ratio of coincidence counts of $|+\rangle|+\rangle$ and $|-\rangle|-\rangle$ to coincidence counts of $|+\rangle|-\rangle$ and $|-\rangle|+\rangle$. A QWP-HWP-QWP setup, which can shift the relative phase between horizontally polarized beam and vertically polarized beam, is responsible for phase compensation, and is placed at the idler field path with both QWPs set at 45° relative to the horizontal [103]. In fact, after the total propagating-induced phase is compensated, the phase ϕ_{AS} in the atom-photon entanglement can also be recognized as a fixed known phase, since the use of the spin-wave state always requires the retrieval process and operations are performed only after the phase is compensated.

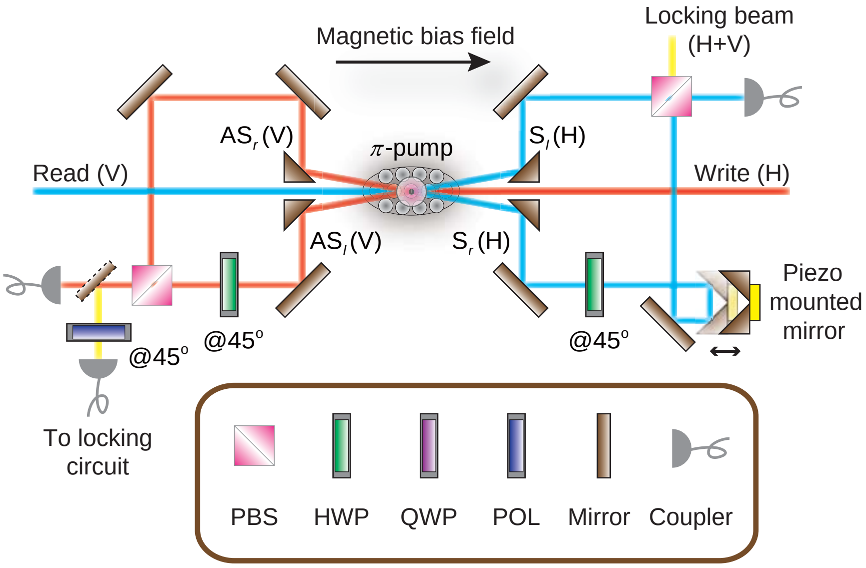

FIGURE 1.10: An schematic view of the atom-photon entanglement source. Magnetic bias field and linearly polarized π-pump beam (parallel to the bias field) are optional according to the purpose of the experiment, where the π-pump is tuned on resonance with the $|F = 2\rangle \to |F' = 2\rangle$ transition of the D-1 line. The signal photon and the idler photon are collected by the single-mode fibers which in turn helps to keep the mode matching condition. The locking beam is aligned a little bit higher than the signal and the idler fields so that it can be reflected by a small mirror illustrated with a dashed border. A polarizer (POL) set at 45° is used to align the polarization in order to obtain the interference.

1.3.3 Bell-State Analyzer

Bell states are maximally entangled states of two qubits, which can be expressed as

$$\begin{aligned}
|\Phi^{+}\rangle &= \frac{1}{\sqrt{2}}(|HH\rangle + |VV\rangle) = \frac{1}{\sqrt{2}}(|++\rangle + |--\rangle)\\
|\Phi^{-}\rangle &= \frac{1}{\sqrt{2}}(|HH\rangle - |VV\rangle) = \frac{1}{\sqrt{2}}(|+-\rangle + |-+\rangle)\\
|\Psi^{+}\rangle &= \frac{1}{\sqrt{2}}(|HV\rangle + |VH\rangle) = \frac{1}{\sqrt{2}}(|++\rangle - |--\rangle)\\
|\Psi^{-}\rangle &= \frac{1}{\sqrt{2}}(|HV\rangle - |VH\rangle) = \frac{1}{\sqrt{2}}(|+-\rangle - |-+\rangle).
\end{aligned} \tag{1.51}$$

They can be inspected by the BSA. In addition, this joint quantum-mechanical measurement will project the qubits, if they were not in a Bell state, into a Bell state.

Three types of BSAs are used in this thesis shown in Fig. 1.11. BSA type-I can detect the state $|\Phi^{+}\rangle$ (coincidence between D_1 and D_4, or D_2 and D_3) and $|\Psi^{+}\rangle$ (D_1 and D_3, or D_2 and D_4), since the first PBS± will only allow the two photons to appear in both of the output modes when they are in the state $|++\rangle$ or $|--\rangle$ and the following PBSs judge the H/V states. Similarly, BSA type-II can detect the state $|\Phi^{+}\rangle$ (D_1 and D_4, or D_2 and D_3) and $|\Phi^{-}\rangle$ (D_1 and D_3, or D_2 and D_4). BSA type-III can detect the state $|\Psi^{+}\rangle$ (D_1 and D_2, or D_3 and D_4) and $|\Psi^{-}\rangle$ (D_1 and D_3, or D_2 and D_4). Different from the first two types, the two photons cannot be separated by the BS unless they are in the state $|\Psi^{-}\rangle$ due to the interference [107]. All the BSAs used in this thesis can only distinguish two of the four Bell states. A complete analysis of the Bell states requires either hyperentangled states [108] or a nonlinear process such as the cross-Kerr effect [109].

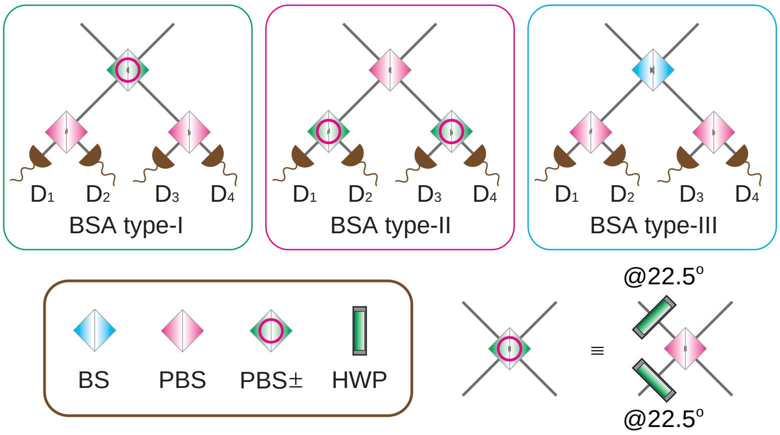

Figure 1.11: Three types of the Bell-state analyzers. A PBS± is composed of a PBS with HWP(s) set at 22.5° and placed in the input mode(s).

Chapter 2

Quantum Teleportation between Atomic-Ensemble Quantum Memories

Quantum teleportation and quantum memory are of great significance to large-scale quantum networks. With the help of quantum entanglement distributed in advance, quantum teleportation provides an intriguing way to transfer quantum states without actual transmission of the physical carriers [6]. It has been demonstrated with single photons [7, 110, 111], from light to matter [71, 112], and between single ions [21–23]. Quantum memory is required for scalability, which enables us to store and retrieve fast-flying photonic qubits with stationary matter.

In this chapter, I report on the realization of quantum teleportation between two remote atomic-ensemble-based quantum memory nodes connected by a 150 m optical fiber [113]. The spin-wave state of one of the atomic ensembles is mapped to the polarization state of a propagating photon, and then sent to a BSA performing Bell-state measurement (BSM) together with another photon which is entangled with the spin-wave state of the other atomic ensemble. In addition, the detection of two-photon coincidence heralds the success of the teleportation with an average fidelity of 88(7)%.

2.1 Scheme of the Experiment

The basic idea of quantum teleportation can be understood as follows. Suppose Alice and Bob stay apart, and they share a maximally entangled state beforehand which has the form of a Bell state, for instance, $|\Phi^+\rangle_{AB} = 1/\sqrt{2}(|0\rangle_A|0\rangle_B + |1\rangle_A|1\rangle_B)$ with $\{|0\rangle, |1\rangle\}$

representing the orthogonal basis, and the subscripts A and B referring to Alice's and Bob's particle, respectively. Later, Alice gets another particle which is in the state $|\psi\rangle_C = \alpha|0\rangle_C + \beta|1\rangle_C$. To convey the state of the particle to Bob, Alice performs a BSM on the two qubits in her possession. The state of the three particles is then given by

$$\begin{aligned}|\Phi^+\rangle_{AB}|\psi\rangle_C =& \frac{1}{\sqrt{2}}(|0\rangle_A|0\rangle_B + |1\rangle_A|1\rangle_B)(\alpha|0\rangle_C + \beta|1\rangle_C)\\ =& \frac{1}{2}\left[|\Phi^+\rangle_{AC}(\alpha|0\rangle_B + \beta|1\rangle_B) + |\Phi^-\rangle_{AC}(\alpha|0\rangle_B - \beta|1\rangle_B)\right.\\ &\left.+|\Psi^+\rangle_{AC}(\beta|0\rangle_B + \alpha|1\rangle_B) + |\Psi^-\rangle_{AC}(\beta|0\rangle_B - \alpha|1\rangle_B)\right]. \end{aligned} \tag{2.1}$$

Thus, Alice only has to transfer two classical bits of information to tell Bob which Bell state she measured, and Bob will obtain the desired state after a proper unitary operation is performed. In this experiment, Alice and Bob have two atomic-ensemble quantum memories. The entanglement shared between them is an atom-photon entanglement where Bob keeps the stationary spin-wave state and Alice keeps the photonic state. We aim to teleport a single spin-wave state from Alice to Bob, which are linked by a 150 m long single-mode optical fiber and physically separated by about 0.6 m.

The layout of the experiment is shown in Fig. 2.1. Two separate atomic ensembles, named atomic ensemble A and atomic ensemble B, respectively, are prepared by MOTs, each consisting of about 10^8 Rubidium 87 atoms. At very beginning, atoms of atomic ensemble A are prepared in the state $|a\rangle = |5^2S_{1/2}, F = 2\rangle$, while atoms of atomic ensemble B are prepared in the state $|b\rangle = |5^2S_{1/2}, F = 1\rangle$ to allow interference between the read-out photon of ensemble A and the write-out photon of ensemble B. All the write and read beams are chosen to be on resonance with the D-1 line and linearly polarized as described in Section 1.3.2. A π-pump beam and a magnetic bias field are applied to ensemble A to utilize the clock state $(|F = 2, m_F = 0\rangle, |F = 1, m_F = 0\rangle)$. The detection angle for ensemble A is set to be 0.5° yielding a storage lifetime of 126(6) μs which is quite close to the theoretical value of 148 μs limited by the thermal motion-induced dephasing as illustrated in Section 1.1.4. The detection angle for ensemble B is chosen to be 3° for ease of alignment. In order to suppress the noise for detecting signal and idler photons, pumping vapor cells (PVCs) are applied. Rubidium atoms inside of the PVCs are optically pumped to the state where the unexpected photons with a frequency of write (or read) are strongly absorbed, while it is transparent to the signal (or idler) photons.

The time sequence is shown in Fig. 2.2. A FPGA card is used to generate all control signals. Atoms are loaded into the MOT in the first 11 ms, and cooled down to ~ 100 μK. Later, the trapping beams and the magnetic quadrupole field are switched off and the experiment is performed within 3 ms after the initial state is prepared with pumping

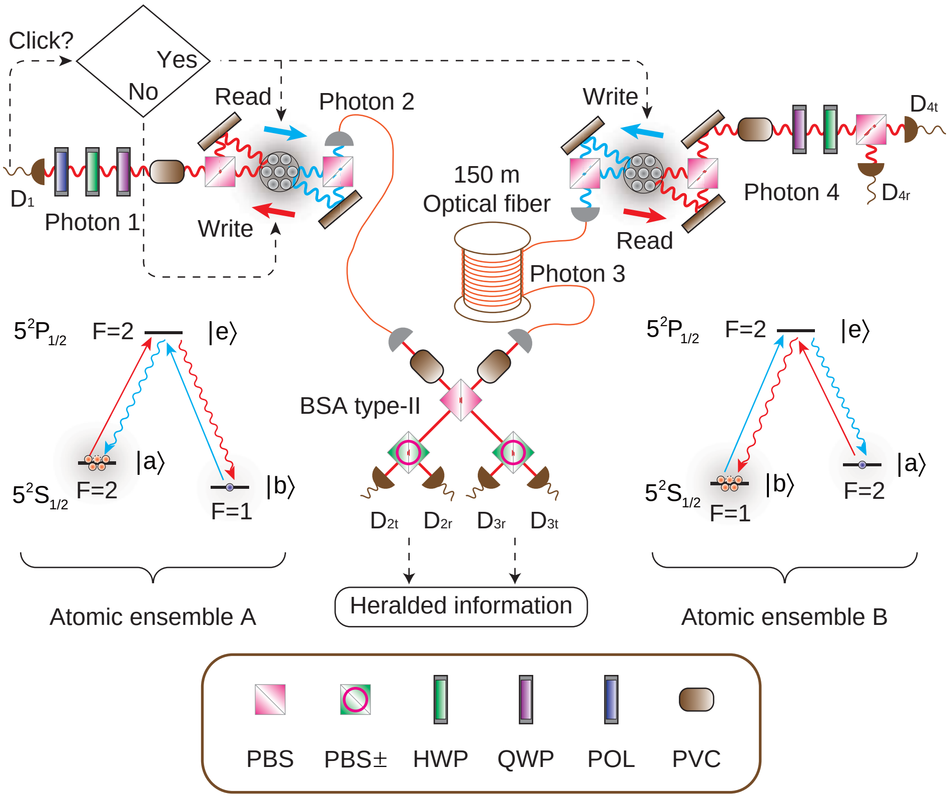
Click?
Yes
No
Read
Photon 2
Write
D_{4t}
D_1
Photon 1
Write
150 m
Optical fiber
Photon 4
D_{4r}
Read
Photon 3
$5^2P_{1/2}$
F=2
\|e⟩
\|a⟩
$5^2S_{1/2}$
F=2
\|b⟩
F=1
BSA type-II
$5^2P_{1/2}$
F=2
\|e⟩
\|b⟩
\|a⟩
$5^2S_{1/2}$
F=1
F=2
D_{2t}
D_{2r}
D_{3r}
D_{3t}
Atomic ensemble A
Heralded information
Atomic ensemble B
PBS
PBS±
HWP
QWP
POL
PVC

FIGURE 2.1: Experimental setup for quantum teleportation between two remote atomic ensembles. The energy levels used for write and read processes are illustrated. Photon 1 (photon 2) corresponds to the write-out (read-out) photon of ensemble A, and photon 3 (photon 4) corresponds to the write-out (read-out) photon of ensemble B. Both atom-photon entanglement sources are locked, and the phases are compensated. To prepare an arbitrary spin-wave state, photon 1 is measured in a corresponding basis by a set-up consisting of a QWP, a HWP, and a POL. Single photon detectors (from PerkinElmer Inc.), working at gated output mode, are responsible for single photon detections.

beams. During the experimental phase, the write pulse is repeated until a write-out photon from ensemble A is registered, heralding the success of the state preparation. Then, the spin-wave state is converted into a single photon (photon 2) through read process. At the same time, atom-photon entanglement is established in ensemble B by a write process. “Read B” is applied at last to convert the teleported state into the polarization state of a single photon for further use. Note that since the excitation probability for write process is made to be sufficiently low (~ 0.003) to suppress the double-excitation probability, the write process is repeated many times to get the spin-wave state prepared successfully.

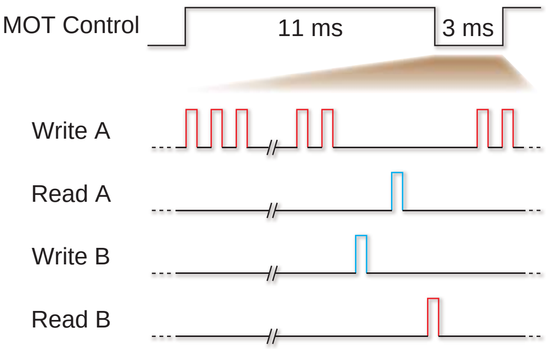

FIGURE 2.2: Time sequence for quantum teleportation between atomic ensembles. Pumping beams, including π-pump, are applied before every "Write A" pulse to purify the state which leads to a total write trial time of 3.38 μs. The write trial time for ensemble B is 975 ns since the π-pump is unnecessary. The delay between "Read A" and "Write B" is made to compensate the delay induced by the different optical path lengths so that photon 2 and photon 3 can meet at the BSA.

2.2 Spin-Wave State Preparation

The experiment starts with initializing the atomic ensemble A in an arbitrary state $|\psi\rangle_A = \alpha|\uparrow\rangle_A + \beta|\downarrow\rangle_A$, where $|\uparrow\rangle$ and $|\downarrow\rangle$ are the spin-wave states with $\uparrow$ and $\downarrow$ denoting the directions of the vectors relative to the write direction, and α and β are arbitrary complex numbers satisfying the condition $|\alpha|^2 + |\beta|^2 = 1$. The preparation procedure is done by taking the method of remote state preparation [114]. After the application of a weak write pulse, entanglement is created between the spin-wave vector and the momentum (emission direction) of the scattered photon via Raman scattering. A PBS later converts the momentum information to polarizations and leaves the atom-photon entanglement in the state

$$|\Psi^-\rangle_{1A} = \frac{1}{\sqrt{2}}(|H\rangle_1|\downarrow\rangle_A - |V\rangle_1|\uparrow\rangle_A). \tag{2.2}$$

Note that the phase induced by the path difference is compensated as explained in Section 1.3.2. A projective measurement is applied on photon 1 in the basis $\{|\psi\rangle_1, |\psi^\perp\rangle_1\}$, where $|\psi\rangle_1 = \alpha|H\rangle_1 + \beta|V\rangle_1$ and $|\psi^\perp\rangle_1 = \beta^*|H\rangle_1 - \alpha^*|V\rangle_1$. According to the antisymmetric nature, the atom-photon entangled state could also be expressed as

$$|\Psi^-\rangle_{1A} = \frac{1}{\sqrt{2}}(|\psi\rangle_1|\psi^\perp\rangle_A - |\psi^\perp\rangle_1|\psi\rangle_A). \tag{2.3}$$

Thus, the ensemble A is projected to $|\psi\rangle_A$ if the measurement on photon 1 gives the result of $|\psi^\perp\rangle_1$.

In the experiment, the following six initial states are chosen to evaluate the preparation process, $|\uparrow\rangle_A$, $|\downarrow\rangle_A$, $|+\rangle_A$, $|-\rangle_A$, $|R\rangle_A$, and $|L\rangle_A$ with $|\pm\rangle_A = 1/\sqrt{2}(|\uparrow\rangle_A \pm |\downarrow\rangle_A)$

and $|R/L\rangle_A = 1/\sqrt{2}(|\uparrow\rangle_A \pm i|\downarrow\rangle_A)$ by projecting photon 1 to the corresponding state $|\psi^{\perp}\rangle_1$. And the verification is done by performing the quantum state tomography to the retrieved photon 2 where $|\uparrow/\downarrow\rangle_A$ is converted to the polarization state $|H/V\rangle_2$ [115]. The six spin-wave states (ρ_j with j=1 to 6) are reconstructed through maximum likelihood technique and plotted in the Bloch sphere as shown in Fig. 2.3. The fidelity is defined as $F(\rho_j, \rho_{j'}) \equiv [\text{trace}(\sqrt{\rho_j}\rho_{j'}\sqrt{\rho_j})^{1/2}]^2$ [116], where ρ_j and $\rho_{j'}$ are arbitrary density matrices. The average fidelity between the measured states and the ideal states is 97.5(2)%.

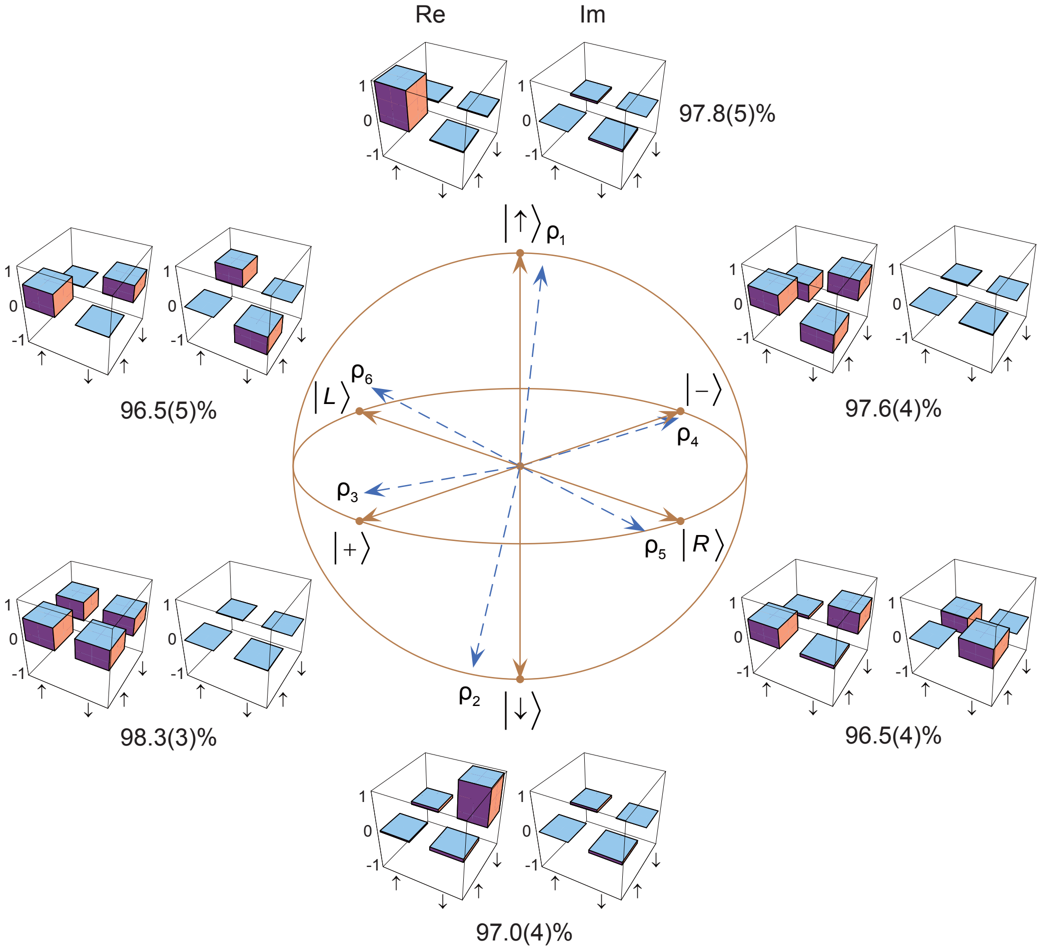

FIGURE 2.3: Tomography results of the prepared atomic states. In the Bloch sphere, the solid arrows represent the six target states, i.e., $|\uparrow\rangle$, $|\downarrow\rangle$, $|+\rangle$, $|-\rangle$, $|R\rangle$, and $|L\rangle$, while the dashed arrows represent the six measured states, i.e., ρ_j with j=1 to 6. The reconstructed matrices are shown beside each of the states with left (right) one presenting the real (imaginary) part. Errors of the fidelities are calculated based on the Poisson statistics of the raw photon counts.

2.3 Spin-Wave State Teleportation

To teleport the prepared state, a quantum channel is established connecting the two atomic ensembles. An atom-photon entanglement is responsible for the quantum channel, where the spin-wave state of ensemble B is entangled with the polarization state of a single photon. After the state is prepared, the write pulse is applied to ensemble B to create such entanglement

$$|\Phi^+\rangle_{3B} = \frac{1}{\sqrt{2}}(|H\rangle_3|\uparrow\rangle_B + |V\rangle_3|\downarrow\rangle_B). \tag{2.4}$$

At the same time, a read pulse is applied to ensemble A to convert the spin-wave state to a single photon (photon 2). The photon 2 and 3 are then guided through single-mode fibers to a BSA for BSM. The BSA type-II allows the discrimination of the states $|\Phi^+\rangle_{23}$ and $|\Phi^-\rangle_{23}$ which in turn indicates the success of the teleportation (to some extent, to be analyzed later). In addition, the classical measurement results are sent to ensemble B's site for necessary π phase shift operation on $|\downarrow\rangle_B$ when $|\Phi^-\rangle_{23}$ is measured.

2.3.1 Quantum Teleportation with Short Fiber

To demonstrate the feasibility of the teleportation, short fibers (2-m-long) are used to guide the photons to the BSA. The teleported state is later converted to a single photon (photon 4) by applying read pulse to ensemble B. The evaluation of the teleportation is done by performing quantum state tomography to the converted photon 4 where all of the six input states (ρ_j with j=1 to 6) are utilized. In the case that $|\Phi^-\rangle$ is measured, an artificial π phase shift operation is applied to the reconstructed states. The fidelities between the prepared input states and the teleported states, as well as the matrices of the reconstructed states, are shown in Tab. 2.1. The average fidelity is 95(1)%, which is well above the threshold of two-thirds predicted by classical theory [117].

With the tomography results of the states, the teleportation process can be characterized further by quantum process tomography [118, 119]. An arbitrary single-qubit operation on an input state ρ_{in} can be described by a process matrix χ, and the output state can be expressed as

$$\rho_{\text{out}} = \sum_{j,j'=0}^{3} \chi_{jj'}\hat{\sigma}_j\rho_{\text{in}}\hat{\sigma}^\dagger_{j'}, \tag{2.5}$$

with Pauli matrices $\hat{\sigma}_0 = \mathbb{1}$, $\hat{\sigma}_1 = \hat{\sigma}_x$, $\hat{\sigma}_2 = \hat{\sigma}_y$, and $\hat{\sigma}_3 = \hat{\sigma}_z$. The matrix is reconstructed in a maximum likelihood sense to ensure physicality [120], and is illustrated in Fig. 2.4. Ideally, teleportation process will not change a state and can be described as a process matrix with only one nonzero element $\chi^{\text{ideal}}_{00} = 1$. Thus, the process fidelity $F_{\text{proc}} \equiv$

TABLE 2.1: Teleportation fidelities with short fiber.

Input state	ρ_1	ρ_2	ρ_3	ρ_4	ρ_5	ρ_6
Fidelity (%)	93(2)	95(2)	90(4)	96(2)	97(2)	99(2)
Real	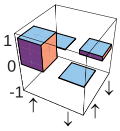	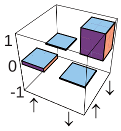	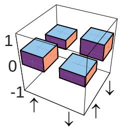	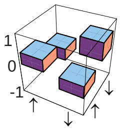	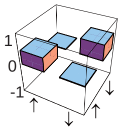	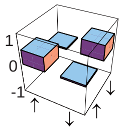
Imaginary	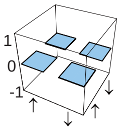	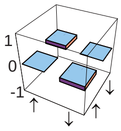	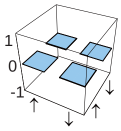	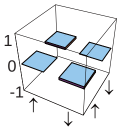	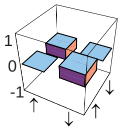	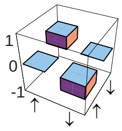

trace($\chi^{\text{ideal}}\chi$) is calculated to be 84(3)% with the error calculated based on the Poisson distribution of the original counts. Both imperfect atom-photon entanglement $|\Phi^+\rangle_{3B}$ and imperfect BSM contribute to the deviation from the unit fidelity.

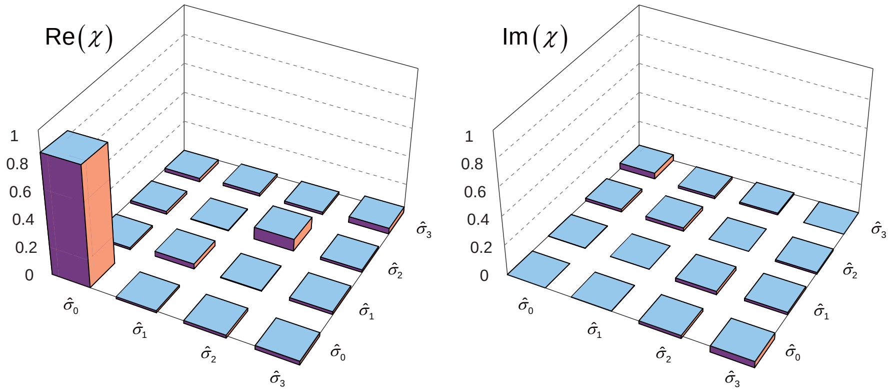

FIGURE 2.4: Measured process matrix χ for the teleportation with short fiber.

2.3.2 Quantum Teleportation with Long Fiber

To demonstrate the robustness of the teleportation over long distance, the short fiber connecting ensemble B's site with the BSA is replaced by a 150-m-long fiber which has an intrinsic loss of about 11.4%. The stress and temperature dependent slow drift of the polarization is checked regularly and compensated carefully by a QWP-HWP-QWP setup [103]. In addition, the fiber is wound on a coil of diameter 1 m to suppress fluctuations of the birefringence, and the contrast ratio keeps higher than 1000 : 1 over 10 hours. This time, the prepared state $|\psi\rangle_A$ is stored for 1.6 μs to compensate the time of the entanglement generation in ensemble B and the propagation delay for photon 3. The fidelities of the teleported states and the process tomography result are shown in Tab. 2.2, and in Fig. 2.5, respectively. The average fidelity of the states is 95(1)%, and the process fidelity is 87(2)%, which are comparable with the teleportation with short fiber.

TABLE 2.2: Teleportation fidelities with long fiber.

Input state	ρ_1	ρ_2	ρ_3	ρ_4	ρ_5	ρ_6
Fidelity (%)	97(1)	93(2)	96(2)	94(3)	97(4)	96(2)
Real	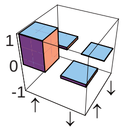	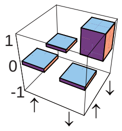	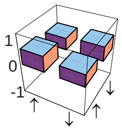	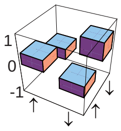	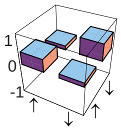	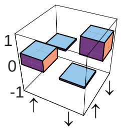
Imaginary	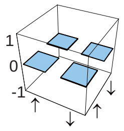	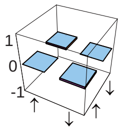	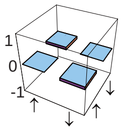	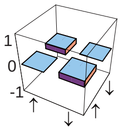	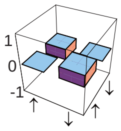	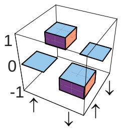

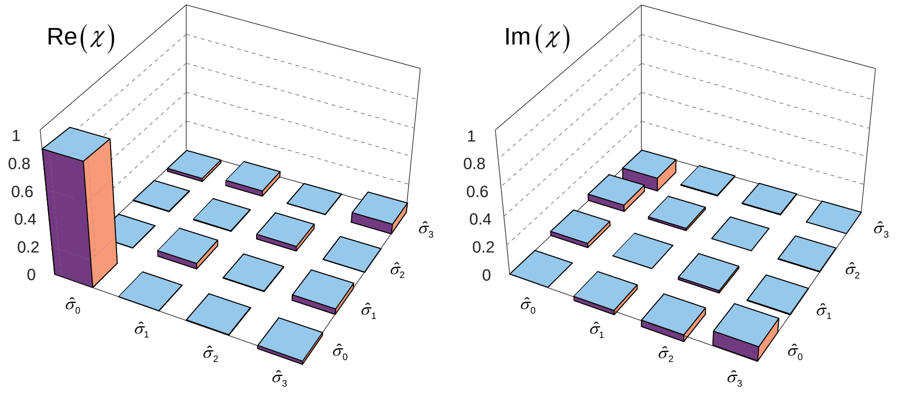

FIGURE 2.5: Measured process matrix χ for the teleportation with long fiber.

2.3.3 Heralded Quantum Teleportation

It has to be emphasized that the teleportation process discussed above is probabilistic since it relies on a probabilistic generation of the auxiliary entanglement pair between ensemble B and photon 3. However, for a prepared input state, the process succeeds with a probability of $\eta_A P_B/2 \simeq 10^{-4}$ which is 4 orders of magnitude larger than the previous trapped-ion teleportation experiment [23]. η_A (7%) is the detected retrieval efficiency of ensemble A, P_B (3×10^{-3}) is the detection probability of a write-out photon from ensemble B, and one half comes from the BSM (two of the four Bell states can be discriminated). Another attractive feature of the presented teleportation scheme is that the coincidence signal from the BSM works as a trigger to herald the success of the teleportation, while the teleported state is stored until required for further use. This will benefit many applications such as long-distance quantum communication [39, 121] and distributed quantum computing [122, 123].

However, the read-out noise of ensemble A and high-order excitations of ensemble B might give fake triggers and have to be suppressed. The BSM trigger signal mainly comes from three sources as listed below,

from	A&B	A	B
probability	$\eta_A P_B$	$\eta_A P_A$	$(1-\eta_A)P_B^2$

with P_A the detection probability of a write-out photon from ensemble A during a single write trial. The first term is the desired one which describes the process of a successful retrieval from ensemble A together with a single excitation from ensemble B. The second term comes from a successful retrieval together with read-out noise which is measured experimentally $\sim P_A$. One major reason of this read-out noise could be explained by a double-excitation of ensemble A. The detection efficiency of a scattered photon d_A is about 30% limited by the efficiency of the single photon detector, coupling efficiency to the fiber, and transmission loss of the PVC. Thus the probability of this double-excitation is P_A^2/d_A, and the probability to get a BSM trigger from this is $\eta_A^2 P_A/d_A$. Another reason responsible for the second term is the spontaneous scattering of the read process. Due to the probabilistic write process, there will be many atoms get excited in other modes which are not relevant to the detection in the desired collection mode. Although the retrieval photons of these atoms do not get enhanced to propagate along the idler collection mode, the strong read beam will lead to a strong spontaneous scattering process which has a chance to emit photons into the idler collection mode. Since the number of excited atoms within each write trial is proportional to P_A, the strength of the mechanism scales as P_A. The third term originates from a failure of retrieval together with double-excitation of ensemble B. The second term does not cause a retrieval of ensemble B, thus will not affect the fidelity of the teleportation as long as the teleported spin-wave state is evaluated after the retrieval. However, the latter two terms will reduce the heralding fidelity unless the following requirement is fulfilled

$$P_A \ll P_B \ll \eta_A. \tag{2.6}$$

For this reason, the excitation probability of ensemble A is further reduced to $P_A \simeq 0.3 \times 10^{-3}$ yielding $0.3 \times 10^{-3} \ll 3 \times 10^{-3} \ll 70 \times 10^{-3}$. Under this condition, the average post-selected fidelity for the six input states is measured to be 93(2)%. The fidelity of the heralded teleportation is defined as $F_{\text{her}} \equiv F\eta_{\text{her}}$, with the heralding efficiency $\eta_{\text{her}} \equiv p_{234}/(p_{23}\eta_B)$ in which p_{234} and p_{23} are the joint detection probabilities of the corresponding detectors, and is measured to be 88(7)% averaged over the six states. For a preparation of $|\uparrow\rangle_A$ and $|\downarrow\rangle_A$ state, Fig. 2.6 shows how the heralding efficiency increases while the excitation probability decreases.

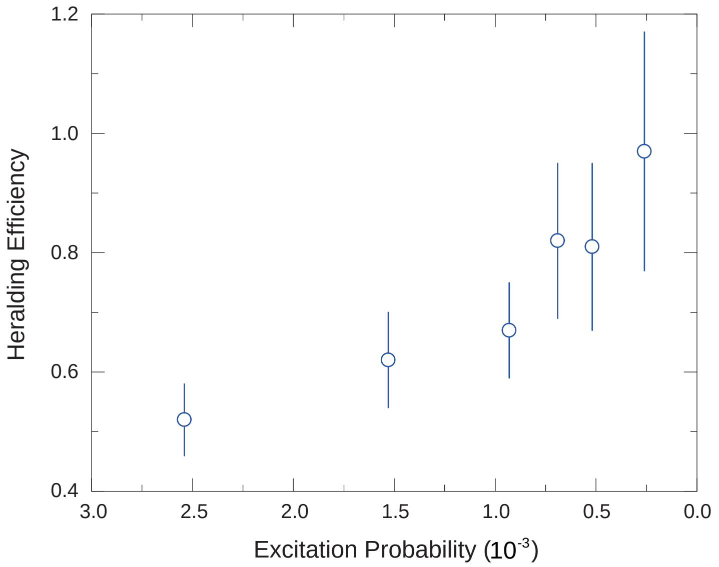

FIGURE 2.6: Heralding efficiency as a function of the excitation probability. The heralding efficiency is averaged over the results for preparing $|\uparrow\rangle_A$ and $|\downarrow\rangle_A$ states.

The slightly lower state fidelity limits the heralding fidelity, which is due to the comparably higher background noise mainly coming from the leakage of control lasers (write, read, filter cell pumping beams, and so on), stray light, and detector dark counts. Moreover, the higher-order excitations also limit the heralding fidelity, which can be inhibited through Rydberg blockade [124, 125].

2.4 Discussion

In summary, a high-fidelity heralded quantum teleportation is demonstrated which teleports an atomic spin-wave state to another atomic ensemble. Since the photons generated here have a coherence length on the order of 10 m, stable synchronization of them is much easier than of the photons generated through parametric down-conversion process used for previous photonic teleportation experiments which coherence length is only a few hundreds of micrometers [7], thus the scheme can be extended to an even larger-scale implementation. In addition, the presented teleportation is performed between two macroscopic sized objects [126] at a distance of macroscopic scale which is of fundamental interest. From a practical perspective, the techniques of the heralded state preparation, coherent mapping between matter and light, and heralded quantum state teleportation, might provide a useful tool kit for quantum information transfer among distant nodes in a quantum network and for measurement-based quantum computing with atomic ensembles. Furthermore, the success probability is 4 orders of magnitude larger than the previous trapped-ion teleportation experiment [23], benefiting from the collective enhancement which enables efficient conversion of atomic qubits to photonic qubits propagating along a specific mode.

Methods for further improvement of the success probability include using a low-finesse optical cavity to improve the conversion efficiency [127] (η_A), and using an auxiliary atomic ensemble to create an atom-atom entanglement and later retrieve one of the atomic state to photonic state which is distributed to ensemble A [42, 128] ($P_B \rightarrow \eta$). Although the storage lifetime in the present experiment (126 μs) is only a little bit more than the average creation time (97.5 μs) required for the latter method, nowadays, the storage lifetime could be easily extended up to 16 s with the help of an optical lattice [93]. With these improvements, one could envision the realization of a quantum teleportation among multi-atomic-ensemble nodes in the near future.

Chapter 3

Efficient Entanglement Swapping Based on Delayed Choice

Entanglement swapping [36] lies at the heart of a quantum repeater [35] and a quantum relay [129,130], which are used to extend the distance of quantum communication. However, the experiments based on the conventional entanglement swapping scheme [42,131] have fairly low success rates due to the probabilistic character of the entanglement source. Take the spontaneous parametric down-conversion (SPDC) [66] source as an example, a pair of entangled photons is created with only a small probability, typically $p < 0.01$. Thus the success probability of the entanglement swapping by using two entanglement sources of this type is limited to p^2, and therefore p^n for n nodes. The exponential decay of the success probability severely limits the applications of entanglement swapping in quantum communication.

In this chapter, I report on the realization of an efficient entanglement swapping where the exponential decay problem is circumvented by adopting a delayed choice entanglement swapping method [132]. Two atomic-ensemble-based quantum memories are responsible for the creation of the entanglement, and the entanglement swapping is performed by a joint measurement on the retrieved photons. The quantum feedback technique [133] together with the quantum memories help to achieve a success probability on the order of $p/2$, which corresponds to an enhancement factor of 257 for the experimental parameters presented.

3.1 Scheme of the Experiment

Delayed choice entanglement swapping was first proposed by Asher Peres in 1999, where entanglement is produced a posteriori [132]. In a conventional entanglement swapping experiment as sketched in Fig. 3.1, joint measurements (for example, BSMs) on the pairs of particles (2 and 3) at the center have to be performed in advance in order to result in entanglement between the two users (1 and 4). Later, the entanglement can be used for different purposes, for example to generate secure keys. In contrast, in the delayed choice entanglement swapping scheme, users measure the particles in their possession at first, and the joint measurements are performed only when the two users would like to communicate with each other. Suppose that user A generates entanglement between particle 1 and 2 in the form of $|\Phi^+\rangle_{12}$ and user B $|\Psi^-\rangle_{34}$, thus the joint state of them can be expressed as

$$\begin{aligned}|\Phi^+\rangle_{12}\otimes|\Psi^-\rangle_{34} \equiv&\frac{1}{2}(|\Phi^+\rangle_{23}|\Psi^-\rangle_{14}+|\Phi^-\rangle_{23}|\Psi^+\rangle_{14}\\ &-|\Psi^+\rangle_{23}|\Phi^-\rangle_{14}-|\Psi^-\rangle_{23}|\Phi^+\rangle_{14}),\end{aligned} \tag{3.1}$$

where $|\Phi^\pm\rangle$ and $|\Psi^\pm\rangle$ are Bell states. Note that, since the preceding local measurements are done independently and completely uncorrelated, the joint state would not collapse to the Bell states before the center performs a BSM. Therefore, after the center announces the results of the BSMs, users can sort their results into four subsets, where each one of the four post-selected subsets will produce statistical results identical to those arising from maximally entangled pairs. If the preceding local measurements are done in basis $\{|0\rangle,|1\rangle\}$, the users are able to create secure keys as in the Ekert91 protocol [32].

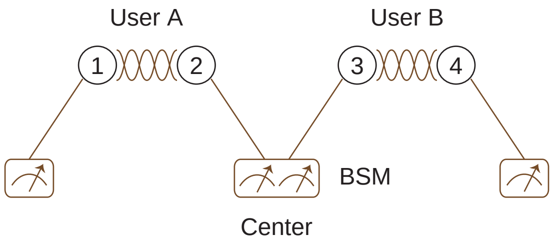

FIGURE 3.1: A sketch of the entanglement swapping scheme. User A (B) holds the entanglement between 1 and 2 (3 and 4), of which particle 1 (4) is measured locally and particle 2 (3) is sent to the center for joint measurement.

The layout of the experiment is shown in Fig. 3.2. Two atomic ensembles are prepared by MOTs, and each consists of about 10^8 Rubidium 87 atoms. The two ground states $|a\rangle = |5^2S_{1/2}, F = 2\rangle$ and $|b\rangle = |5^2S_{1/2}, F = 1\rangle$, and the excited state $|e\rangle = |5^2P_{1/2}, F = 2\rangle$ form a Λ-type atomic system. The atom-photon entanglement of ensemble A can be expressed as $|\Phi^+\rangle_{1A} = 1/\sqrt{2}(|H\rangle_1|\uparrow\rangle_A + |V\rangle_1|\downarrow\rangle_A)$, and the entanglement generated from ensemble B $|\Psi^-\rangle_{B4} = 1/\sqrt{2}(|\uparrow\rangle_B|V\rangle_4 - |\downarrow\rangle_B|H\rangle_4)$, where $|\uparrow\rangle$ and

$|\downarrow\rangle$ are the spin-wave states with ↑ and ↓ denoting the direction of the vectors relative to the write direction. The detection angle is chosen to be 0.5° for ensemble A and 1.5° for ensemble B. In addition, a π-pump and a magnetic bias field are applied to ensemble A to utilize the clock state $(|F=2, m_F=0\rangle, |F=1, m_F=0\rangle)$, and the lifetime is measured to be 126(6) μs. The lifetime of about 7 μs is measured for ensemble B which is limited by inhomogeneity of magnetic field-induced dephasing as illustrated in Section 1.1.4. The write-out photon of ensemble A (B), labelled as photon 1 (photon 4), is guided through a single-mode fiber to a polarization state analyzer $\mathrm{SA_A}$ ($\mathrm{SA_B}$). And the read-out photons (photon 2 and photon 3) are sent, through single-mode fibers, to a type-II BSA for joint BSM of which the result is used to sort the preceding measurements on photon 1 and photon 4.

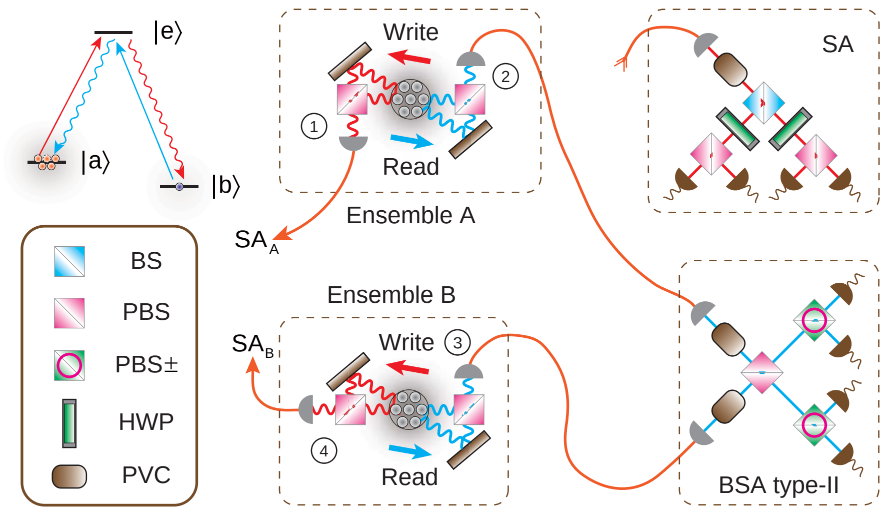

FIGURE 3.2: Experimental setup for the efficient entanglement swapping. The circled number ⓙ $(j=1,2,3,4)$ refers to the label "photon j". The BS in the SA helps to randomly choose the measurement basis between $\{|H\rangle, |V\rangle\}$ and $\{|+\rangle, |-\rangle\}$ with $|\pm\rangle = 1/\sqrt{2}(|H\rangle \pm |V\rangle)$. PVCs are used to suppress the noise photons.

The time sequence is shown in Fig. 3.3. Atoms are loaded into the MOT during the first 20 ms. In the first millisecond of the subsequent experiment phase of 5 ms, pumping beams are applied to initialize the atoms to the proper states. After the atoms are prepared, a group of "Write A" pulses are applied successively until a write-out photon is registered by the single photon detectors. Then, "Write B" pulses are applied in a similar way. The read processes commence only when a write-out photon from ensemble B is also registered. The hundred-microsecond lifetime of ensemble A allows a long preparation time for ensemble B. If in the worst case that ensemble B fails to emit a signal photon within the coherence time of ensemble A, the states are cleaned and "Write A" pulses are applied again.

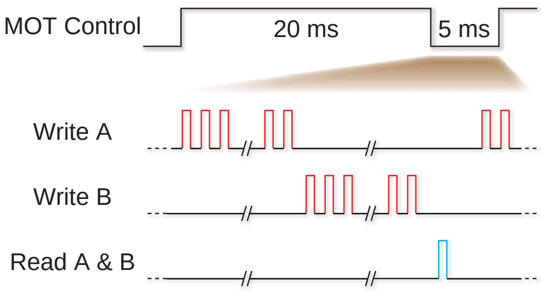

FIGURE 3.3: Time sequence for the efficient entanglement swapping. A short clean pulse made of pumping beam(s) always precedes the write pulse. The write cycle duration for ensemble A is $T_A = 2.9\ \mu$s, and for ensemble B is $T_B = 0.9\ \mu$s. Since the write process of ensemble B starts after the write process of ensemble A has been finished, the success probability obtains a one-half factor and yields $p/2$ as claimed.

3.2 Results of the Experiment

During the write process, the spin-wave state is stored in the ensemble A until ensemble B succeeds. Thus the coherence time of the spin-wave state of ensemble A will determine the maximum wait time. The coherence lifetime is characterized by measuring the visibility of pairs of entangled photons (photon 1 and photon 2) as a function of storage time τ_A, which is defined as

$$\mathcal{V} = \frac{N_{\text{desired}} - N_{\text{undesired}}}{N_{\text{desired}} + N_{\text{undesired}}}, \tag{3.2}$$

in which N_{desired} denotes the number of coincidence counts for the desired polarization state, and $N_{\text{undesired}}$ denotes for the undesired state. The measurements are performed in both basis $\{|H\rangle, |V\rangle\}$ and $\{|+\rangle, |-\rangle\}$ and are presented in Fig. 3.4.

Armed with such a long-lifetime quantum memory, the enhancement is verified by measuring the four-fold coincidence count rate, as well as the visibility measured between photon 1 and photon 4 averaged in basis $\{|H\rangle, |V\rangle\}$ and $\{|+\rangle, |-\rangle\}$, as a function of the storage time of ensemble A (τ_A). The results are shown in Fig. 3.5. It can be readily seen that an enhancement factor of 257 ± 16 is observed when the storage time is set to be 180 μs, where the average visibility is $(0.76 \pm 0.04) > 1/\sqrt{2}$, large enough to violate the Clauser-Horne-Shimony-Holt (CHSH) form of the Bell inequality [12, 134] with Werner state assumption [135, 136].

To evaluate the quality of the entanglement swapping, the CHSH form of the Bell inequality is measured, which is defined as

$$S = |E(\phi_1, \phi_4) + E(\phi_1, \phi_4') + E(\phi_1', \phi_4) - E(\phi_1', \phi_4')| \leq 2, \tag{3.3}$$

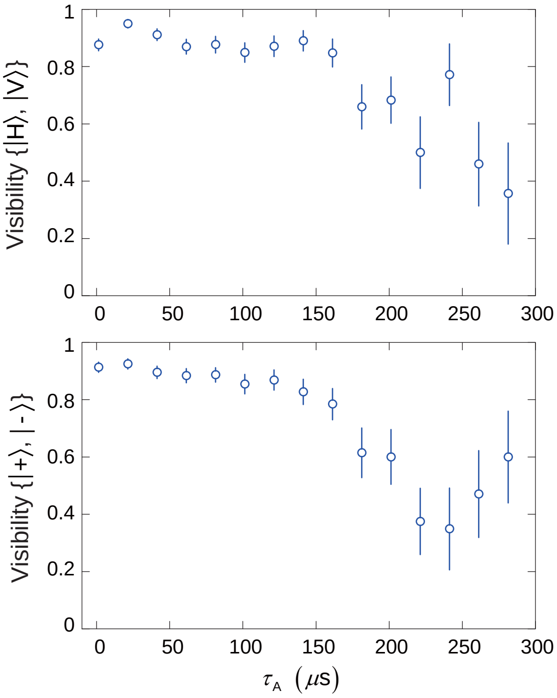

FIGURE 3.4: Visibility measurements on pairs of entangled photons of ensemble A. The upper one refers to the measurements in basis $\{|H\rangle, |V\rangle\}$, while the lower one refers to basis $\{|+\rangle, |-\rangle\}$. Error bars represent standard deviation based on photoelectron counting statistics.

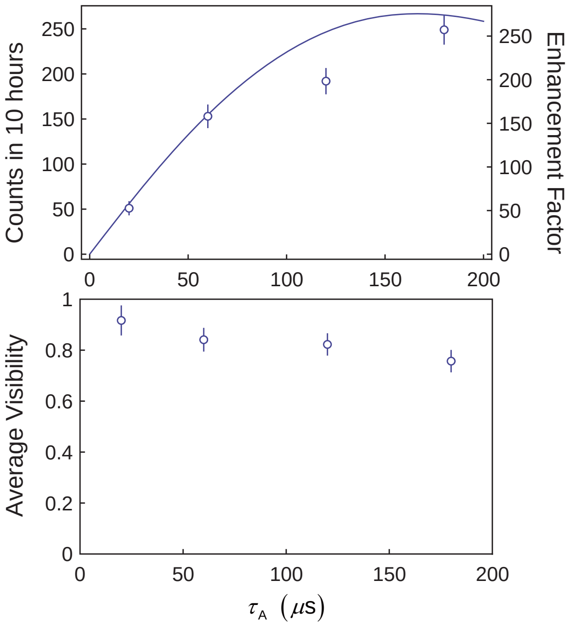

FIGURE 3.5: Demonstration of enhancement with the feedback technique. The solid line represents a theoretical calculation of number of counts according to the experimental parameters, such as excitation probability, retrieval efficiency, write cycle time, and so on. The enhancement factor is defined as the ratio of count rate with feedback to count rate without feedback, and the latter is numerically equivalent to a conventional entanglement swapping count rate.

where $E(\alpha, \beta)$ represent the correlation functions and ϕ_j (ϕ'_j), $j = 1, 4$, denotes the corresponding basis for polarization measurements on photon j [66]. A violation of the CHSH inequality is a direct proof for quantum entanglement. With proper bases for measurements, $S = 2.67 \pm 0.35$ is measured for BSM result $|\Phi^+\rangle_{23}$, and $S = 2.40 \pm 0.37$ for BSM result $|\Phi^-\rangle_{23}$.

The delayed choice entanglement swapping demonstrated here not only helps to improve the efficiency of the entanglement generation between distant nodes, but also allows a variety of applications with the help of the quantum feedback technique and quantum memories. One interesting idea is to distribute quantum keys “at will” where a quantum channel is unnecessary at the time of key generation. The center provides a large number of atom-photon entangled pairs. Each of the users comes to the center to measure the photonic qubits in bases randomly chosen between $\{|H\rangle, |V\rangle\}$ and $\{|+\rangle, |-\rangle\}$, and records the results as well as the chosen bases, while the atomic spin-wave states will be stored in the center. When user A and B would like to generate secure keys shared with each other, they just make a phone call to the center to ask him/her to convert the atomic states to photonic states for joint BSMs. After the center tells them the results, user A and B can just follow the standard procedure of quantum cryptography to extract the final secure keys. In this way, the center can not gain any knowledge about the keys, and thus needs not to be trustworthy. With the help of a BS to perform random basis selection, a series of keys are created with our setup where the information of the chosen bases and measurement results are recorded in an electric memory card. The spin-wave state of ensemble B is stored for 3.35 μs. The quantum bit error rate is measured to be $(9.3 \pm 2.2)\%$, and secure keys can be derived by applying classical error correction and privacy amplification [4].

3.3 Discussion

In summary, a delayed choice entanglement swapping is demonstrated by the aid of a quantum feedback technique and quantum memories, and an enhancement factor of 257 is observed. The quality of the entanglement is verified by a violation of the CHSH inequality. In addition, the idea of key generation on demand is realized and a series of secure keys are generated. However, the delayed choice entanglement swapping fails when one tries to integrate it into a multistage entanglement swapping scheme [137], since there is no stationary state any longer after the measurement on the first stage. And the storage lifetime of the current setup also limits the efficiency of the swapping.

Chapter 4

One-Way Quantum Computing with Photon-Matter Hyperentanglement

Quantum Computing offers tremendous speedup of certain computing tasks such as factorization of large numbers [25], database searching [46], simulation of quantum systems [43,138], and so on. Especially, optical quantum computing has attracted extensive interest due to its weak coupling to the environment, ease of manipulation, and potential for high experimental repetition rate [139, 140]. In the past few years, experiments have been done both in the circuit-based model [139] and in the one-way model [48, 51–56]. However, the probabilistic photon sources [141,142] and entangling operations [139] make efficient optical quantum computing fail without quantum memories [143, 144]. For instance, creation of a large cluster state [49] can be made much more efficient by using quantum memories to store intermediate entangled states in order to wait for the preparation of the auxiliary resources. Especially in one-way quantum computing [50, 145], storage of the remaining qubits with quantum memories is necessary so that feedforward operations can be applied according to previous measurement results.

In this chapter, I report on the realization of optical one-way quantum computing with stationary quantum memory involved [92]. The quantum information is encoded in a four-qubit hyperentangled photon-spin-wave cluster state, where the spin-wave is stored in a laser-cooled atomic ensemble. The storage capability of quantum memory allows the realization of active feedforward operations performed by fast electro-optic modulators (EOMs). Deterministic single-qubit rotations are demonstrated, as well as the two-qubit controlled-phase (C-Phase) gate and Grover's searching algorithm. In comparison with previous experiments [53, 54], in which long optical fibers were used to delay the photonic qubits for feedforward operations, the present scheme features flexibility and potentially low loss for future large-scale applications.

4.1 Introduction to One-Way Quantum Computing

The one-way model not only formulates quantum computation in a different way than the circuit model, but also provides new theoretical insights [50, 146]. In one-way quantum computation, any quantum circuit is imprinted into a cluster state of a certain pattern, and arbitrary unitary operations on the encoded qubits such as single-qubit rotations and two-qubit entangling gates are realized through a series of single-qubit measurements on the physical qubits in a specific order.

The resource of one-way quantum computing, a cluster state [49] or graph state [147], is a highly entangled multi-qubit quantum state of a certain structure designed for a specific purpose. A typical cluster state [49] is shown in Fig. 4.1, where each vertex on the graph corresponds to a qubit. The typical way to construct a cluster state is to prepare every qubit in the state $|+\rangle = (|0\rangle + |1\rangle)/\sqrt{2}$ and then apply a C-Phase operation $|0\rangle\langle 0| \otimes \mathbb{1} + |1\rangle\langle 1| \otimes \hat{\sigma}_z$ on every pair of qubits whose vertices are connected by a graph edge. Note that $\mathbb{1}$ represents the 2×2 identity matrix, and the Pauli matrices are described as $\hat{\sigma}_x = |0\rangle\langle 1| + |1\rangle\langle 0|$, $\hat{\sigma}_y = -i|0\rangle\langle 1| + i|1\rangle\langle 0|$, and $\hat{\sigma}_z = |0\rangle\langle 0| - |1\rangle\langle 1|$.

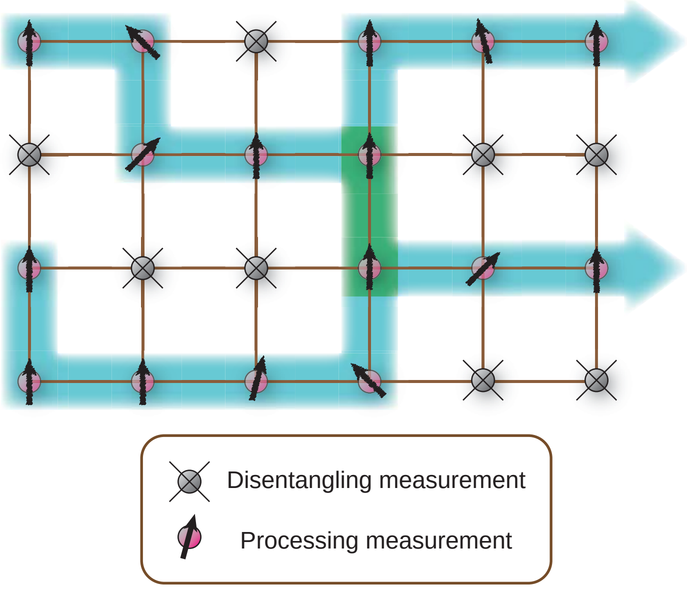

FIGURE 4.1: A typical cluster state configuration. After the generation of the generalized cluster state, necessary disentangling measurements are performed to modify the structure for a specific purpose. The blue area with arrows points the way that information flows. And the physical qubits are measured one after another to perform the computation. The green area represents an operation of a two-qubit quantum gate.

During the computing process, two kinds of single-qubit measurements should be employed, one for disentangling and the other for processing as depicted in Fig. 4.1. The disentangling effect is induced by measuring the j-th qubit of the cluster state in the computational basis $\{|0\rangle_j, |1\rangle_j\}$, which removes the qubit and leaves a smaller cluster state. The measurement in basis $B_j(\alpha) = \{|\alpha_+\rangle_j, |\alpha_-\rangle_j\}$ with $|\alpha_\pm\rangle_j = (|0\rangle_j \pm e^{i\alpha}|1\rangle_j)/\sqrt{2}$ and $\alpha \in \mathbb{R}$, will introduce a single-qubit rotation $R_z(-\alpha)$ with $R_z(\alpha) = \exp(-i\alpha\hat{\sigma}_z/2)$ a rotation through angle α around the z-axis in the Bloch sphere, followed by a Hadamard operation Had $= (\hat{\sigma}_x + \hat{\sigma}_z)/\sqrt{2}$ on the encoded qubit [48] in the cluster. The outcome $|\alpha_+\rangle_j$ is defined as "0" indicating the computation proceeds with no error, while the outcome $|\alpha_-\rangle_j$ is defined as "1" indicating a well-defined Pauli error has been introduced. After the byproduct operators are permuted to the end, one realizes that the bases of later measurements depend on ealier measurement outcomes. Thus, deterministic logical operations necessitate active feedforward techniques in order to adapt the bases of later measurements according to the previous results as well as to compensate Pauli errors. It has to be emphasized that the byproduct operator can be considered as a modification of the input state of the following qubit before applying the C-Phase operation. Swapping a Pauli error acting on a qubit and a C-Phase operation would result in a chain effect which applies additional Pauli errors to the connected qubits, thus makes the correction of the byproduct operator by manipulating the following qubit in the cluster unadvisable. The byproduct operators have to be permuted to the end, and compensated by manipulating the last qubit.

4.2 Cluster State Preparation

The cluster in this experiment is shared between a single photon and an atomic ensemble which serves as the quantum memory. In previous experiments, different methods have been used to create atom-photon entanglement, including using the interference of different spacial modes [60] and of different Raman pathways [104]. To create a hyperentangled four-qubit state, we make use of both methods at the same time. The layout of the experiment is shown in Fig. 4.2. An atomic ensemble of about 10^8 atoms of Rubidium 87 is loaded into a MOT and prepared initially in the state $|a\rangle = |5^2S_{1/2}, F = 1, m_F = 0\rangle$. After one applies a weak right-handed circularly polarized write pulse to the atomic ensemble, a spin-wave excitation is created through Raman scattering either in the state $|b_0\rangle$ accompanied by a σ^+-polarized Stokes photon, or in the state $|b_{+2}\rangle$ accompanied by a σ^--polarized Stokes photon. This signal photon is collected either in the spatial mode l (noted as S_l in Fig. 4.2) with the spin-wave wave vector in the direction of $\uparrow$, or in the spatial mode r (noted as S_r in Fig. 4.2) with the spin-wave wave vector in the direction of $\downarrow$. In this way, a hyperentangled photon-matter state is created which has the form of

$$|\psi\rangle = \frac{1}{2}(|\sigma^+\rangle_\mathrm{S}|b_0\rangle + |\sigma^-\rangle_\mathrm{S}|b_{+2}\rangle) \otimes (|l\rangle_\mathrm{S}|\uparrow\rangle + e^{i\theta}|r\rangle_\mathrm{S}|\downarrow\rangle), \tag{4.1}$$

where the subscript “S” denotes the Stokes photon. The propagation phase θ can be compensated by moving a PIEZO-mounted mirror (M_2). Later, the polarization of the Stokes photon is transformed from σ^+/σ^- to H/V with a QWP, respectively. In addition, a π phase shift is introduced between the H and V polarizations in the spatial mode r for the Stokes photon with a QWP-HWP-QWP setup. Therefore, the desired cluster is derived in the form of

$$\begin{aligned} |C_4\rangle =& \frac{1}{2}(|Hl\rangle_S|b_0\uparrow\rangle + |Vl\rangle_S|b_{+2}\uparrow\rangle + |Hr\rangle_S|b_0\downarrow\rangle - |Vr\rangle_S|b_{+2}\downarrow\rangle) \\ \equiv& \frac{1}{2}(|0\rangle_1|0\rangle_2|0\rangle_3|0\rangle_4 + |1\rangle_1|0\rangle_2|1\rangle_3|0\rangle_4 + |0\rangle_1|1\rangle_2|0\rangle_3|1\rangle_4 - |1\rangle_1|1\rangle_2|1\rangle_3|1\rangle_4), \end{aligned} \tag{4.2}$$

in which $|H,V\rangle_S \leftrightarrow |0,1\rangle_1$, $|l,r\rangle_S \leftrightarrow |0,1\rangle_2$, $|b_0,b_{+2}\rangle \leftrightarrow |0,1\rangle_3$, and $|\uparrow,\downarrow\rangle \leftrightarrow |0,1\rangle_4$.

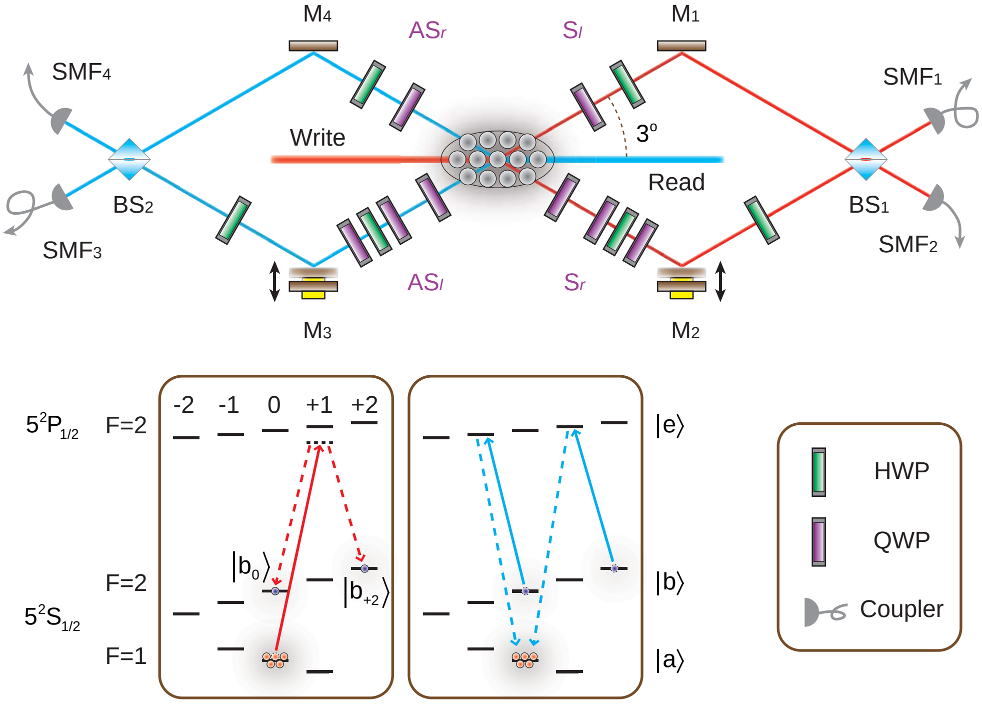

FIGURE 4.2: Experimental setup for the one-way quantum computing with photon-matter hyperentanglement. The write beam is 10 MHz red-detuned from the transition $|a\rangle \rightarrow |e\rangle$. Double-pathway Raman scattering (to either $|b_0\rangle$ or $|b_{+2}\rangle$) is utilized to create photon-matter entanglemet in the polarization degree. QWP-HWP-QWP setups help to change the phase between the H and V polarizations in order to compensate the unwanted phase induced by the glass cell and to modify the state. PIEZO-mounted mirrors M_2 and M_3 are used to compensate the phase as well as to perform spatial mode measurements together with BS. All the photonic modes are guided by single-mode fibers (SMFs) to the extended setup.

It has to be emphasized that the phase compensation method in this experiment is different from the former two. In the former experiments, the beam path difference is locked according to the signal generated by interference of phase locking beams passing through the Mach-Zehnder interferometer. Then the phase is compensated with a QWP-HWP-QWP setup by maximizing the coincidence counts ratio for specific polarizations as described in Section 1.3.2. However, the phase is compensated here by moving PIEZO-mounted mirrors while changing the locking point. By taking a closer look at the hyperentangled state, the phase is only imposed onto the photonic spatial mode states and would be independent of the polarization states. Therefore, the hyperentanglement can be expressed as

$$|\psi\rangle_{\text{read-out}} = \frac{1}{2}(|HH\rangle + |VV\rangle) \otimes (|ll\rangle + e^{i\phi}|rr\rangle), \tag{4.3}$$

where the phase ϕ contains the propagation phase of both write-out and read-out photons, after the matter states are converted into photonic states as $|b_0, b_{+2}\rangle \to |H, V\rangle_{\text{AS}}$ and $|\uparrow, \downarrow\rangle \to |l, r\rangle_{\text{AS}}$. Applying Hadamard operations to the spatial mode states ($|l, r\rangle \to |l+r, l-r\rangle/\sqrt{2}$) of both write-out and read-out photons through the BSs, the state will evolve to

$$|\psi\rangle_{\text{BS}} = \frac{1}{4}(|HH\rangle + |VV\rangle)\left[(1+e^{i\phi})(|l_{\text{BS}}l_{\text{BS}}\rangle + |r_{\text{BS}}r_{\text{BS}}\rangle) + (1-e^{i\phi})(|l_{\text{BS}}r_{\text{BS}}\rangle + |r_{\text{BS}}l_{\text{BS}}\rangle)\right]. \tag{4.4}$$

Thus compensating the phase to zero is equivalent to maximizing the ratio of coincidence counts of $|ll\rangle$ and $|rr\rangle$ to coincidence counts of $|lr\rangle$ and $|rl\rangle$. Note that the l_{BS} and the r_{BS} modes represent specific output modes of the BSs.

4.3 Cluster State Characterization

The cluster state is first evaluated by an optimal entanglement witness via the stabilizer operators [148, 149], which has the form

$$\begin{aligned}\mathcal{W} =& \frac{1}{2}[4\mathbb{1}^{\otimes 4} - (\hat{\sigma}_x\mathbb{1}\hat{\sigma}_x\hat{\sigma}_z + \hat{\sigma}_x\hat{\sigma}_z\hat{\sigma}_x\mathbb{1} + \mathbb{1}\hat{\sigma}_z\mathbb{1}\hat{\sigma}_z \\ &+ \mathbb{1}\hat{\sigma}_x\hat{\sigma}_z\hat{\sigma}_x + \hat{\sigma}_z\hat{\sigma}_x\mathbb{1}\hat{\sigma}_x + \hat{\sigma}_z\mathbb{1}\hat{\sigma}_z\mathbb{1})].\end{aligned} \tag{4.5}$$

An ideal cluster state of $|C_4\rangle$ predicts a minimum value of -1, and negative $\mathcal{W}$ implies the existence of quadripartite entanglement character. In addition, the lower bound of fidelity for the entangled state can be estimated as $F \geq F_{\text{low}} \equiv (1 - \langle\mathcal{W}\rangle_{\text{expt}})/2$ [149]. In this experiment, the polarization state is inspected by a combination of QWP-HWP-PBS, and the photonic spatial degree is measured by using of a BS and a PIEZO-mounted mirror for the basis $\{(|0\rangle + e^{i\alpha}|1\rangle)/\sqrt{2}, (|0\rangle - e^{i\alpha}|1\rangle)/\sqrt{2}\}$ or removing the BS for the basis $\{|0\rangle, |1\rangle\}$. The spin-wave is converted efficiently by a read pulse to a propagating anti-Stokes photon, where the polarization of the spin-wave is mapped onto the polarization of the photon by the relation $|b_0, b_{+2}\rangle \to |H, V\rangle_{\text{AS}}$ and the spatial degree of the spin-wave is mapped onto that of the photon $|\uparrow, \downarrow\rangle \to |l, r\rangle_{\text{AS}}$. Thus the evaluation of the spin-wave states are transformed into the measurement of the idler photons. The lower bound of the fidelity is measured as a function of storage time shown in Fig. 4.3. A minimum value of the witness $\langle \mathcal{W} \rangle_{\text{expt}} = -0.60 \pm 0.01$ is observed when the spin-wave is stored for 2.27 μs. This is a clear proof of genuine quadripartite entanglement and yields a fidelity $F \geq 0.800 \pm 0.007$. Moreover, the points of which the fidelity is larger than 0.5 indicate that the lifetime is longer than 14.27 μs. The oscillation of the fidelity originates from the oscillation of the retrieval efficiency when multiple atomic states are involved [150]. An intuitive understanding is that the retrieval efficiency of a superposition of two spin-wave polarization states (e.g., $|b_0\rangle + e^{i\Delta\phi}|b_{+2}\rangle$) will oscillate since the spin-wave related to $|b_{+2}\rangle$ will precess at a specific Larmor frequency so that two states evolve with different phases. The angular frequency of the relative phase of the two states is $\mu_{\text{B}} B_0 g_b \Delta m_F / \hbar \simeq 2\pi \times 420$ kHz with the Landé factor of state $|b\rangle$ $g_b \simeq 0.5$ and magnetic field $B_0 \simeq 300$ mG. A direct measurement is done by observing the oscillation of the retrieval efficiency of $|\pm\rangle$ polarized photons which is presented in Fig. 4.4. A damped sine fitting gives the oscillation frequency of (421 ± 1) kHz which coincides with the theoretical estimation.

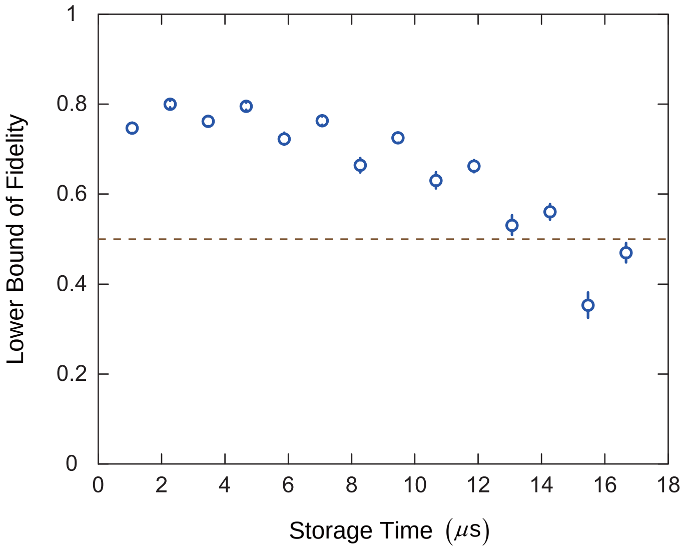

FIGURE 4.3: Measured lower bound of fidelity of the cluster state. The values are calculated from witness measurements. The dashed line marks a fidelity of 0.5, the theoretical threshold for a four-qubit entangled state [149]. Error bars represent statistical errors.

Furthermore, the density matrix of the cluster with a storage time of 2.27 μs is reconstructed by quantum state tomography via the maximum likelihood technique [115]. The reconstructed matrix is shown in Fig. 4.5, and the fidelity is calculated to be 0.817 ± 0.004 which agrees with the witness result. Note that the error is given by a total of 100 simulations, and each of them takes the data drawn randomly from a Poissonian distribution with mean equal to the original number of counts. To investigate the reason for the imperfect cluster state preparation, the reduced density matrices for each of the degrees

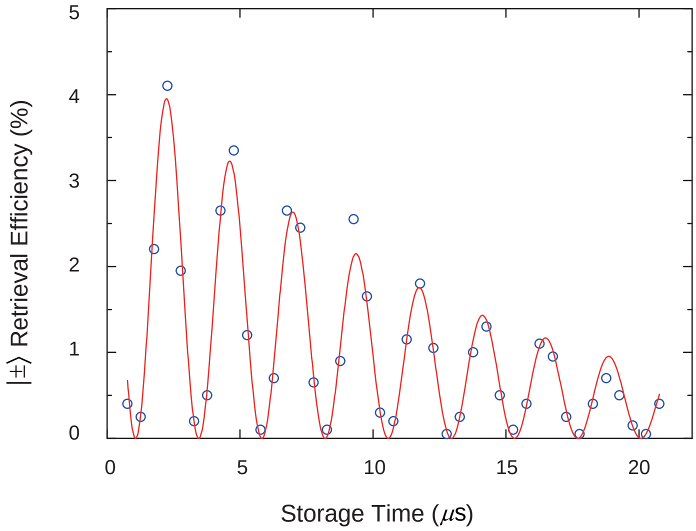

FIGURE 4.4: Averaged retrieval efficiency oscillation of $|\pm\rangle$ states. Only one spatial mode is chosen. The polarization of write-out photons and of read-out photons are orthogonal and are chosen from $\{|+\rangle, |-\rangle\}$.

are also reconstructed. The four reduced density matrices are shown in Tab. 4.1, with $|\psi_{\mathrm{p}}^{l\uparrow}\rangle = (|H\rangle_{\mathrm{S}}|b_0\rangle + |V\rangle_{\mathrm{S}}|b_{+2}\rangle)/\sqrt{2}$ for the polarization degree when the spatial degree state is $|l\rangle_{\mathrm{S}}|\uparrow\rangle$, $|\psi_{\mathrm{p}}^{r\downarrow}\rangle = (|H\rangle_{\mathrm{S}}|b_0\rangle - |V\rangle_{\mathrm{S}}|b_{+2}\rangle)/\sqrt{2}$ for the polarization degree when the spatial degree state is $|r\rangle_{\mathrm{S}}|\downarrow\rangle$, $|\psi_{\mathrm{k}}^{Hb_0}\rangle = (|l\rangle_{\mathrm{S}}|\uparrow\rangle + |r\rangle_{\mathrm{S}}|\downarrow\rangle)/\sqrt{2}$ for the spatial degree when the polarization degree state is $|H\rangle_{\mathrm{S}}|b_0\rangle$, and $|\psi_{\mathrm{k}}^{Vb_{+2}}\rangle = (|l\rangle_{\mathrm{S}}|\uparrow\rangle - |r\rangle_{\mathrm{S}}|\downarrow\rangle)/\sqrt{2}$ for the spatial degree when the polarization degree state is $|V\rangle_{\mathrm{S}}|b_{+2}\rangle$. The relatively low fidelity for polarization degree is mainly due to the imbalance of the coupling strength of the corresponding transitions used in the write process. And the non-ideal entanglement preparation for spatial degree is mainly caused by higher-order excitations and the imperfection of the BSs.

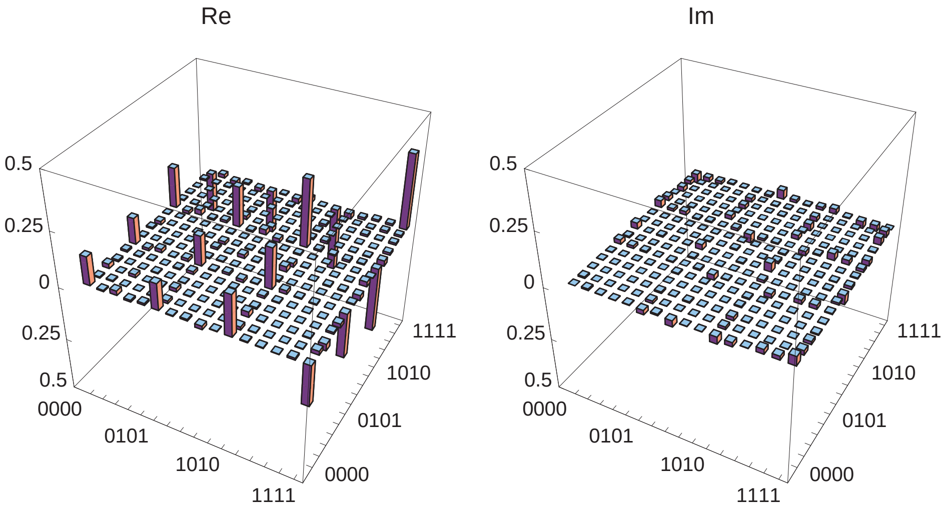

FIGURE 4.5: Quantum state tomography of the cluster state.

Table 4.1: Reduced density matrices and fidelities.

Ideal state	$\lvert\psi_{\mathrm{p}}^{l\uparrow}\rangle$	$\lvert\psi_{\mathrm{p}}^{r\downarrow}\rangle$	$\lvert\psi_{\mathrm{k}}^{Hb_0}\rangle$	$\lvert\psi_{\mathrm{k}}^{Vb_{+2}}\rangle$
Fidelity (%)	89.1(7)	87.9(7)	96.2(7)	94.8(5)
Real	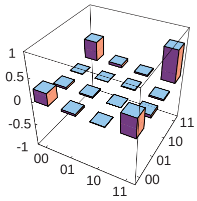	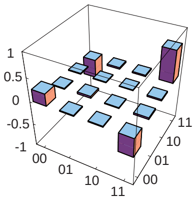	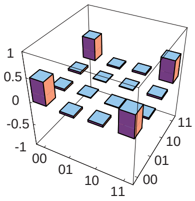	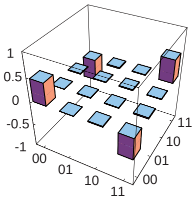
Imaginary	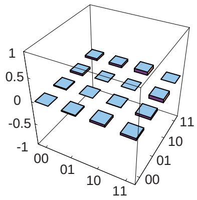	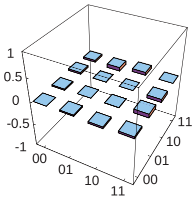	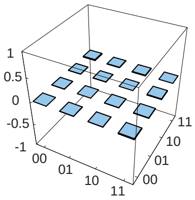	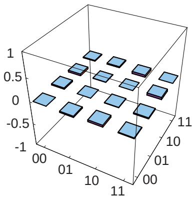

4.4 Results of the One-Way Quantum Computing

The hybrid cluster state enables us to demonstrate active one-way quantum computing with the built-in quantum memory. In this section, deterministic single-qubit rotations are demonstrated, as well as the two-qubit C-Phase gate, which constitute a basic set of necessary elements for an arbitrary unitary operation. Results on the realization of Grover's searching algorithm are presented afterwards.

4.4.1 Single-Qubit Rotations

In one-way quantum computing, implementation of an arbitrary single-qubit rotation requires a three-qubit linear cluster state $|\Phi_{\mathrm{lin3}}\rangle$ as shown in Fig. 4.6(a). The $|\Phi_{\mathrm{lin3}}\rangle$ cluster can be obtained from the prepared $|C_4\rangle$ cluster by the following three steps: (a) rearranging the order of the four qubits as $(1, 2, 3, 4) = (\mathbf{k}^{\mathrm{s}}, \mathbf{k}_{\mathrm{S}}^{\mathrm{p}}, \mathrm{p}_{\mathrm{S}}^{\mathrm{p}}, \mathrm{a}^{\mathrm{s}})$, where the notation "$\mathrm{p}_{\mathrm{S}}^{\mathrm{p}}$" represents the polarization degree of the Stokes photon, "$\mathbf{k}_{\mathrm{S}}^{\mathrm{p}}$" represents the spatial degree of the Stokes photon, "a^{s}" represents the polarization degree of the spin-wave, and "$\mathbf{k}^{\mathrm{s}}$" represents the spatial degree of the spin-wave; (b) implementing a unitary operation $\mathrm{Had} \otimes \mathbb{1} \otimes \mathbb{1} \otimes \mathrm{Had}$ on the experimental state; (c) removing the first qubit $\mathbf{k}^{\mathrm{s}}$ by post-selecting the corresponding results measured in the computational basis $\{|0\rangle_1, |1\rangle_1\}$. In this experiment, the Hadamard transformation on qubit 1 ($\mathbf{k}^{\mathrm{s}}$) is realized by BS_2, while the Hadamard transformation on qubit 4 (a^{s}) is realized by setting the last HWP of the two read-out photon paths at 67.5°. Although, the Hadamard operations on qubit 1 and qubit 4 are performed after the measurements on qubit 2 and qubit 3, the operations commute with each other and thus are permutable. To remove the physical qubit $\mathbf{k}^s$, the results relating to the outcome of $s_1 = 0$ are selected. Note that the post-selection introduces a reduction of 50% to the state preparation efficiency for $|\Psi_{\text{in}}\rangle$, however, it does not affect the deterministic character of the single-qubit gate. Actually, the outcome of $s_1 = 1$ implies that the input state is $|-\rangle$.

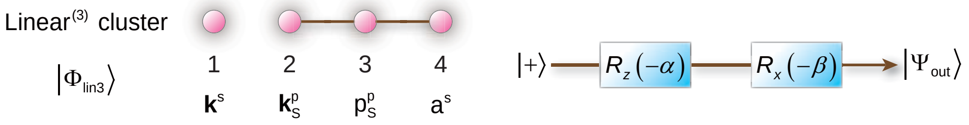
Linear(3) cluster
$|\Phi_{\text{lin3}}\rangle$
1
2
3
4
$\mathbf{k}^s$
$\mathbf{k}^p_s$
p^p_s
a^s
$|+\rangle$
$R_z(-\alpha)$
$R_x(-\beta)$
$|\Psi_{\text{out}}\rangle$

(a) One-way quantum circuit configuration of single-qubit rotations

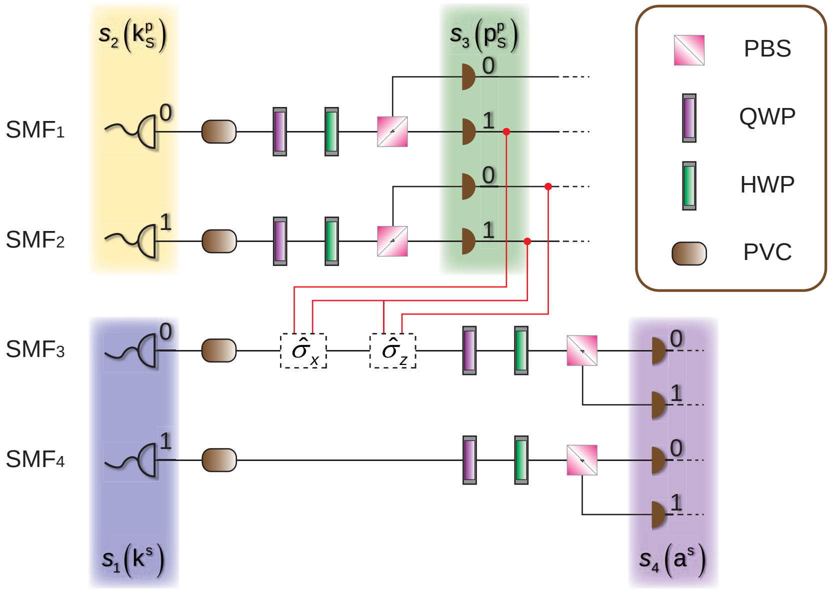
$s_2(\mathrm{k}^p_s)$
$s_3(\mathrm{p}^p_s)$
SMF1
SMF2
SMF3
SMF4
0
1
$\hat{\sigma}_x$
$\hat{\sigma}_z$
$s_1(\mathrm{k}^s)$
$s_4(\mathrm{a}^s)$
PBS
QWP
HWP
PVC

(b) Extended setup for active one-way quantum computing

FIGURE 4.6: Single-qubit rotations. (a) shows the one-way quantum circuit configuration of single-qubit rotations. (b) shows the extended setup to realize an active arbitrary single-qubit rotation. The measurement basis is set to be $B_3(\beta)$ at $s_2 = 0$ mode while $B_3(-\beta)$ at $s_2 = 1$ mode to correct type-I error. The measured outcomes of s_2 and s_3 are fed forward to EOMs for correction of type-II errors. The overall detection efficiency for the Stokes (anti-Stokes) photon is ~ 0.25 (~ 0.20) including propagation efficiency, coupling efficiency, detector efficiency, and so on. PVCs are used to suppress the noise photons.

An arbitrary single-qubit rotation can be realized by consecutively measuring qubit 2 and 3 of the cluster in the basis $B_2(\alpha)$ and $B_3(\beta)$, respectively. And the effective operation of rotations applied to the encoded qubit is expressed as

$$|\Psi_{\text{out}}\rangle = \hat{\sigma}_x^{s_3}\hat{\sigma}_z^{s_2} R_x((-1)^{s_2+1}\beta) R_z(-\alpha)|\Psi_{\text{in}}\rangle, \tag{4.6}$$

where the single-qubit rotation $R_x(\alpha) = \exp(-i\alpha\hat{\sigma}_x/2)$ is defined similar as $R_z(\alpha)$, $|\Psi_{\text{in}}\rangle = |+\rangle$ is the encoded qubit, and s_j taking the value of 0 or 1 is the outcome of the measurement on qubit j. Equation 4.6 implies that the choice of measurement basis $B_3(\pm\beta)$ on qubit 3 does depend on the previous measurement outcome s_2 on qubit 2 (type-I error), and the random measurement outcomes s_2 and s_3 will introduce random Pauli errors (type-II error). Thus a deterministic single-qubit rotation necessitates active feedforward to correct both types of errors.

Intuitively, errors can be corrected by making use of fast switchable optical elements such as EOMs with the help of quantum memory to store the subsequent qubits so that the time cost due to feedforward and the response time of the EOMs are compensated. In this experiment, correction of type-I error requires feedforward from the spatial degree of the Stokes photon $\mathbf{k}_{\mathrm{S}}^{\mathrm{p}}$ to the polarization degree of the Stokes photon $\mathrm{p}_{\mathrm{S}}^{\mathrm{p}}$, which means the choice of measurement basis of the polarization of the Stokes photon depends on the output modes of BS_1 that carries out the measurement $B_2(\alpha)$ with M_2 as shown in Fig. 4.2. Thus, the feedforward is simply realized by setting different measurement bases $B_3(\pm\beta)$ at different output modes of BS_1 ($s_2 = 0$ or $s_2 = 1$). However, type-II errors have to be compensated by applying $\hat{\sigma}_x^{s_3}$ and $\hat{\sigma}_z^{s_2}$ to the last qubit successively. In this experiment, EOMs are responsible for correction of the errors, where the $\hat{\sigma}_x$ operation is performed by introducing a π phase shift between $|+\rangle$ and $|-\rangle$ and the $\hat{\sigma}_z$ operation is performed by introducing a π phase shift between $|0\rangle$ and $|1\rangle$. The total time cost for preparing the Pauli error correction is about 1.69 μs, in which the response time of the EOM system contributes 1.56 μs, optical propagation contributes 20 ns, and electrical signal processing and transmission contributes 110 ns. For this reason, qubit 4 is stored in the atomic ensemble for 2.27 μs before being retrieved and subjected to the Pauli error corrections. The extended setup to realize single-qubit rotations is shown in Fig. 4.6(b) to specify the error corrections.

Fig. 4.7 shows the results of the single-qubit rotation $R_x(-\beta)$ and $R_z(-\alpha)$ from 0 to 2π in steps of $\pi/8$. The average fidelity is 0.82 ± 0.02 for $R_x(-\beta)$ rotations, and 0.91 ± 0.03 for $R_z(-\alpha)$ rotations. The difference between the fidelities reflects the characteristics of the prepared cluster. $R_z(-\alpha)$ rotations are realized by measuring qubit 2 ($\mathbf{k}_{\mathrm{S}}^{\mathrm{p}}$) in various bases, referring to the spatial degree of the cluster state that has a better quality as shown in Tab. 4.1; while $R_x(-\beta)$ rotations are realized by measuring qubit 3 ($\mathrm{p}_{\mathrm{S}}^{\mathrm{p}}$) in various bases, referring to the polarization degree of the cluster state that has a lower quality.

In order to show the ability of arbitrary rotations, two groups of specific angles are chosen. The experimental results are presented in the Bloch sphere, where Fig. 4.8(a) corresponds to a rotation operation to the input state with $\alpha = \pi/8$ and $\beta = \pi/6$ which has a fidelity of 0.94 ± 0.02, and Fig. 4.8(b) corresponds to a rotation operation to the input state with $\alpha = \pi/4$ and $\beta = \pi/4$ which has a fidelity of 0.93 ± 0.02.

A further analysis is made by reconstructing matrices of Pauli error correction operations and applying these operations onto proceeded clusters with assumption of ideal measurements. The Pauli error correction operations are evaluated and reconstructed

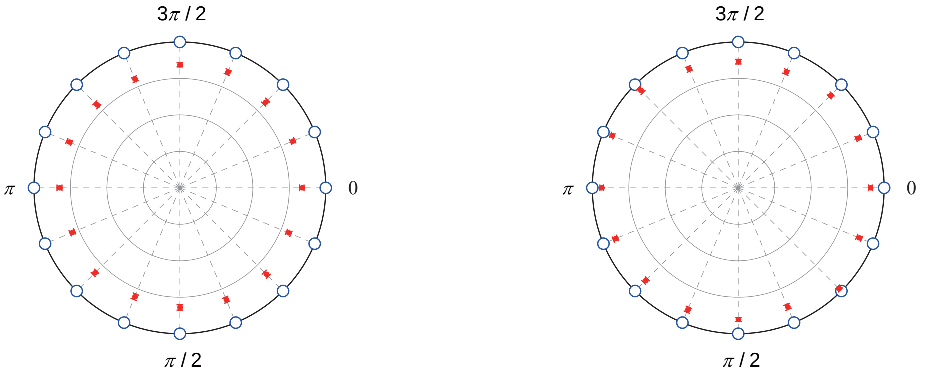

(a) Single-qubit rotation $R_x(-\beta)$ (b) Single-qubit rotation $R_z(-\alpha)$

FIGURE 4.7: Fidelities of the single-qubit rotations. The blue open dots show the ideal states with fidelity of 1, and each of the red dots with error bars shows the experimental result for the corresponding state. The value of fidelity is represented by the distance to the circle center. The four concentric circles mark fidelities of 0.25, 0.5, 0.75, and 1 sequentially from the center. (a) shows the results of $R_x(-\beta)$ rotations, where $\alpha = \pi/2$ and β is set from 0 to 2π in steps of $\pi/8$. (b) shows the results of $R_z(-\alpha)$ rotations, where $\beta = 0$ and α is set from 0 to 2π in steps of $\pi/8$.

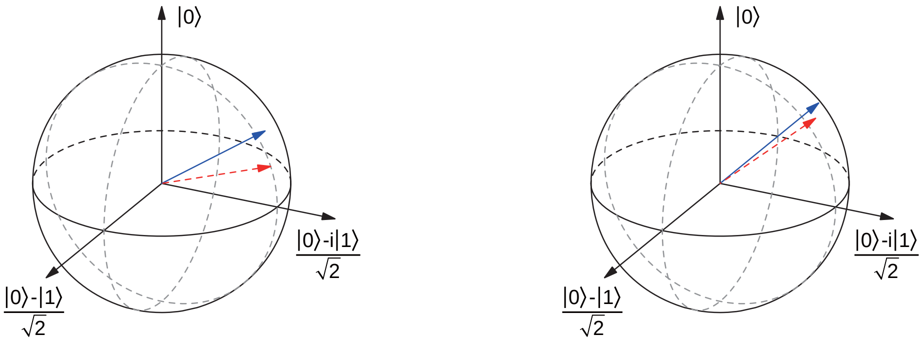
$|0\rangle$
$\frac{|0\rangle - i|1\rangle}{\sqrt{2}}$
$\frac{|0\rangle - |1\rangle}{\sqrt{2}}$
$|0\rangle$
$\frac{|0\rangle - i|1\rangle}{\sqrt{2}}$
$\frac{|0\rangle - |1\rangle}{\sqrt{2}}$

(a) $R_x(-\pi/6)R_z(-\pi/8)|+\rangle$ (b) $R_x(-\pi/4)R_z(-\pi/4)|+\rangle$

FIGURE 4.8: Bloch sphere representation of arbitrary single-qubit rotations. (a) shows rotation operation $R_x(-\pi/6)R_z(-\pi/8)$ on $|+\rangle$. (b) shows rotation operation $R_x(-\pi/4)R_z(-\pi/4)$ on $|+\rangle$. The blue arrows depict the ideal states, while the red dashed arrows depict the measured states obtained from the reconstructed density matrices.

via quantum process tomography in a maximum likelihood way [120], and the results are shown in Tab. 4.2. The rotations are simulated by numerically performing ideal measurements to the experimental cluster matrix, and later the Pauli errors are numerically corrected with the reconstructed process matrices. The simulated results (sim.) are compared to the experimental results (exp.), and are presented in Tab. 4.3 in which “Ave.” represents “average”. The errors of simulated results originate from the difference between rotated states with different Pauli errors. The deviation is ascribed mainly to imperfections of optical elements that, when used to evaluate the cluster, lead to underestimation of the cluster quality, and when used to perform single-qubit measurements, might induce additional modifications to the density matrices of the experimental results. The instability of the system also contributes to the errors.

Table 4.2: Reconstructed process matrices of Pauli error correction operations.

Operation	Real	Imaginary	Fidelity (%)
$\mathbb{1}$	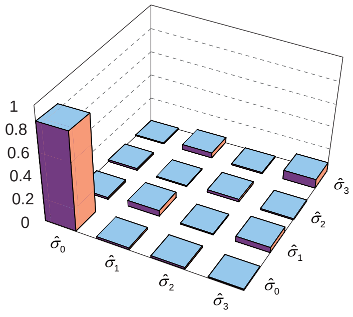	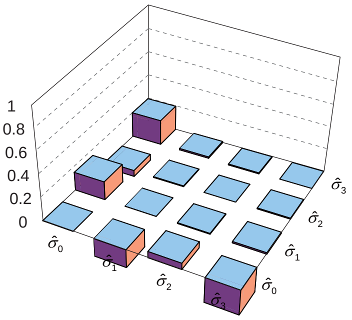	85.6(8)
$\hat{\sigma}_x$	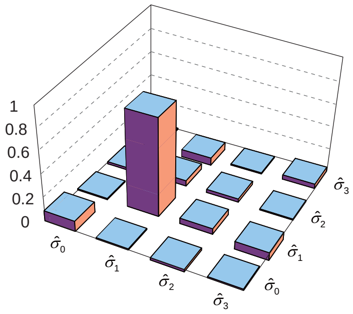	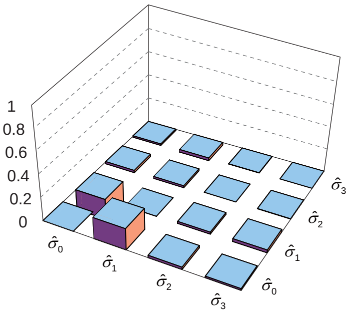	85.5(8)
$\hat{\sigma}_z$	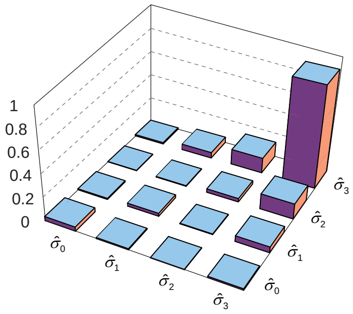	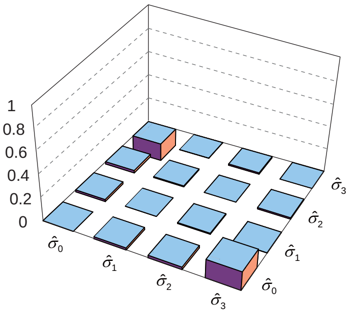	91.0(7)
$\hat{\sigma}_z \cdot \hat{\sigma}_x$	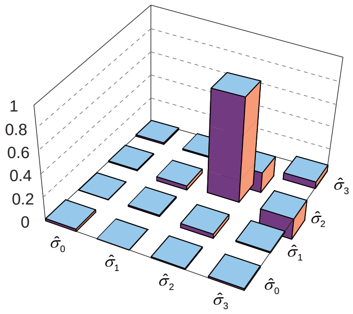	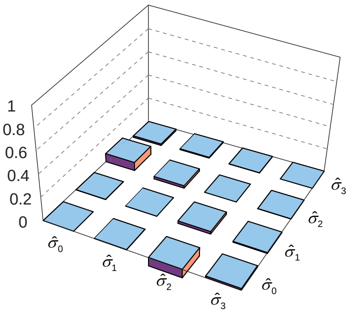	91.6(9)

4.4.2 Two-Qubit Controlled-Phase Gate

In one-way quantum computing, implementation of the two-qubit C-Phase gate requires a four-qubit horseshoe cluster state $|\Phi_{\subset 4}\rangle$ as shown in Fig. 4.9(a). The $|\Phi_{\subset 4}\rangle$ cluster can be obtained from the prepared $|C_4\rangle$ cluster by the following steps: (a) rearranging

TABLE 4.3: Simulation of the single-qubit rotations.

	$R_x(-\beta)$	$R_z(-\alpha)$	$R_x(-\frac{\pi}{6})R_z(-\frac{\pi}{8})$	$R_x(-\frac{\pi}{4})R_z(-\frac{\pi}{4})$
Ave. fidelity (exp.) (%)	82(2)	91(3)	94(2)	93(2)
Ave. fidelity (sim.) (%)	82(1)	84(1)	89(3)	89(4)
Fidelity (exp. & sim.) (%)	92(1)	95(1)	93(5)	95(5)

the order of the four qubits as $(1,2,3,4) = (\mathbf{k}^{\mathrm{s}}, \mathbf{k}_{\mathrm{S}}^{\mathrm{p}}, \mathrm{p}_{\mathrm{S}}^{\mathrm{p}}, \mathrm{a}^{\mathrm{s}})$; (b) implementing a unitary operation Had $\otimes \mathbb{1} \otimes \mathbb{1} \otimes$ Had on the experimental state. By measuring qubit 2 and 3 of the cluster in the basis $B_2(\alpha)$ and $B_3(\beta)$, respectively, one would get an output state of the form

$$|\Psi_{\mathrm{out}}\rangle = (\hat{\sigma}_x^{s_2} \otimes \hat{\sigma}_x^{s_3})(\mathrm{Had} \otimes \mathrm{Had})[R_z(-\alpha) \otimes R_z(-\beta)]\text{C-Phase}|\Psi_{\mathrm{in}}\rangle, \tag{4.7}$$

where $|\Psi_{\mathrm{in}}\rangle = |+\rangle|+\rangle$ is the encoded two-qubit input state. Thus a C-Phase operation is realized when $B_2(0)$ and $B_3(0)$ are chosen leaving a maximally entangled output state $|\Psi_{\mathrm{out}}\rangle = (|+\rangle|0\rangle + |-\rangle|1\rangle)/\sqrt{2}$ with an error $\hat{\sigma}_x^{s_2} \otimes \hat{\sigma}_x^{s_3}$. The Pauli error $\hat{\sigma}_x^{s_3}$ can be corrected by a normal EOM with feedforward information to modify the polarization of the retrieved photon, whereas the compensation of the Pauli error $\hat{\sigma}_x^{s_2}$ requires a polarization-independent EOM or a fast PIEZO-mounted mirror to change the relative phase between the two spatial modes of retrieved side before they meet at BS_2 with feedforward technique. This is because the operation $\hat{\sigma}_x^{s_2}$ Had on qubit 1 is equivalent to the operation Had $\hat{\sigma}_z^{s_2}$ where $\hat{\sigma}_z$ applies a relative phase between the two spatial modes. In this thesis, only a proof-of-principle C-Phase operation is demonstrated where the Pauli errors are corrected by post-processing. Fig. 4.9(b) shows the reconstructed density matrix of the state owning a fidelity of 0.845 ± 0.004 to an ideal state. Furthermore, a violation of the CHSH inequality is proved with the S parameter $S = 2.29 \pm 0.01$ that violates the inequality by 29 standard deviations. It is worth noting that the Hadamard operation on qubit 1 ($\mathbf{k}^{\mathrm{s}}$) can be absorbed to the measurement on it: a Hadamard operation followed by a measurement in basis $\{|0\rangle, |1\rangle\}$ is equivalent to measuring in basis $\{|+\rangle, |-\rangle\}$ since $\langle\psi|\mathrm{Had}^{\dagger}\hat{\sigma}_z\mathrm{Had}|\psi\rangle = \langle\psi|\hat{\sigma}_x|\psi\rangle$; a Hadamard operation followed by a measurement in basis $\{|+\rangle, |-\rangle\}$ is equivalent to measuring in basis $\{|0\rangle, |1\rangle\}$ since $\langle\psi|\mathrm{Had}^{\dagger}\hat{\sigma}_x\mathrm{Had}|\psi\rangle = \langle\psi|\hat{\sigma}_z|\psi\rangle$; a Hadamard operation followed by a measurement in basis $\{|R\rangle, |L\rangle\}$ is equivalent to measuring in basis $\{|L\rangle, |R\rangle\}$ since $\langle\psi|\mathrm{Had}^{\dagger}\hat{\sigma}_y\mathrm{Had}|\psi\rangle = -\langle\psi|\hat{\sigma}_y|\psi\rangle$ with $|R/L\rangle = (|0\rangle \pm i|1\rangle)/\sqrt{2}$.

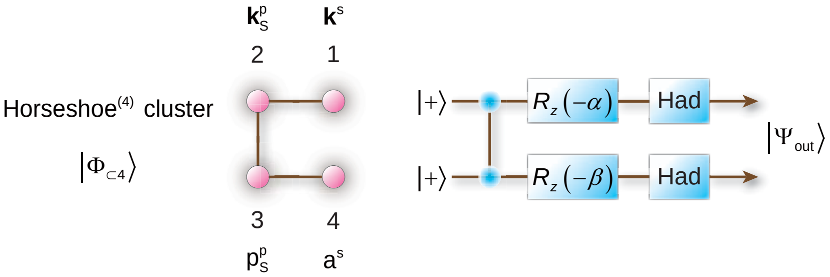
$\mathbf{k}_S^p$
$\mathbf{k}^s$
2
1
Horseshoe$^{(4)}$ cluster
$|\Phi_{\subset 4}\rangle$
3
4
p_S^p
a^s
$|+\rangle$
$|+\rangle$
$R_z(-\alpha)$
$R_z(-\beta)$
Had
Had
$|\Psi_{out}\rangle$

(a) One-way quantum circuit configuration of the C-Phase gate

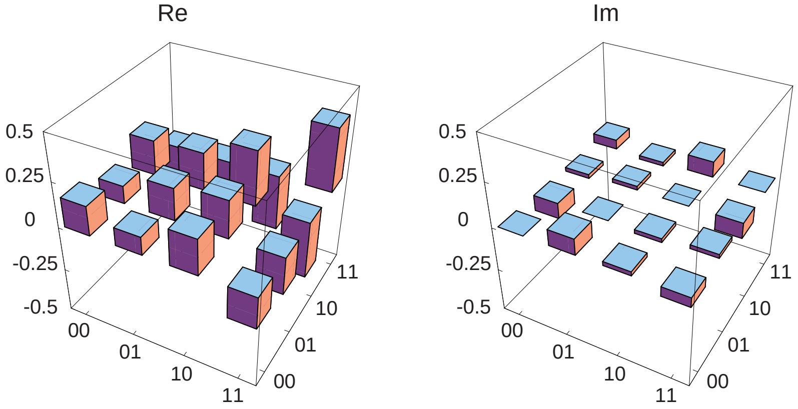

(b) Reconstructed density matrix of the two-qubit entangled state

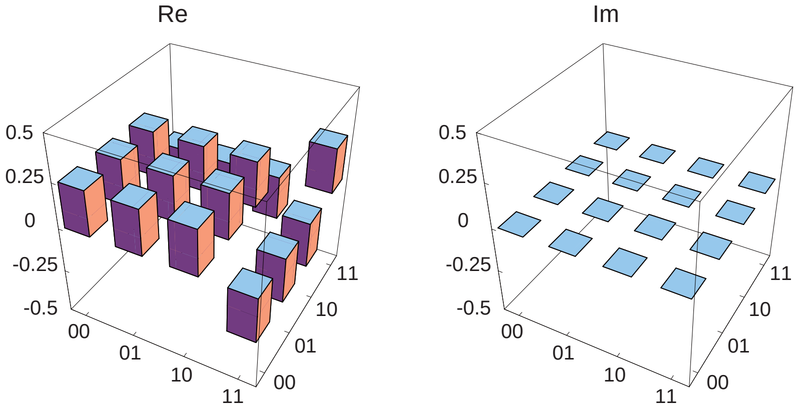

(c) Ideal density matrix of the two-qubit entangled state

FIGURE 4.9: Two-qubit C-Phase gate. (a) shows the one-way quantum circuit configuration of the two-qubit C-Phase gate. (b) shows the reconstructed density matrix of the resultant entangled state. (c) shows the density matrix of the ideal state $(|+\rangle|0\rangle + |-\rangle|1\rangle)/\sqrt{2}$ for comparison.

4.4.3 Grover's Searching Algorithm

Grover's searching algorithm promises to efficiently find a marked entry from an unsorted database with N entries and shows a quadratic speed-up over the classical counterparts. Given a database $|\psi_{\mathrm{db}}\rangle = \sum_{n=1}^{N} |n\rangle/\sqrt{N}$, the algorithm succeeds by performing the following operations: (a) a quantum device "oracle" marks the element to be searched $|m\rangle$ by inverting its phase, which can be expressed as $U_m|\psi_{\mathrm{db}}\rangle$ with the operator $U_m = \mathbb{1} - 2|m\rangle\langle m|$; (b) applying the Diffusion operator $U_d = 2|\psi_{\mathrm{db}}\rangle\langle\psi_{\mathrm{db}}| - \mathbb{1}$ which can be seen as an "inversion about the mean"; (c) repeating step (a) and step (b) where each iteration would increase the probability amplitude of state $|m\rangle$ by about $2/\sqrt{N}$. In the case of four entries, one can get the expected entry with certainty by running the algorithm only once.

In one-way quantum computing, implementation of Grover's algorithm requires a four-qubit box cluster state $|\Phi_{\square 4}\rangle$ as shown in Fig. 4.10(a). The $|\Phi_{\square 4}\rangle$ cluster helps to find a specific entry from the four, and can be obtained from the prepared $|C_4\rangle$ cluster by the following steps: (a) rearranging the order of the four qubits as $(1, 2, 3, 4) = (\mathbf{k}^{\mathrm{s}}, \mathrm{p}_{\mathrm{S}}^{\mathrm{p}}, \mathbf{k}_{\mathrm{S}}^{\mathrm{p}}, \mathrm{a}^{\mathrm{s}})$; (b) implementing a unitary operation Had ⊗ Had ⊗ Had ⊗ Had on the experimental state. By measuring qubit 2 and 3 of the cluster in the basis $B_2(\alpha)$ and $B_3(\beta)$, respectively, one would get an output state of the form

$$|\Psi_{\mathrm{out}}\rangle = (\hat{\sigma}_z \otimes \hat{\sigma}_x)^{s_3}(\hat{\sigma}_x \otimes \hat{\sigma}_z)^{s_2}\text{C-Phase}(\text{Had} \otimes \text{Had})[R_z(-\alpha) \otimes R_z(-\beta)]\text{C-Phase}|\Psi_{\mathrm{in}}\rangle, \tag{4.8}$$

where $|\Psi_{\mathrm{in}}\rangle = |+\rangle|+\rangle$ is the encoded two-qubit input state, a superposition of all four computational basis states $|0\rangle|0\rangle$, $|0\rangle|1\rangle$, $|1\rangle|0\rangle$, and $|1\rangle|1\rangle$. The oracle labels the state by measuring the physical qubit 2 and 3 in corresponding bases, with a relation of $00 \leftrightarrow (\alpha = 180°, \beta = 180°)$, $01 \leftrightarrow (\alpha = 0°, \beta = 180°)$, $10 \leftrightarrow (\alpha = 180°, \beta = 0°)$, and $11 \leftrightarrow (\alpha = 0°, \beta = 0°)$. The inversion about the mean is realized by first compensating the Pauli errors and then applying $(\text{Had} \otimes \text{Had})(\hat{\sigma}_z \otimes \hat{\sigma}_z)$ in a post-processing way in this thesis. The results are presented in Fig. 4.10(b), with an average identification probability of 91.9(3)%.

4.5 Discussion

In summary, an active feedforward one-way quantum computing is demonstrated with the built-in quantum memory which helps to store the qubits until necessary operations have been prepared depending on previous measurements. A hybrid four-qubit cluster serves as the essential resource, which is shared between a single-photon and a spin-wave of an atomic ensemble. Deterministic arbitrary single-qubit rotations are

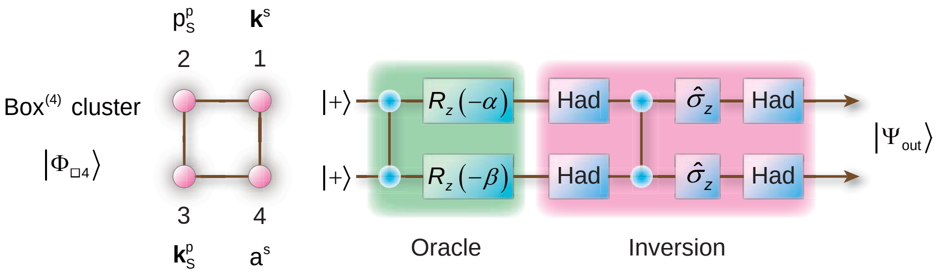
p_S^p
$\mathbf{k}^s$
2
1
Box$^{(4)}$ cluster
$|\Phi_{\square 4}\rangle$
3
4
$\mathbf{k}_S^p$
a^s
$|+\rangle$
$|+\rangle$
$R_z(-\alpha)$
$R_z(-\beta)$
Had
Had
$\hat{\sigma}_z$
$\hat{\sigma}_z$
Had
Had
$|\Psi_{out}\rangle$
Oracle
Inversion

(a) One-way quantum circuit configuration of Grover's algorithm

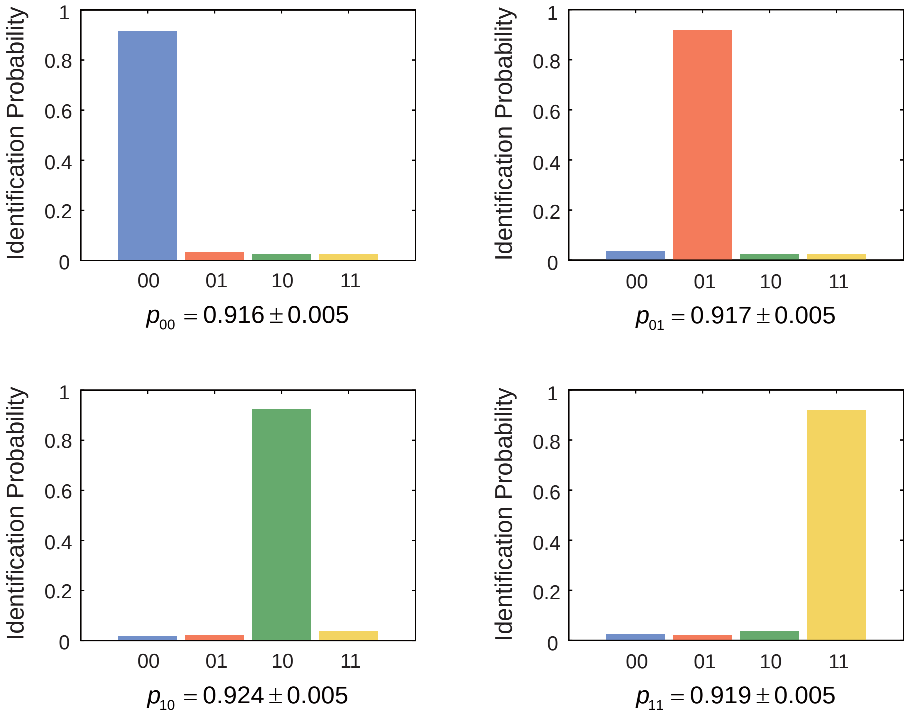

(b) Identification probabilities of the four entries

FIGURE 4.10: Grover's searching algorithm. (a) shows the one-way quantum circuit configuration of Grover's searching algorithm. (b) shows the identification probabilities for four entries with 0.916 ± 0.005, 0.917 ± 0.005, 0.924 ± 0.005, and 0.919 ± 0.005 for outcomes "00", "01", "10", and "11", respectively.

reported by the aid of EOMs and a quantum memory. In addition, the C-Phase gate and Grover's searching algorithm are presented where the Pauli errors are corrected by post-processing. In comparison with previous experiments with photons, the atomic ensemble not only acts as a quantum memory to store part of the cluster, but also provides the capability to tune the frequency [151], the pulse duration [152], and the retrieval time of the converted photon, which are advantageous to further connection with other physical systems in quantum networks [122].

In the present experiment, the cluster state loses coherence after 14 μs due to the short spin-wave coherence lifetime that is mainly limited by the dephasing of the spin-wave. In addition, the rise time of the EOM driver used in the experiment is slow, which, together with the short lifetime, leads to numbered feedforward steps. If faster EOM drivers [53] (65 ns rise time) are employed and an optical lattice is utilized to confine the motion of individual atoms [93] (16 s storage lifetime), realization of 10^8 feedforward steps is foreseeable in the near future. Furthermore, a larger cluster state can be in principle generated by encoding more information on one atomic ensemble like selecting more spatial modes [153], using the angular momentum degree [154], and more ground states, or by connecting many counterparts. However, it is technically hard to manipulate one qubit in one degree of freedom without disturbing the qubit encoded in the same physical entity but in a different degree of freedom. This makes the method of using multiple degrees of freedom to create large cluster fail, to some extent, in the sense of being scalable in general. Recently, Sean D. Barrett and his colleagues proposed a scalable scheme to generate a large cluster state with many photons and quantum memory units [123].

Chapter 5

Preparing a Two-Dimensional Ultracold Quantum Gas

On the last chapter, photon-matter entanglement generated by interactions between photon and atomic-ensemble has been used to study quantum computing. However, a quantum computer that can perform complex operations may require a large number of qubits. For example, for an odd integer N, $\lceil \log_2(N) \rceil + 1$ qubits are necessary to implement Shor's factoring algorithm even with the up-to-date protocol [155], where "$\lceil\ \rceil$" represents the ceiling function. Especially in one-way architecture, many more qubits are needed to form a cluster state. Unfortunately, the construction of such large entangled state is less efficient by connecting many photon-matter entanglement sources. In the past decade, there has been substantial studies on ultracold atoms in optical lattices, which turns out to be a promising way to realize large-scale one-way quantum computation with the help of single-site addressing techniques [145]. Especially, a pioneer work has demonstrated the generation of multi-particle entanglement through controlled collisions [62]. Although the system is less possible to be extended to realize universal quantum gates due the the lack of tunability, the work did intrigue several potential protocols with optical superlattices [156, 157]. In the following chapters, I will present current experimental results made towards this goal, including the study of a two-dimensional quantum gas, quantum phase transition in an optical lattice, and the experimental plan to entangle four bosons in each of the 2×2 plaquettes in the optical superlattice.

5.1 Theory of Three-Dimensional Bose-Einstein Condensates

Although the formation of BEC was predicted in the 1920s [158–160], it took about 70 years to observe it experimentally on vapors of alkali atoms [58, 161]. In these experiments, trapped atoms are cooled by laser and evaporative cooling techniques to ultra-low temperatures resulting in phase space densities beyond the critical value, so that the quantum-mechanical wave packets of individual atoms start to overlap implying the formation of a condensate [162]. Moreover, dilute repulsive trapped Bose gas, such as Rubidium 87 atoms, possesses peculiar features [163]: the inhomogeneity due to the harmonic trapping would lead to condensation not only in momentum space, but also in coordinate space; the repulsive interaction reduces the central density and enlarges the system to macroscopic scale; the dilute nature decreases the three-body recombination rate and allows a simple description to the interaction with s-wave scattering length. The theory of weakly interacting bosons can be understood by the Gross-Pitaevskii equation and the Bogoliubov theory [163]. Nowadays, achieving a BEC is an essential step to ensure quantum phase transition in an optical lattice. In this section, I will review the necessary knowledge required to understand the experiment presented in this thesis based on the paper [163] and the book [164].

5.1.1 Quantum Statistics

In classical mechanics, particles are considered distinguishable and governed by the Maxwell-Boltzmann statistics, in which the mean number of particles in a specific energy state ε_j is

$$\langle n_j \rangle_{\mathrm{MB}} = \frac{g_j}{\exp[(\varepsilon_j - \mu)/(k_{\mathrm{B}}T)]}, \tag{5.1}$$

where g_j is the degeneracy of energy level j, μ is the chemical potential, k_{B} is the Boltzmann's constant, and T is the absolute temperature. However, in quantum mechanics, particles of a particular type are indistinguishable, in other words, an exchange of them cannot be detected.

Quantum-mechanical particles are mainly divided into two categories named bosons, which have a symmetric wave function with integer spin, and fermions, which have an antisymmetric wave function with half-integer spin. Identical bosons obey Bose-Einstein statistics

$$\langle n_j \rangle_{\mathrm{BE}} = \frac{g_j}{\exp[(\varepsilon_j - \mu)/(k_{\mathrm{B}}T)] - 1}, \tag{5.2}$$

with $\mu \leq \varepsilon_j$ in order to conserve the particle number, whereas identical fermions obey Fermi-Dirac statistics

$$\langle n_j \rangle_{\mathrm{FD}} = \frac{g_j}{\exp[(\varepsilon_j - \mu)/(k_{\mathrm{B}}T)] + 1}, \tag{5.3}$$

with no further constraint for the chemical potential with respect to ε_j. In addition, identical fermions cannot occupy the same state due to the antisymmetric nature, which is known as the Pauli exclusion principle. In the case of identical bosons, as the temperature is lowered, the chemical potential rises due to the Maxwell relation, and thus the mean occupation numbers for low-lying energy states would increase. When the chemical potential reaches the ground-state energy, the number of particles in excited states consequently achieves its maximum value. Thus if the total number of particles is larger than this maximum allowable value, the superfluous particles must be accommodated in the lowest accessible quantum state, resulting in the BEC [164].

5.1.2 Non-interacting Bosons in a Harmonic Trap

When N non-interacting bosons are trapped in a harmonic trap $V_{\mathrm{ext}}(\mathbf{r}) = m(\omega_x^2 x^2 + \omega_y^2 y^2 + \omega_z^2 z^2)/2$, the ground state can be derived by putting all the particles in the lowest single-particle state $\varphi_0(\mathbf{r})$ and has the form of $\phi_N(\mathbf{r}_1, \cdots, \mathbf{r}_N) = \prod_j \varphi_0(\mathbf{r}_j)$, where $\varphi_0(\mathbf{r})$ is given by

$$\varphi_0(\mathbf{r}) = \left(\frac{m\omega_{\mathrm{ho}}}{\pi\hbar}\right)^{3/4} \exp\left[-\frac{m}{2\hbar}(\omega_x x^2 + \omega_y y^2 + \omega_z z^2)\right], \tag{5.4}$$

with the geometric average of the oscillator frequencies $\omega_{\mathrm{ho}} = (\omega_x\omega_y\omega_z)^{1/3}$. Thus the density distribution becomes $n(\mathbf{r}) = N|\varphi_0(\mathbf{r})|^2$.

At finite temperature, from the grand canonical ensemble representation, the transition temperature $T_{\mathrm{c}}^{\mathrm{ideal}}$ is obtained by imposing that the number of atoms at the lowest energy state is zero

$$k_{\mathrm{B}}T_{\mathrm{c}}^{\mathrm{ideal}} = \hbar\omega_{\mathrm{ho}} \left(\frac{N}{\zeta(3)}\right)^{1/3}, \tag{5.5}$$

with the Riemann zeta function $\zeta(3) \simeq 1.202$. Moreover, by introducing the phase space density as the number of particles contained within a volume equal to the cube of the thermal de Broglie wavelength $\lambda_{\mathrm{dB}} = \sqrt{2\pi\hbar^2/(mk_{\mathrm{B}}T)}$, one obtains a critical phase space density at which a BEC will appear

$$\mathrm{PSD}_c^{\mathrm{3D}} = \sum_{j=1}^{\infty} \frac{\exp[-\frac{jV_{\mathrm{ext}}(\mathbf{r})}{k_{\mathrm{B}}T}]}{j^{3/2}}. \tag{5.6}$$

Especially, if one neglects the external potential energy, the critical phase space density catches a constant value $\zeta(3/2) \simeq 2.612$ [165] and can be easily used to experimentally evaluate the process of reaching the phase transition.

5.1.3 Weakly Interacting Bose Gas

When atoms interact with each other, the behaviour of the system can be quite different from the non-interacting case. In second quantization, the many-body Hamiltonian describing N interacting bosons is given by

$$\begin{aligned} H = & \int d\mathbf{r} \hat{\Psi}^\dagger(\mathbf{r}) \left[-\frac{\hbar^2}{2m}\nabla^2 + V_{\text{ext}}(\mathbf{r}) \right] \hat{\Psi}(\mathbf{r}) \\ & + \frac{1}{2} \int d\mathbf{r} d\mathbf{r}' \hat{\Psi}^\dagger(\mathbf{r}) \hat{\Psi}^\dagger(\mathbf{r}') V_{\text{int}}(\mathbf{r}-\mathbf{r}') \hat{\Psi}(\mathbf{r}') \hat{\Psi}(\mathbf{r}), \end{aligned} \tag{5.7}$$

where $\hat{\Psi}(\mathbf{r})$ and $\hat{\Psi}^\dagger(\mathbf{r})$ are the bosonic field operators that annihilates and creates a particle at the position $\mathbf{r}$, respectively, and $V_{\text{int}}(\mathbf{r}-\mathbf{r}')$ describes the two-body interaction.

In the case of a dilute Bose gas, the Hamiltonian can be solved under a mean-field description formulated by Nikolay N. Bogoliubov in 1947 [166]. The key point of the mean-field theory is to separate out the condensate contribution to the bosonic field operator, which has the form of

$$\hat{\Psi}(\mathbf{r}, t) = \Phi(\mathbf{r}, t) + \delta\hat{\Psi}(\mathbf{r}, t), \tag{5.8}$$

where $\Phi(\mathbf{r}, t)$ is defined as the expectation value of the field operator $\Phi(\mathbf{r}, t) \equiv \langle \hat{\Psi}(\mathbf{r}, t) \rangle$, and $\delta\hat{\Psi}(\mathbf{r}, t)$ denotes a small perturbation. It is worth noticing that the complex function $\Phi(\mathbf{r}, t)$ is a classical field and is often called the condensate wave function, since it can be divided into several parts that can interfere with each other. Moreover, the function $\Phi(\mathbf{r}, t)$ is an order parameter which has a well-defined phase implying a broken gauge symmetry since adding a phase factor to this order parameter would produce a different state. When the average distance between the atoms is much larger than the s-wave scattering length a_{s}, namely, $\bar{n}|a_{\text{s}}|^3 \ll 1$ with $\bar{n}$ the average density, the two-body interatomic potential can be replaced by an effective contact interaction

$$V_{\text{int}}(\mathbf{r}-\mathbf{r}') = g_{\text{3D}}\delta(\mathbf{r}-\mathbf{r}'), \tag{5.9}$$

where the coupling constant of a three-dimensional system is given by $g_{\text{3D}} = 4\pi\hbar^2 a_{\text{s}}/m$. Using the above assumptions and neglecting the small perturbation term, the Gross-Pitaevskii (GP) equation [167, 168] is formulated as

$$i\hbar\frac{\partial}{\partial t}\Phi(\mathbf{r}, t) = \left(-\frac{\hbar^2\nabla^2}{2m} + V_{\text{ext}}(\mathbf{r}) + g_{\text{3D}}|\Phi(\mathbf{r}, t)|^2 \right) \Phi(\mathbf{r}, t). \tag{5.10}$$

Different from the Gaussian density distribution of the condensate derived from non-interacting bosons in a harmonic trap, the shape of the condensate can change drastically if the atoms are interacting. An effective parameter to describe the interaction strength is given by the ratio of the interaction energy to the kinetic energy which is proportional to $N|a_\mathrm{s}|/a_\mathrm{ho}$, where $a_\mathrm{ho} = \sqrt{\hbar/m\omega_\mathrm{ho}}$ is the harmonic oscillator length. For Rubidium 87 that is used throughout the thesis, the s-wave scattering length is about $103a_0 \simeq 5.45$ nm with a_0 the Bohr radius [169], which implies a repulsion between atoms. When N is large, the Thomas-Fermi (TF) approximation becomes valid in which the kinetic energy can be safely neglected, yielding the density profile in the form

$$n(\mathbf{r}) = \begin{cases} g_{3\mathrm{D}}^{-1}[\mu - V_\mathrm{ext}(\mathbf{r})] & \text{if } \mu > V_\mathrm{ext}(\mathbf{r}) \\ 0 & \text{if } \mu \leq V_\mathrm{ext}(\mathbf{r}) \end{cases} . \tag{5.11}$$

And according to the normalization condition on $n(\mathbf{r})$, the chemical potential μ takes the form

$$\mu = \frac{\hbar\omega_\mathrm{ho}}{2}\left(\frac{15Na_\mathrm{s}}{a_\mathrm{ho}}\right)^{2/5}, \tag{5.12}$$

which can be understood as the energy needed to add one more particle to a condensate having N atoms.

The GP equation is demonstrated as a versatile tool to study properties of the condensate. And a better description of the system beyond the mean-field theory could be derived by including the small perturbation $\delta\hat{\Psi}(\mathbf{r}, t)$ which will correct the chemical potential and the energy of the system. However, the depletion of them from the mean-field prediction is on the order of $\sqrt{na_\mathrm{s}^3}$ which is typically less than 1% for the current experiments, thus can be neglected in most of the cases.

5.2 Theory of Two-Dimensional Bose Fluids

In this thesis, I aim to generate entangled atoms that are trapped in a two-dimensional optical superlattice. In order to take advantage of the commensurate filling in a Mott insulator state, realization of two-dimensional superfluids is necessary, which in turn requires the understanding of the phase transition in a two-dimensional system.

In a three-dimensional system, the most familiar phase transitions are associated with the emergence of true long-range order (LRO) embedded in the order parameter. For example, the phase transition from a liquid to a crystal is relating to translational symmetry breaking, and a condensate would choose a particular phase in spite of the lack of a preferred value, which is also referred to as a spontaneous breaking of gauge symmetry. Unfortunately, the Mermin-Wagner theorem [170–172] states that continuous symmetries cannot be spontaneously broken at finite temperature in one-dimensional and two-dimensional systems with short-range interactions. The low-energy long-wavelength thermal fluctuations will always restore the symmetry of the Hamiltonian. Although true LRO is absent, quasi-LRO will allow the phase transition between the superfluid and the normal state at finite temperature, which is known as the Berezinskii-Kosterlitz-Thouless (BKT) transition [173, 174], associated with the emergence of a topological order. In this section, I will review the fundamental theory of the two-dimensional Bose gas in order to understand the experiment presented in this thesis based on the paper [65].

5.2.1 Effective Two-Body Interaction

In the last section, a contact potential (Eq. 5.9) has been introduced to describe the two-body interaction for dilute three-dimensional quantum gases. In the present experiment where the atoms are confined in a disk shape harmonic trap with $\omega_z/(2\pi) \simeq 4.9$ kHz, the thickness of the sample along the tightly confined direction ($\sim \sqrt{\hbar/m\omega_z} \simeq 154$ nm) is still much larger than the s-wave scattering length. This means that although the third dimension could be thermodynamically frozen, the interaction can be safely described by the three-dimensional scattering length a_s. Thus the two-dimensional interaction can be derived by simply integrating the frozen direction, assumed to be z, over the atomic cloud

$$g_\mathrm{2D} = g_\mathrm{3D} \int |\varphi(z)|^4 dz = \frac{\hbar^2}{m}\tilde{g} \tag{5.13}$$

where the wave function $\varphi(z) = \sqrt[4]{m\omega_z/(\pi\hbar)}\exp[-m\omega_z z^2/(2\hbar)]$ denotes the ground state along the z-axis in a harmonic trap, and $\tilde{g} = \sqrt{8\pi}a_\mathrm{s}/a_z$ is the dimensionless factor with $a_z = \sqrt{\hbar/m\omega_z}$ the harmonic oscillator length.

5.2.2 Berezinskii-Kosterlitz-Thouless Transition

In a uniform ideal two-dimensional Bose gas, by assuming no condensation, the phase space density is derived to be

$$\mathrm{PSD}_\mathrm{2D} \equiv n\lambda_\mathrm{dB}^2 = -\ln(1 - Z), \tag{5.14}$$

with the fugacity $Z = \exp[\mu/(k_\mathrm{B}T)]$. This relation implies that the chemical potential of the uniform gas has to be not positive, and for any non-infinite phase space density, there always exists a negative μ which allows the normalization of the thermal distribution of particles in the excited states to the total number of particles. This indicates the absence of the BEC at a finite temperature. However, the phase transition between the normal state and the superfluid state still takes place in the degenerate regime

($n\lambda^2 > 1$) as explained by the BKT theory, which does not involve any spontaneous symmetry breaking [65].

In the BKT theory, apart from the long-wavelength photon, vortex is introduced to be another source of phase fluctuations. A full analysis of the theory yields the transition between the superfluid state and the normal state. Below the transition temperature, vortices only appear in the form of bound pairs with opposite circulation, so that no net circulation exists at large distances. However, when the temperature increases, the density of the pairs as well as the sizes of the vortices grows due to the thermal fluctuations that lead to overlapping of them. Finally, when the temperature reaches the transition point, the vortices are no longer bound, thus affect the phase non-locally and destroy the superfluidity.

A simple understanding of the BKT transition is illustrated below by considering the free energy associated with the spontaneous creation of a single free vortex [174]. The kinetic energy of a free vortex is $E = \hbar^2 \pi n_{\mathrm{s}} \ln(R/\xi)/m$, where n_{s} is the superfluid density, R is the radius of the system, and $\xi = 1/\sqrt{gn}$ is the healing length. The healing length characterizes the length scale in which the interaction could help to remove the fluctuations, and can therefore be used as an estimation of the vortex size. The entropy of a free vortex is formulated as $S = 2k_{\mathrm{B}} \ln(R/\xi)$. Therefore the Helmholtz free energy of a single vortex is given as

$$F = E - TS = \frac{n_{\mathrm{s}}\lambda_{\mathrm{dB}}^2 - 4}{2} k_{\mathrm{B}} T \ln(R/\xi). \tag{5.15}$$

It can be readily seen that the free energy changes its sign at the point $n_{\mathrm{s}}\lambda_{\mathrm{dB}}^2 = 4$. A positive F indicates that the system is stable against the creation of a free vortex, while a system with a negative F would be favorable to the proliferation of free vortices. Especially when vortices appear, they will reduce the superfluid density making the creation of further vortices even easier. Such an avalanche effect will finally suppress the superfluid density to zero. Therefore, the transition will show a universal jump for the superfluid density. Note that the above self-consistent result only relates the phase transition to the superfluid density. Later, a detailed analysis is given for a system with weak-coupling $\tilde{g} \ll 1$, and the critical phase space density is calculated as [175–177]

$$\mathrm{PSD}_{\mathrm{BKT}} = \ln(C/\tilde{g}), \tag{5.16}$$

where the constant $C = 380 \pm 3$.

In fact, the superfluid state would exhibit quasi-LRO since the decay of the first-order correlation function $g^{(1)}(\mathbf{r}) \equiv \langle \hat{\Psi}^\dagger(\mathbf{r})\hat{\Psi}(0)\rangle$ will change from exponential in the normal state to algebraic in the superfluid state that has the form $g^{(1)}(r) = n_{\mathrm{s}}(\xi/r)^{1/\left(n_{\mathrm{s}}\lambda_{\mathrm{dB}}^2\right)}$.

Especially, $n_s\lambda_{\mathrm{dB}}^2$ is greater than or equal to 4 in the superfluid state which makes the decay of $g^{(1)}(r)$ even slower. In addition, the slow decay of correlations is of great importance that implies the possibility to reach a true BEC at non-zero temperature if atoms are confined in a finite region.

5.2.3 Two-Dimensional Bose Gas in a Harmonic Trap

In contrast to the uniform case, a BEC can occur if bosons are confined in a trap since the number of particles in the excited states is saturated at finite temperature. This can be seen by taking ideal bosons in an isotropic two-dimensional harmonic trap as an example which has an potential energy as the form of $V(r) = m\omega^2 r^2/2$. Thus the single-particle energy levels are $E_j = (j+1)\hbar\omega$ with $j \geq 0$ and each level having a degeneracy $g_j = j+1$. The number of particles in the excited states is then given as

$$N_{\mathrm{ex}} = \sum_{j=1}^{\infty} \frac{g_j}{\exp[(\varepsilon_j - \mu)/(k_{\mathrm{B}}T)] - 1}. \tag{5.17}$$

The maximum value of N_{ex} takes place when the chemical potential reaches the ground-state energy. And by assuming $k_{\mathrm{B}}T \gg \hbar\omega$, the maximum value becomes finite

$$N_c^{\mathrm{ex}} \simeq \frac{\pi^2}{6}\left(\frac{k_{\mathrm{B}}T}{\hbar\omega}\right)^2. \tag{5.18}$$

Therefore, for a given number of atoms, a significant fraction of atoms will be accommodated in the ground state when the temperature goes below the critical value

$$k_{\mathrm{B}}T_c^{\mathrm{ideal}} = \frac{\sqrt{6}}{\pi}\hbar\omega\sqrt{N}. \tag{5.19}$$

The same conclusion can be drawn by applying the local density approximation (LDA) to Eq. 5.14, where the uniform chemical potential is replaced by a local one $\mu_{\mathrm{global}} - V(r)$, yielding the total number of particles with the assumption of no condensation

$$N_{\mathrm{ex}} = -\lambda_{\mathrm{dB}}^{-2}\int_0^{\infty} \ln\left[1 - e^{\frac{\mu_{\mathrm{global}} - V(r)}{k_{\mathrm{B}}T}}\right] 2\pi r dr. \tag{5.20}$$

In this case, the maximum value takes place when the global chemical potential μ_{global} is equal to zero, and the result coincides with Eq. 5.18. Without loss of generality, the local phase space density for an interacting Bose gas is given as

$$n(r)\lambda_{\mathrm{dB}}^2 = -\ln\left\{1 - \exp\left[\frac{\mu_{\mathrm{global}} - V(r) - 2g_{2\mathrm{D}}n(r)}{k_{\mathrm{B}}T}\right]\right\}, \tag{5.21}$$

where the interaction energy is taken into account by adding $2g_{2D}n(r)$ to the external potential energy according to the mean-field Hartree-Fock approximation when no condensate is present [164]. Eq. 5.21 is of great importance to deriving the temperature and the global chemical potential by imaging the density profile.

5.3 Experimental Realization of a Two-Dimensional Degenerate Bose Gas

The process of achieving a two-dimensional superfluid gas is commenced by first loading Rubidium 87 atoms into a MOT and then magnetically transferring them to an ultra-high vacuum (UHV) glass cell. Radio-frequency-induced evaporation [58, 178] is applied to cool the atoms until the loss of atoms due to Majorana spin-flips becomes significant. Then the atoms are transferred to an optical dipole trap which is offset by about a beam waist distance from the center of the magnetic trap, and a BEC with about 10^5 Rubidium 87 atoms is produced by lowering the trap potential to force the evaporation [179]. Later, the third dimension (labelled as z-axis) is thermodynamically frozen by loading the compressed condensate into a single layer of an optical lattice with a periodicity of 4.2 μm, and the BKT transition is achieved by further lowering the trap potential along the other two axes. This thin layer of atoms are trapped only 2 mm away from the surface of the glass cell and thus can be imaged with high-resolution *in situ* imaging techniques. A typical experimental time sequence is illustrated in Fig. 5.1.

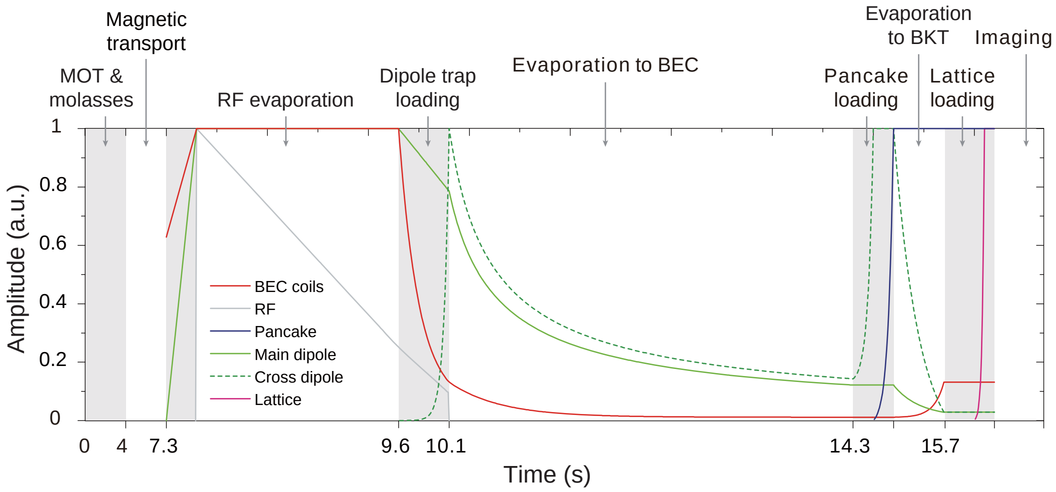

FIGURE 5.1: A typical experimental time sequence. It consists of MOT and molasses, magnetic transport, dipole trap loading, evaporation to achieve BEC, pancake loading, evaporation to achieve BKT, lattice loading, and experiment. RF represents for radio frequency.

5.3.1 Vacuum System

The formation of the condensate requires an UHV environment, however, a relatively high ambient pressure is necessary to ensure efficient atom collection in a MOT. To fulfill both conditions, the vacuum system is devided into two regions, the MOT-vacuum region and the BEC-vacuum region, illustrated in Fig. 5.2. The two regions are connected by a large L-shaped tube, and are further separated by a 16 cm long cooper tube with an inner diameter of 8 mm. The differential pumping tube can maintain a pressure differential between the regions of a factor 200, so that the efficient pumping in the BEC-vacuum region does not have any considerable effect on the MOT-vacuum region. The pressure of the BEC-vacuum region is kept at about 1×10^{-11} mbar by a Varian Vaclon Plus 75 Starcell ion pump (65 L/s) together with a Titanium sublimation pump (TSP). In the Mot-vacuum region, a Varian Vaclon Plus 20 Starcell ion pump (20 L/s) is connected and the pressure is kept at about 1×10^{-9} mbar.

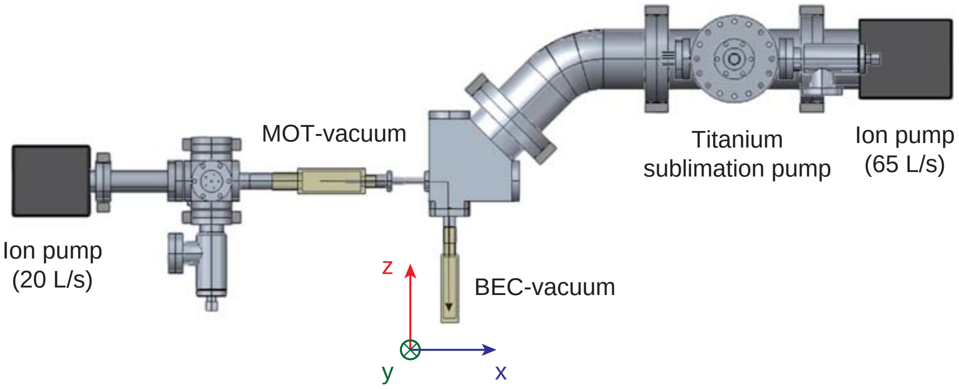

FIGURE 5.2: An illustration of the vacuum system. The large L-shaped tube allows performing absorption imaging of the atoms along the z-axis. The gravitational direction is specified as y direction.

5.3.2 Diode Laser System

In total three diode lasers are employed in the experiment, a Toptica DLX110, a Toptica DL100, and a homemade diode laser. Each of them is stabilized by the Pound-Drever-Hall FM method with the help of a fast photodiode (fast-PD), and the layout is shown in Fig. 5.3. They provide the following necessary laser beams to prepare a cold atomic ensemble for the BEC production, including “cooler” and “imaging” by the DLX110, “dark-repumper”, “normal-repumper”, and “σ^--pump” by the DL100, and “depump” by the homemade laser. The frequencies of the laser beams are summarized in Fig. 5.4, and are explained below.

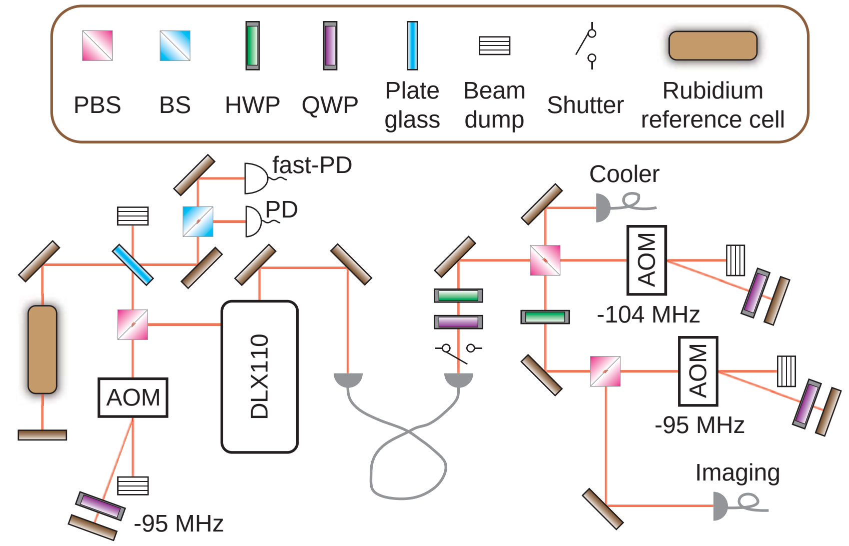
PBS
BS
HWP
QWP
Plate glass
Beam dump
Shutter
Rubidium reference cell
fast-PD
PD
Cooler
AOM
-104 MHz
AOM
-95 MHz
DLX110
AOM
-95 MHz
Imaging

(a) DLX110 laser system for cooler and imaging

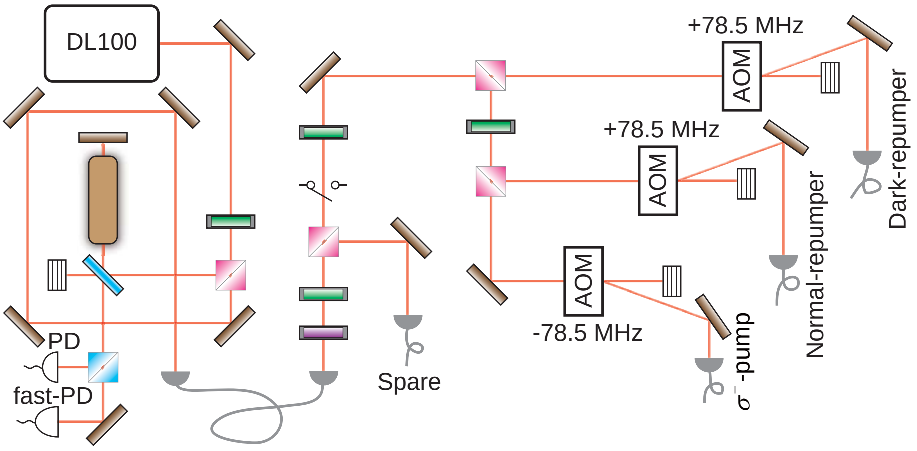
DL100
+78.5 MHz
AOM
+78.5 MHz
AOM
Dark-repumper
Normal-repumper
AOM
-78.5 MHz
σ^--pump
PD
fast-PD
Spare

(b) DL100 laser system for dark-repumper, normal-repumper, and σ^--pump

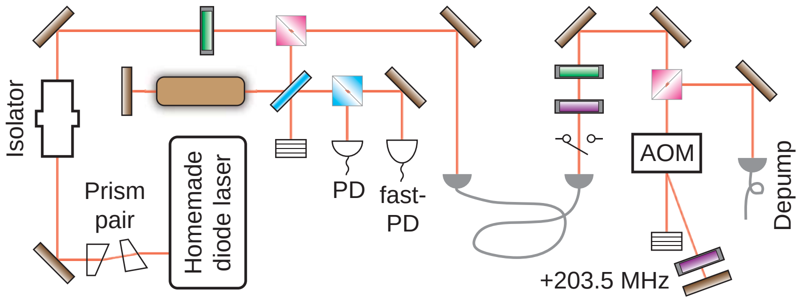
Isolator
Prism pair
Homemade diode laser
PD
fast-PD
AOM
Depump
+203.5 MHz

(c) Homemade laser system for depump

FIGURE 5.3: An illustration of the diode laser system. (a) shows the DLX110 laser system. Both cooler and imaging beams take double-pass acousto-optic modulator (AOM) configuration so that the frequencies can be tuned with high efficiencies. (b) shows the DL100 laser system. A spare laser beam is reserved for alignment purpose. (c) shows the homemade laser system. A pair of identical wedge prisms are placed at the beginning to transform the beam profile into a circle. Plate glass has a typical reflection efficiency of 10%. Photodiodes (PDs) are used to monitor the spectrum, and shutters are employed to block beams when necessary to suppress the noise.

Cooler is necessary to cool the atoms. It is red-detuned by 18 MHz from the cycling transition of the D-2 line in the MOT phase, and is further red-detuned by 72 MHz in the molasses phase.

Imaging is used to acquire the density profile of the atomic cloud through absorption. It is tuned on resonance with the $|F=2\rangle \rightarrow |F'=3\rangle$ transition of the D-2 line. In the case of an optically thick thermal cloud, the imaging beam is usually detuned by up to 10 MHz.

Dark-repumper is of great importance to the dark spontaneous-force optical trap (Dark SPOT) [180], and is tuned on resonance with the $|F=1\rangle \rightarrow |F'=2\rangle$ transition of the D-2 line.

Normal-repumper is tuned on resonance with the $|F=1\rangle \rightarrow |F'=2\rangle$ transition of the D-2 line and is used to pump the atoms to $|5^2S_{1/2}, F=2\rangle$ for absorption imaging.

σ^--pump is tuned on resonance with the $|F=1\rangle \rightarrow |F'=1\rangle$ transition of the D-2 line and is σ^- polarized so that the atoms will be accumulated in the state $|5^2S_{1/2}, F=1, m_F=-1\rangle$ which can be captured by a magnetic trap.

Depump is tuned on resonance with the $|F=2\rangle \rightarrow |F'=2\rangle$ transition of the D-1 line which assists the σ^--pump in the preparation of the state.

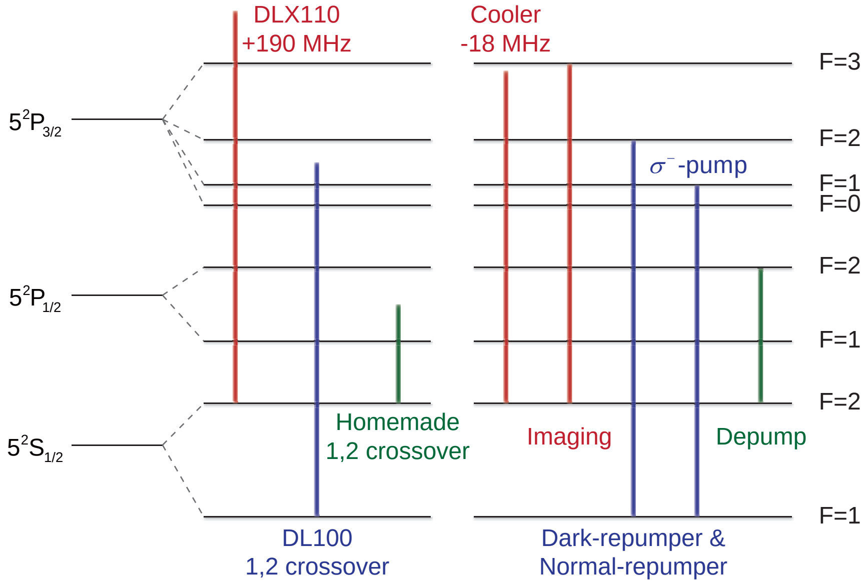
DLX110
+190 MHz
Cooler
-18 MHz
$5^2P_{3/2}$
$5^2P_{1/2}$
$5^2S_{1/2}$
F=3
F=2
F=1
F=0
F=2
F=1
F=2
F=1
σ^--pump
Homemade
1,2 crossover
Imaging
Depump
DL100
1,2 crossover
Dark-repumper &
Normal-repumper

FIGURE 5.4: Frequencies of the laser beams. The locking points of the diode lasers are illustrated at the left part, and the frequencies of the laser beams are specified at the right part.

5.3.3 Absorption Imaging

Absorption imaging is widely used to characterize the density profile of the atoms. The idea is based on a measurement of the transmission efficiency of a laser beam passing through the atomic cloud. Together with the time-of-flight (TOF) method [181] or with the *in situ* method [65], temperature information can be acquired.

5.3.3.1 Absorption Imaging of a Three-Dimensional Atomic Cloud

When a near-resonant laser beam, with intensity I, propagates through an atomic vapor along the z-axis, the intensity attenuation is governed by

$$\frac{dI}{dz} = -n_{\mathrm{3D}}(x, y, z)\sigma I, \tag{5.22}$$

where n_{3D} is the three-dimensional atomic density, and $\sigma = \sigma_0/[1+4(\Delta/\Gamma)^2+(I/I_{\mathrm{sat}})]$ is the cross section with the on-resonance cross section $\sigma_0 = \hbar\omega_0\Gamma/(2I_{\mathrm{sat}})$ and saturation intensity $I_{\mathrm{sat}} = 1.67\ \mathrm{mW/cm^2}$ for Rubidium 87 [3]. For a resonant laser pulse with intensity $I_0 \ll I_{\mathrm{sat}}$, one would obtain the transmission efficiency according to the Beer's law

$$\frac{I_{\mathrm{t}}(x, y)}{I_0(x, y)} = e^{-\sigma_0 n(x,y)}, \tag{5.23}$$

where $n(x, y) = \int n_{\mathrm{3D}}(x, y, z)dz$ is the atomic column density. Thus, by recording the intensity distribution without the atoms $I_0(x, y)$ and with the atoms $I_{\mathrm{t}}(x, y)$, one can derive the density distribution. In the experiment, a charge-coupled device (CCD) camera (iKon-M934 from Andor) is used for the purpose which generates a specific number of photoelectrons that is proportional to the intensity of the light, and the number distribution of the photoelectrons is given by

$$P(x_j, y_{j'}) = \frac{Q_{\mathrm{qe}} A I(x_j, y_{j'})\tau_{\mathrm{exp}}}{\hbar\omega_0}, \tag{5.24}$$

where x_j/y_j denotes the j-th pixel of x/y direction, Q_{qe} is the quantum efficiency, A is the area of a single pixel, and τ_{exp} is the exposure time. Thus, the atomic column density is described as

$$n(x_j, y_{j'}) = -\frac{1}{\sigma_0}\ln\frac{P_{\mathrm{t}}(x_j, y_{j'})}{P_0(x_j, y_{j'})} \tag{5.25}$$

in the weak imaging limit, where the background contributions have been subtracted off to derive $P_{\mathrm{t}}(x_j, y_{j'})$ and $P_0(x_j, y_{j'})$.

However, in the case of a degenerate quantum gas, the atomic cloud is optically dense, $n\sigma_0 \gg 1$, leading to a strong absorption. One therefore has to either adopt a long imaging pulse or apply imaging beam of high intensity in order to keep $P_{\mathrm{t}}(x_j, y_{j'})$ non-zero. The former idea is quite limited since the atoms should travel less than the depth of focus during the exposure. Meanwhile, the latter idea requires a careful calibration of the effective saturation intensity $I_{\mathrm{eff}}^{\mathrm{sat}} = \alpha I_{\mathrm{sat}}$ which deviates from the ideal saturation intensity due to the imperfection of the polarization, optical pumping effects, and the broadened transition line width caused by laser jitter and atomic collisions [182, 183]. A typical way to calibrate it is to vary the intensity of the imaging beam while keeping the total number of photons in a similar order by changing the exposure time. By assuming that the atoms are prepared in the same condition, the α parameter can be derived through a least-square fit [182]. In addition, a calibration of the effective line width $\Gamma_{\mathrm{eff}} = \beta\Gamma$ is necessary when the laser jitter or the energy splitting induced by the stray magnetic field is large compared to the natural line width [184], which can be derived by inserting the β parameter into any density fitting model [183, 185]. By applying the modifications, one gets the density distribution

$$n(x_j, y_{j'})\sigma_0\beta = -\alpha \ln\left[\frac{P_{\mathrm{t}}(x_j, y_{j'})}{P_0(x_j, y_{j'})}\right] - \frac{P_{\mathrm{t}}(x_j, y_{j'}) - P_0(x_j, y_{j'})}{P_{\mathrm{sat}}}, \tag{5.26}$$

where P_{sat} denotes the theoretical number of photoelectrons per pixel for saturation intensity.

5.3.3.2 Absorption Imaging of a Two-Dimensional Atomic Cloud

For a two-dimensional dense gas, Eq. 5.22 is no longer applicable since a two-dimensional cloud does not allow a continuous absorption. To deduce the density distribution from absorption imaging, one should consider the number of photons that are scattered off by individual atoms during the exposure [183].

When a resonant laser beam shines on a single atom, the photon scattering rate is given by

$$\gamma \equiv \frac{\sigma_{\mathrm{eff}} I}{\hbar\omega_0} = \frac{\Gamma_{\mathrm{eff}}}{2}\frac{I}{I + I_{\mathrm{eff}}^{\mathrm{sat}}}, \tag{5.27}$$

where $\sigma_{\mathrm{eff}} = \sigma_{\mathrm{eff}}^0/[1 + 4(\Delta/\Gamma_{\mathrm{eff}})^2 + (I/I_{\mathrm{eff}}^{\mathrm{sat}})]$ is the effective cross section with $\sigma_{\mathrm{eff}}^0 = \hbar\omega_0\Gamma_{\mathrm{eff}}/(2I_{\mathrm{eff}}^{\mathrm{sat}})$. Inside one pixel of the CCD camera, the intensity of the laser beam can be assumed to be constant. Within a small time interval $d\tau$, there will be $\gamma d\tau$ photons scattered out from $AI d\tau/(\hbar\omega_0)$ incident photons by a single atom. The transmission probability of the probe beam passing through N atoms is then $(1 - \gamma\hbar\omega_0/AI)^N = (1 - \sigma_{\mathrm{eff}}/A)^N \simeq e^{-\sigma_{\mathrm{eff}} n}$ when $\sigma_{\mathrm{eff}} \ll A$, which is equivalent to

$$\sigma_{\mathrm{eff}} n = -\ln\left[\frac{I_{\mathrm{t}}(x_j, y_{j'})}{I_0(x_j, y_{j'})}\right], \tag{5.28}$$

with $n = N/A$. In addition, the number of incident photons N_{p0}, the number of transmitted photons N_{pt}, and the number of atoms N should fulfill the relation

$$\begin{aligned} N_{\mathrm{p0}} - N_{\mathrm{pt}} &= N\gamma\tau \\ \frac{I_0 A\tau}{\hbar\omega_0} - \frac{I_{\mathrm{t}} A\tau}{\hbar\omega_0} &= \frac{nA\sigma_{\mathrm{eff}} I\tau}{\hbar\omega_0}. \end{aligned} \tag{5.29}$$

This implies that the effective intensity I should be determined in a self-consistent manner as

$$I_{\mathrm{t}} = I_0 - n\sigma_{\mathrm{eff}} I. \tag{5.30}$$

Then one could get the useful formula

$$n(x_j, y_{j'})\sigma_0\beta = -\alpha \ln\left[\frac{I_{\mathrm{t}}(x_j, y_{j'})}{I_0(x_j, y_{j'})}\right] - \frac{I_{\mathrm{t}}(x_j, y_{j'}) - I_0(x_j, y_{j'})}{I_{\mathrm{sat}}}, \tag{5.31}$$

which happens to be identical to the three-dimensional case.

5.3.4 Real-Time Control System

Throughout the experiment, lasers and magnetic fields are controlled by both analog signals and digital signals provided by an internally developed real-time control system as illustrated in Fig. 5.5. The analog signals are provided by a ADWin-Pro II system (from Jäger) with the precision of the signal set to 30 μs, and are used to control such as the currents of the coils, the frequencies of the AOMs, and so on. The digital signals are provided by two FPGA boxes (from Electronic Workshop, University of Heidelberg) with the precision of the signal set to 10 ns, and are used to control such as the TTL switch for the radio frequency (RF) signals, the shutters, and so on. In addition, FPGA1 will trigger the ADWin system in order to synchronize the signals. Two computers are responsible for communicating with the signal providers, of which the control computer sends the orders of the programmed signals and the data computer collects the image data as well as controls the other computer remotely.

5.3.5 Magneto-Optical Trap and Optical Molasses

In this experiment, atoms doled out by a Rubidium dispenser are first captured and cooled in a modified MOT, the so-called Dark SPOT, where the dark-repumper beam has a shadow in the center with the size of 1 cm. Atoms in the dark region will most probably stay in the state $|5^2S_{1/2}, F = 1\rangle$ and not absorb the cooler light. In this way, losses both due to excited-state collisions and by multiple scattering of light will be highly suppressed, leading to a much higher atomic density as well as the total number of

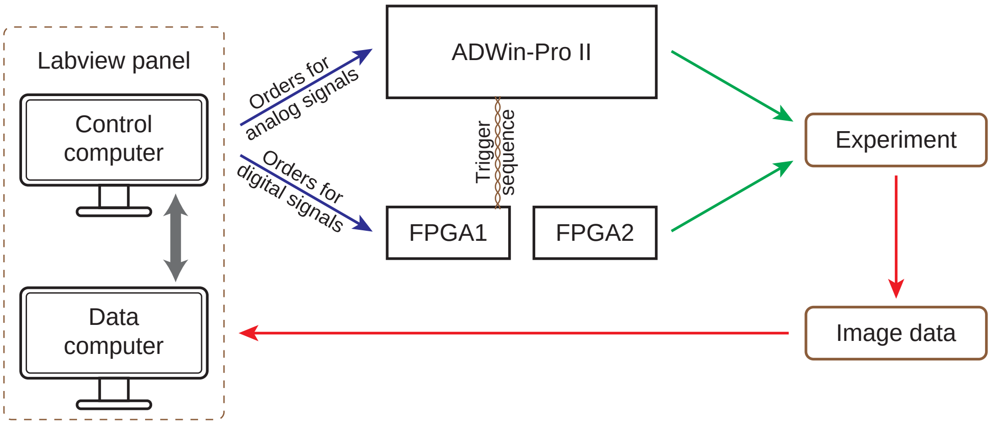
Labview panel
Control computer
Data computer
Orders for analog signals
Orders for digital signals
ADWin-Pro II
Trigger sequence
FPGA1
FPGA2
Experiment
Image data

Figure 5.5: A schematic view of the real-time control system.

atoms [180]. The construction of the MOT takes a retroreflection structure, where each of the beams has a cooler power of 60 mW and a beam diameter of about 3.5 cm. The gradient of the magnetic field is kept to 9 G/cm. Thanks to the Dark SPOT method, 8×10^8 atoms are captured within 4 s with a temperature of about 150 μK.

In the next 6 ms, the magnetic field is switched off and the optical molasses is applied to further cool the atoms. Note that, Sisyphus effect is absent since the light shifts of the ground-state sublevels remain constant, however, the atoms are cooled due to a net friction force induced by unbalanced radiation pressures [186]. In the molasses phase, the detuning of the cooler is continuously changed from 18 MHz (3 linewidths) to 72 MHz (12 linewidths), together with a decrease of the intensity to about 1/3 within 3 ms which then stays constant. The temperature of the atoms is measured to be 28(3) μK.

5.3.6 Magnetic Trap and Magnetic Transport

Once the atoms have been laser cooled, a σ^--pump and a depump are applied to prepare the atoms in the low-field-seeking state $|5^2S_{1/2}, F = 1, m_F = -1\rangle$ which are then transferred to a magnetic quadrupole trap with a gradient of 70 G/cm. In the magnetic trap, atoms are first compressed by increasing the gradient of the field to 140 G/cm in 100 ms, and then transported to the BEC-vacuum region.

5.3.6.1 Magnetic Trapping

According to the Biot-Savart law, expressed in cylindrical coordinates, the magnetic field components generated by a loop of radius a are expressed as

$$B_\rho(\rho, z) = \frac{\mu_0 I}{2\pi} \frac{z}{\rho\sqrt{(\rho+a)^2+z^2}} \left[\frac{a^2+\rho^2+z^2}{(a-\rho)^2+z^2} E(k) - K(k)\right], \tag{5.32}$$

$$B_z(\rho, z) = \frac{\mu_0 I}{2\pi} \frac{1}{\sqrt{(\rho+a)^2+z^2}} \left[\frac{a^2-\rho^2-z^2}{(a-\rho)^2+z^2} E(k) + K(k)\right], \tag{5.33}$$

where I is the current, μ_0 is the vacuum permeability, $k^2 = 4a\rho/[(a+\rho)^2+z^2]$, and $K(k) = \int_0^{\pi/2}[1/\sqrt{1-k^2\sin^2(\phi)}]d\phi$ and $E(k) = \int_0^{\pi/2}[\sqrt{1-k^2\sin^2(\phi)}]d\phi$ are the complete elliptic integral of the first kind and of the second kind, respectively. When two loops are positioned in an anti-Helmholtz configuration with a distance between them of $2b$ as shown in Fig. 5.6(a), the magnetic field at a point on the axis of the loops is then

$$B_{\text{axis}}(z) = \frac{\mu_0 I a^2}{2} \left\{\frac{1}{[a^2+(z-b)^2]^{3/2}} - \frac{1}{[a^2+(z+b)^2]^{3/2}}\right\}. \tag{5.34}$$

As a result, the gradient of the magnetic field along the axis takes the form

$$\frac{\partial B_{\text{axis}}(z)}{\partial z} = \frac{\mu_0 I a^2}{2} \left\{-\frac{3(z-b)}{[a^2+(z-b)^2]^{5/2}} + \frac{3(z+b)}{[a^2+(z+b)^2]^{5/2}}\right\}. \tag{5.35}$$

At the midpoint, $z = 0$, the gradient has the value

$$\left.\frac{\partial B_{\text{axis}}(z)}{\partial z}\right|_{z=0} = \frac{\mu_0 I a^2}{2} \frac{6b}{(a^2+b^2)^{5/2}} \neq 0. \tag{5.36}$$

Fig. 5.6(b) shows the theoretical magnetic field and the field gradient along the axis of the MOT coils. It is worth noting that the field gradient along the radial direction near the center of the trap is half of the one along the axis of the coils due to the Gauss's law for magnetism, hence the magnitude of the magnetic field can be estimated as

$$|\mathbf{B}| = \frac{\mu_0 I a^2}{2} \frac{3b}{(a^2+b^2)^{5/2}} \sqrt{x^2+y^2+4z^2}. \tag{5.37}$$

In the presence of a magnetic field, the energy levels of the atom will split linearly according to the first-order Zeeman effect as

$$E_{|F,m_F\rangle} = \mu_{\text{B}} g_F m_F |\mathbf{B}|, \tag{5.38}$$

where g_F denotes the hyperfine Landé g-factor. Therefore, a quadrupole field will exert a force on the prepared atom through the relation $\mathbf{F} = -\nabla E_{|F,m_F\rangle}$, trapping the atom in the center where the local minimum is. The efficiency of the magnetic trap loading is 60% and the temperature of the atoms is $98(5)\mu$K.

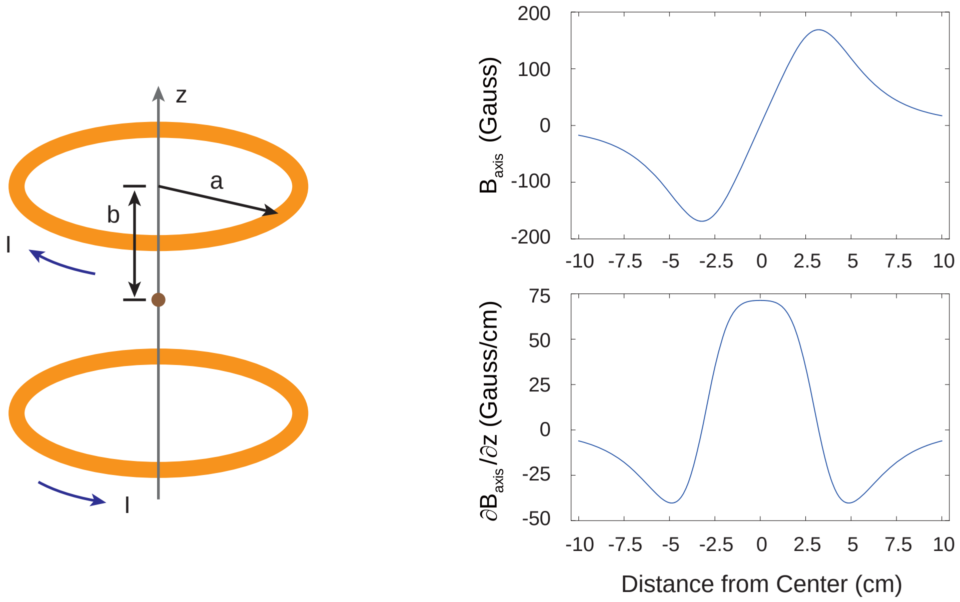

(a) Anti-Helmholtz loops

(b) Magnetic field and field gradient

FIGURE 5.6: Magnetic field generated by anti-Helmholtz coils. (a) shows a pair of loops placed in an anti-Helmholtz configuration. (b) shows the theoretical magnetic field and the gradient of the field along the axis of the MOT coils with a current of 35 A. Each of the coils has a number of turns of 34, an inner diameter of 56 mm, and an outer diameter of 99 mm, and the distance between the two coils is about 60 mm.

5.3.6.2 Magnetic Transport

The magnetic transport system is composed of in total 14 pairs of coils and a push coil as illustrated in Fig. 5.7 [187]. By regulating the currents of the coils, atoms can be transported following the change of the trapping potential. And by using three pairs of the coils, the aspect ratio of the trapping potential can be kept constant which can significantly reduce the heating [188]. In addition, the adiabaticity condition has to be satisfied to avoid excitation

$$\frac{|(\mathbf{v}\cdot\nabla)\mathbf{B}(\mathbf{r})|}{|\mathbf{B}(\mathbf{r})|} \ll |\omega_L|, \tag{5.39}$$

which means that the rate of the change of the magnetic field in the moving frame has to be kept much smaller than the Larmor frequency $\omega_L = \mu_{\mathrm{B}} g_F |\mathbf{B}|/\hbar$. Finally, after a 3.1 s long magnetic transport, 4×10^8 atoms are trapped in the BEC-vacuum region with a temperature of $104(6)$ μK.

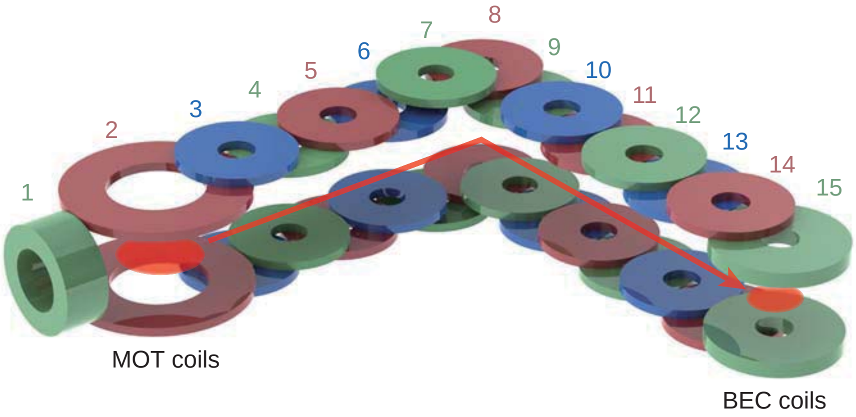

(a) A schematic view of the magnetic transport system

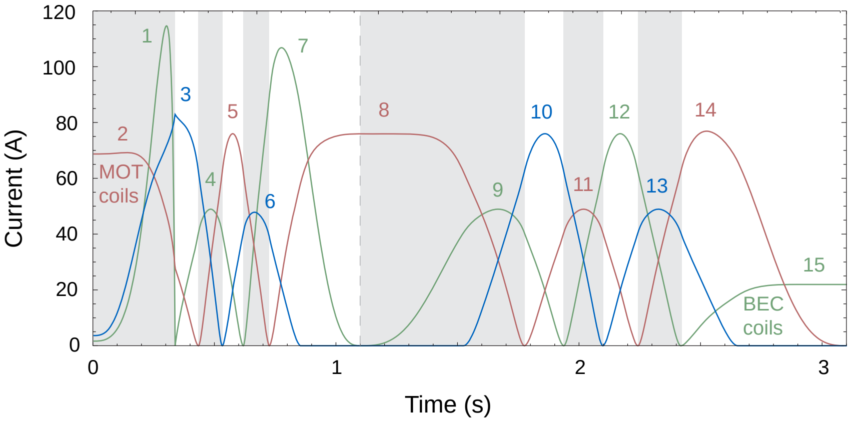

(b) Currents applied to the coils

FIGURE 5.7: Magnetic transport system. (a) shows the configuration of the magnetic transport system where coil 1 is the push coil, coils 2 are the MOT coils, and coils 15 are responsible for trapping the atoms in the BEC-vacuum region. (b) shows the currents applied to the coils.

5.3.7 Transfer to a Dipole Trap

Next, the magnetic trap is ramped up from 130 G/cm to 210 G/cm to increase the collision rate while the atoms are heated to 125(13) μK. Then a RF magnetic field is applied with the frequency swept from 15 MHz to 3.75 MHz within 2 s. Through collisions, energetic atoms will be excited to untrapped spin states by the RF and thus escape the trap, removing energy from the system. After the radio-frequency-induced evaporation, 4×10^7 atoms with the temperature of 26(2) μK and the density of about 4×10^{11} cm^{-3} are loaded into a crossed dipole trap formed by two 1070 nm laser beams.

5.3.7.1 Optical Dipole Potential

The optical dipole trap relies on the electric dipole interaction with the light field [189, 190]. When an atom is placed into a laser light field, the electric field $\mathbf{E}$ will induce an oscillating atomic dipole moment $\mathbf{d}$ of which the amplitude $\tilde{d}$ is related to the field amplitude $\tilde{E}$ by $\tilde{d} = \alpha(\omega)\tilde{E}$ with the complex polarizability $\alpha(\omega)$ depending on the driven frequency ω [191]. The resulting potential is given by

$$V_{\text{dip}} = -\frac{1}{2}\langle \mathbf{d} \cdot \mathbf{E} \rangle = -\frac{1}{2\epsilon_0 c}\text{Re}(\alpha)I, \tag{5.40}$$

with the laser field intensity $I = 2\epsilon_0 c|\tilde{E}|^2$. Meanwhile, the scattering rate can be derived as

$$\Gamma_{\text{sc}} = \frac{\langle \dot{\mathbf{d}} \cdot \mathbf{E} \rangle}{\hbar\omega} = \frac{1}{\hbar\epsilon_0 c}\text{Im}(\alpha)I. \tag{5.41}$$

After the polarizability is calculated by considering the atom in Lorentz's model of a classical oscillator [192], one obtains the useful expressions for the dipole potential and the scattering rate

$$V_{\text{dip}}(\mathbf{r}) = -\frac{3\pi c^2}{2\omega_0}\left(\frac{\Gamma}{\omega_0 - \omega} + \frac{\Gamma}{\omega_0 + \omega}\right) I(\mathbf{r}), \tag{5.42}$$

$$\Gamma_{\text{sc}}(\mathbf{r}) = \frac{3\pi c^2}{2\hbar\omega_0}\left(\frac{\omega}{\omega_0}\right)^3 \left(\frac{\Gamma}{\omega_0 - \omega} + \frac{\Gamma}{\omega_0 + \omega}\right)^2 I(\mathbf{r}). \tag{5.43}$$

It can be readily seen that a red-detuned light field ($\Delta \equiv \omega - \omega_0 < 0$) creates a potential minimum at the position with maximum intensity, while a blue-detuned light field ($\Delta > 0$) creates a potential maximum at the position with maximum intensity. In the experiment, the dipole laser has a wavelength of 1070 nm which is far red-detuned with respect to the atomic transition lines, indicating that the atoms are trapped in the center. In addition, the dipole potential can be approximated as a harmonic potential with a trap depth $V_{\text{dip}}(r = 0)$ near the trap center, since the time-averaged intensity distribution of a Gaussian beam is given by

$$I(r, z) = \frac{2P_0}{\pi \text{w}^2(z)} \exp\left(\frac{-2r^2}{\text{w}^2(z)}\right), \tag{5.44}$$

where P_0 represents the total power of the beam, and $\text{w}(z) = \text{w}_0\sqrt{1 + (z/z_{\text{R}})^2}$ is the radius at which the field intensity drops to $1/e^2$ of its axial value with the Rayleigh length $z_{\text{R}} = \pi \text{w}_0/\lambda$. Note that the dipole potential can be alternatively described by the dressed state picture where a combined system of atom and quantized field is considered, and the energy shift can be calculated via second-order perturbation theory [193].

5.3.7.2 Experimental Setup for the Optical Dipole Trap

Two dipole beams, "main dipole" and "cross dipole", are responsible for the formation of the crossed dipole trap, both of which are generated by a single mode fiber laser YLR-50-LP (from IPG Photonics) as illustrated in Fig. 5.8. The intensity of each of the dipole beams is controlled by regulating the modulation strength of the AOM and the intensity noise is highly suppressed by using a feedback loop discussed in Appx. C. The main dipole beam shines through the atomic cloud in the x-y plane, while having an angle of 5° with respect to the x-axis to save space for the lattice beams. It has a beam waist of 95 μm and is positioned 95 μm below the magnetic trap center, so that the Majorana loss is diminished once the atoms are transferred to the dipole trap. The cross dipole beam is perpendicular to the main dipole beam and is applied to the atoms in the x-y plane as well. Note that, the beam waist of the cross dipole at the atoms along the z-axis is compressed to 28 μm which is a quarter of the one in the other direction, 112 μm, with the help of two cylindrical lenses. Therefore, the condensate will have a small diameter along the z-axis, and could be loaded into a single layer of an optical lattice with a comparable periodicity.

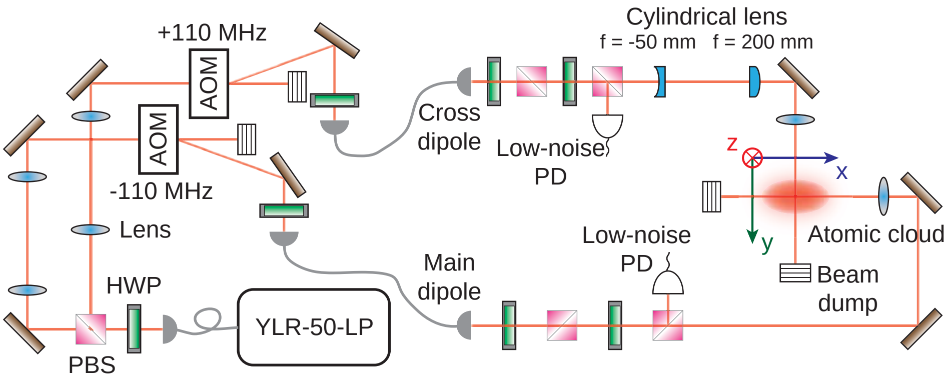

Figure 5.8: Optical dipole trap setup. The fiber laser typically works at 40% of its full power which gives about 20 W in total. The AOMs are used to control as well as to stabilize the intensity of the dipole beams. Polarization-maintaining single mode fibers are used to guide the beams to the vacuum system, where the polarizations of the beams are first purified by PBSs. Then a small portion of each beam, typically several percent or less, is split off by a true zero order HWP and a PBS, and is measured by a low-noise photodiode. The signal is then used as a feedback for intensity stabilization. The coordinates help to specify the directions of the system, and are in accord with Fig. 5.2.

During the transfer to the dipole trap, the effective trap volume increases, leading to an expansion of the atomic cloud. The energetic atoms thus stays at the low-density tails of the combined trap during the adiabatic expansion, and will leave the trap after the quadrupole field gradient drops below gravity (30.5 G/cm for Rubidium 87 magnetically trapped in $|F=1, m_F=-1\rangle$). As a result, the final temperature of the transferred atoms is estimated as one tenth of the trap depth [194]. In the experiment, the temperature of the transferred atoms is 8(1) μK which coincides with the theoretical value 7.5 μK.

5.3.8 Achieving a Bose-Einstein Condensate

Once the atoms are loaded into the dipole trap, a forced evaporation is performed by continuously lowering down the dipole trap depth as well as the magnetic field potential in 4 s and then holding for 0.2 s. The transition process is shown in Fig. 5.9 where the main dipole beam is lowered down to 1 W, the cross dipole beam to 0.23 W, and the magnetic field gradient to about 2.7 G/cm. At last, in total 2.34×10^5 atoms are obtained with a condensate fraction of 57%. To get a pure condensate, the final power of the main dipole beam is set to 0.8 W yielding 6×10^4 atoms with a condensate fraction larger than 95%.

The trap frequencies are measured by two methods. For the x and the y directions, the trap frequencies are measured by applying a blue-detuned beam pulse to kick the atoms and monitoring the trajectory of the oscillation. While for the z direction, it is measured by the parametric excitation method where the cross dipole beam intensity is modulated by a sine wave. When the modulation frequency f_{mod} is twice the trap frequency, the atoms will absorb energy and escape from the trap. The results of the trap frequencies for the pure BEC are shown in Fig. 5.10, which give $\omega_x = 2\pi \times (69.3 \pm 0.1)$ Hz, $\omega_y = 2\pi \times (47.6 \pm 0.5)$ Hz, and $\omega_z = 2\pi \times (298 \pm 6)$ Hz. Thus the chemical potential can be calculated as $\mu_{\text{TF}} \simeq k_B \times 69$ nK according to the Thomas-Fermi model, and the size of the condensate is $R_{\text{TF},x} = 8.4\ \mu$m, $R_{\text{TF},y} = 12.2\ \mu$m, and $R_{\text{TF},z} = 1.9\ \mu$m.

5.3.9 Achieving a Two-Dimensional Superfluid

In practice, to achieve a two-dimensional superfluid, one has to thermodynamically freeze the third dimension assumed to be the z-axis, which is to say the energy gap between the ground state and the first excited state of the z motion is much larger than both the temperature of the system $k_{\text{B}}T$ and the interaction energy $2g_{\text{2D}}n$ [65]. For harmonically trapped atoms, it is equivalent to requiring a strong trap frequency ω_z. A typical way to reach the two-dimensional condition is to load the atoms into a one-dimensional standing wave and remove the atoms in other layers by using position-dependent microwave transfer [195]. An alternative way, that is used in the present experiment, is to compress the condensate first and then load it into a single well of a lattice along the z-axis [196].

5.3.9.1 Loading Atoms into a One-Dimensional Optical Lattice

Interference of two laser beams will result in a periodic potential that traps neutral atoms. In the experiment, as is illustrated in Fig. 5.11, an optical lattice along the z-axis,

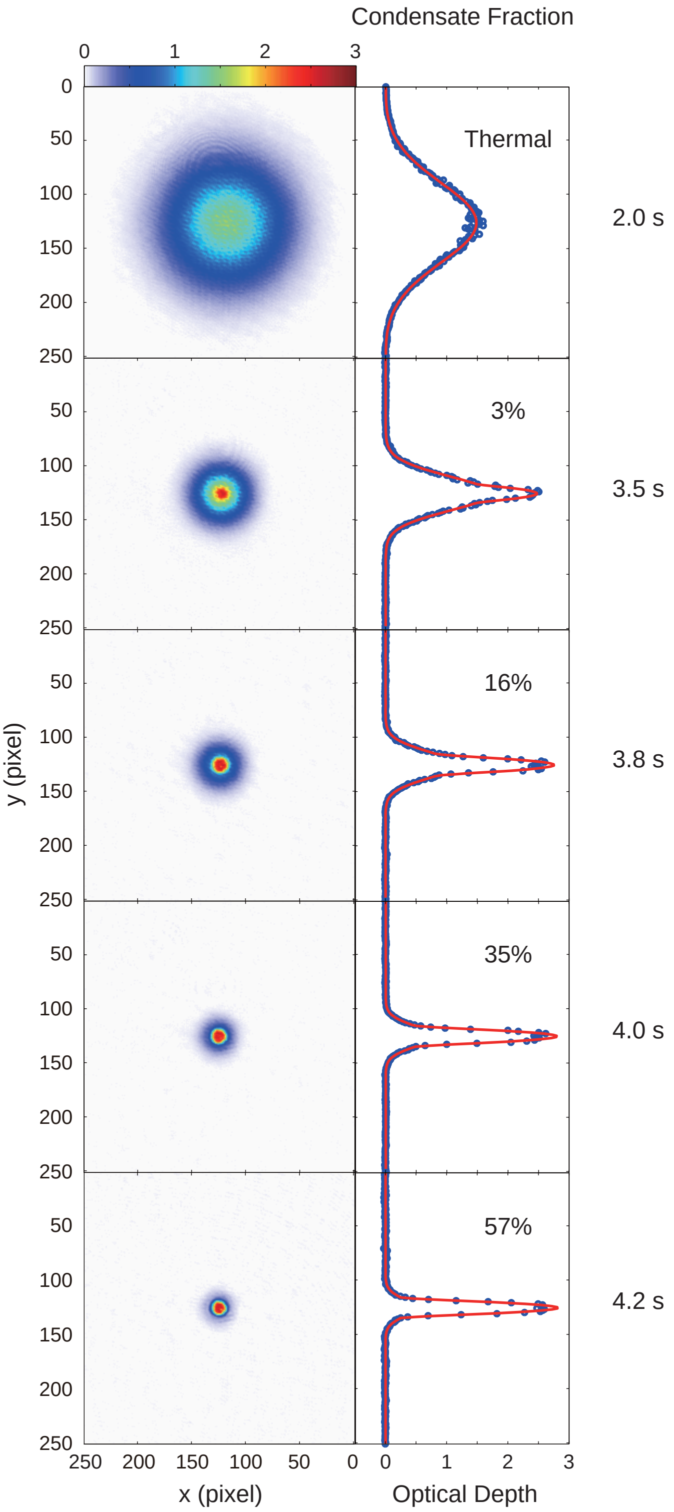

FIGURE 5.9: Evaporation in the dipole trap to achieve a BEC. Images are taken after 12 ms free expansion, and the condensate fraction is calculated through a bimodal fitting (red curve).

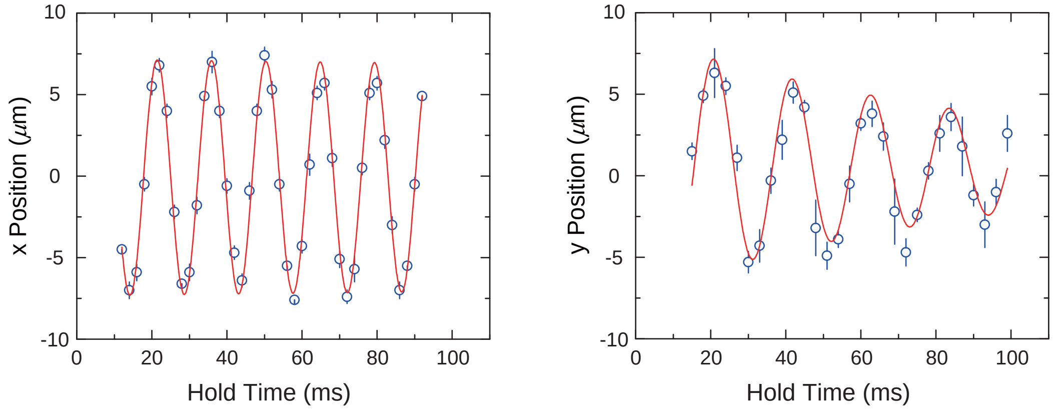

(a) Trap frequency of the x-axis

(b) Trap frequency of the y-axis

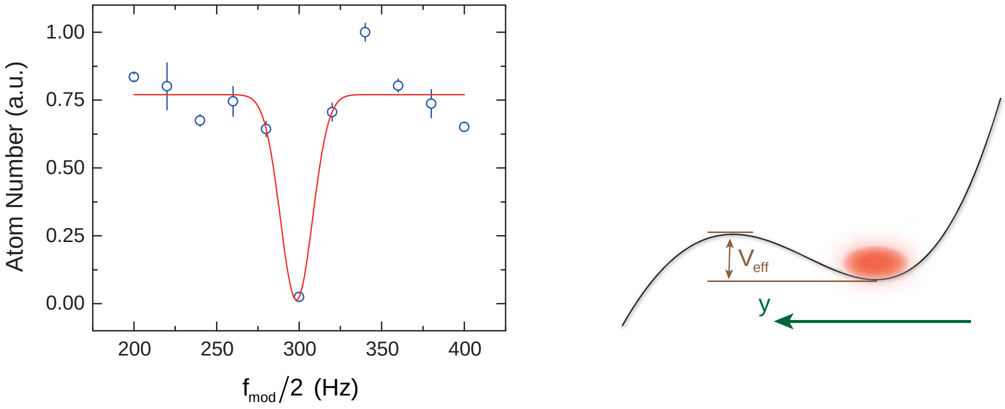

(c) Trap frequency of the z-axis

(d) Trap potential of the y direction

FIGURE 5.10: Characteristics of the BEC trap. (a) shows the trap frequency of the x-axis. (b) shows the trap frequency of the y-axis. (c) shows the trap frequency of the z-axis. (d) shows the trap potential in the y direction. Due to the gravitational potential, the trap potential minimum is shifted about 30 μm from the main dipole beam center, and the energetic atoms are more likely to escape along the gravitational direction.

named as "pancake", is formed by two blue-detuned laser beams provided by a Matisse TX-light Titanium:sapphire ring laser (from Sirah) which is tuned to a wavelength of 767 nm and is stabilized with the help of a reference cavity through the Pound-Drever-Hall technique. The two pancake beams are inclined at $+5.3°$ and $-5.3°$ to the x-axis, respectively, so that the lattice has a periodicity of $d_z = \lambda/[2\sin(\theta)] \simeq 4.2\ \mu$m. In addition, the optical elements for the pancake lattice formation are placed on a motorized stage driven by a motorized actuator (Z806, from Thorlabs) which has a resolution of 29 nm. Therefore, the atoms can be loaded to the potential minimum with high accuracy to suppress the heating by moving the lattice potential.

The pancake lattice periodicity is evaluated experimentally by measuring the number of atoms as a function of lattice position. Since the pancake lattice is blue-detuned, atoms can not be trapped effectively at the anti-nodes. By moving the motorized stage

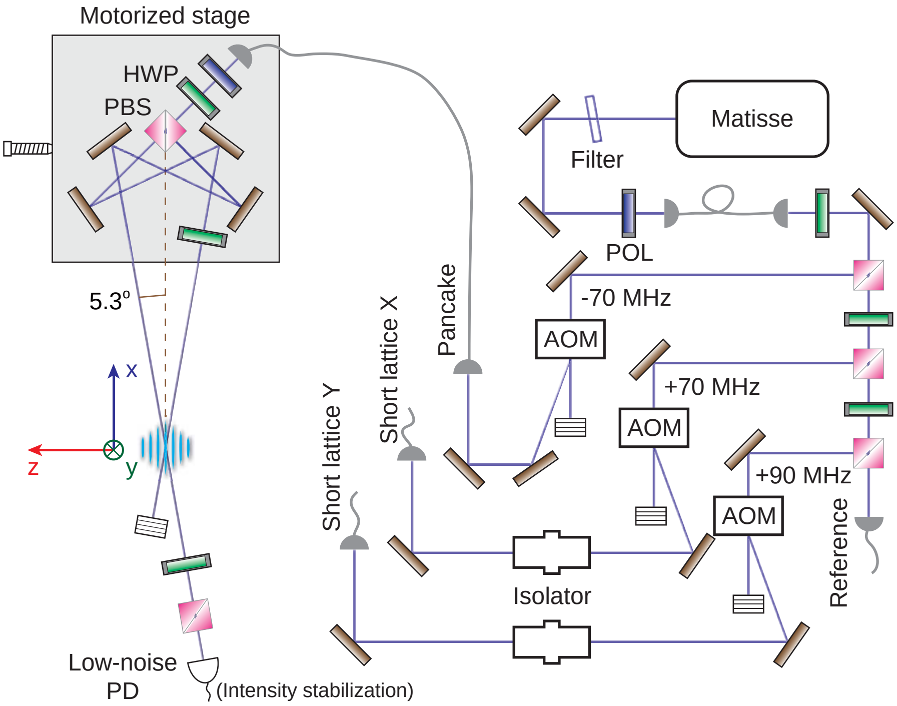

FIGURE 5.11: Realization of the pancake lattice. Each of the pancake beams has a beam waist of about 200 μm focused on the atoms. The POL on the motorized stage is used to purify the polarization so that the intensity difference between the two pancake beams will not be sensitive to the polarization fluctuation of the incident beam. The absolute intensity fluctuation is stabilized by the feedback loop. The reference beam is used for laser phase-locking.

in steps of 0.5 μm, the number of atoms are recorded through absorption imaging along the x-axis shown in Fig. 5.12. A sine curve fitting indicates that the periodicity of the lattice is (4.2 ± 0.1) μm which coincides with the theoretical value. In this way, the loading process is optimized by maximizing the loading efficiency.

However, a direct loading from the condensate does not fulfill a good single layer condition since the size of the condensate along the z-axis is about $2 \times R_{\mathrm{TF},z} = 3.8$ μm which is similar to the periodicity 4.2 μm. In order to load the condensate into a single layer, the power of the cross dipole beam is increased by about seven times within 100 ms, leading to trap frequencies $(\omega_x, \omega_y, \omega_z) \simeq (2\pi \times 181\ \mathrm{Hz}, 2\pi \times 48\ \mathrm{Hz}, 2\pi \times 754\ \mathrm{Hz})$. Under this condition, the Thomas-Fermi radius of the z-axis is decreased to about 1.1 μm which can be then loaded into a single layer. The single layer loading is evaluated by observing the interference pattern. When a condensate is loaded into several layers of a lattice, a pattern of interference fringes can be observed after a free expansion which has a period $2\pi\hbar t/(md_z)$ [197]. Thus an efficient single layer loading is achieved after the visibility of the fringes is minimized. Fig. 5.13 shows a single layer loading with a total atom number of about 5×10^4, which is proved by the absence of fringes.

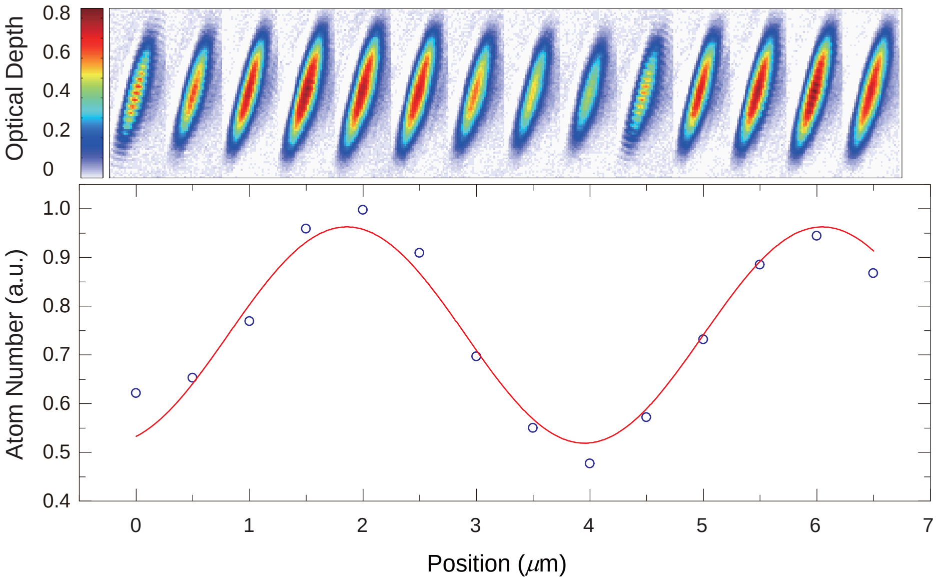

FIGURE 5.12: Pancake lattice periodicity. The atoms are imaged along the x-axis after 14 ms TOF.

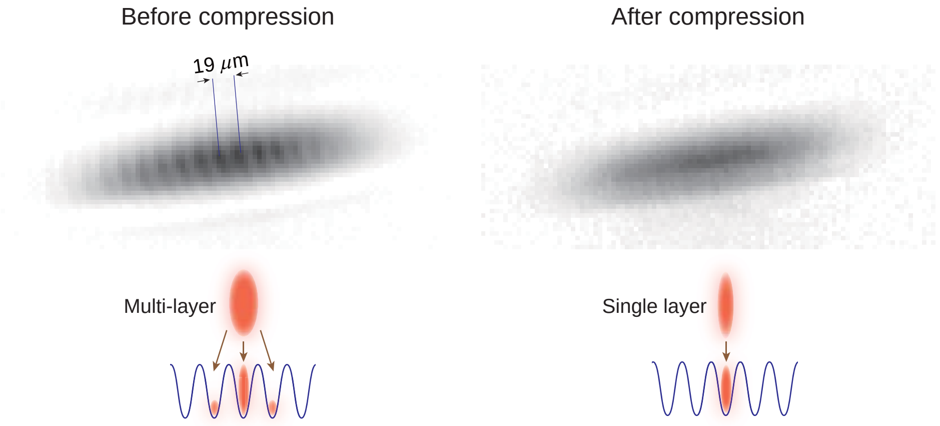

FIGURE 5.13: Loading atoms into a single layer. Images are taken along the x-axis after 16 ms TOF. The interference pattern shown in the left picture implies a multi-layer loading when the condensate has a large size compared to the periodicity of the lattice even when the pancake lattice position is optimized. The fringe period is measured to be 19 μm which is similar to the theoretical value 17.5 μm. A compressed condensate can be loaded into a single layer and no fringes are observed as depicted in the right picture.

5.3.9.2 Making and Probing Two-Dimensional Superfluid

Although the fringes reflect the coherence to some extend, it is hard to be used to characterize the superfluidity of the system. To reach a perfect two-dimensional superfluid, the temperature is further lowered by decreasing the effective trap depth where the intensities of the dipole beams are lowered and the gradient of the magnetic quadrupole trap is raised to just compensate the gravitational force. Finally, $\sim 10^4$ atoms are left in a trap with frequencies $(\omega_r, \omega_z) \simeq (2\pi \times 43\ \text{Hz}, 2\pi \times 4886\ \text{Hz})$.

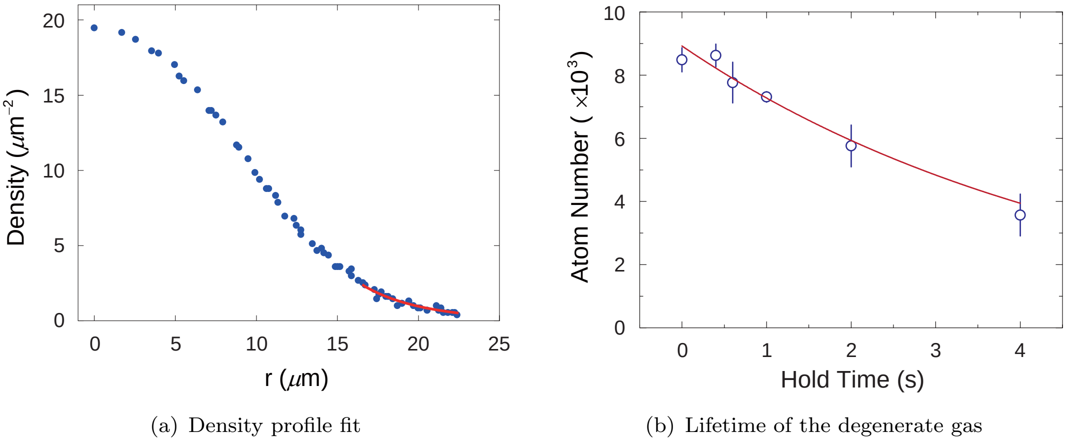

(a) Density profile fit (b) Lifetime of the degenerate gas

FIGURE 5.14: Characterizing the two-dimensional quantum gas. (a) shows the density profile fit with the mean-field Hartree-Fock theory. The presented data (blue dots), which are obtained with a 50 μs long weak probe beam ($I/I_{\text{eff}}^{\text{sat}} \simeq 0.5$), have been rescaled according to the scaling factor. The fitting domain is restricted to the area in which the phase space density is smaller than 2.5 to fulfill the mean-field requirement, and the optical density is lower than 0.2 to avoid multiple scattering [184]. It has to be emphasized that the central density is underestimated due to collective effects [183]. (b) shows the measured lifetime of the two-dimensional degenerate gas.

The superfluidity of the system can be directly evaluated by measuring the phase space density. However, the conventional three-dimensional TOF method is no longer practical since a very long TOF is required to reflect the momentum distribution [65]. Instead, in this experiment, a measurement on density profile is performed to fit for the temperature as well as the chemical potential. The atoms are first subject to a two-dimensional ballistic expansion for 4 ms by suddenly releasing the confinement in the x and the y directions while keeping the z-axis tightly confined. The 4 ms expansion will not affect the confinement condition of the z-axis effectively due to the large pancake beam waist, however, it can help to decrease the density of the cloud which scales as [184]

$$n(r,t) = \eta_t^2 n_{\text{eq}}(\eta_t r), \tag{5.45}$$

where $\eta_t = (1+\omega^2 t^2)^{-1/2}$ is the scaling factor, and $n_{\text{eq}}(r)$ represents the initial equilibrium density profile. In this way, after the calibration of the effective saturation intensity with $\alpha = 1.92 \pm 0.06$, the wings of the density profile are fed into the model Eq. 5.21 which yields the temperature $T = (69 \pm 10)$ nK, the global chemical potential $\mu_{\text{global}} = k_{\text{B}} \times (80 \pm 9)$ nK, and the parameter related to the effective line width $\beta = 0.99 \pm 0.10$. Note that the β parameter should be close to 1 since there is no residual magnetic field and the laser used for imaging has a narrow line width (< 1 MHz) compared to the natural line width of Rubidium. Thus the phase space density of the central area picks up the value 9.5 ± 1.6 which is larger than the critical phase space density 7.67 calculated from Eq. 5.16, indicating that the system is in the superfluid phase. A typical fitting result is presented in Fig. 5.14(a) and in total 100 pictures are taken in order to get the final results. The lifetime of the two-dimensional degenerate gas is measured to be (4.9 ± 0.7) s as shown in Fig. 5.14(b).

Chapter 6

Quantum Gases in Two-Dimensional Optical Lattices

When two opposing waves meet, a spatially periodic pattern is created which could be used to trap cold neutral atoms via the Stark effect. Compared with the crystalline solid, the parameters of an optical lattice can be easily controlled which in turn makes it a versatile research tool. Especially by simply modifying the lattice depth, a quantum phase transition from a superfluid to a Mott insulator is observed [198]. In this thesis, I would like to take the advantages of the commensurate filling in the Mott phase as well as the controllability of the interactions for entanglement generation.

6.1 Single Particle in a Periodic Potential

To begin with, the behaviour of a single particle placed in a one-dimensional optical lattice is briefly reviewed. Since the lattice beams in two directions possess different frequencies and orthogonal polarizations, the wave functions can be considered independently and the total energy is just the sum of the eigenvalues.

6.1.1 Bloch Bands

When a particle is placed in a periodic potential which is described by the Hamiltonian $H = \hat{p}^2/(2m) + V_{\text{lat}}(x)$, Bloch's theorem states that the eigenstates of the particle can be written as a product of a plane wave and a periodic function [199]

$$\phi_q^{(n)}(x) = e^{iqx} u_q^{(n)}(x), \tag{6.1}$$

where the periodic function $u_q^{(n)}(x+a) = u_q^{(n)}(x)$ takes the same periodicity a as the periodic potential. Inserting the ansatz into the Schrödinger equation yields

$$\left[\frac{(\hat{p}+\hbar q)^2}{2m} + V_{\text{lat}}(x)\right] u_q^{(n)}(x) = E_q^{(n)} u_q^{(n)}(x), \tag{6.2}$$

where q is recognized as a wave vector that is typically confined to the first Brillouin zone ($-\pi/a < q \leq \pi/a$), and $\hbar q$ as quasimomentum or crystal momentum. Note that according to the periodic boundary condition, one finds $\phi_q^{(n)}(x + M_x a) = \phi_q^{(n)}(x)$ with M_x the number of lattice sites. Thus for a given band index n, q is a quantum number that has M_x possible values.

The equation 6.2 can be solved directly by considering the Fourier transform of the elements of the equation and truncating the Hamiltonian [200, 201]. Alternatively [202], in the case of a simple sinusoidal potential $V_{\text{lat}} = V_0 \sin^2(k_{\text{lat}} x)$ as is used in the experiment, the Schrödinger equation takes the form of the Mathieu equation

$$\frac{d^2}{dy^2}\phi_q^{(n)}(y) + [A - 2s\cos(2y)]\,\phi_q^{(n)}(y) = 0, \tag{6.3}$$

with $y = k_{\text{lat}} x$, $A = E_q^{(n)}/E_{\text{R}} - V_0/(2E_{\text{R}})$, the recoil energy $E_{\text{R}} = \hbar^2 k_{\text{lat}}^2/(2m)$, and $s = -V_0/(4E_{\text{R}})$. Fig 6.1 shows the band structure with various lattice depths V_0, where the energy band gaps become more apparent for deeper lattice depths. Fig 6.2 shows the probability density of the Bloch wave function $\phi_q^{(n=1)}(x)$ with various lattice depths. It can be readily seen that the eigenstates tend to get localized at each lattice sites as the lattice depth increases.

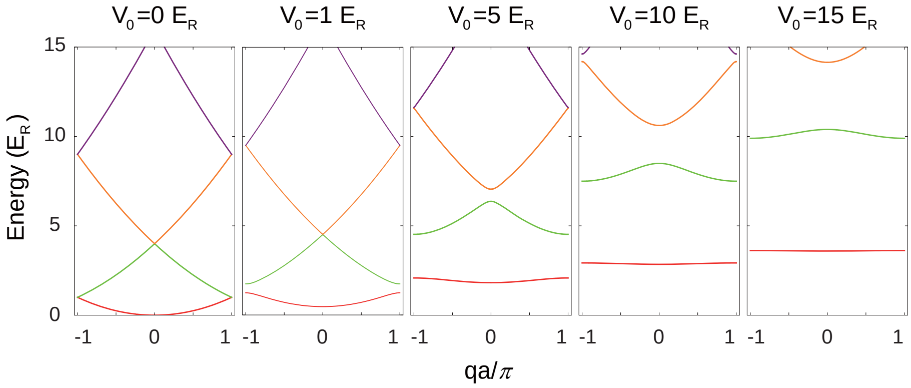

FIGURE 6.1: Energy bands of the one-dimensional optical lattices.

6.1.2 Wannier Functions

Wannier functions, which are a set of orthogonal wave functions, are alternatives that can describe the periodic system. Unlike the Bloch functions, which are delocalized, Wannier

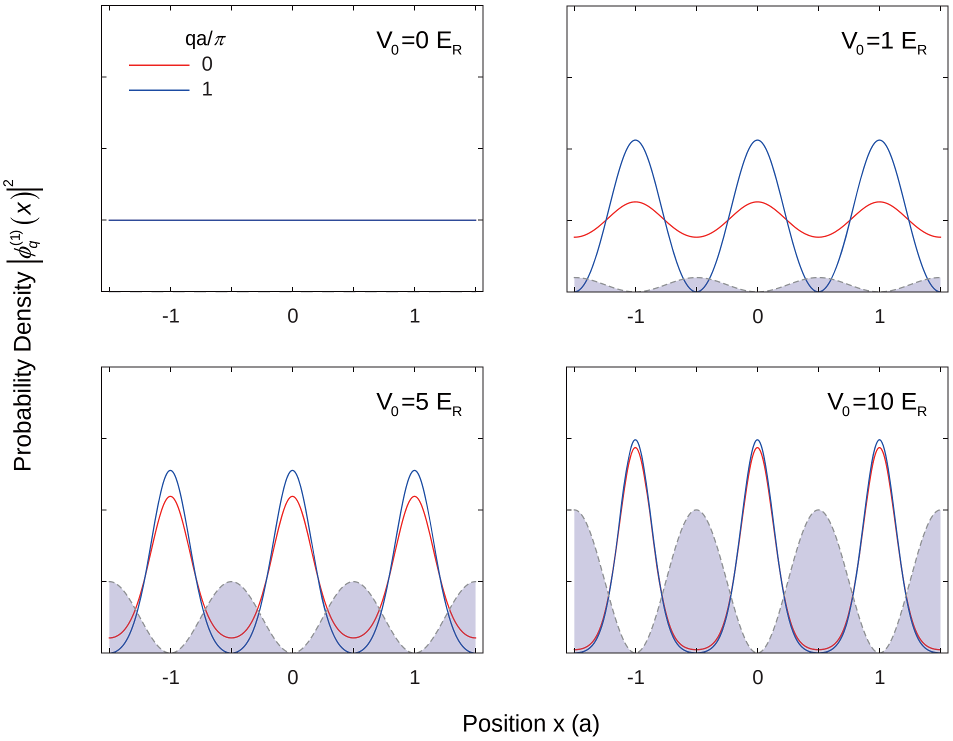

FIGURE 6.2: Probability density of the Bloch wave function in the lowest band. The filled area represents the lattice potential.

functions are maximally localized to individual lattice sites. For a given band, they are defined as the Fourier transformation of the Bloch functions of the same band [199]

$$w_n(x - x_j) = \frac{1}{\sqrt{\mathcal{N}}} \sum_q e^{-iqx_j} \phi_q^{(n)}(x), \tag{6.4}$$

where x_j is the central position of the j-th lattice site, and $\mathcal{N}$ is the normalization factor. Fig. 6.3 shows the Wannier functions for the lowest band $n = 1$ with a lattice depth of 1 E_{R} and 10 E_{R}. It can be readily seen that the Wannier function cannot be localized tightly with low lattice depth which implies the possibility of quantum tunneling. In addition, the Wannier functions is a good basis for studying issues related to localized particles such as on-site interaction.

6.1.3 Tight Binding Approximation

Under the tight binding approximation, single particle wave functions can be safely expanded by Wannier functions $\psi(x,t) = \sum_{n,j} c_j^{(n)}(t) w_n(x - x_j)$. Restricting to only nearest-neighbor tunneling and the lowest band, one obtains a discrete Schrödinger equation [203]

$$i\hbar \frac{\partial}{\partial t} c_j^{(1)}(t) = -J \left[c_{j+1}^{(1)}(t) + c_{j-1}^{(1)}(t) \right] + \epsilon_1 c_j^{(1)}(t), \tag{6.5}$$

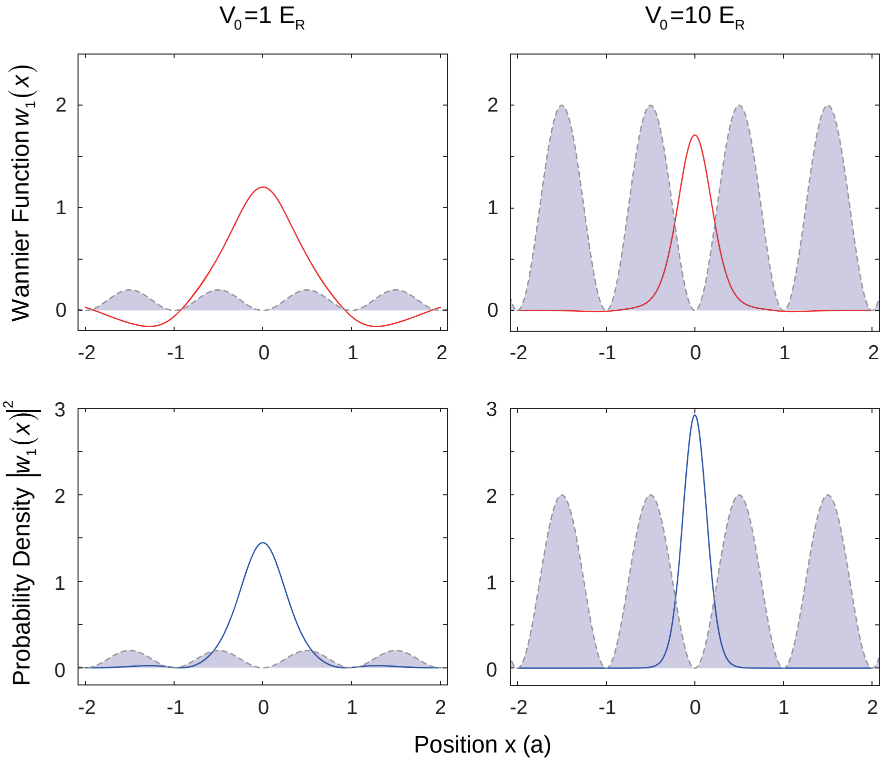

FIGURE 6.3: Wannier function and probability density. The filled area represents the lattice potential.

with

$$J = -\int dx\, w_1^*(x)\left[\hat{p}^2/(2m) + V_{\text{lat}}(x)\right] w_1(x-a), \tag{6.6}$$

$$\epsilon_1 = \int dx\, w_1^*(x)\left[\hat{p}^2/(2m) + V_{\text{lat}}(x)\right] w_1(x), \tag{6.7}$$

where J is the tunneling matrix element, and ϵ_1 is the on-site linear energy. Since plane waves are the solutions of the discrete Schrödinger equation, by expanding the equation and assuming periodic boundary conditions, one obtains $E_q^{(1)} = -2J\cos(qa)$ which relates the tunneling matrix element to the band width via [202, 204]

$$J = \frac{E^{(1)}_{q=\frac{\pi}{a}} - E^{(1)}_{q=0}}{4}. \tag{6.8}$$

6.2 Bose-Hubbard Model and the Superfluid to Mott Insulator Transition

In order to analyze a multi-particle system, two-body interactions have to be involved, and the Bose-Hubbard model is suggested which considers particles instead of a classical field in the GP equation [59]. With the repulsive interaction, a phase transition from a superfluid state to a Mott insulator state is predicted as the interaction energy grows much larger than the kinetic energy.

6.2.1 Bose-Hubbard Hamiltonian

For a two-dimensional Bose gas which is trapped in a two-dimensional optical lattice, the second quantized Hamiltonian that describes the system is given by [59]

$$H = \int d\mathbf{r}\, \hat{\Phi}^\dagger(\mathbf{r})[H_0 + V_{\text{ext}}(\mathbf{r})]\hat{\Phi}(\mathbf{r}) + \frac{g_{2\text{D}}}{2}\int d\mathbf{r}\, \hat{\Phi}^\dagger(\mathbf{r})\hat{\Phi}^\dagger(\mathbf{r})\hat{\Phi}(\mathbf{r})\hat{\Phi}(\mathbf{r}), \tag{6.9}$$

where $\hat{\Phi}(\mathbf{r})$ represents the bosonic field operator, the Hamiltonian H_0 is described as $H_0 = -\hbar^2\nabla^2/(2m) + V_0[\sin^2(k_x x) + \sin^2(k_y y)]$ with $k_x = k_y = k_{\text{lat}}$, $V_{\text{ext}}(\mathbf{r})$ represents the external trap potential, and $\mathbf{r} = (x, y)$ represents the position. Under the tight binding approximation, the bosonic operator can be expanded as $\hat{\Phi}(\mathbf{r}) = \sum_j \hat{a}_j w_1(\mathbf{r} - \mathbf{r}_j)$ with $\hat{a}_j$ the annihilation operator at the j-th site, which yields the Bose-Hubbard Hamiltonian

$$H_{\text{BH}} = -J\sum_{\langle j,j'\rangle} \hat{a}_j^\dagger \hat{a}_{j'} + \frac{U}{2}\sum_j \hat{a}_j^\dagger \hat{a}_j^\dagger \hat{a}_j \hat{a}_j + \sum_j [V_{\text{ext}}(\mathbf{r}_j) - \mu]\, \hat{a}_j^\dagger \hat{a}_j, \tag{6.10}$$

with $\langle j, j'\rangle$ denoting the summation over the nearest neighboring sites, and the tunneling matrix element J and the on-site interaction U defined as

$$J = -\int d\mathbf{r} w_1^*(\mathbf{r} - \mathbf{r}_j) H_0 w_1(\mathbf{r} - \mathbf{r}_{j+1}), \tag{6.11}$$

$$U = g_{2\text{D}}\int d\mathbf{r}|w_1(\mathbf{r})|^4 = g_{2\text{D}}\left[\int dx|w_1(x)|^4\right]^2. \tag{6.12}$$

Note that the on-site linear energy is absorbed into the third term which acts like a spatially varying chemical potential [205].

In practice, the third dimension has to be considered which is assumed to be a Gaussian wave function as discussed in Section 5.2.1, and has been already taken into account in the interaction parameter U. In addition, in the deep lattice where the Wannier functions are well localized, the tunneling parameter can be estimated as Eq. 6.6 due to little overlap between the neighboring Wannier states. Fig. 6.4 shows the calculated parameters for the current system.

The Bose-Hubbard Hamiltonian is an effective model that describes ultracold bosons in an optical lattice. Since the separation to the first excited band is typically much larger than the thermal and mean interaction energies, dynamics can be studied within the lowest band. However, the eigenstates of the system might be modified by the

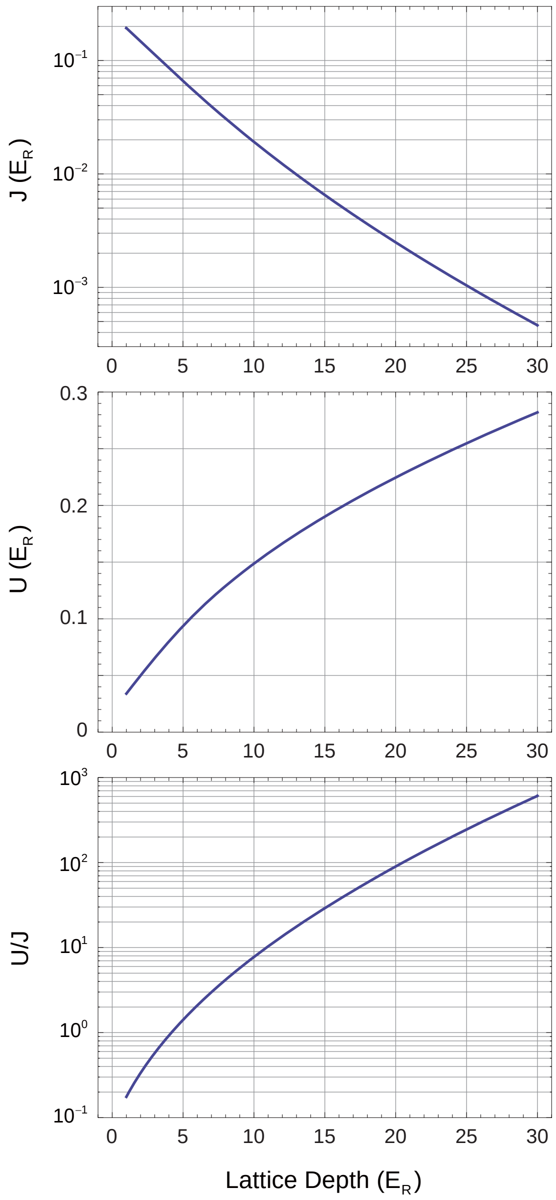

FIGURE 6.4: Bose-Hubbard parameters.

interaction between particles yielding J and U that are different from the estimation derived by single particle Wannier functions.

6.2.2 Superfluid to Mott Insulator Transition

The Bose-Hubbard Hamiltonian predicts two different regimes, the kinetic energy dominated regime ($U \ll J$) and the interaction energy dominated regime ($U \gg J$). A quantum phase transition occurs when the ratio of U/J crosses a critical value.

6.2.2.1 Superfluid Ground State

When the tunneling overwhelms the interaction, the kinetic energy tries to delocalize the particles yielding a superfluid system which has the ground state

$$|\Psi_{\mathrm{SF}}\rangle_{U/J\simeq 0} = \frac{1}{\sqrt{N!}}\left(\frac{1}{\sqrt{M}}\sum_{j=1}^{M}\hat{a}_j^{\dagger}\right)^{N}|\mathrm{vac}\rangle, \tag{6.13}$$

with N the number of particles and M the number of lattice sites. For a large system, it becomes a coherent state [205]

$$|\Psi_{\mathrm{SF}}\rangle \sim \prod_{j=1}^{M}\left[\exp\left(\sqrt{\frac{N}{M}}\hat{a}_j^{\dagger}\right)|0\rangle_j\right], \tag{6.14}$$

which indicates that each lattice site is filled with $\bar{n} = N/M$ atoms with a standard deviation $\sqrt{\bar{n}}$ according to the Poisson distribution as shown in Fig. 6.5. When the system is in the ground state, it involves a macroscopic phase which is constant over the lattice sites yielding an interference pattern [198].

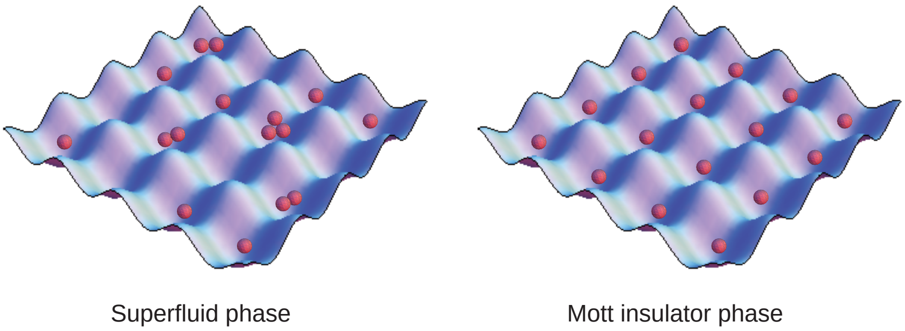

FIGURE 6.5: Distribution of atoms in the superfluid phase and the Mott insulator phase.

6.2.2.2 Mott Insulator Ground State

As interaction increases, the required kinetic energy for an atom to hop to an occupied site also increases, and atoms tend to get localized at individual sites. Finally, the system reaches the Mott insulator phase in the limit $U \gg J$, and the ground state can be described as a product of local Fock states

$$|\Psi_{\mathrm{MI}}\rangle_{J/U\simeq 0} = \left(\frac{1}{\sqrt{n!}}\right)^{M}\left[\prod_{j=1}^{M}(\hat{a}_j^{\dagger})^{n}\right]|\mathrm{vac}\rangle, \tag{6.15}$$

with n the number of atoms per lattice site. Energy gaps exist in the Mott insulator phase, and the first excited state relates to a particle-hole excitation. In addition, phases at different lattice sites are no longer correlated yielding a loss of the interference pattern.

6.2.2.3 Quantum Phase Transition

From the analysis above, the phase transition from a superfluid to a Mott insulator can be achieved by adjusting the ratio of U/J. However, the Mott insulator state requires a commensurate filling, any redundant particle or hole would thus tunnel freely and recover the coherence. This implies another phase transition mechanism in the limit $U \gg J$ that is driven by the competition between the interaction energy and the chemical potential. The phase boundary can be calculated by mean-field theory yielding an analytical form [206, 207]

$$\frac{\mu}{U} = n_{\mathrm{MI}} - \frac{1}{2} - D\frac{J}{U} \pm \sqrt{(D\frac{J}{U})^2 - D\frac{J}{U}(2n_{\mathrm{MI}}+1) + \frac{1}{4}}, \tag{6.16}$$

where n_{MI} is the filling number and D is the dimensionality. The critical point is defined as a value of J/U for which the square root vanishes

$$\left(\frac{J}{U}\right)_{\mathrm{c}} = \frac{1}{D}\left[n_{\mathrm{MI}} + \frac{1}{2} - \sqrt{n_{\mathrm{MI}}(n_{\mathrm{MI}}+1)}\right]. \tag{6.17}$$

Fig. 6.6 shows the calculated phase diagram of a two-dimensional system ($D = 2$) based on mean-field theory. A Monte Carlo study shows the critical point $(U/J)_{\mathrm{c}}^{\mathrm{MC}}(n_{\mathrm{MI}} = 1) = 16.7$ for unit filling [208], which is more precise than the mean-field prediction $(U/J)_{\mathrm{c}}^{\mathrm{MF}}(n_{\mathrm{MI}} = 1) = 23.3$.

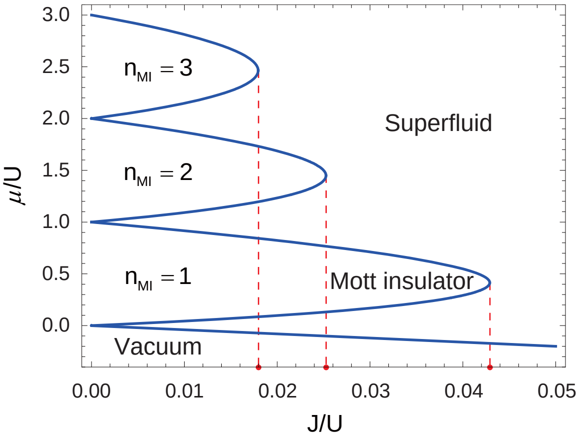

FIGURE 6.6: Two-dimensional Bose-Hubbard model phase diagram. The phase diagram is calculated by mean-field theory where the red dashed lines mark the critical points.

For an inhomogeneous system where atoms are confined with an external confinement, however, both the superfluid phase and the Mott insulator phase will exist in the same sample since the chemical potential varies as the LDA predicts. Especially, in a harmonic trap, the density profile takes a wedding cake form where superfluid alternates with Mott insulator [196, 209, 210].

6.2.2.4 Mott Insulator at Finite Temperature

In practice, atoms are prepared with a finite temperature which modifies the Bose-Hubbard predictions due to the thermal fluctuations. In the limit of negligible tunneling where $J \ll k_{\mathrm{B}}T, U$, the system is in the thermal Mott insulator regime where the thermal fluctuations would lead to particle-hole excitations. Since the wells are independent of each other, the global partition function could be described as a product of single-site partition functions [211]

$$Z_j = \sum_{n_j=0}^{\infty} \exp[\frac{U}{2}n_j(n_j-1) - \mu_j n_j] \exp[-1/(k_{\mathrm{B}}T)], \tag{6.18}$$

where $\mu_j = \mu_{\mathrm{global}} - V_{\mathrm{ext}}(\mathbf{r}_j)$ is the local chemical potential at site j. The probability of n_j particles occupying site j is then given by

$$P_{n_j,j} = \frac{1}{Z_j} \exp[\frac{U}{2}n_j(n_j-1) - \mu_j n_j] \exp[-1/(k_{\mathrm{B}}T)]. \tag{6.19}$$

Therefore, the mean occupation number of the j-th site is $\langle n_j \rangle = \sum_{n_j} n_j P_{n_j,j}$. In a similar way, the variance can be determined by

$$\sigma_{n,j}^2 = \langle n_j^2 \rangle - \langle n_j \rangle^2 = \sum_{n_j} n_j^2 P_{n_j,j} - \langle n_j \rangle^2. \tag{6.20}$$

In the current experiment, the parameters are set as the on-site interaction $U \simeq k_{\mathrm{B}} \times$ 49 nK in the deep lattice limit (at a lattice depth of 26 E_{R}) and the external trap frequency $\omega_r \simeq 2\pi \times 43$ Hz. In order to achieve unit filling, the number of atoms has to be restricted to around 2700. Fig. 6.7 shows the density profile and the variance profile for the current system along the x-axis with a fixed number of atoms. It can be readily seen that the plateau feature only survives up to a temperature around $0.2U/k_{\mathrm{B}}$ which is in accord with the conclusion in the paper [211] and the variance of the center becomes larger as the temperature increases. These features provide fundamental means to inspect a Mott insulator with an *in situ* imaging technique.

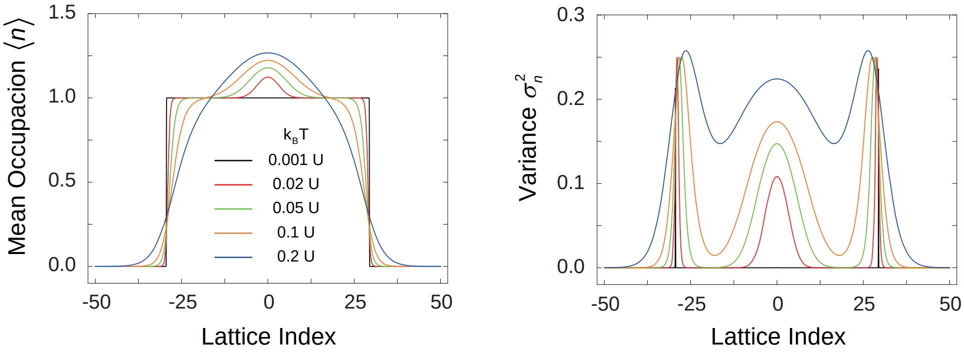

FIGURE 6.7: Density and variance in the deep Mott insulator. Experimental parameters of the current setup are taken, and the number of atoms is kept constant at 2700.

6.3 Experimental Observation of Superfluid to Mott Insulator Transition

By loading a two-dimensional superfluid gas into a two-dimensional optical lattice, a Mott insulator can be achieved by simply increasing the lattice depth to cross the critical point. A TOF absorption imaging provides evidence of the phase transition where the interference disappears in the Mott insulator regime.

6.3.1 Forming a Lattice Potential

When a blue-detuned (767 nm) Gaussian beam interferes with the retro-reflected beam, a standing wave potential is created as

$$V(x,y,z) = V_0\, e^{-2(x^2+y^2)/\mathrm{w}_0^2}\,\sin^2(kz) \simeq V_0\left(1 - \frac{2(x^2+y^2)}{\mathrm{w}_0^2}\right)\sin^2(kz), \tag{6.21}$$

where w_0 denotes the beam waist and $k = 2\pi/\lambda$ is the wave vector. It is worth noting that an effective external trapping potential exists due to the Gaussian beam profile. Thus two such standing waves with orthogonal polarizations create a square lattice in the x-y plane ($z = 0$)

$$V(x,y) \simeq V_0[\sin^2(kx) + \sin^2(ky)] - \frac{m}{2}(\omega_{\mathrm{ext}}^{\mathrm{eff}})^2(x^2+y^2), \tag{6.22}$$

where $\omega_{\mathrm{ext}}^{\mathrm{eff}} = \sqrt{4V_0/(m\mathrm{w}_0^2)}$ is the frequency of the effective external trapping potential near the trap center and the beam waists of both beams are assumed to be w_0.

Fig. 6.8 shows the realization of the two-dimensional optical lattice. The short lattice laser beams come from the Matisse laser with a wavelength of 767 nm. Four doublet lenses are specially designed by Lens-Optics which have an effective focal length of 251.3 mm for both short lattice beams (767 nm) and long lattice beams (1534 nm). The beam waist of the short lattice beam is tuned to ∼ 120 μm at the center of the atomic cloud. In order to avoid the interference, the polarizations of short lattice X, short lattice Y and pancake are chosen to be orthogonal to each other and different frequencies are chosen for them as shown in Fig. 5.11.

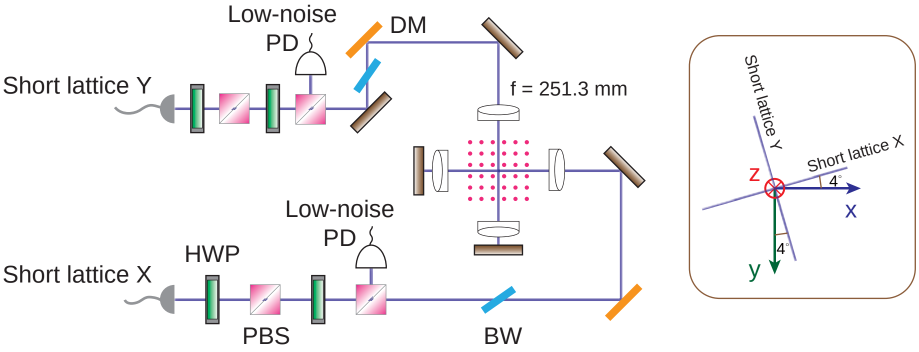

FIGURE 6.8: Realization of the short wavelength optical lattice. DM stands for dichroic mirror which passes long lattice beams while reflects short lattice beams. BW represents Brewster window and is used to assist in the alignment of the superlattice. Both of the beams are in the x-y plane, however, are tilted to an angle of 4° with respect to the axes.

6.3.2 Calibration of the Lattice Depth

As depicted in Fig. 6.4, ramping the lattice potential will change the ratio U/J exponentially. However, the lattice depth is sensitive to the overlap of the beams and the efficiency of the optical elements, which would lead to considerable deviations from the theoretical calculation. Thus a calibration of the lattice depth is necessary.

When a condensate diffracts from a standing wave, the momentum of the atoms will change by either zero or two photon momenta for each two-photon scattering event, and a number of momentum states will appear which is known as the Kapitz-Dirac (KD) effect [212, 213]. The evolution of the condensate in a one-dimensional optical lattice can be derived by numerically solving the time-dependent Schrödinger equation with the lattice Hamiltonian and condensate wave function $\psi(t) = \sum_n c_n(t)\exp(i2nkz)$ which is expanded in the basis of plane waves [214]. For short pulse time, for example $\tau = 25$ μs, Fig. 6.9 shows that the population of the first diffracted order ($\pm 2\hbar k$) grows when the depth of the lattice increases in the weak lattice limit. Therefore, after the incident beam is aligned by checking the kick of the atoms, the reflected beam can be optimized by maximizing the population of the first order with a weak lattice potential.

The calibration of the lattice depth also relies on the KD effect. However, a pulse of duration 40 μs is applied instead so that higher order diffractions appear more obviously which help to derive the depth information precise. The experimental spectra are shown

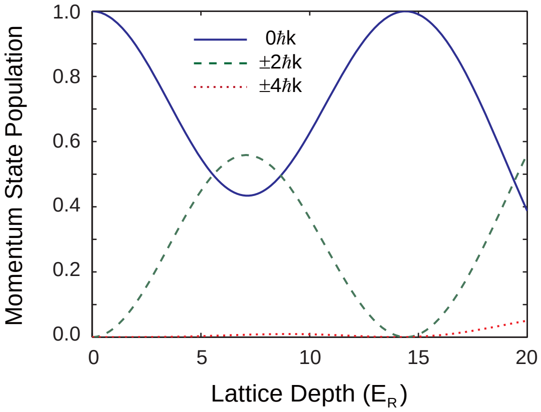

FIGURE 6.9: Kapitza-Dirac effect of the short lattice pulse. The population of an order other than the zeroth is the sum of the populations of both the positive order and the negative order. The pulse duration is fixed at 25 μs.

together with the numerical fits of both directions in Fig. 6.10, which implies that the relation between the control voltage and the lattice depth is (11.14 ± 0.17) E_R/V for short lattice X and (8.79 ± 0.19) E_R/V for short lattice Y. Throughout the experiment, the power of the incident lattice beams are fixed at 10 mW for the control voltage of 1 V at the transmission mode of the PBS used for intensity stabilization, and the actual beam waists are adjusted to compensate the attenuation in the beam path in order to achieve the best extinction ratio. The measured beam waists are

	Incident beam waist	Reflected beam waist
Short lattice X	121 μm	108 μm
Short lattice Y	134 μm	111 μm

,

and the theoretical relations support the experimental results which are 11.88 E_R/V for short lattice X and 9.42 E_R/V for short lattice Y.

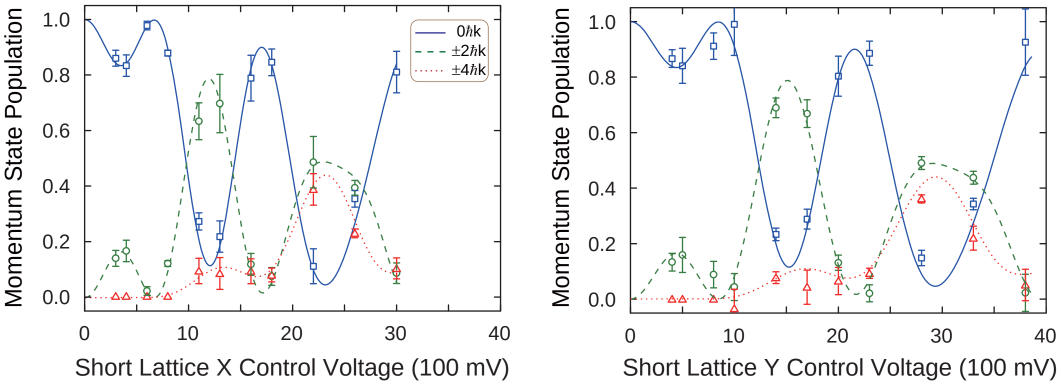

FIGURE 6.10: Lattice depth calibration by the Kapitza-Dirac effect. The lattice control voltage is given by the ADWin through the feedback loop. During the measurements, the pulse duration is fixed at 40 μs.

The calibration of the lattice depth is also cross-checked by finding the resonance frequency that couples the ground band and the second excited band. When the amplitude of the lattice is modulated, it would introduce a Raman transition between bands of same parity since the two carrier-sideband beating signals are in phase [215]. In the experiment, the lattice depth is set to 40 E_{R} with calibrated relations, and the lattice depth is modulated by about 8% for 50 cycles. The population is then measured by adiabatically ramping down the lattice which maps the bands into plane waves as shown in Fig. 6.11(a). By scanning the frequency, the population in the second excited band varies. Fig. 6.11(b) shows the experimental results for both short lattice X and short lattice Y with the Lorentzian fit which corresponds to (10.90 ± 0.01) $E_{\mathrm{R}}/\mathrm{V}$ for short lattice X and (9.05 ± 0.01) $E_{\mathrm{R}}/\mathrm{V}$ for short lattice Y, showing good agreement with the KD calibration.

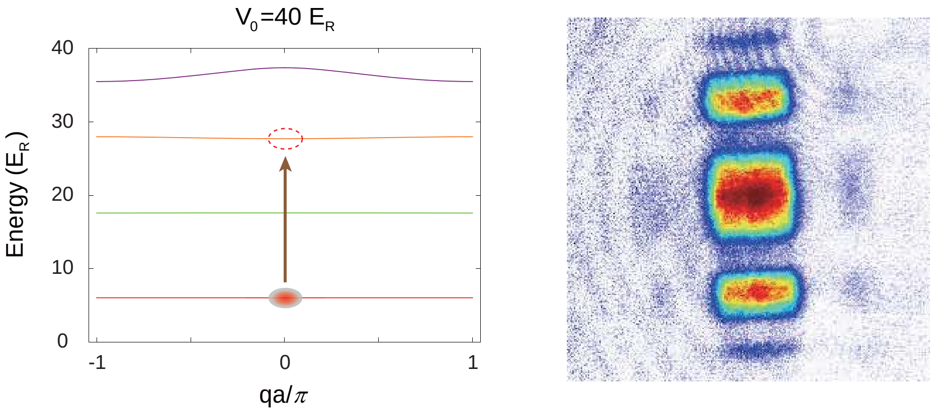

(a) Transferring population into the second excited band

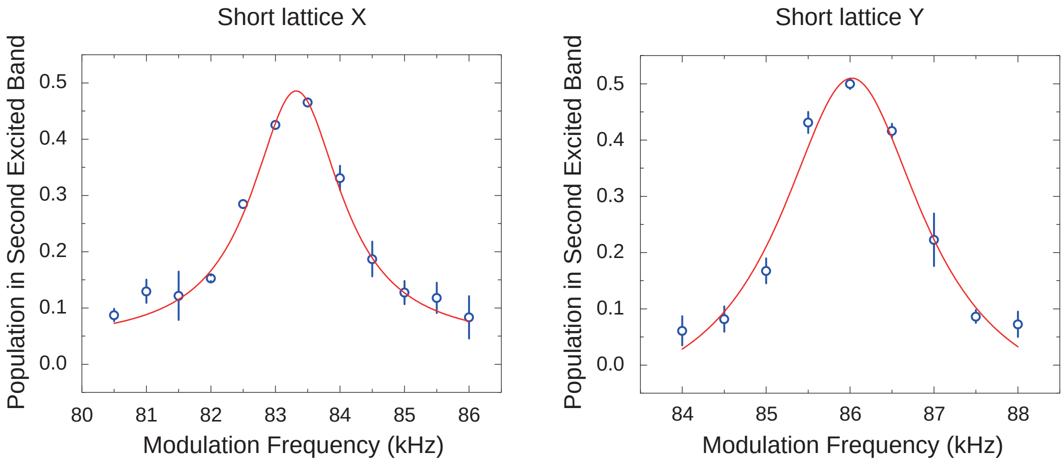

(b) Experimental data of population in the second excited band

FIGURE 6.11: Lattice depth calibration by the band excitation. (a) shows the scheme of transferring population into the second excited band. (b) shows the experimental data of the population in the second excited band. The fitted results are 83.32 ± 0.03 kHz for the x direction and 86.02 ± 0.05 kHz for the y direction.

6.3.3 Achieving the Mott Insulator Regime

To avoid heating, adiabaticity condition is generally required for ramping the lattice depth. In this experiment, lattice is first linearly ramped to a depth $V_\mathrm{s} = 0.4\ E_\mathrm{R}$ in $t_\mathrm{i} = 30$ ms, and then a S-shaped curve is applied which is suggested by the papers [185, 216]

$$V_\mathrm{lat}(t) = V_\mathrm{f} \frac{1+\gamma}{1+\gamma e^{4(t-t_\mathrm{i}-t_\mathrm{c})^2/t_\mathrm{c}^2}} \tag{6.23}$$

with

$$\gamma = -\frac{V_\mathrm{f} - V_\mathrm{s}}{V_\mathrm{f} - e^4 V_\mathrm{s}}, \tag{6.24}$$

where V_f is the final depth which is reached when $t = t_\mathrm{i} + t_\mathrm{c}$. The adiabaticity condition is ensured by restricting the adibaticity parameter of the ramp $\mathcal{A} = \hbar|\dot{J}|/J^2$ to be smaller than 1 [217].

While ramping the lattice depth to enter the Mott insulator regime, one has to ensure that the physical process is within the lowest energy band so that the simple Bose-Hubbard model is valid. In addition, phase coherence is studied for the phase transition.

6.3.3.1 Investigation of the Lattice Band Population

Before the observation of the quantum phase transition, band population is investigated by mapping crystal momentum to free particle momentum and analyzing the Brillouin zone population [218, 219]. As in the solid state physics, the n-th Brillouin zone is defined as a set of points in momentum space that can be reached from the origin by crossing exactly $(n-1)$ Bragg planes, and an illustration of Brillouin zones for a two-dimensional lattice is given in Fig. 6.12(a). In the experiment, a mapping onto the Brillouin zones is done by first ramping the lattice adiabatically to 50 E_R, and then exponentially ramping down within 300 μs with a time constant of 50 μs. It is slow compared to the vibrational frequency of the lattice to inhibit the excitation, while fast compared to the tunneling processes so that the population is kept. After 12 ms TOF, Fig. 6.12(b) shows a homogenous population in the first Brillouin zone which corresponds to the lowest band, and no visible population in higher bands is observed. In contrast, Fig. 6.12(c) exhibits a pronounced population in higher energy bands with an abruptly ramp to a lattice depth of 20 E_R. In the current experiment, by inspecting the band population, the physics is restricted to the lowest band.

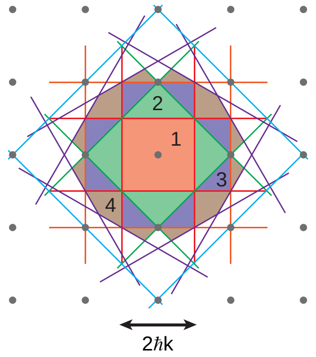

(a) Brillouin zones of a two-dimensional lattice

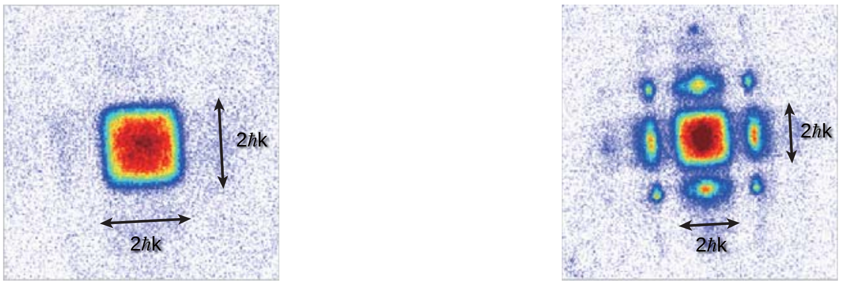

(b) Band population with adiabatic ramp

(c) Band population in excited bands

Figure 6.12: Investigating the band population. (a) shows Brillouin zones of a two-dimensional square lattice. (b) shows band population with adiabatic ramp where the atoms are restricted to the lowest energy band. (c) shows band population in excited bands by a sudden loading. Note that some of the bands, for example band 2 and band 3, are degenerate thus can not be separated [201].

6.3.3.2 Deep Lattice Condition

In the Mott insulator phase, finite tunneling would result in a coherent admixture of particle-hole pairs to the ground state so that short-range coherence is reserved [220]. To achieve a well-defined Mott insulator, one has to inhibit such coherence by reaching the deep lattice condition.

In a TOF measurement, the density distribution of the expanding cloud can be expressed as [220, 221]

$$n(\mathbf{r}) = \left(\frac{m}{\hbar t}\right)^3 \left|\tilde{w}_1\left(\mathbf{k} = \frac{m\mathbf{r}}{\hbar t}\right)\right|^2 \mathcal{S}\left(\mathbf{k} = \frac{m\mathbf{r}}{\hbar t}\right), \tag{6.25}$$

with

$$\mathcal{S}(\mathbf{k}) = \sum_{j,j'} e^{i\mathbf{k}\cdot(\mathbf{r}_j - \mathbf{r}_{j'})} \langle \hat{a}_j^\dagger \hat{a}_{j'} \rangle, \tag{6.26}$$

where $\tilde{w}_1(\mathbf{k})$ is the Fourier transform of the Wannier function in the lowest Bloch band, and $\hat{a}_j^\dagger$ ($\hat{a}_j$) creates (annihilates) an atom at the j-th site. In the superfluid phase, the correlation function $\langle \hat{a}_j^\dagger \hat{a}_{j'} \rangle$ varies smoothly across the lattice sites which is responsible for the sharp diffraction pattern. In the Mott insulator phase, however, the correlation function extends only a few sites resulting in a disappearance of the interference pattern. Therefore, an effective way to characterize the phase coherence is given by a measurement on the visibility of interference fringes which is defined as [220]

$$\mathcal{V} = \frac{N_{\max} - N_{\min}}{N_{\max} + N_{\min}} = \frac{\mathcal{S}_{\max} - \mathcal{S}_{\min}}{\mathcal{S}_{\max} + \mathcal{S}_{\min}}, \tag{6.27}$$

where $N_{\max}$ corresponds to a sum of number of atoms in the four nearest lateral peaks, and $N_{\min}$ corresponds to a sum of number of atoms in the four areas which form a diagonal cross and have same distance from the central peak as shown in the inset of Fig. 6.13(b). The visibility will change from 1 in the superfluid regime to 0 in the ideal Mott insulator phase. Note that the Wannier envelopes cancel out since the distance for each term is the same.

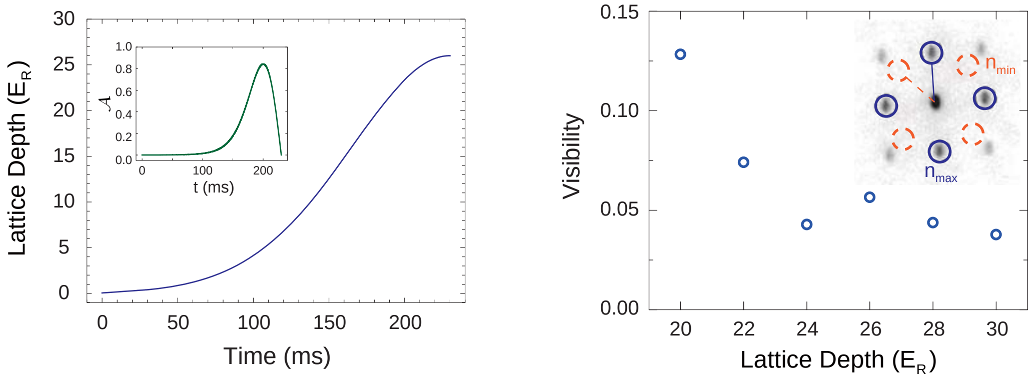

(a) S-shaped adiabatic ramp curve

(b) Visibility measurements for deep lattice

FIGURE 6.13: Evaluation of the deep lattice condition. (a) depicts the adiabatic ramp used in the experiment which is a 200 ms S-shaped curve preceded by a 30 ms linear ramp. When the final depth is 26 E_{R}, the adiabaticity parameter is restricted to be smaller than 0.85 as shown in the inset. (b) shows the experimental results of the measured visibility for each depth, where the inset illustrates the definition of the visibility.

Armed with the idea, lattice is ramped to a variety of depths adiabatically with a 200 ms S-curve as shown in Fig. 6.13(a), and the visibility of the interference pattern for each depth is recorded as shown in Fig. 6.13(b). It can be readily seen that the visibility tends to zero as the depth is increased and the phase coherence is efficiently suppressed at a lattice depth of 26 E_{R} which corresponds to $U/J \simeq 296.2$.

To demonstrate that the measured visibility is a direct observation of phase coherence, a measurement of the collapse and revival of the macroscopic phase is performed [222]. In an isolated well, the Hamiltonian that describes the system is given by $H = U\hat{n}(\hat{n}-1)/2$ with the eigenstates being Fock states $|n\rangle$ and eigenenergies $E_n = Un(n-1)/2$. Thus a coherent state in this system will evolve as

$$|\alpha(t)\rangle = e^{-|\alpha|^2/2}\sum_n \frac{\alpha^n}{\sqrt{n!}} e^{-iUn(n-1)t/(2\hbar)}|n\rangle. \tag{6.28}$$

The macroscopic phase can be inspected by calculating the mean value of the atomic field operator [223, 224]

$$\psi(t) = \langle\alpha(t)|\hat{a}|\alpha(t)\rangle = \sqrt{\bar{n}}\exp\left[\bar{n}(e^{-iUt/\hbar}-1)\right], \tag{6.29}$$

and for short times

$$\psi(t) \simeq \sqrt{\bar{n}}e^{-i\bar{n}Ut/\hbar}\, e^{-\bar{n}U^2t^2/(2\hbar^2)}. \tag{6.30}$$

Therefore, estimated by the Gaussian function, the macroscopic matter wave field ψ will collapse with a time constant $t_{\mathrm{col}} = \hbar/(\sqrt{\bar{n}}U)$. However, since the Eq. 6.29 is periodic, the macroscopic matter wave field will revive at every period where each number state acquires a phase of an integer multiple of 2π giving a revival time $t_{\mathrm{rev}} = h/U$.

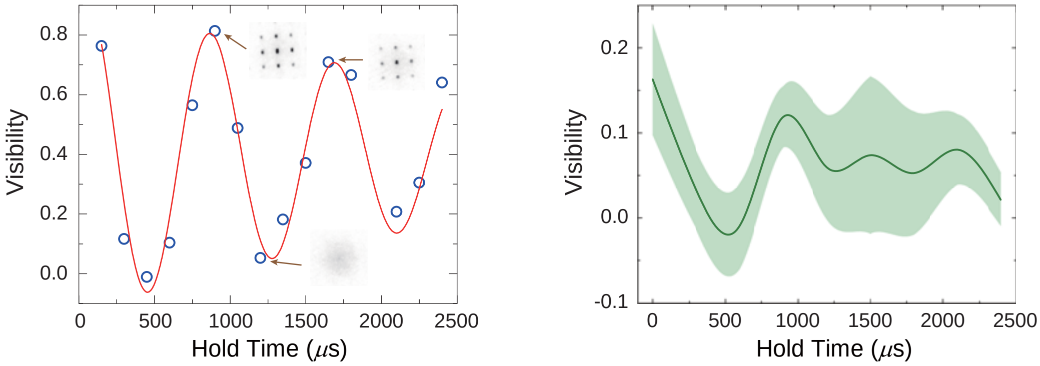

(a) Prepared at 8 E_{R} (b) Prepared at 20 E_{R}

FIGURE 6.14: Collapse and revival of the residual superfluid. (a) shows the visibility versus hold time with the red curve being a fit for the periodicity after a rapid increase of the potential from 8 E_{R} to 40 E_{R}. (b) shows the visibility versus hold time after a rapid increase from 20 E_{R} to 40 E_{R}. Although the large error makes the fitting for periodicity hard, it is clear that the residual superfluid part at a depth of 20 E_{R} does yield a collapse and revival of the phase.

When the system is in the superfluid regime, the superfluid state will exhibit like a coherent state as depicted in Eq. 6.14. Thus after the lattice depth is rapidly ramped to the deep Mott insulator regime, one could record the phase evolution by monitoring the visibility. In the current experiment, lattice is first adiabatically ramped to 8 E_{R}, which is in the superfluid regime, by following a 100 ms exponential curve. Later, the depth is increased to 40 E_{R} in 60 μs which is fast enough to keep the number statistics while slow enough to avoid excitation. Fig. 6.14(a) shows the measured result and a periodicity is fitted as (826 ± 3) μs which is a little bit larger than the theoretical value $t_{\mathrm{rev}} \simeq 780$ μs. The deviation is ascribed to the error of the system calibration and the accuracy of the simple Bose-Hubbard model used for interaction calculation. The phase evolution with the superfluid part prepared at a depth of 20 E_R is also studied. The result is shown in Fig. 6.14(b) which confirms that the finite visibility is the evidence of residual phase coherence, and higher depth is required in order to enter the deep Mott insulator regime. In addition, it is worth noting that a comprehensive measurement on the phase revival could help to calibrate the on-site interaction with high accuracy [225].

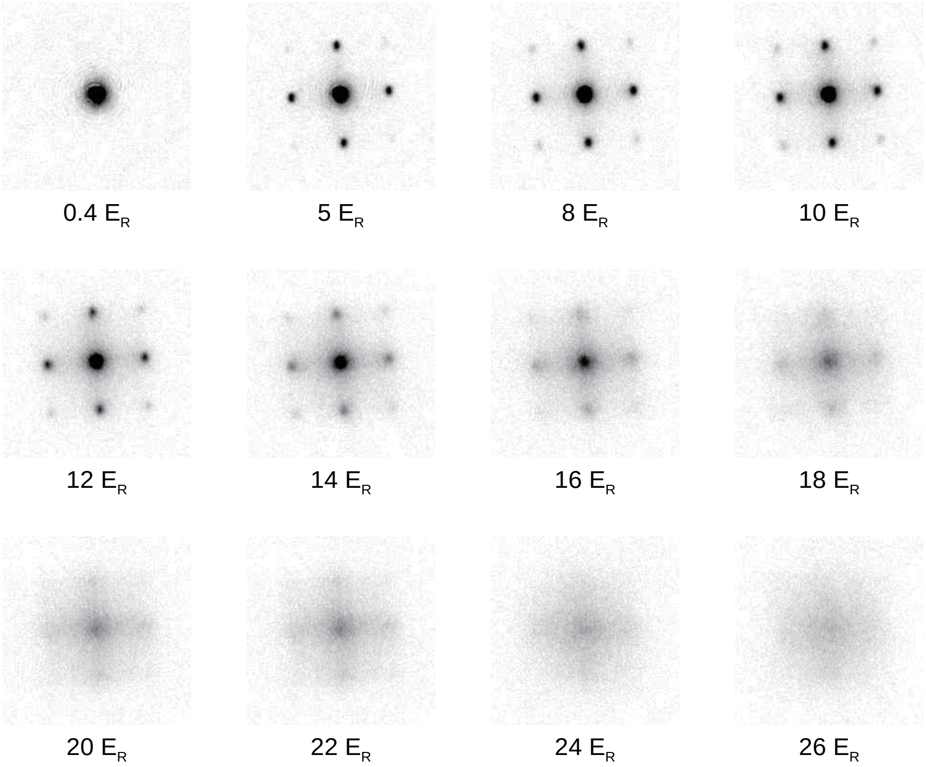

0.4 E_R 5 E_R 8 E_R 10 E_R

12 E_R 14 E_R 16 E_R 18 E_R

20 E_R 22 E_R 24 E_R 26 E_R

FIGURE 6.15: Interference pattern for different lattice depths. The range of the coherence is diminishing as the lattice depth increases, and the interference pattern is completely lost at the deep lattice depth. Each figure is an average of about 10 pictures and the number of atoms is about 10000.

6.3.3.3 Observation of the Quantum Phase Transition

According to the above investigation, lattice is ramped by the 200 ms S-shaped curve to a depth of 26 E_R for the observation of the quantum phase transition. A change of the phase coherence is observed by suddenly switching off the trap at a variety of depths, and imaging the interference pattern after 12 ms TOF as shown in Fig. 6.15. At the very beginning, the high-order interference peaks become more prominent as the depth is increased since atoms are localized tighter. After about 12 E_R the peaks are smeared and a cross like structure is observed which is related to the short-ranged phase coherence [201]. At last, the interference pattern is completely lost leaving a Gaussian shape structure which is related to the Wannier envelope. In order to confirm that the transition is within the quantum regime, after a 100 ms hold at 26 E_{R}, lattice is linearly ramped down to 6 E_{R} in 20 ms to restore the phase coherence. Fig. 6.16 shows the measured interference pattern in which only a little heating effect is observed.

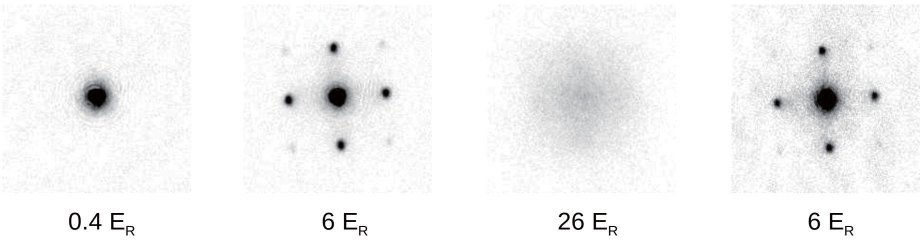

FIGURE 6.16: Restoring the phase coherence. No obvious heating effect is observed which confirms the quantum phase transition.

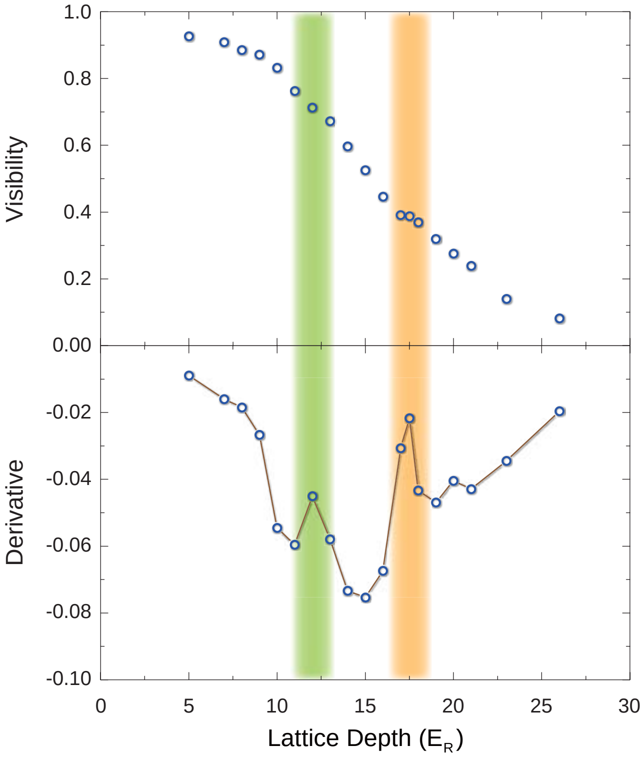

FIGURE 6.17: Visibility versus lattice depth. Two kinks are observed which are reproducible.

The change of the visibility is then carefully studied and the result is shown in Fig. 6.17. In the numerical derivative plot, two reproducible kinks are observed which are around 12 E_{R} and 17.5 E_{R}, respectively. The kink appearing at 12 E_{R} coincides with the interference pattern (Fig. 6.15) at which the peaks become smeared. And the kink at 17.5 E_{R} corresponds to $J/U \simeq 0.019$ which is roughly the theoretical transition point to $n_{\mathrm{MI}} = 3$ Mott insulator state as shown in the phase diagram (Fig. 6.6). Since the kinks are ascribed to the redistribution of density among Mott insulator and superfluid regions [220,226], the kink at 17.5 E_{R} might reflect that the number density in the middle of the trap is more than 2. This result coincides with the estimation taken in Section

6.2.2.4 where the filling 1 requires the total number of atoms no more than 2700. In addition, more kinks could be observed for an ideal system which are responsible for every regional formation of the superfluid and the Mott insulator as well as the redistribution between the Mott insulator states with different filling numbers [226].

Chapter 7

Creating Entanglement in Two-Dimensional Optical Superlattices

When a second lattice with a wavelength twice of the first is added to the system, an optical superlattice is formed which allows one to study multi-body physics by performing both intrawell and interwell manipulations [205]. Especially, superlattices can help to realize arrays of double-well potentials [64, 227] and four-site plaquettes [228] with high-order tunneling effects involved which is an effective way to generate multi-qubit entanglement [229]. In this chapter, I will first review the basic theory of a single particle in an optical superlattice as well as the Bose-Hubbard model. Then the current setup to form the superlattice is explained. With the help of the knowledge, an experimental scheme to generate four-qubit entanglement is proposed.

7.1 Superlattice Band Struncture

The superlattice that is employed in the experiment is formed by combining a blue-detuned lattice (named as "short lattice" with a wavelength of 767 nm) and a red-detuned lattice (named as "long lattice" with a wavelength of 1534 nm). It has a different band structure compared with the monochromatic lattice described in Chapter 6. A calculation of the band structure can be done by considering the Fourier transform of the elements of the equation [200].

The potential of a one-dimensional superlattice can be described as

$$V_{\text{slat}}(x) = -V_{\text{red}} \cos^2(kx + \Theta) + V_{\text{blue}} \cos^2(2kx), \tag{7.1}$$

where $k = k_{\text{red}} = 2\pi/\lambda_{\text{red}}$ is the wave vector related to the red-detuned light, Θ is the relative phase between the two standing waves, and V_{red} and V_{blue} are the trap depth of the red- and blue-detuned lattice, respectively. When a single particle is placed in such a potential, according to the Bloch's theorem, the eigenstates of the system are Bloch functions

$$\phi_q^{(n)}(x) = e^{iqx} u_q^{(n)}(x), \tag{7.2}$$

with $u_q^{(n)}(x + \lambda_{\text{red}}/2) = u_q^{(n)}(x)$ taking the same periodicity as $V_{\text{slat}}(x)$. With this ansatz, a relation for $u_q^{(n)}(x)$ can be derived from the Schrödinger equation

$$\left[\frac{(\hat{p} + \hbar q)^2}{2m} + V_{\text{slat}}(x) \right] u_q^{(n)}(x) = E_q^{(n)} u_q^{(n)}(x). \tag{7.3}$$

Since both $V_{\text{slat}}(x)$ and $u_q^{(n)}(x)$ are periodic functions, one can expand them in Fourier series as $V_{\text{slat}}(x) = \sum_\alpha V_\alpha \exp(i2\alpha kx)$ and $u_q^{(n)}(x) = \sum_\beta c_\beta^{(n,q)} \exp(i2\beta kx)$, respectively, with α and β integers. Therefore, the left part of the Eq. 7.3 becomes

$$\begin{array}{lccc} \text{Kinetic energy term:} & \dfrac{(\hat{p} + \hbar q)^2}{2m} u_q^{(n)}(x) & = & \displaystyle\sum_\beta \frac{(2\hbar\beta k + \hbar q)^2}{2m} c_\beta^{(n,q)} e^{i2\beta kx} \\ \text{Potential energy term:} & V_{\text{slat}}(x)\, u_q^{(n)}(x) & = & \displaystyle\sum_\beta \sum_\alpha V_\alpha c_\beta^{(n,q)} e^{i2(\alpha+\beta)kx} \end{array} . \tag{7.4}$$

After the lattice potential is expanded as

$$V_{\text{slat}}(x) = \frac{V_{\text{blue}} - V_{\text{red}}}{2} - \frac{V_{\text{red}}}{4} \left(e^{i2\Theta} e^{i2kx} + e^{-i2\Theta} e^{-i2kx} \right) + \frac{V_{\text{blue}}}{4} \left(e^{i4kx} + e^{-i4kx} \right), \tag{7.5}$$

the Eq. 7.3 can be written in a matrix form

$$\sum_{\beta'} H_{\beta,\beta'} \cdot c_{\beta'}^{(n,q)} = E_q^{(n)} c_\beta^{(n,q)}, \tag{7.6}$$

with

$$H_{\beta,\beta'} = \begin{cases} (2\beta + q/k)^2 E_{\text{R}}^{\text{red}} & \text{if } \beta = \beta' \\ -V_{\text{red}}/4 \exp[i(\beta - \beta')2\Theta] & \text{if } |\beta - \beta'| = 1 \\ V_{\text{blue}}/4 & \text{if } |\beta - \beta'| = 2 \\ 0 & \text{else} \end{cases} , \tag{7.7}$$

where $E_{\mathrm{R}}^{\mathrm{red}} = (\hbar k)^2/(2m)$ is the recoil energy for the red-detuned lattice, and the zeroth order Fourier term of the potential energy is neglected. Such a Hamiltonian can be solved by truncating the matrix into a size that is large enough to neglect the coefficients $c_\beta^{(n,q)}$ for large β, which is chosen to be $-10 \leq \beta \leq 10$ in this thesis. The Bloch functions are then determined as $\phi_q^{(n)}(x) = \sum_\beta c_\beta^{(n,q)} \exp[i(q + 2\beta k)x]$.

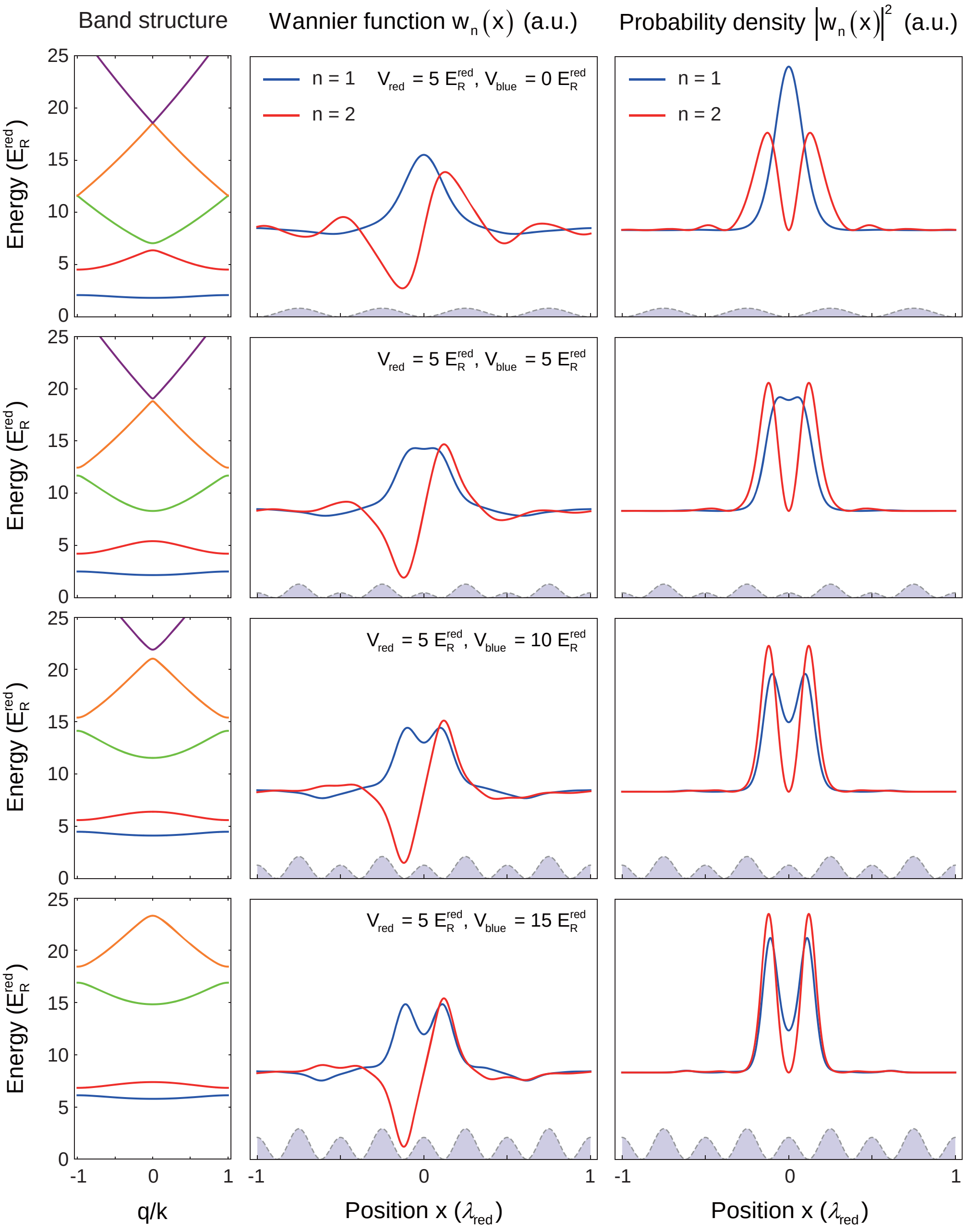

FIGURE 7.1: Band structure of shallow superlattices. The filled area represents the lattice potential.

Similar to a single particle in a monochromatic lattice, the localized Wannier functions are useful to study the superlattice system which are defined as Eq. 6.4. With these definitions, the band structure and Wannier functions for the two lowest bands are calculated for shallow superlattices with $\Theta = 0$ as shown in Fig. 7.1. In comparison with the monochromatic lattice, bands are paired in the appearance of a symmetric double-well structure [230]. Within each pair, the band of lower-energy has a symmetric Wannier function, while the band of higher-energy has an antisymmetric Wannier function, and both functions extend over both wells. In addition, the tunneling matrix element between nearest-neighbor superlattice sites can be determined in the same way as in Section 6.1.3 which has the form $J^{(n)}_{\text{ext}} = [\max(E^{(n)}_q) - \min(E^{(n)}_q)]/4$ for the n-th band.

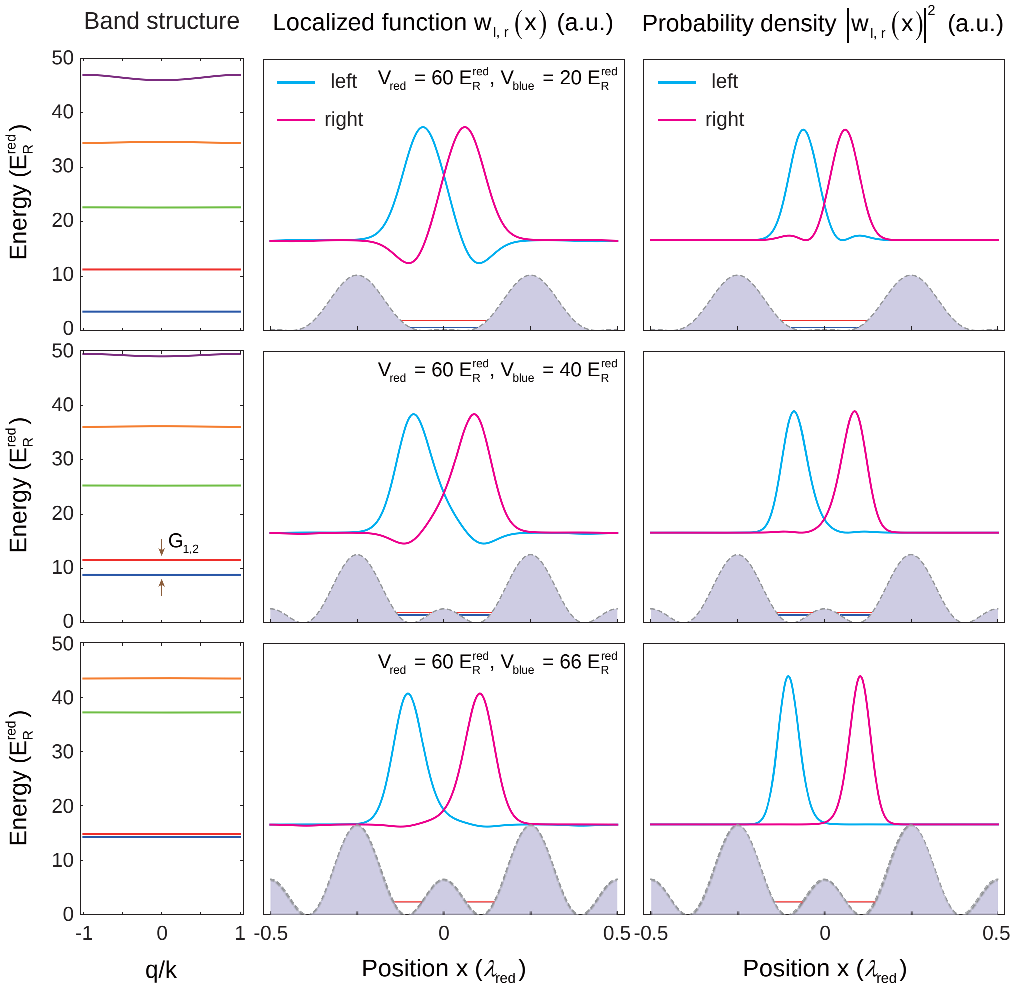

FIGURE 7.2: Band structure of deep superlattices. The filled area represents the lattice potential. The two lowest energy levels are also depicted with the lattice potential to specify the relation between them.

When the depth of the long lattice is large, tunneling between superlattice sites is highly suppressed leaving isolated double wells. In this case, raising the short lattice potential will result in a decrease of the energy gap between the two lowest bands $G_{1,2}$. At last, the energy gap $G_{1,2}$ becomes negligible, and the two lowest bands can be approximated as two degenerate energy levels [230]. By superposing the two Wannier functions, one can obtain two useful wave functions which are localized in the left and right well for the lowest pair of energy levels

$$w_l(x) = \frac{1}{\sqrt{2}}[w_1(x) - w_2(x)], \tag{7.8}$$

$$w_r(x) = \frac{1}{\sqrt{2}}[w_1(x) + w_2(x)]. \tag{7.9}$$

The localized functions are important to describe the evolution of particles in a double-well system, and the definition can be extended to any band pair. Fig. 7.2 shows the band structure and the localized functions with a long lattice depth of 60 $E_{\mathrm{R}}^{\mathrm{red}}$, where the wave functions $w_{l,r}(x)$ are getting more localized as the short lattice depth increases. It has to be emphasized that the two localized wave functions $w_{l,r}(x)$ are not eigenstates of the system and thus evolve in time according to the energy gap. When such a state is prepared, it will oscillate between the two wells with a period of $h/G_{1,2}$.

7.2 Bose-Hubbard Model for Superlattices

In order to study physics of interacting bosons on a superlattice, Bose-Hubbard model is extended for superlattices. By analyzing the Hamiltonian, superexchange and ring-exchange interactions are presented which can be used for entanglement generation.

7.2.1 Double-Well Bose-Hubbard Model

When the long lattice is applied to only the x direction, in the limit of deep long lattice, system can be simplified to isolated double wells, and the Hamiltonian can be generalized from the Josephson Hamiltonian [231, 232]

$$H_{\mathrm{DW}} = -J(\hat{a}_l^\dagger \hat{a}_r + \hat{a}_r^\dagger \hat{a}_l) + \frac{U_l}{2}\hat{n}_l(\hat{n}_l - 1) + \frac{U_r}{2}\hat{n}_r(\hat{n}_r - 1) - \frac{\Delta}{2}(\hat{n}_l - \hat{n}_r), \tag{7.10}$$

with $\Delta = E_r - E_l$ the energy bias between the two states $|l\rangle$ and $|r\rangle$ describing the particle in the left well and right well, respectively. The tunneling between two wells J and the on-site interaction $U_{l,r}$ are defined as

$$J = -\int dx w_l^*(x)\left[-\frac{\hbar^2}{2m}\nabla^2 + V_{\mathrm{slat}}(x)\right] w_r(x), \tag{7.11}$$

$$U_{l,r} = g_{\mathrm{2D}} \int dx |w_{l,r}(x)|^4 \int dy |w_1(y)|^4, \tag{7.12}$$

where $w_1(y)$ is the Wannier function describing the localized particle in the y direction.

7.2.1.1 Single Particle in a Double Well

When a single particle is placed in a double well, on-site interaction can be neglected, and the Hamiltonian can be written in a matrix form with states $\{|l\rangle, |r\rangle\}$ being the basis

$$H_1 = \begin{pmatrix} -\Delta/2 & -J \\ -J & \Delta/2 \end{pmatrix}. \tag{7.13}$$

In the case of zero bias $\Delta = 0$, the eigenstates of the Hamiltonian are calculated as

$$|+\rangle = \frac{1}{\sqrt{2}}(|r\rangle + |l\rangle), \tag{7.14}$$

$$|-\rangle = \frac{1}{\sqrt{2}}(|r\rangle - |l\rangle), \tag{7.15}$$

with eigenvalues $E_\pm = \mp J$. By comparing to Eq. 7.8 and Eq. 7.9, one can relate the energy gap to the tunneling matrix element by $G_{1,2} = 2J$.

7.2.1.2 Two Particles in a Double Well

If one adds an additional particle into the double well, the Hamiltonian can be expanded in the basis $\{|ll\rangle, (|lr\rangle + |rl\rangle)/\sqrt{2}, |rr\rangle\}$ as

$$H_2 = \begin{pmatrix} U_l - \Delta & -\sqrt{2}J & 0 \\ -\sqrt{2}J & 0 & -\sqrt{2}J \\ 0 & -\sqrt{2}J & U_r + \Delta \end{pmatrix}. \tag{7.16}$$

Note that the state $(|lr\rangle - |rl\rangle)/\sqrt{2}$ is forbidden by the symmetry requirement of indistinguishable bosons. When the on-site interactions are assumed to be the same $U_l = U_r = U$ and the energy bias is set to zero, the Hamiltonian is solved yielding

Eigenvalue	Eigenstate
$E_1 = U$	$\|\psi_1\rangle = (1, 0, -1)$
$E_2 = (U - \sqrt{16J^2 + U^2})/2$	$\|\psi_2\rangle = (\sqrt{2}J/E_3, 1, \sqrt{2}J/E_3)$
$E_3 = (U + \sqrt{16J^2 + U^2})/2$	$\|\psi_3\rangle = (\sqrt{2}J/E_2, 1, \sqrt{2}J/E_2)$

.

In addition, in the case of deep short lattice where $J \ll U$, the results are simplified as

Eigenvalue	Eigenstate
$E_1 = U$	$\vert\psi_1\rangle = (\vert ll\rangle - \vert rr\rangle)/\sqrt{2} \equiv \vert --\rangle$
$E_2 \simeq -4J^2/U \to 0$	$\vert\psi_2\rangle \simeq (\vert lr\rangle + \vert rl\rangle)/\sqrt{2} \equiv \vert SS\rangle$
$E_3 \simeq U + 4J^2/U \to U$	$\vert\psi_3\rangle \simeq (\vert ll\rangle + \vert rr\rangle)/\sqrt{2} \equiv \vert ++\rangle$

.

Thus a state prepared in $|ll\rangle$ will evolve as

$$|\psi(t)\rangle = \frac{1}{\sqrt{2}}\left[|++\rangle + e^{i(E_3-E_1)t/\hbar}|--\rangle\right], \tag{7.17}$$

which shows an oscillation between $|ll\rangle$ and $|rr\rangle$. Note that there is no single particle tunneling process occurring since the $|SS\rangle$ state has a different energy which is U less than the other states. However, the particles tunnel as a pair indicating a second order tunneling process which is determined by the energy gap as $J_{(2)} = (E_3 - E_1)/2 \simeq 2J^2/U$ [230].

7.2.1.3 Superexchange in a Double Well

When the two bosonic atoms have different spin states, the Hamiltonian has to be modified as [64]

$$H = \sum_{\sigma=\uparrow,\downarrow}\left[-J(\hat{a}^{\dagger}_{\sigma l}\hat{a}_{\sigma r} + \hat{a}^{\dagger}_{\sigma r}\hat{a}_{\sigma l}) - \frac{\Delta}{2}(\hat{n}_{\sigma l} - \hat{n}_{\sigma r})\right] + U(\hat{n}_{\uparrow l}\hat{n}_{\downarrow l} + \hat{n}_{\uparrow r}\hat{n}_{\downarrow r}), \tag{7.18}$$

where the two spin states $|\uparrow\rangle$ and $|\downarrow\rangle$ are imprinted, for example, in $|F=1, m_F=+1\rangle$ and $|F=1, m_F=-1\rangle$, respectively, and $U = U_{\uparrow\downarrow}$ is the on-site interaction energy between two atoms with different spin states. Because of the introduction of the spin states, a basis that can be used to expand the Hamiltonian is given by $\{|\uparrow\downarrow, 0\rangle, |t\rangle, |s\rangle, |0, \uparrow\downarrow\rangle\}$ with $|t/s\rangle \equiv (|\uparrow,\downarrow\rangle \pm |\downarrow,\uparrow\rangle)/\sqrt{2}$. Under this basis, the Hamiltonian is written as

$$H = \begin{pmatrix} U-\Delta & -\sqrt{2}J & 0 & 0 \\ -\sqrt{2}J & 0 & 0 & -\sqrt{2}J \\ 0 & 0 & 0 & 0 \\ 0 & -\sqrt{2}J & 0 & U+\Delta \end{pmatrix}. \tag{7.19}$$

In the symmetric case ($\Delta = 0$) and $J \ll U$, the solutions of the Hamiltonian are

Eigenvalue	Eigenstate
$E_1 = 0$	$\vert\psi_1\rangle = \vert s\rangle$
$E_2 = U$	$\vert\psi_2\rangle = (\vert\uparrow\downarrow, 0\rangle - \vert 0, \uparrow\downarrow\rangle)/\sqrt{2}$
$E_3 \simeq -4J^2/U \to 0$	$\vert\psi_3\rangle \simeq \vert t\rangle$
$E_4 \simeq U + 4J^2/U \to U$	$\vert\psi_4\rangle \simeq (\vert\uparrow\downarrow, 0\rangle + \vert 0, \uparrow\downarrow\rangle)/\sqrt{2}$

As in the case of identical bosons, the state $|\psi_2\rangle$ and $|\psi_4\rangle$ are degenerate in the limit $J \ll U$ which implies that a state prepared in $|\uparrow\downarrow, 0\rangle$ or $|0, \uparrow\downarrow\rangle$ will oscillate between the two wells as a pair in time. However, a state that is initialized in $|\uparrow, \downarrow\rangle = (|t\rangle + |s\rangle)/\sqrt{2}$ will evolve as

$$|\psi(t)\rangle = \frac{1}{\sqrt{2}}\left[|s\rangle + e^{i(E_1 - E_3)t/\hbar}|t\rangle\right], \tag{7.20}$$

showing an oscillation between $|\uparrow, \downarrow\rangle$ and $|\downarrow, \uparrow\rangle$. Single particle tunneling is inhibited due to an energy gap of U, hence the non-local spin-exchange process is of second order which is known as superexchange with an effective tunneling matrix element $J_{\mathrm{ex}} = (E_1 - E_3)/2 \simeq 2J^2/U$ [64]. Moreover, it is worthy to note that an entangled state $(|\uparrow, \downarrow\rangle + i|\downarrow, \uparrow\rangle)/\sqrt{2}$ is generated at $t = \pi\hbar/(4J_{\mathrm{ex}})$. Note that the superexchange tunneling matrix element J_{ex} can also be calculated from the time-independent perturbation theory with second order correction.

7.2.2 Ring-Exchange in an Optical Plaquette

Extending the superlattices to a two-dimensional system, one could obtain an array of disconnected plaquettes as shown in Fig. 7.3(a), which has been already used to investigate the resonating valence-bond state [228, 233, 234]. On the way to study the topologically ordered states with the plaquettes, Belén Paredes and Immanuel Bloch proposed an approach to realize a ring-exchange interaction which, by restricting to a subspace, can be used to generate a four-particle entangled state [229].

When the spin states are involved, the Hamiltonian that describes the dynamics of atoms in a plaquette is given by

$$H = -\sum_{\langle j,j'\rangle,\sigma} J_{jj'}\hat{a}^{\dagger}_{j\sigma}\hat{a}_{j'\sigma} + U\left[\frac{1}{2}\sum_{j,\sigma}\hat{n}_{j\sigma}(\hat{n}_{j\sigma} - 1) + \sum_{j}\hat{n}_{j\uparrow}\hat{n}_{j\downarrow}\right] + \sum_{j,\sigma}\mu_{j\sigma}\hat{n}_{j\sigma}, \tag{7.21}$$

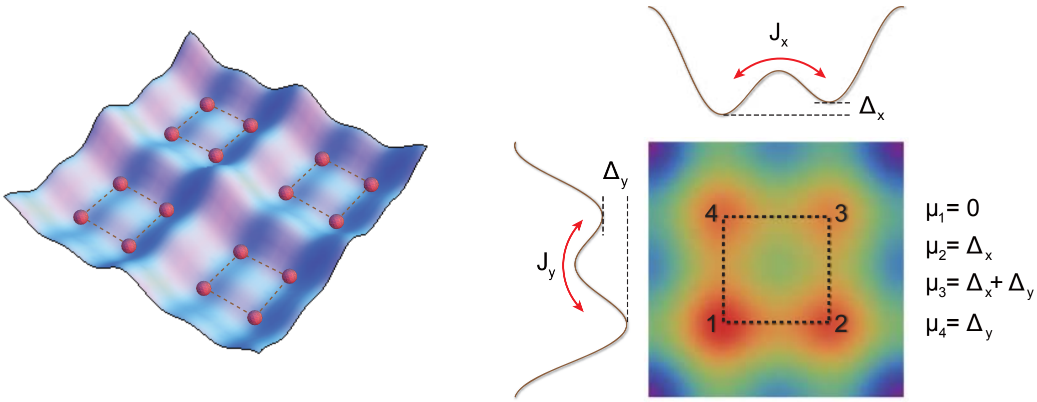

(a) An array of decoupled plaquettes (b) Tilted plaquette

FIGURE 7.3: A schematic view of optical plaquettes. (a) shows a two-dimensional superlattice with decoupled optical plaquettes. (b) shows a tilted plaquette where the potential bias Δ_x and Δ_y are introduced by controlling the phase between the short lattice and the long lattice. Note that tilting the lattice will not only change the energy offsets of the wells, but also lead to different vibrational level splittings.

where $J_x \equiv J_{12} = J_{34}$ and $J_y \equiv J_{14} = J_{23}$ describe the tunneling between the numbered wells as shown in Fig. 7.3(b), and $\mu_{j\sigma}$ denotes the energy offsets. Restricting to four spins, one could derive a lattice gauge Hamiltonian by employing lattice gauge theory [229, 235]

$$H_{\mathrm{G}} = -J_{\Box}\hat{S}_1^x\hat{S}_2^x\hat{S}_3^x\hat{S}_4^x + J_{+}(\hat{S}_1^z\hat{S}_2^z + \hat{S}_2^z\hat{S}_3^z + \hat{S}_3^z\hat{S}_4^z + \hat{S}_4^z\hat{S}_1^z), \tag{7.22}$$

where $J_{\Box}$ denotes the strength of the ring-exchange interaction with $\hat{S}_1^x\hat{S}_2^x\hat{S}_3^x\hat{S}_4^x$ being a ring operator, J_{+} denotes the strength of the charge interaction between neighboring spins, and the operator $\hat{S}_j^{\alpha}$, $\alpha \in \{x, y, z\}$ denotes the corresponding Pauli matrix acting on the spin in j-th well. Solving the Hamiltonian yields the eigenstates as shown in Fig. 7.4, including a ground state $|\Box\rangle$ which is a string-net condensate [236, 237], a fluxlike excitation $|\boxdot\rangle$, and chargelike excitations.

When the system is prepared in the state $|\uparrow\downarrow\uparrow\downarrow\rangle$, as the Hamiltonian H_{G} predicts, it will evolve as

$$|\psi(t)\rangle = \frac{1}{\sqrt{2}}\left(|\Box\rangle + e^{-i2J_{\Box}t/\hbar}|\boxdot\rangle\right). \tag{7.23}$$

However, the superexchange between two neighboring wells would dominate the evolution, since it is large compared to the ring-exchange interaction which relates to the fourth order tunneling. To inhibit the second order processes, one can apply a magnetic field gradient along a diagonal direction which results in an energy splitting Δ between each pair of states coupled by the superexchange interaction as shown in Fig. 7.5. The second order processes are thus suppressed when the induced energy splitting is much larger than the superexchange energy ($\gg 2J^2/U$). The Hamiltonian is then

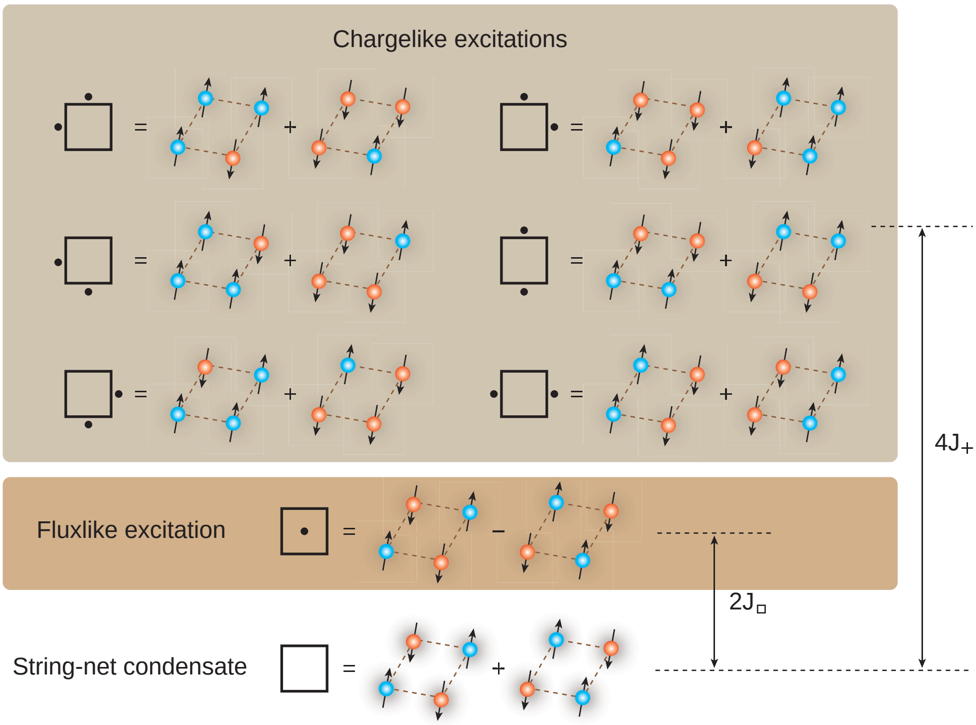

FIGURE 7.4: Eigenstates of the lattice gauge Hamiltonian.

given by [229]

$$\begin{aligned}H_{\mathrm{R}} = &- J_{\square}(\hat{S}_1^+\hat{S}_2^-\hat{S}_3^+\hat{S}_4^- + \hat{S}_1^-\hat{S}_2^+\hat{S}_3^-\hat{S}_4^+) + J_+(\hat{S}_1^z\hat{S}_2^z + \hat{S}_2^z\hat{S}_3^z + \hat{S}_3^z\hat{S}_4^z + \hat{S}_4^z\hat{S}_1^z)\\ &+ J_\times(\hat{S}_2^+\hat{S}_4^- + \hat{S}_2^-\hat{S}_4^+) - \frac{\Delta}{2}\sum_j B_j S_j^z,\end{aligned} \tag{7.24}$$

with the raising and lowering operators $S_j^\pm = (\hat{S}_j^x \pm i\hat{S}_j^y)/2$, the tunneling matrix elements $J_\square \simeq 24J^4/U^3$, $J_+ \simeq 4J^2/U$, and $J_\times \simeq 16J^4/U^3$, and the coefficients $\{B_1, B_2, B_3, B_4\} = \{0, 1, 2, 1\}$. The Hamiltonian H_{R} is equivalent to the Hamiltonian H_{G} within the subspace that is generated by the states $|\uparrow\downarrow\uparrow\downarrow\rangle$ and $|\downarrow\uparrow\downarrow\uparrow\rangle$, thus $|\square\rangle$ and $|\boxdot\rangle$ are still the eigenstates of the Hamiltonian and the state $|\uparrow\downarrow\uparrow\downarrow\rangle$ will evolve as in Eq. 7.23. The four-qubit entangled state $(|\uparrow\downarrow\uparrow\downarrow\rangle + i|\downarrow\uparrow\downarrow\uparrow\rangle)/\sqrt{2}$ will be generated after an evolution time of $t = \pi\hbar/(4J_\square)$. In addition, the eigenstate $|\square\rangle$ is actually the minimum version of a string-net condensate [236], and as suggested by Michael Levin and Xiao-Gang Wen [237], the string-net condensation in our vacuum is likely to be the origin of the elementary particles like electrons and photons.

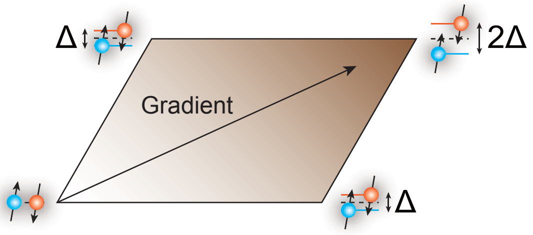

FIGURE 7.5: Suppressing superexchange with a magnetic field gradient.

7.3 Realizing an Optical Superlattice

The optical superlattice used in the experiment is created by superimposing the long lattice (1534 nm) on the short lattice (767 nm). There exists a relative phase between them as shown in Eq. 7.1 which can be used to tune the energy offsets as well as the vibrational level splittings. Fig. 7.6 gives an schematic view of the relation between the superlattice potential and the relative phase, where a symmetric double well appears at $\Theta = 0$, and an antisymmetric configuration shows up at $\Theta = \pi/4$.

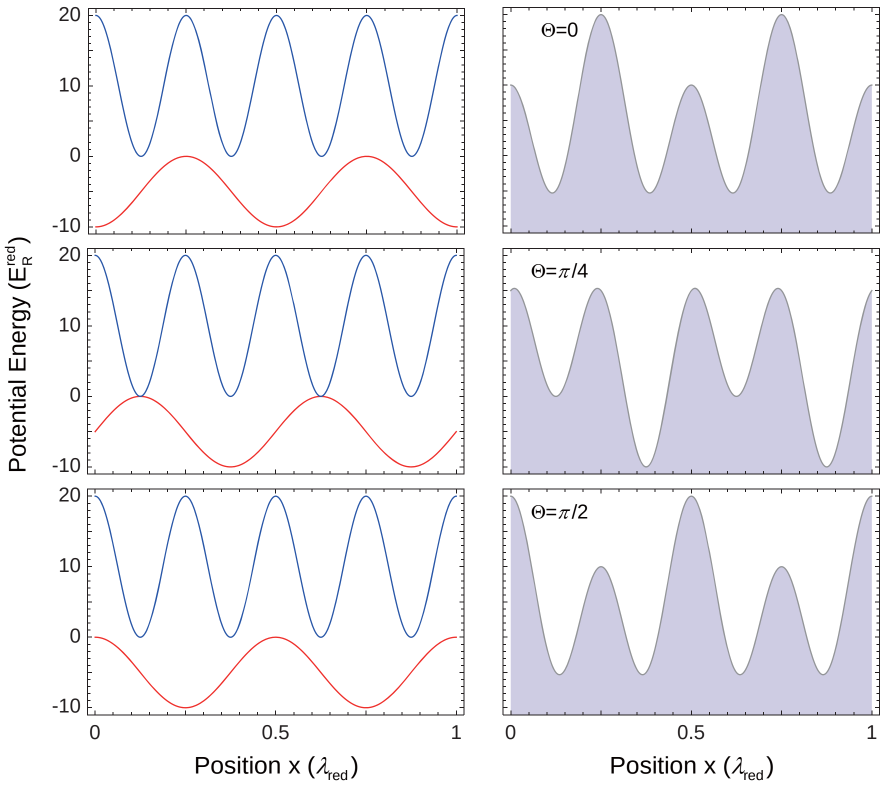

FIGURE 7.6: Superlattice potential and the relative phase. The long lattice is set to a depth of 10 $E_{\mathrm{R}}^{\mathrm{red}}$, while the short lattice is set to 20 $E_{\mathrm{R}}^{\mathrm{red}}$.

7.3.1 Relative Phase Control

In the current experiment, the standing waves are formed by taking retroreflection structures as shown in Fig. 7.7. Both lattice beams have a node at the reflection surface, resulting in a potential maximum for the long lattice while a potential minimum for the short lattice. In order to reach a symmetric double well at the atomic cloud, the wavelength of the red-detuned lattice beams are detuned from the $2\lambda_{\text{blue}}$ yielding the phase

$$\Theta(x) = \frac{k_{\text{blue}}}{2}x - k_{\text{red}}x = 2\pi\frac{\delta x}{c}, \tag{7.25}$$

where x is the distance from the reflection surface, $\delta = f_{\text{blue}}/2 - f_{\text{red}}$ is the detuning, and c is the speed of light. The fiber lasers (RFLSA-1534, from NP Photonics) that are responsible for the long lattices have a tuning range of ±500 MHz which corresponds to an effective phase tuning range $\Delta\Theta \simeq 1.9\pi$, large enough to tilt the lattice over a full span (π) after compensating the drift.

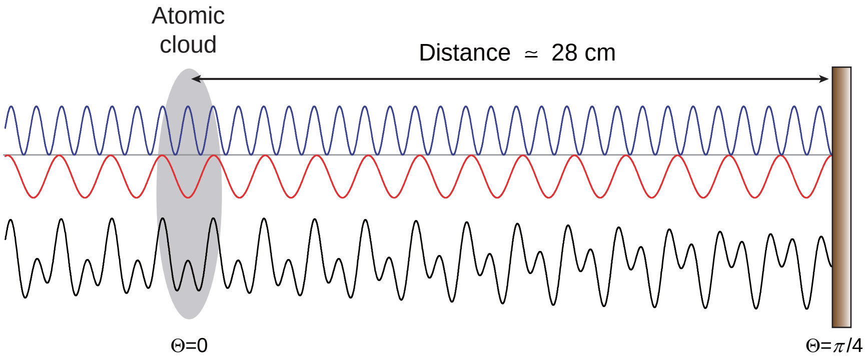

FIGURE 7.7: Phase control via the laser frequency tuning. The atomic cloud is about 28 cm away from the mirror, and a phase of $\pi/4$ is compensated by detuning the frequency of the long lattice laser.

The method to control the relative frequency is given in Fig. 7.8. For each fiber laser, a small amount of light is guided to a periodically poled Lithium Niobate (PPLN) crystal (MSHG1550-0.5-20, from Conversion), which doubles the frequency of the light. After getting filtered by a DM, the light is superimposed with the reference beam from the Matisse laser. The beat signal, $|2f_{\text{red}} - f_{\text{blue}}|$, is recorded by a fast-PD (from Hamamatsu Photonics) and is locked to a reference frequency f_{VCO} provided by a voltage-controlled oscillator (VCO, JTOS-150, from Mini-Circuits) via a digital optical phase lock loop (DP-Lock, from University of Science and Technology of China) with the relation [238]

$$|2f_{\text{red}} - f_{\text{blue}}| = 32 \times f_{\text{VCO}}. \tag{7.26}$$

The error signal from the DP-Lock is sent to the fiber laser and is used to control the cavity PIEZO. The frequency of the VCO can be tuned within the range of 75 to

150 MHz by the ADWin, and has a response of 4.86(4) MHz/V.

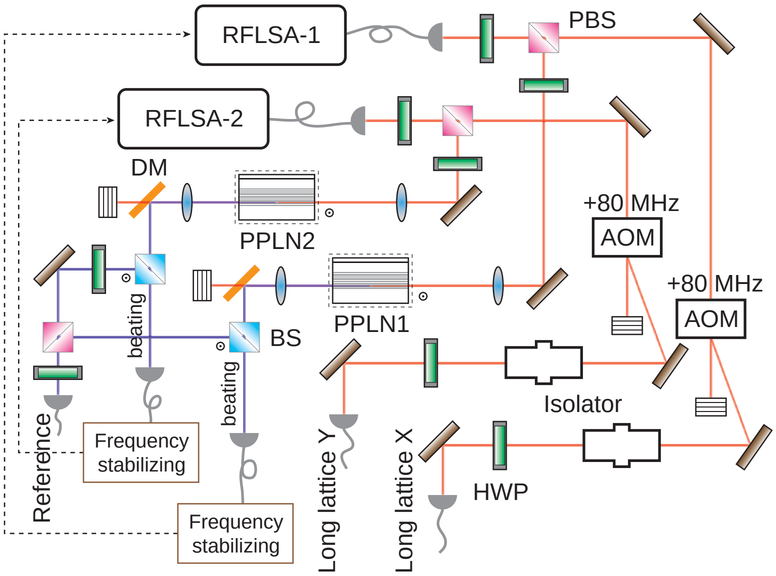

FIGURE 7.8: A schematic view of the relative phase control. Each PPLN has a size of about 20 mm, and is placed in a small oven where the temperature is controlled by a digital temperature control instrument (LFI3751, from Wavelength Electronics). Each beam is focused to a waist of about 100 μm, and the efficiency of 0.6% is reached at a temperature of 74.5°C.

During the experiment, the Matisse laser is stabilized at a wavelength $\lambda_{\text{blue}} = 767.000$ nm, and RFLSA-1 and RFLSA-2 are set to 1534.012 nm and 1533.988 nm, respectively, yielding a beat signal frequency of about 3.06 GHz corresponding to a VCO frequency 96 MHz. Since the phase change is related to the VCO frequency change through $\Delta\Theta = 32\pi\Delta f_{\text{VCO}}L/c$ with L the distance between the atomic cloud and the mirror, a change of the superlattice from a symmetric configuration to an antisymmetric configuration ($\Delta\Theta = \pi/4$) requires a change of VCO frequency of 8.37 MHz. In addition, the width of the beat signal is measured to be smaller than 600 kHz, which corresponds to a phase noise being less than $(5.6 \times 10^{-4})\pi$.

7.3.2 Suppressing Air Refraction Effect

The refractive index of air would vary in different ways for different wavelengths as the temperature, the pressure, and the humidity change, thus alter the relative phase. The refractive index can be calculated through the modified Edlén equation specified in Appx. D [239]. For a typical environment of the lab $t = 21$°C, $P = (0.98 \times 10^5)$ Pa, and relative humidity $RH = 40\%$, the refractive index is $n_{767} = 1.000260417$ for the short lattice beams and $n_{1534} = 1.000258529$ for the long lattice beams. Therefore, lattice beams of different wavelengthes will propagate through different optical path lengths accumulating different phases.

To include the refractive index effect, the Eq. 7.25 is modified as

$$\Theta(x) = \pi\frac{n_{767}x}{\lambda_{\text{blue}}} - 2\pi\frac{n_{1534}x}{\lambda_{\text{red}}}. \tag{7.27}$$

In the case of $\lambda_{\text{blue}} = 767$ nm, $\lambda_{\text{red}} = 1534$ nm, and $x = 25$ cm the transmission distance of lattice beams in the air , the phase change is depicted in Fig. 7.9 where the reference phase Θ_0 is chosen for the condition of $t = 21°\text{C}$, $P = (0.98 \times 10^5)$ Pa, and $RH = 40\%$. The environment of the lab is affected by the weather leading to the lab temperature 20 to 22°C, the pressure 94 to 102 kPa, and relative humidity 20% to 60%. Among these parameters, pressure is the dominant factor which will cause a phase fluctuation of about $\pm 0.025\pi$, a hundred times lager than the phase lock noise. When the superlattice is tuned to symmetric at $V_{\text{red}} = V_{\text{blue}} = 50\ E_{\text{R}}^{\text{red}}$, the phase change of 0.05π will result in a tilt yielding a difference between the depths of the neighboring wells of $|V_l - V_r| \simeq h \times 14.6$ kHz, and a difference between the trap frequencies $|f_l - f_r| \simeq 2.5$ kHz. This will severely affect the manipulation of the atoms. Therefore, sealed glass tubes are designed which cover the paths that lattice beams transmit. Since the volume is fixed, the ratio of the temperature (in Kelvin) to the pressure keeps constant, and the refractive index of the air within the tube is only determined by the temperature of the lab resulting in a phase-temperature relation as shown in Fig. 7.9. In this way, the phase fluctuation is highly suppressed to smaller than $(2 \times 10^{-4})\pi$, thus the total phase fluctuation including the phase lock noise is smaller than $(8 \times 10^{-4})\pi$ which corresponds to $|V_l - V_r| \lesssim h \times 200$ Hz and $|f_l - f_r| \lesssim 40$ Hz.

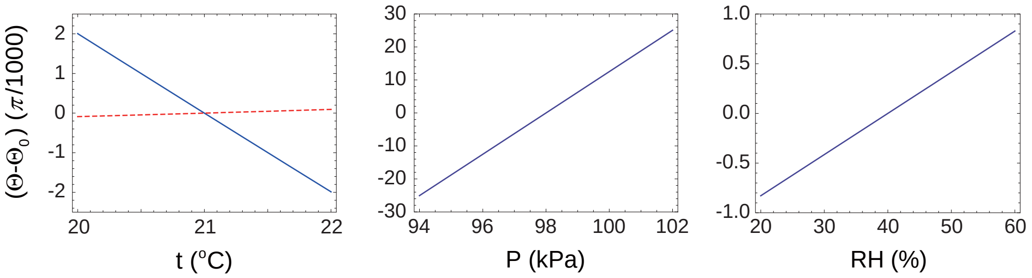

FIGURE 7.9: Superlattice phase with the environment change. The blue curves represent the phase change as the temperature, the pressure, and the relative humidity change, compared to a reference phase at $t = 21°\text{C}$, $P = (0.98 \times 10^5)$ Pa, and $RH = 40\%$. When sealed glass tubes are applied, the phase fluctuation is highly suppressed as depicted in a red dashed curve.

7.3.3 Loading Condensates into Superlattices

The experimental realization of the two-dimensional optical superlattice is shown in Fig. 7.10. The short lattice beams are provided by the Matisse laser which has a line width of 40 kHz, and the long lattice beams by the RFLSA fiber lasers with a line width smaller than 3 kHz. All the beams are stabilized by the feedback loops, and each pair of them are overlapped by a DM (from Semrock). The protected silver mirrors (PF10-03-P01, from Thorlabs) are used to reflect lattice beams which have high reflection ($R_{767} > 96\%$, $R_{1534} > 98\%$) for both wavelengths at 0° angle of incident. The incident beams of the short lattice are carefully aligned by checking the motion of the atoms, and the long lattice is then superposed with high precision. After the retro-reflected beams are aligned by optimizing the depths referred to the short lattice, the Brewster windows are used to make the beams concentric and parallel by maximizing the coherence time through the double-slit experiment.

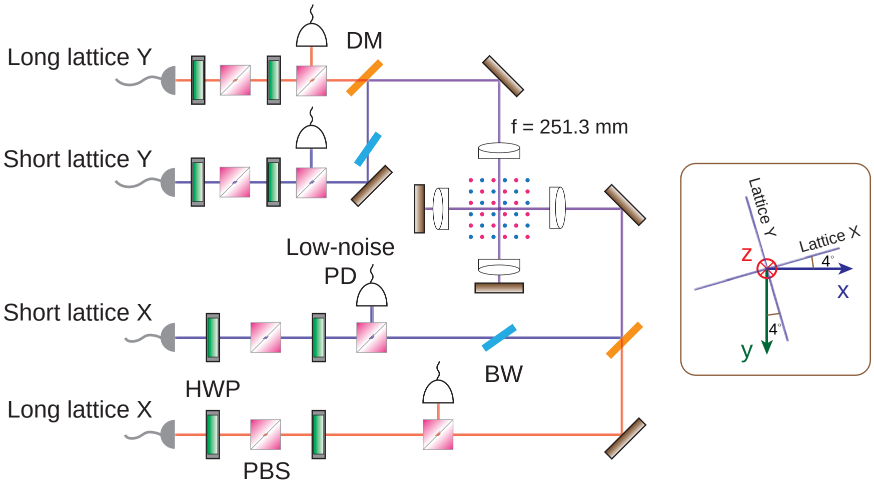

FIGURE 7.10: Realization of the optical superlattice.

The long lattice system is first evaluated by observing the superfluid to Mott insulator phase transition as shown in Fig. 7.11. In order to satisfy the adiabaticity condition, the ramp time is extended to 600 ms, and the interference peaks are totally smeared at a lattice depth of 25 E_R^{red}. It has to be emphasized that the trap depth of the long lattice has not yet been calibrated in the current experiment, and the depth values are derived from the theoretical calculations with the measured waist and intensity.

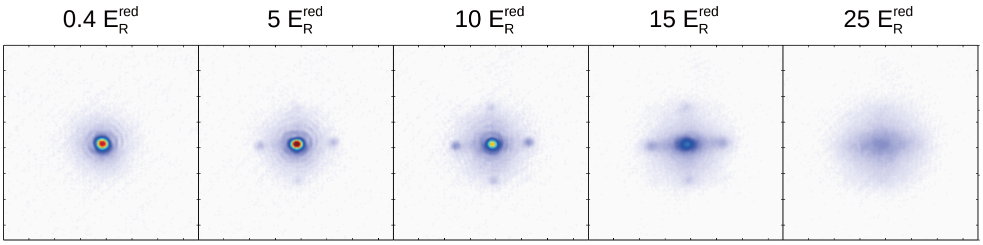

FIGURE 7.11: Observation of the quantum phase transition with long lattice.

When a condensate is loaded into a superlattice, a TOF measurement on the momentum distribution will reflect the relative phase of the superlattice. To observe the interference pattern, both lattices are adiabatically ramped up to $V_{\text{red}} = 7.5\ E_R^{\text{red}}$ and $V_{\text{blue}} = 25\ E_R^{\text{red}}$ within 80 ms, which is still in the superfluid regime. Under this condition, the matter wave still keeps a constant phase over the atomic cloud, and an interference pattern with sharp peaks will appear after a free expansion. Fig. 7.12 shows the measurements of the interference patterns at different phases. When the relative phase is zero, superlattice is an array of symmetric double wells, and the population of atoms exhibits a periodicity of $\lambda_{\text{blue}}/2$. Therefore, the distance between the interference peaks takes the value of $2\hbar k_{\text{blue}}t/m$ with t the free expansion time. However, when the relative phase is $\pi/4$, superlattice is of an antisymmetric configuration, and atoms are more likely to be filled in the deeper wells exhibiting a periodicity of $\lambda_{\text{red}}/2$. A TOF measurement thus gives an interference pattern with a distance between peaks of $2\hbar k_{\text{red}}t/m$ which is half of the one in the symmetric case. By monitoring the number of atoms in the nearest lateral peaks that are related to the long lattice scattering, the relation between the relative phase and the frequency of the VCO can be calibrated. A sine-curve fitting gives

$$\Delta\Theta = \pi\frac{\Delta f_{\text{VCO}}}{33.38(66)\ \text{MHz}} = \pi\frac{\Delta U_{\text{ADWin}}}{6.86(14)\ \text{V}}, \tag{7.28}$$

indicating that a phase change of $\pi/4$ requires a frequency change of 8.34(16) MHz which agrees well with the theoretical estimation 8.37 MHz.

7.4 Experimental Plan of the Four-Qubit Entanglement Generation

Optical superlattices are considered to be potential systems which can generate large entangled states efficiently. There are many kinds of interactions involved in such a complex system, which are related to the tunable tunneling and on-site interaction. By controlling these interactions, the system will evolve in an expected way, thus making it a versatile tool for quantum information processing such as quantum simulation and quantum computation. As a first step, I would like to present a proposal to generate four-qubit entangled states with the help of the ring-exchange process in the current two-dimensional optical superlattice.

At the very beginning, a Mott insulator state is achieved in the short lattice with the number filling for each well of 1. Then the long lattice is raised resulting in isolated plaquettes, within each of which the four atoms are in the state $|{\downarrow\downarrow\downarrow\downarrow}\rangle$. Staring from this condition, a detailed experimental plan is given in this section and the calculated experimental parameters are presented.

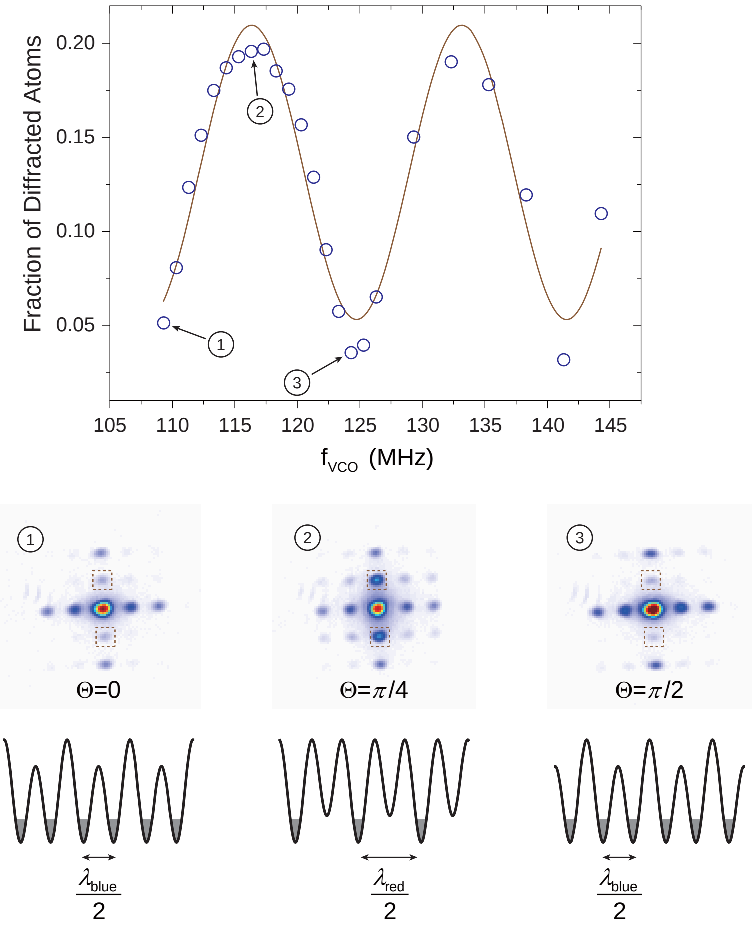

FIGURE 7.12: Interference pattern of the condensates in superlattices. The circled number ① and ③ denote the case in which atoms are populated with a periodicity of $\lambda_{\text{blue}}/2$, while the circled number ② denotes the case for $\lambda_{\text{red}}/2$. Measurements are done with direct loading of the three-dimensional condensates in order to get strong signals.

7.4.1 Removing Defects

In practice, a pure Mott insulator state is hard to achieve, however, any defect will decrease the fidelity of the expected entangled state. In order to remove the defects, a filtering sequence is suggested as shown in Fig. 7.13 [228]. After the Mott insulator state is prepared, a microwave rapid adiabatic passage is used to transfer all atoms into $|F = 1, m_F = 0\rangle$ [240]. After the pairs of wells are merged along the x-axis, the spin-changing collision is performed and atoms of each pair will be converted to $|\uparrow\rangle$ and $|\downarrow\rangle$ through the collision [241]. If there is only one atom in the merged well, the spin is kept and a resonant microwave π-pulse will then transfer it to $|F = 2, m_F = 0\rangle$. After another spin-changing collision process, the pairs of atoms are converted back to $|F = 1, m_F = 0\rangle$. The wells are then split along the x-axis while merged along the y-axis, and an application of spin-changing collision will only work on the four-particle case. Later, the defects are removed by a microwave pulse followed by a cleaning pulse.

Splitting the wells along the y-axis with existence of a gradient field thus results in state $|{\downarrow\downarrow\uparrow\uparrow}\rangle$.

It has to be emphasized that the filtering sequence is optional. The drawback of the filtering sequence is obvious that the efficiency of the spin-changing collision process and the efficiency of the resonant microwave π-pulse will limit the efficiency of the protocol. If the Mott insulator state can be achieved adiabatically with little defect, the filtering sequence is unnecessary.

7.4.2 State Preparation

To obtain the initial state $|{\uparrow\downarrow\uparrow\downarrow}\rangle$ for observing the ring-exchange, the ability to address an atom in a single well among the four is necessary. In the current plan, the addressability is done by including the vibrational states by tilting the lattice.

When the lattice is tilted, trap frequencies of the left well and the right well are different. Thus the excitation energy varies at different wells if the vibrational level is included. With the current setup, Fig. 7.14(a) shows an effective tilt when the long lattice has a depth of 60 $E_{\mathrm{R}}^{\mathrm{red}}$, the short lattice 100 $E_{\mathrm{R}}^{\mathrm{red}}$, and the relative phase $\Theta = \pi/4$. In this case, the transition frequencies are $\omega_l^{12} \simeq 2\pi \times 38.0$ kHz, $\omega_l^{23} \simeq 2\pi \times 33.4$ kHz, and $\omega_r^{12} \simeq 2\pi \times 30.4$ kHz, and the depth of the right well is $h \times 55.0$ kHz. Since the transition frequencies are different between the two wells of about $2\pi \times 7.6$ kHz, a stimulated two-photon Raman process [242] which couples $|{\downarrow}\rangle = |F = 1, m_{\mathrm{F}} = -1, n = 1\rangle$ and $|{\uparrow'}\rangle = |F = 2, m_{\mathrm{F}} = +1, n = 2\rangle$ of the left well will not affect the state in the right well. In addition, the anharmonicity of the trapping potential helps to avoid additional coupling of the higher vibrational states, and the depth of the right well is larger than the left well excitation energy which helps to avoid the excitation to the continuous spectra.

With the help of the ability to addressing atoms in certain wells, Fig. 7.14(b) shows the way to transfer the filtered state $|{\downarrow\downarrow\uparrow\uparrow}\rangle$ to the initial state of the experiment $|{\uparrow\downarrow\uparrow\downarrow}\rangle$. At the very beginning, a stimulated two-photon Raman process is applied which transfers $|{\uparrow}\rangle$ to $|{\uparrow'}\rangle$, yielding the state in a plaquette $|{\downarrow\downarrow\uparrow'\uparrow'}\rangle$. Then the lattice is tilted along the x-axis leading to different trap frequencies $\omega_1 = \omega_4 > \omega_2 = \omega_3$. Thus another Raman process can convert the states in the well 1 and well 4, resulting in a plaquette state $|{\uparrow'\downarrow\uparrow'\downarrow}\rangle$. At last, all the $|{\uparrow'}\rangle$ states are transferred to $|{\uparrow}\rangle$ in a symmetric plaquette and the initial state is obtained. If the filtering sequence is inapplicable, one has to first tilt lattice along the y-axis to address atoms in the well 3 and well 4, and then transfer them to $|{\uparrow'}\rangle$ with the vibrational states getting excited in the y-axis as shown in Fig. 7.14(c).

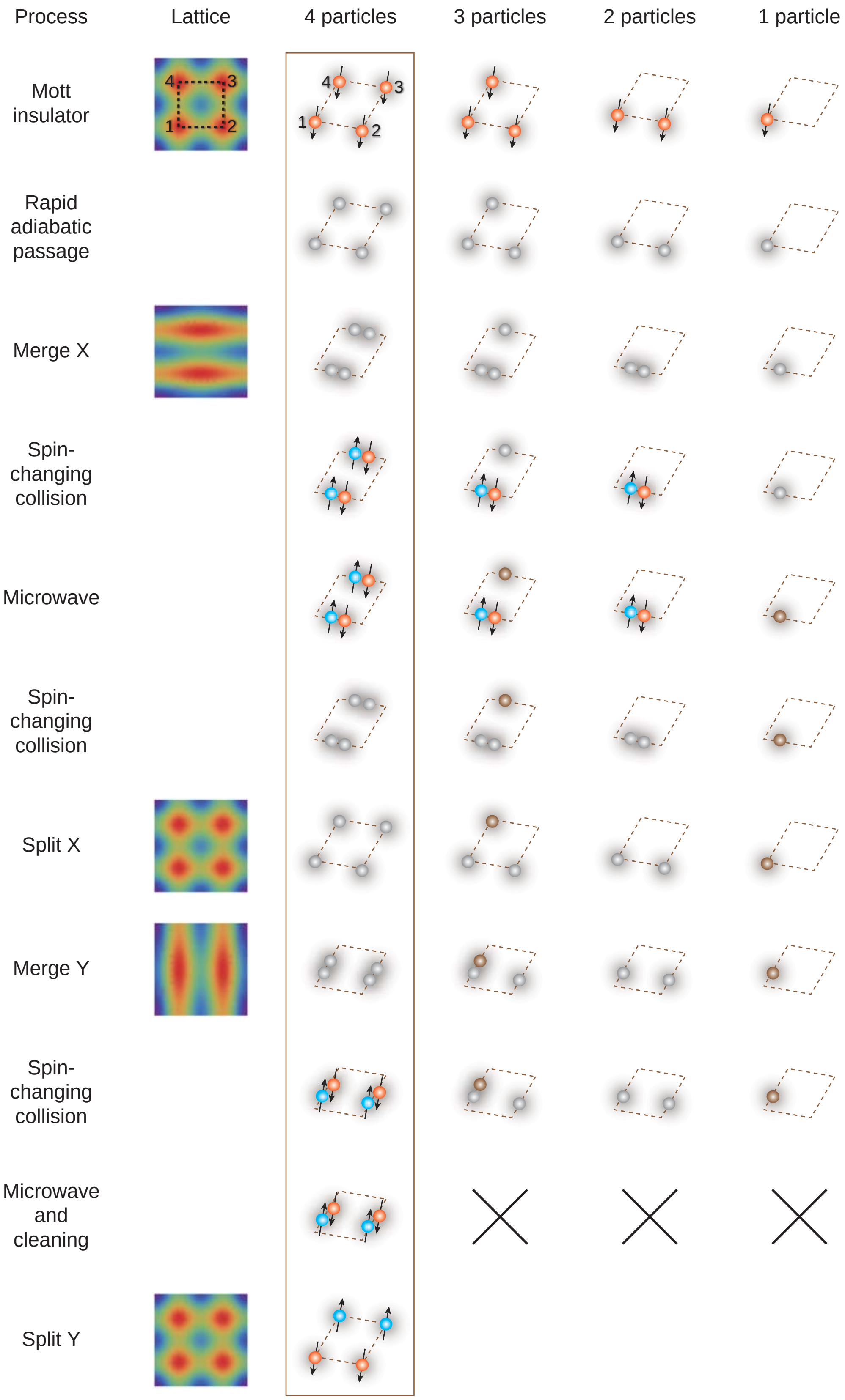
Process
Lattice
4 particles
3 particles
2 particles
1 particle
Mott insulator
4
3
1
2
Rapid adiabatic passage
Merge X
Spin-changing collision
Microwave
Spin-changing collision
Split X
Merge Y
Spin-changing collision
Microwave and cleaning
Split Y

FIGURE 7.13: Filtering sequence for plaquettes.

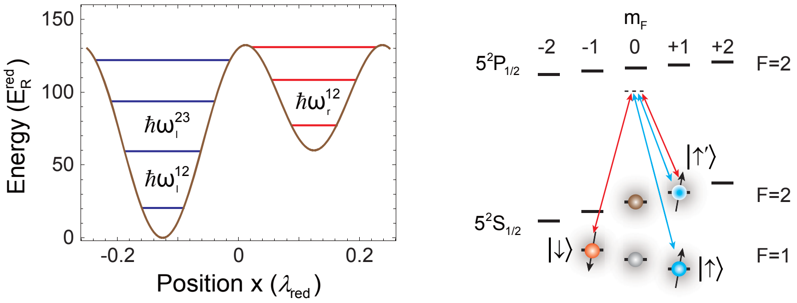

(a) Addressing single wells by vibrational states

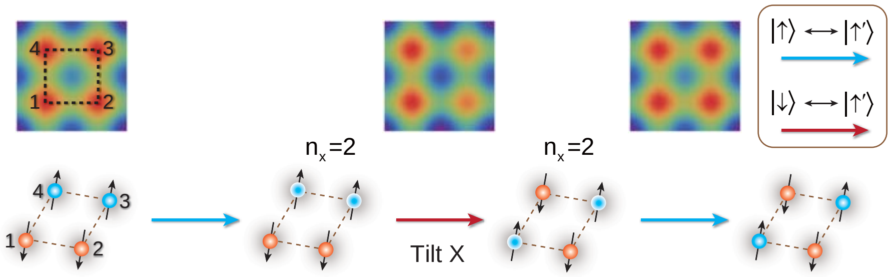

(b) State preparation process with filtering sequence

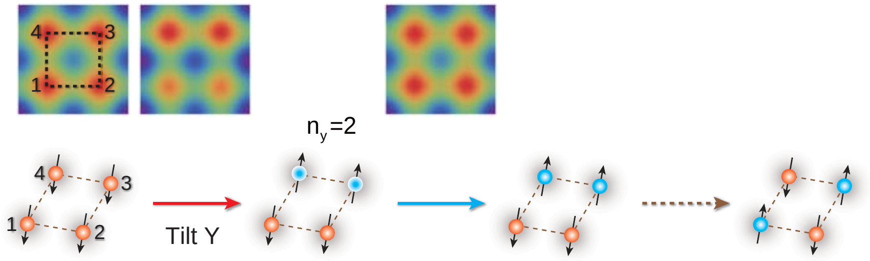

(c) State preparation process without filtering sequence

FIGURE 7.14: State preparation by tilting the lattice. (a) shows the strategy to address single wells with the aid of vibrational states. The energy levels are given in $E_{\mathrm{R}}^{\mathrm{red}}$ in the left figure where the blue levels are related to the left well and the red to the right well. The single-photon recoil energy and the frequency is related as $E_{\mathrm{R}}^{\mathrm{red}} \simeq h \times 0.98$ kHz. In the right figure, two different stimulated two-photon Raman processes are employed in the plan which are represented with different colors, and both of them are red-detuned. Note that the red one is related to a vibrational state in antisymmetric lattice configuration, while the blue one to a state in symmetric lattice configuration. The state $|\downarrow\rangle$ and $|\uparrow\rangle$ are related to the ground state of the trapping potential, while the state $|\uparrow'\rangle$ is related to the first excited state. (b) shows the process of the state preparation with the filtering sequence. (c) shows the process of the state preparation without the filtering sequence.

Later a second Raman process is applied which drives them back to $|\uparrow\rangle$ in a symmetric lattice configuration. A state $|\uparrow\downarrow\uparrow\downarrow\rangle$ will then be prepared by following the former steps.

The method of tilting the lattice relies on the excitation of the vibrational state. The matrix element for a vibrational transition is proportional to $\langle n'_x|\exp(i\Delta\mathbf{k}\cdot\mathbf{x})|n_x\rangle$ [101], with $\Delta\mathbf{k} = \mathbf{k}_1 - \mathbf{k}_2$ the difference of the wave vectors of the Raman beams. Since the motion is highly suppressed in a lattice well, pairs of the Raman beams are suggested to be aligned in a counter-propagating configuration along the expected axis in order to maximize the effective wave vector. Therefore, it is suggested to take four pairs of Raman beams of which two are aligned along the x-axis and the other two along the y-axis.

7.4.3 State Evolution

When the initial state is prepared, a magnetic field gradient along 1-3 will be applied in order to suppress the next neighbor superexchange. And the ring exchange is initiated after the short lattice is rapidly ramped down to a proper depth. The experimental parameters are designed as $V_{\text{red}} = 60\ E_{\text{R}}^{\text{red}}$, $V_{\text{blue}} = 66\ E_{\text{R}}^{\text{red}}$, and $\omega_z = 2\pi \times 10$ kHz to increase the on-site interaction. With these parameters, the tunneling matrix element is calculated to be $J \simeq h\times 248$ Hz and the on-site interaction is $U_l = U_r = U \simeq h\times 1041$ Hz, yielding $J_{\text{ex}} \simeq h\times 118$ Hz and $J_{\Box} \simeq h\times 80$ Hz. By choosing the gradient as 62 G/cm, the energy splitting Δ is twenty times of the neighboring superexchange interaction energy, and the second order tunneling is therefore highly suppressed. Under these conditions, an entangled state $(|\uparrow\downarrow\uparrow\downarrow\rangle + i|\downarrow\uparrow\downarrow\uparrow\rangle)/\sqrt{2}$ will be generated at $t = \pi\hbar/(4J_{\Box})$. It is worthy to note that the angle of the gradient field is not critical, since a geometric analysis shows that a tilt of the gradient direction will not split the energy of the two oscillating states $|\uparrow\downarrow\uparrow\downarrow\rangle$ and $|\downarrow\uparrow\downarrow\uparrow\rangle$ when restricting to the linear Zeeman effect.

7.4.4 State Detection

The ring-exchange can be observed by evaluating the spin dynamics, that is, to monitor the change of the population of the state $|\uparrow\downarrow\uparrow\downarrow\rangle$ and $|\downarrow\uparrow\downarrow\uparrow\rangle$. At a certain time of evolution, the short lattice is rapidly ramped up which freezes out the spin configuration. Then by applying the Raman pulses, the state $|\uparrow\downarrow\uparrow\downarrow\rangle$ is transferred to $|\downarrow\downarrow\downarrow\downarrow\rangle$, while the state $|\downarrow\uparrow\downarrow\uparrow\rangle$ to $|\uparrow'\uparrow'\uparrow'\uparrow'\rangle$ as shown in Fig. 7.15. In this way, a direct application of the *in situ* absorbtion imaging can record the density profile of the atoms that was in the state $|\downarrow\uparrow\downarrow\uparrow\rangle$, and the number of atoms in such a state is noted down as $N_{|\downarrow\uparrow\downarrow\uparrow\rangle}$. Later imaging is applied for a second time, however, preceded by a normal-repumper pulse which pumps the remaining atoms to $|F=2\rangle$, and the density profile of $|\uparrow\downarrow\uparrow\downarrow\rangle$ is recorded, as well as $N_{|\uparrow\downarrow\uparrow\downarrow\rangle}$. The spin dynamics can be then evaluated by a parameter

$$\mathcal{N} = \frac{N_{|\uparrow\downarrow\uparrow\downarrow\rangle} - N_{|\downarrow\uparrow\downarrow\uparrow\rangle}}{2(N_{|\uparrow\downarrow\uparrow\downarrow\rangle} + N_{|\downarrow\uparrow\downarrow\uparrow\rangle})}. \tag{7.29}$$

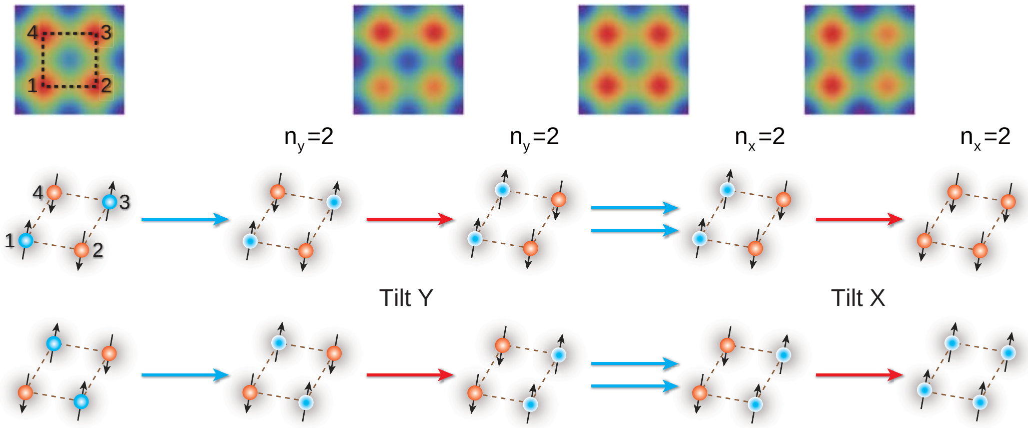

FIGURE 7.15: State detection process.

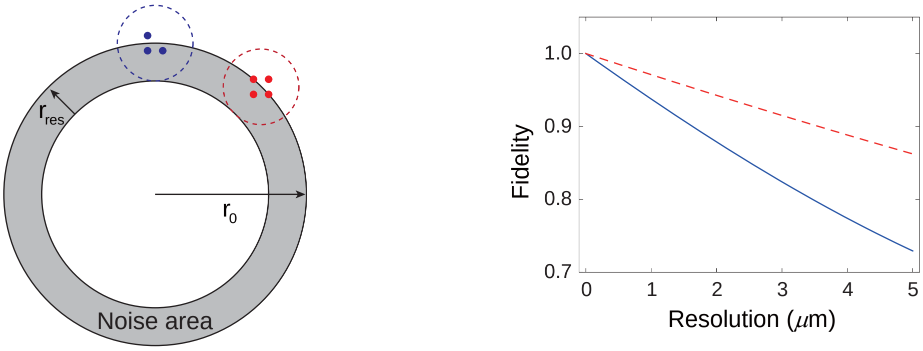

(a) Noise area illustration

(b) Fidelity versus resolution

FIGURE 7.16: Loss of fidelity due to limited optical resolution. (a) explains the assumptions of the noise. The blue circle illustrates the influence area of the noise induced by the finite temperature. The red circle illustrates the influence area of the true signal. (b) shows the fidelity as a function of the optical resolution of the imaging system. The blue curve refers to the current setup with $\omega_r = 2\pi \times 43$ Hz and a number of atoms 2700, while the red dashed line refers to $\omega_r = 2\pi \times 20$ Hz and a number of atoms 12000.

In practice, the temperature of the system is finite, which would allow the existence of the superfluid state mainly on the edge of the Mott insulator regime. In order to get rid of such kind of defects when an efficient filtering sequence is inapplicable, an imaging system of high enough resolution is required which can select an area with Mott insulator of unit filing. In the current setup with $\omega_r \simeq 2\pi \times 43$ Hz, applying the model presented in Section 6.2.2.4, one can obtain that there are maximally about 2700 atoms that can be hold in a unit filling Mott insulator at zero temperature which corresponds to a diameter of 22 μm. Assuming that the area on the edge and out of the Mott insulator regime have a 0.75 filling thus 3 atoms in a plaquette, it will provide noise while selecting the expected area ($r_0 = 22/2\ \mu$m) with an optical resolution of r_{res}. A good approximation is to restrict the resolution effect to within an annulus as depicted in Fig. 7.16(a), where half of the expected signal and the noise signal are recorded, and the noise would affect the detection of both experimental states equally. Under these assumptions, one derives

Theoretical state $\lvert\uparrow\downarrow\uparrow\downarrow\rangle$	
$N_{\lvert\uparrow\downarrow\uparrow\downarrow\rangle}$	$\pi(r_0 - r_{\text{res}})^2 + \pi[r_0^2 - (r_0 - r_{\text{res}})^2] \times (1/2 + 0.75/4)$
$N_{\lvert\downarrow\uparrow\downarrow\uparrow\rangle}$	$\pi[r_0^2 - (r_0 - r_{\text{res}})^2] \times 0.75/4$

Theoretical state $\lvert\downarrow\uparrow\downarrow\uparrow\rangle$	
$N_{\lvert\uparrow\downarrow\uparrow\downarrow\rangle}$	$\pi[r_0^2 - (r_0 - r_{\text{res}})^2] \times 0.75/4$
$N_{\lvert\downarrow\uparrow\downarrow\uparrow\rangle}$	$\pi(r_0 - r_{\text{res}})^2 + \pi[r_0^2 - (r_0 - r_{\text{res}})^2] \times (1/2 + 0.75/4)$

The visibility of the evolution is thus given by $|\mathcal{N}_{|\uparrow\downarrow\uparrow\downarrow\rangle}|+|\mathcal{N}_{|\downarrow\uparrow\downarrow\uparrow\rangle}|$. The measured visibility is then mapped to a Werner state with a density matrix $p\rho(t) + (1-p)\mathbb{1}^{\otimes 4}/4^2$ [135,243], where $\rho(t)$ is the density matrix of the state $|\psi(t)\rangle$ in Eq. 7.23. The white noise of the state will not evolve in time, thus contribute to both situations, and the visibility is mapped to the probability of the state p. At $t = \pi\hbar/(4J_{\square})$ where the entangled state is expected, the fidelity of such a Werner state is given by $F = p + (1-p)/4^2$. Fig. 7.16(b) shows the relation between the fidelity and the resolution, and a resolution of 1.6 μm is necessary to ensure that the fidelity is larger than 0.9. If the trap frequency can be decreased to about 20 Hz by using a single-coil magnetic quadrupole field to levitate the atoms instead, the requirement for resolution can be relaxed to 3.5 μm.

7.4.5 In Situ Imaging System Design

The *in situ* imaging system is designed as shown in Fig. 7.17(a). The atomic cloud is about 1.92 mm away from the glass cell, and a compensator (from Lens-Optics) is used to compensate the wavefront distortion imprinted by the 8 mm glass cell. The objective is an aspheric lens (from Asphericon) which has a numerical aperture of 0.54 and an effective focal length of 20 mm. The eyepiece is a plano-convex lens (from Melles Griot) with a focal length of 500 mm. A simulation by ZEMAX gives the effective numerical aperture of the system 0.56, the amplification factor 28.9, and the resolution of 0.85 μm determined by the Rayleigh criterion.

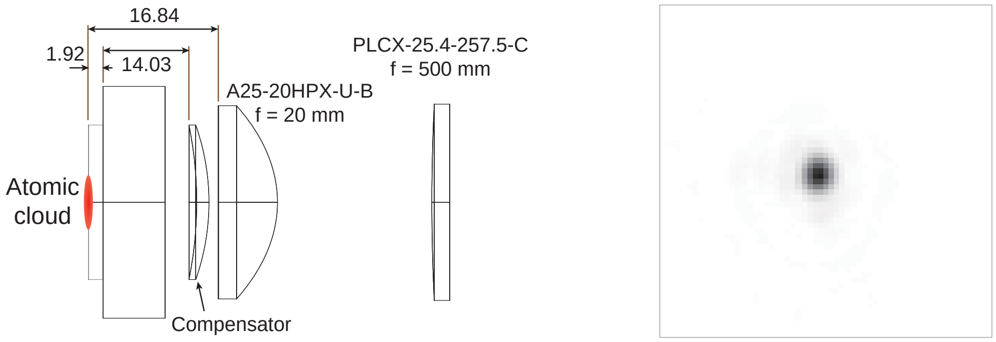

(a) Imaging system (b) Airy disk of a point source

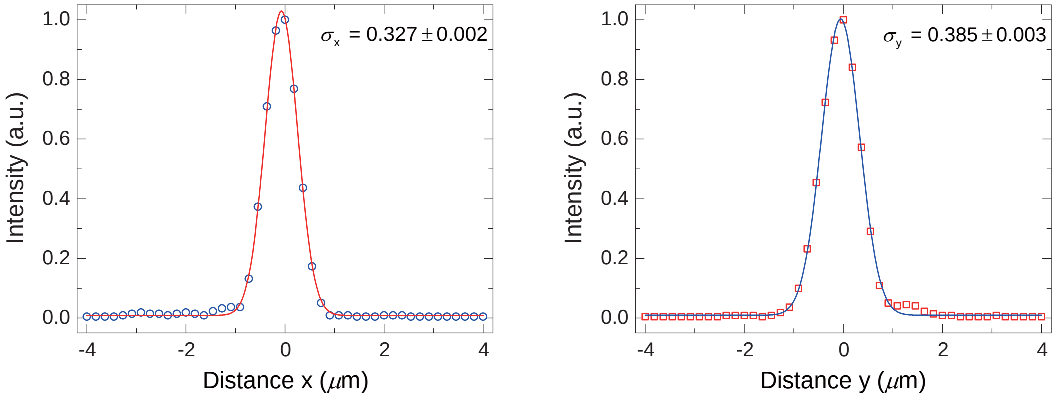

(c) Intensity distribution along x (d) Intensity distribution along y

FIGURE 7.17: High-resolution imaging system. (a) shows the configuration of the imaging system where the positions of the lenses are optimized through ZEMAX. (b) shows a typical image of a point source. (c) shows the intensity distribution along the x-axis. A Gaussian fit yields the standard deviation of (0.327 ± 0.002) μm. (d) shows the intensity distribution along the y-axis. A Gaussian fit yields the standard deviation of (0.385 ± 0.003) μm.

The calibration of the imaging system relies on the point spread function. In the experiment, a pinhole with a diameter of 600 nm is used to generate such a point source, and the intensity distribution of the diffraction pattern takes the form of $I(r) = I_0[2J_1(r)/r]^2$. To simplify the fitting, a Gaussian profile is used which predicts the resolution of the system as three times of the standard deviation by the Rayleigh criterion. A typical image of the Airy disk is shown in Fig. 7.17(b), and the intensity distributions along the x- and y-axis are shown in Fig. 7.17(c) and Fig. 7.17(d), respectively. The optical resolution of the system is then estimated by the Gaussian fit as (0.98 ± 0.01) μm for the x direction and (1.16 ± 0.01) μm for the y direction. Moreover, the small amplitude of the first ring indicates a negligible spherical aberration.

After the setup is installed, the calibration is planned by using the same objective to focus a normal-repumper beam to select a small amount of atoms which simulates the quasi-point source. The imaging imperfections can be analyzed by constructing the imaging response function and comparing it with the theoretical result based on the Fraunhofer diffraction and aberration theory [185].

7.4.6 Discussion

The plan of four-qubit entanglement generation relies on the efficiency of the two-photon Raman process which has to be performed for eight times. An alternative idea is to use a spin-dependent short lattice to assist [244–246], which can make the coupling energies between $|\uparrow\rangle$ and $|\downarrow\rangle$ different at different wells. When two counter-propagating beams are linearly polarized, however, enclosing an angle of θ, the standing wave that is formed can be considered as a superposition of two standing wave fields, σ^+ and σ^-, which are shifted with respect to each other according to the relation $\Delta x = \theta/\pi \times \lambda/2$ [244]. Since the AC Stark shift is spin-dependent [191], different Zeeman substates will undergo different potentials in which the spin-dependent parts can be understood as potentials generated by pseudo-magnetic fields [247]. After combined with a long lattice, the coupling energies at different wells are thus split as shown in Fig. 7.18. In this way, the spins at different wells can be manipulated separately, and a two-dimensional spin-dependent superlattice can generate the initial state for the ring-exchange by simply performing spin flips on well 1 and well 3.

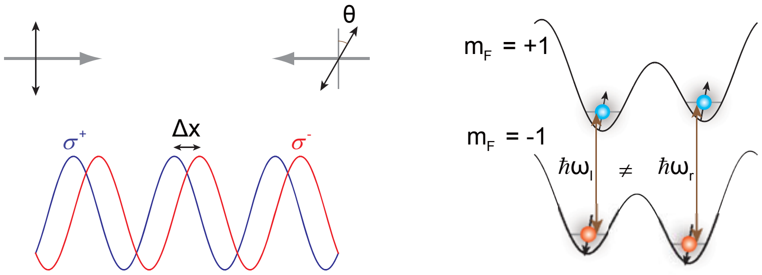

FIGURE 7.18: Spin-dependent optical lattice. The spin-dependent lattice potential will drive a spin at different wells to undergo different energy shifts as well as small position shifts. In this way, the coupling energies between $|\downarrow\rangle$ and $|\uparrow\rangle$ are different between the left well and the right well. Thus the spins at different wells can be addressed separately.

Another possible improvement is to replace the current magnetic quadrupole trap with a single-coil configuration for levitation. In the current setup, magnetic trap is used to oppose gravity by introducing a levitation force while reaching a Mott insulator state. However, it will also provide a trapping potential along the horizontal plane, which limits the lowest attainable trap frequency along the x-axis to about 30 Hz. A single-coil magnetic quadrupole field could overcome this problem which has a large ratio of the axial gradient to the radial gradient. With the help of a controllable switch, the single-coil configuration will be activated when the magnetic trapping is unnecessary. In this way, the effective area of the Mott insulator with unit filling can be largely extended which will relax the requirement of the resolution of the imaging system.

Conclusion and Outlook

Quantum information science is going to change the world in every aspect. Many researchers are contributing to it by using various means. During my doctoral studies, I have worked on generating entangled states by manipulating neutral atoms, and, with the help of them, developing scalable quantum networks and quantum computers.

The photon-matter entanglement source is one of the candidates which has a built-in memory function. It can work as a basic module and a complex system can be constructed by integrating many of the modules. In addition, owing to the collective enhancement, the atomic state can be efficiently converted into a flying photonic state, allowing the extension of the entanglement to a large distance. By employing two of them, a heralded quantum teleportation is presented where an atomic spin-wave is teleported to another atomic ensemble. And the success probability of the teleportation is enhanced by 4 orders of magnitude with respect to the previous experiment with ions. In a later study, an efficient entanglement swapping is demonstrated with an enhancement factor of 257, benefiting from the quantum feedback technique. Both demonstrations have significant meaning to long-distance quantum communication, thus scalable quantum networks. Moreover, by upgrading the system to a hyperentanglement source, active feedforward one-way quantum computing is realized with the built-in quantum memory. The demonstrations of the single-qubit rotations, the C-Phase gate, and Grover's searching algorithm reveal the potential of the photon-matter source to be a candidate for quantum computing. Although large-scale entanglement can be generated by using many of the photon-matter sources in principle, the preparation efficiency as well as the complexity might fail an efficient integration. In this respect, optical lattice turns out to be more competent, which can trap an array of atoms that are entangled through interactions. In the current presentation, a two-dimensional optical superlattice is developed and calibrated. With the help of a high-resolution imaging system and the addressability, four-qubit entanglement is going to be generated through the ring-exchange interaction.

Further steps can be done to improve the performance of the photon-matter source, such as extending the storage lifetime by using an optical lattice to freeze the motion of atoms [93], and enhancing the retrieval efficiency by employing a ring cavity to support both signal and idler fields through the Purcell effect [152]. The long storage lifetime enables a deterministic spin-wave preparation thus a deterministic quantum teleportation, and the high retrieval efficiency benefits the connection between the atomic-ensemble nodes. With these improvements, large-scale quantum teleportation with multi-atomic-ensemble nodes is made possible, therefore a global quantum network is foreseeable. Furthermore, the delayed choice entanglement swapping allows the possibility to implement a "quantum key bank". It saves and stores spin-wave states where the write-out photons have been measured by the customers. The secure keys between customers are then generated through joint BSMs.

As for the quantum computation based on quantum memories, larger cluster states can be generated by either using more degrees of freedom, or connecting multiple atomic-ensemble nodes through joint measurements. The former idea has the limitation that the measurement of one qubit might affect the others which are encoded in the same physical entity, and the latter idea has the limitation of the low detection efficiency of a multi-photon coincidence. A compromise has to be made and a proper scheme is under investigation.

Two-dimensional optical superlattices are more competent to generate large-scale entanglement. By varying the barrier of the double-well potential, cold collisions can be switched on and off which can coherently change the spins while conserving the total magnetization. Extending the idea to the barriers between the double wells, a two-dimensional Bell-encoded-like cluster state can be generated which can serve as a resource for measurement-based quantum computation [156]. In another reference [157], the authors proposed to generate a two-dimensional cluster state with each logical qubit being encoded in a plaquette, so that the decoherence induced by uniform magnetic field fluctuations can be inhibited. The single-qubit rotations are realized with the help of superexchange couplings, and the C-Phase gates can be achieved by using vibrational levels and the geometric phases, applying superexchange interactions between neighboring plaquettes, or performing a series of operators related to specific operations. In a later study, a new method is proposed, where a ring-exchange interaction is exploited to implement the C-Phase gate [248]. Besides of the mentioned methods, if extra degrees of freedom are employed, the cluster state is expected to be generated with high-fidelity through the perturbative spin-spin interactions [249].

To implement a quantum computer, studies on addressing and measuring single atoms are of high importance. The current system only allows one to address a group of single atoms each in a specific well among the four within a plaquette. To extend the addressability, a good choice is to employ a spatial light modulator. It can change the intensity distribution of a beam which is then focused to the lattice. With the help of this tightly focused beam of a special pattern, any single well or any group of wells can be addressed and then manipulated by a microwave field [250]. By tuning the phase of the microwave pulse, Pauli operations on the spins can be realized [251], and a quantum state tomography is made possible. In this way, complex quantum computing might be achieved. In addition, even without the addressability, the two-dimensional optical superlattice provides a good platform to simulate condensed matter Hamiltonians [252, 253].

Appendix A

Hyperfine Structure for Rubidium 87

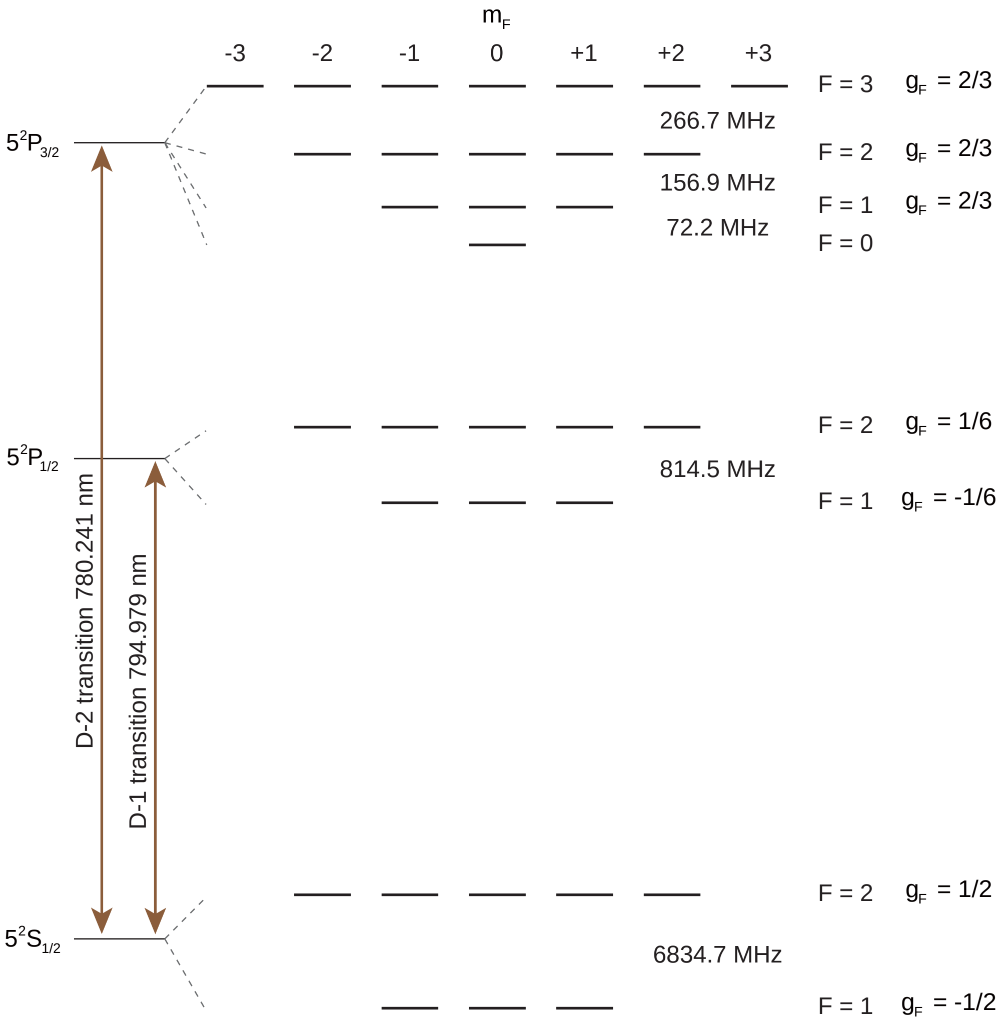
m_F
-3
-2
-1
0
+1
+2
+3
5²P3/2
5²P1/2
5²S1/2
F = 3
g_F = 2/3
266.7 MHz
F = 2
g_F = 2/3
156.9 MHz
F = 1
g_F = 2/3
72.2 MHz
F = 0
F = 2
g_F = 1/6
814.5 MHz
F = 1
g_F = -1/6
F = 2
g_F = 1/2
6834.7 MHz
F = 1
g_F = -1/2
D-2 transition 780.241 nm
D-1 transition 794.979 nm

Figure A.1: Rubidium 87 hyperfine structure [3].

Appendix B

Characterization of Quantum States and Quantum Processes

Characterization of a quantum state and a quantum process is of great importance to quantum information science. One of the most efficient way to characterize a quantum state is to reconstruct the density matrix of the state through quantum state tomography. In a similar way, quantum process tomography will reconstruct a matrix that completely describes the process. Once the matrix is known, one could deduce any physical property of the state or the process.

B.1 Characterization of a Quantum State

A quantum state can be represented by a density matrix ρ. For example, the density matrix of a single-qubit state can be expressed as

$$\rho = \sum_j P_j |\psi_j\rangle\langle\psi_j| = \begin{array}{c} \\ |0\rangle \\ |1\rangle \end{array} \begin{array}{c} \begin{array}{cc} \langle 0| & \langle 1| \end{array} \\ \begin{pmatrix} A & Ce^{i\phi} \\ Ce^{-i\phi} & B, \end{pmatrix} \end{array} \tag{B.1}$$

where the probabilistic weighting P_j satisfies $\sum_j P_j = 1$, and the real, non-negative number A, B and C satisfy $A + B = 1$ and $C \leq \sqrt{AB}$ [5]. Furthermore, any density matrix can be expanded by a set of linearly independent matrices. Especially when Pauli matrices are applied to form the basis states, a n-qubit state can be represented as

$$\rho = \frac{1}{2^n} \sum_{j_1, j_2, \ldots, j_n = 0}^{3} S_{j_1, j_2, \ldots, j_n} \hat{\sigma}_{j_1} \otimes \hat{\sigma}_{j_2} \otimes \cdots \otimes \hat{\sigma}_{j_n}, \tag{B.2}$$

where the Pauli matrices $\hat{\sigma}_j$ are

$$\hat{\sigma}_0 \equiv \begin{pmatrix} 1 & 0 \\ 0 & 1 \end{pmatrix}, \hat{\sigma}_1 \equiv \begin{pmatrix} 0 & 1 \\ 1 & 0 \end{pmatrix}, \hat{\sigma}_2 \equiv \begin{pmatrix} 0 & -i \\ i & 0 \end{pmatrix}, \hat{\sigma}_3 \equiv \begin{pmatrix} 1 & 0 \\ 0 & -1 \end{pmatrix}, \tag{B.3}$$

and the $S_{j_1,j_2,\ldots,j_n}$ values are given by

$$S_{j_1,j_2,\ldots,j_n} \equiv \mathrm{trace}(\hat{\sigma}_{j_1} \otimes \hat{\sigma}_{j_2} \otimes \cdots \otimes \hat{\sigma}_{j_n} \cdot \rho). \tag{B.4}$$

Since the Pauli matrices can be expressed further as

$$\begin{aligned} \hat{\sigma}_0 =& |0\rangle\langle 0| + |1\rangle\langle 1| \\ \hat{\sigma}_1 =& |+\rangle\langle +| - |-\rangle\langle -| \\ \hat{\sigma}_2 =& |R\rangle\langle R| - |L\rangle\langle L| \\ \hat{\sigma}_3 =& |0\rangle\langle 0| - |1\rangle\langle 1|, \end{aligned} \tag{B.5}$$

with $|+/-\rangle = (|0\rangle \pm |1\rangle)/\sqrt{2}$ and $|R/L\rangle = (|0\rangle \pm i|1\rangle)/\sqrt{2}$, the $S_{j_1,j_2,\ldots,j_n}$ values are just linear combinations of the probabilities of specific measurement basis. In the single-qubit case, one obtains

$$\begin{aligned} S_0 =& P_{|0\rangle} + P_{|1\rangle} \\ S_1 =& P_{|+\rangle} - P_{|-\rangle} \\ S_2 =& P_{|R\rangle} - P_{|L\rangle} \\ S_3 =& P_{|0\rangle} - P_{|1\rangle}. \end{aligned} \tag{B.6}$$

Thus the density matrix can be reconstructed after the S_j values are calculated.

However, a typical characterization of a multi-qubit state requires a large number of measured events for each measurement basis to suppress the statistical error, and there are many measurement bases have to be chosen to complete the tomography. Therefore, the instability of the system would most likely lead to a non-physical result. In practice, the problem of reconstructing illegal density matrices is resolved by applying the maximum likelihood technique, which will search for a legitimate state that is most likely to have returned the measured counts [115].

A legitimate state has to meet the following three conditions: (a) the density matrix is non-negative definite; (b) the density matrix is Hermitian; (c) the trace of the density matrix is one. The first condition is due to the fact that the probability can not be negative for measurement in any state. The latter two conditions are required naturally from the definition of density matrix. It can be demonstrated that a good expression of a physical density matrix is

$$\rho_{\text{phy}} = \frac{T^{\dagger}T}{\text{trace}(T^{\dagger}T)}, \tag{B.7}$$

where the matrix T has a tri-diagonal form

$$T = \begin{pmatrix} t_1 & 0 & \cdots & 0 \\ t_{2^n+1} + it_{2^n+2} & t_2 & \cdots & 0 \\ \vdots & \vdots & \vdots & \vdots \\ t_{4^n-1} + it_{4^n} & t_{4^n-3} + it_{4^n-2} & \cdots & t_{2^n} \end{pmatrix}, \tag{B.8}$$

with t_j real numbers and n number of qubits. When a Poisson counting statistics is assumed with large total number of events (Gaussian distribution), the total probability of the state yielding the measured counts is given by

$$P(n_{j,j'}) = \frac{1}{\text{norm}} \prod_{j,j'} \exp\left[-\frac{(\bar{n}_{j,j'} - n_{j,j'})^2}{2\bar{n}_{j,j'}} \right], \tag{B.9}$$

where "norm" is the normalization constant, $\bar{n}_{j,j'}$ represents expected counts predicted by measuring the physical density matrix ρ_{phy} on the j'-th state of the j-th measurement setting and can be understood as the mean value, $n_{j,j'}$ represents the experimental results of the corresponding measurement, and the standard deviation is given approximately by $\sqrt{\bar{n}_{j,j'}}$. Note that for each measurement setting j, all the orthogonal states, which form a set of basis, have to be measured in order to get the total number of measurement $n_j = \sum_{j'} n_{j,j'}$. Thus, an ideal density matrix can be obtained by maximizing the probability function. In practice, one would like to take the logarithm of the function yielding a likelihood function

$$\begin{aligned} \mathcal{L}(t_k) &= \sum_{j,j'} \frac{(\bar{n}_{j,j'} - n_{j,j'})^2}{2\bar{n}_{j,j'}} \\ &= \sum_{j,j'} n_j \frac{(\langle \psi_{j,j'} | \rho_{\text{phy}} | \psi_{j,j'} \rangle - p_{j,j'})^2}{2\langle \psi_{j,j'} | \rho_{\text{phy}} | \psi_{j,j'} \rangle}, \end{aligned} \tag{B.10}$$

with $p_{j,j'}$ the experimental probability of measuring $|\psi_{j,j'}\rangle$ state. In this way, after a minimum is found, the density matrix can be reconstructed from the values of t_k.

A typical way to evaluate the state is to measure the overlap between the experimental state and the expected state, which is defined as fidelity [116, 254]

$$F(\rho_1, \rho_2) \equiv \left[\text{trace}(\sqrt{\rho_1}\rho_2\sqrt{\rho_1})^{1/2} \right]^2. \tag{B.11}$$

With the definition, fidelity satisfies the following axioms [116]:

F1 $0 \leq F(\rho_1, \rho_2) \leq 1$ and $F(\rho_1, \rho_2) = 1$ if and only if $\rho_1 = \rho_2$;

F2 $F(\rho_1, \rho_2) = F(\rho_2, \rho_1)$;

F3 If any of ρ_1 or ρ_2 is pure then $F(\rho_1, \rho_2) = \text{trace}(\rho_1\rho_2)$;

F4 $F(\rho_1, \rho_2)$ is invariant under unitary transformations on the state space.

When the density matrix is a Hermitian 2 × 2 matrix (in a two-dimensional complex vector space), the fidelity takes a simple form [255]

$$F(\rho_1, \rho_2) = \text{trace}(\rho_1\rho_2) + 2\sqrt{\text{det}(\rho_1)\text{det}(\rho_2)}, \tag{B.12}$$

where "det" represents determinant. The fidelity of a state can be derived after the density matrix is reconstructed, and the error of the fidelity is given by "Monte Carlo" analysis. To derive the error of the quantity, Poisson distribution is generally assumed to count statistics throughout the thesis, and a group of numerical data are generated by taking experimental result as mean value as well as variance. A set of density matrices are then calculated by feeding these simulated data to the maximum likelihood reconstructing process, and are used to derive standard error on any quantity, fidelity in this case. In this thesis, errors are estimated from 100 simulations for each, so that the difference between the quantity derived from the reconstructed matrix and the one which is the mean value of the simulated results is much smaller than the statistical error.

B.2 Characterization of a Quantum Process

Quantum process tomography is a way to characterize the dynamics of a quantum system [5, 118]. Any quantum process acting on an arbitrary input state ρ can be expressed as an operator-sum [118]

$$\mathcal{E}(\rho) = \sum_j \hat{E}_j \rho \hat{E}_j^\dagger, \tag{B.13}$$

where $\hat{E}_j$ are operators acting on ρ which completely describe any possible unitary operation, projection and environmental effect. To determine $\hat{E}_j$, it is convenient to expand them in a fixed set of operators $\hat{A}_m$ that form a basis, $\hat{E}_j = \sum_m a_{jm}\hat{A}_m$ with a_{jm} complex numbers. Then the quantum process is written as

$$\mathcal{E}(\rho) = \sum_{m,n=0}^{d^2-1} \chi_{mn} \hat{A}_m \rho \hat{A}_n^\dagger, \tag{B.14}$$

where $\chi_{mn} \equiv \sum_j a_{jm}a^*_{jn}$ are the entries of a non-negative definite Hermitian matrix χ by definition, which completely and uniquely describes the process, and $d = 2^n$ implies a $d \times d$ density matrix with n the number of qubits. In practice, additional constraint $\sum_{m,n} \chi_{mn}\hat{A}^\dagger_n\hat{A}_m = \mathbb{1}$ must be satisfied due to the fact that the output state has to be Hermitian with trace one.

To reconstruct matrix χ, one can first choose a linearly independent basis $\hat{\rho}_j$, $\{|0\rangle\langle 0|, |1\rangle\langle 1|, |+\rangle\langle +|, |R\rangle\langle R|\}$ for the single-qubit case, for example. Then one will get [118]

$$\mathcal{E}(\hat{\rho}_j) = \sum_k \lambda_{jk}\hat{\rho}_k, \tag{B.15}$$

and

$$\hat{A}_m\hat{\rho}_j\hat{A}^\dagger_n = \sum_k \beta^{mn}_{jk}\hat{\rho}_k. \tag{B.16}$$

Since $\mathcal{E}(\hat{\rho}_j)$ will be known from state tomography, both λ_{jk} and β^{mn}_{jk} can be calculated through linear algebra. Combining the last two expressions and Eq. B.14, one has

$$\sum_{m,n} \beta^{mn}_{jk}\chi_{mn} = \lambda_{jk}. \tag{B.17}$$

To further solve the relation, one could think of χ and λ as vectors χ_{vec} and λ_{vec}, respectively, while β as a $d^4 \times d^4$ matrix β_{mat} with mn/jk being the index of the column/row. Thus the matrix of a process χ can be derived by solving $\chi_{\text{vec}} = \beta^{-1}_{\text{mat}}\lambda_{\text{vec}}$ where β^{-1}_{mat} is the inverse of β_{mat}.

However, this standard quantum process tomography reconstruction technique would result in an illegal process matrix due to the instability of the system. In practice, one will follow a maximum likelihood way to search for a non-negative definite Hermitian matrix χ_{phy} that is the closest fit in a least-squares sense with additional constraints to keep trace-preserving [120]. A non-negative definite Hermitian matrix can be expressed as

$$\chi_{\text{phy}} = T^\dagger T, \tag{B.18}$$

with T having the form

$$T = \begin{pmatrix} t_1 & 0 & \cdots & 0 \\ t_{2^d+1} + it_{2^d+2} & t_2 & \cdots & 0 \\ \vdots & \vdots & \vdots & \vdots \\ t_{4^d-1} + it_{4^d} & t_{4^d-3} + it_{4^d-2} & \cdots & t_{2^d} \end{pmatrix}. \tag{B.19}$$

Note that there is no explicit requirement that the trace of χ_{phy} is one. A likelihood function used to search for the parameters t_j is given by

$$\begin{aligned}\mathcal{L}_{\chi}(t_j) =& \sum_{a,b}\left[p_{a,b} - \sum_{m,n=0}^{d^2-1}(\chi_{\text{phy},mn}\langle\psi_b|\hat{A}_m\rho_a\hat{A}_n^{\dagger}|\psi_b\rangle)\right]^2 \\ &+ \lambda_{\text{para}}\sum_{k=0}^{d^2-1}\left[\sum_{m,n=0}^{d^2-1}\Big(\chi_{\text{phy},mn}\text{trace}(\hat{A}_n^{\dagger}\hat{A}_m\hat{A}_k)\Big) - \text{trace}(\hat{A}_k)\right], \end{aligned} \tag{B.20}$$

where $p_{a,b}$ represents the measured probability of the a-th input state on the b-th analyzer setting, $|\psi_b\rangle$ is the b-th measurement analyzer setting, ρ_a is the reconstructed density matrix of the a-th input state, and λ_{para} is a weighting factor. The first term represents a least-squares fit, while the second term enforces further constraints. In practice, $\hat{A}_m$ are normally chosen to be Pauli matrices for single-qubit operations, or a set of basis expressed by Kronecker products of Pauli matrices for multi-qubit operations. And λ_{para} is typically set to 0.1 to 1 in this thesis to stress trace-preserving property. A process fidelity is defined as

$$F_{\text{proc}} = \text{trace}(\chi^{\text{ideal}}\chi). \tag{B.21}$$

And the statistical error is given by Monte Carlo simulation.

Appendix C

Laser Beam Intensity Stabilization

The intensities of the laser beams of main dipole, cross dipole, pancake, and all of the four lattice beams are controlled and stabilized by feedback loops as illustrated in Fig. C.1. RF signal, generated by a voltage-controlled oscillator (VCO) (ZOS-100+ or ZOS-150+, from Mini-Circuits), is attenuated by a controllable attenuator (ZAS-3+) and by a fixed attenuator typically 3 to 6 dB. Later a RF switch (ZASWA-2-50DR+) is used to isolate the signal when necessary which is controlled by the FPGA. The signal is then applied to the AOM after being amplified (ZHL-03-5WF or ZHL-3A). The maximum power of the RF signal is carefully adjusted by limiting the attenuation so that the AOM can work in its full range safely. The laser intensity is tuned by varying the strength of the RF and a portion of the laser beam is measured by a low-noise photodiode to give the feedback to a proportional-integral controller (PI controller, modified A368N from Electronic Workshop, University of Heidelberg). The PI controller will then compare the feedback signal with the setting value provided by the ADWin and try to drive the laser intensity to the set point by tuning the attenuation of the RF signal.

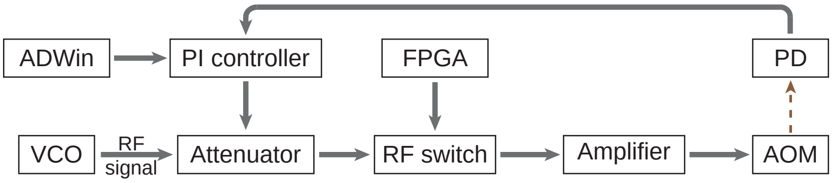

FIGURE C.1: A schematic view of the feedback loop.

The feedback loop is characterized by measuring the frequency response. The results are presented as Bode diagrams in Fig. C.2(a) and Fig. C.2(b), where the blue cross relates to a reference signal with a form of $[4 + 0.2\ \sin(f)]$ V simulating a typical modification of the curve in the experiment, and the red diagonal cross relates to a reference signal $[3 + 3\ \sin(f)]$ V simulating a full range modulation. It can be seen that both modulation signals yield similar frequency response, and the intensity of the laser can

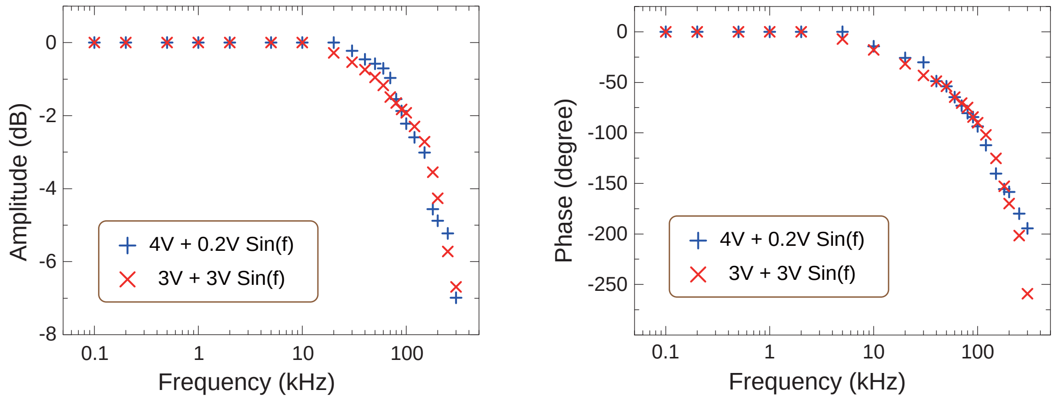

(a) Bode amplitude plot (b) Bode phase plot

FIGURE C.2: Bode diagrams of the feedback loop. (a) shows the magnitude of the frequency response gain. Since the measured value of the photodiode output is proportional to the power of the laser, dB = $10 \log_{10} x$ is employed for the plot. (b) shows the frequency response phase shift.

follow the programmed value up to a frequency of about 100 kHz at which the phase is delayed by 90°. Moreover, the amplitude of the signal will only drop below half when the driven frequency is larger than 150 kHz. In addition, the intensity noise of the laser is highly suppressed as shown in Fig. C.3(a) and Fig. C.3(b), and the dynamic range of the system is measured to be about 36 dB.

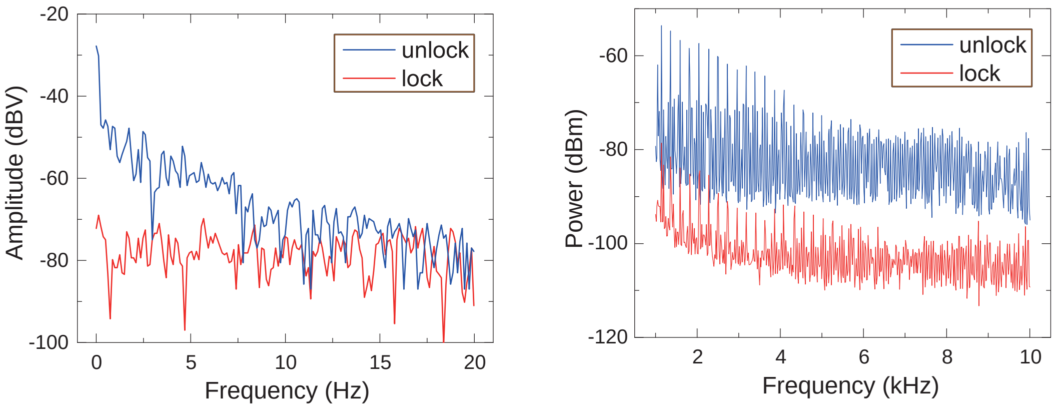

(a) Measured noise amplitude (b) Noise power spectrum

FIGURE C.3: Intensity noise suppression. (a) shows the noise amplitude measured by a digital oscilloscope in the low frequency range. (b) shows the noise power spectrum measured by a spectrum analyzer within 10 kHz. Note that the spectrum analyzer has an intrinsic attenuation for low frequency range (< 10 kHz) which has been corrected in the figure. The many peaks are the noise of the laser.

The essential part of the feedback loop is a PI controller. In order to achieve the best performance, several modifications on an old model A368N are made: (a) internal wave generator is disconnected to suppress unnecessary noise and the external scan port is used as a reference input as depicted in Fig. C.4(a); (b) the output is restricted within 0 to 5 V to protect the AOM as depicted in Fig. C.4(b).

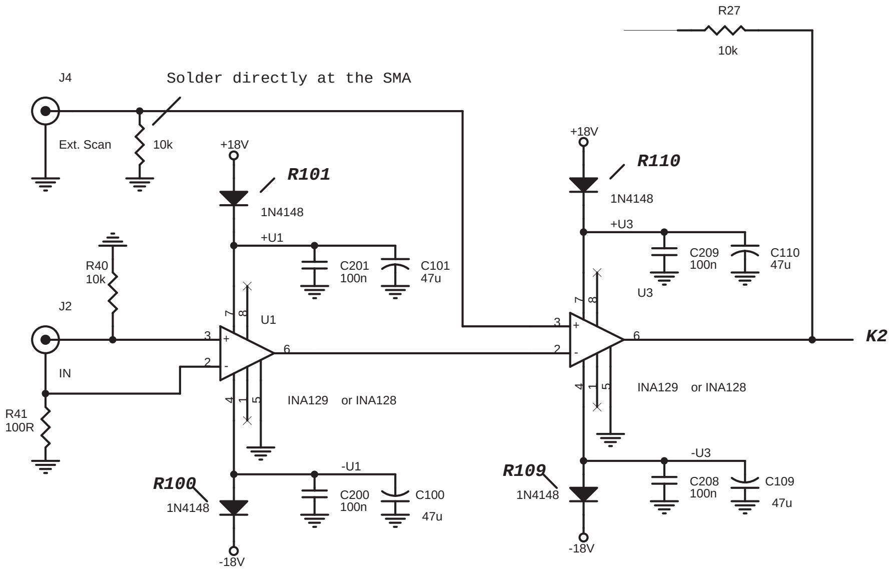
R27
10k
J4
Solder directly at the SMA
Ext. Scan
10k
+18V
R101
1N4148
+U1
C201
100n
C101
47u
R40
10k
J2
U1
IN
R41
100R
INA129 or INA128
R100
1N4148
-U1
C200
100n
C100
47u
-18V
+18V
R110
1N4148
+U3
C209
100n
C110
47u
U3
K2
INA129 or INA128
R109
1N4148
-U3
C208
100n
C109
47u
-18V

(a) Input modification

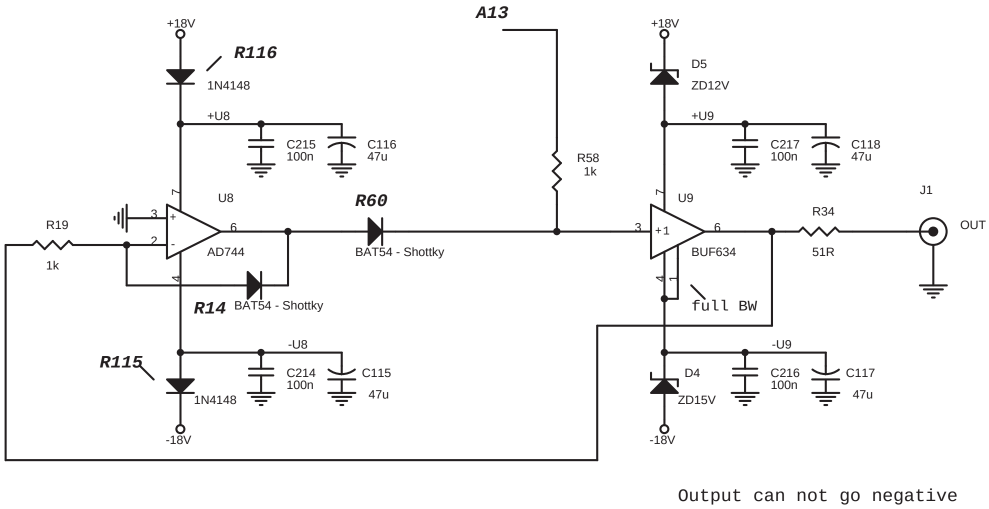
+18V
R116
1N4148
+U8
C215
100n
C116
47u
A13
R58
1k
+18V
D5
ZD12V
+U9
C217
100n
C118
47u
U8
AD744
R60
BAT54 - Shottky
R19
1k
R14
BAT54 - Shottky
U9
+1
BUF634
R34
51R
J1
OUT
full BW
R115
1N4148
-U8
C214
100n
C115
47u
-18V
D4
ZD15V
-U9
C216
100n
C117
47u
-18V
Output can not go negative

(b) Output modification

FIGURE C.4: PI controller modification (courtesy of Dr. Venelin Angelov).

Appendix D

Modified Edlén Equation

The refractive index of air is typically modelled by the modified Edlén equation [239, 256–258] which has the form

$$n = 1 + \frac{P(n_{\mathrm{sa}} - 1)X}{96095.43} - 10^{-10}\frac{292.75}{t + 273.15}(3.7345 - 0.0401S)p_{\mathrm{v}}, \tag{D.1}$$

where P is pressure in Pa, t is temperature in Celsius, and $S = 1/\lambda^2$ is a factor with the wavelength in vacuum λ in μm. The parameter n_{sa} is the refractive index of standard air at 1 atmosphere and 15°C, which is given as

$$n_{\mathrm{sa}} = 1 + 10^{-8}\left(8342.54 + \frac{2406147}{130 - S} + \frac{15998}{38.9 - S}\right). \tag{D.2}$$

The parameter X is given by

$$X = \frac{1 + 10^{-8}(0.601 - 0.00972t)P}{1 + 0.003661t}. \tag{D.3}$$

The parameter p_{v} is the water vapor partial pressure which is $p_{\mathrm{v}} = RH \times p_{\mathrm{sv}}/100$ with RH the relative humidity in percent and p_{sv} the saturation vapor pressure over water. The expression of p_{sv} is

$$p_{\mathrm{sv}} = 10^6\left(\frac{2C}{-B + \sqrt{B^2 - 4AC}}\right)^4, \tag{D.4}$$

with the coefficients

$$\begin{aligned}
A =& \Omega^2 + K_1\Omega + K_2 \\
B =& K_3\Omega^2 + K_4\Omega + K_5 \\
C =& K_6\Omega^2 + K_7\Omega + K_8 \\
\Omega =& (t + 273.15) + \frac{K_9}{t + 273.15 - K_{10}},
\end{aligned}$$

and

K_1	$1.16705214528 \times 10^3$	K_6	$1.49151086135 \times 10^1$
K_2	$-7.24213167032 \times 10^5$	K_7	$-4.82326573616 \times 10^3$
K_3	$-1.70738469401 \times 10^1$	K_8	$4.05113405421 \times 10^5$
K_4	$1.20208247025 \times 10^4$	K_9	$-2.38555575678 \times 10^1$
K_5	$-3.23255503223 \times 10^6$	K_{10}	$6.50175348448 \times 10^2$

.

List of Publications

PhD work

[1] **Xiao-Fan Xu**, Xiao-Hui Bao, and Jian-Wei Pan, *Demonstration of active feedforward one-way quantum computing with photon-matter hyperentanglement*, Physical Review A 86, 050304(R) (2012). (Chap. 4)

[2] Xiao-Hui Bao, **Xiao-Fan Xu**, Che-Ming Li, Zhen-Sheng Yuan, Chao-Yang Lu, and Jian-Wei Pan, *Quantum teleportation between remote atomic-ensemble quantum memories*, Proceedings of the National Academy of Sciences 109, 20347-20351 (2012). (Chap. 2)

Former publication

[1] Xian-Min Jin, Ji-Gang Ren, Bin Yang, Zhen-Huan Yi, Fei Zhou, **Xiao-Fan Xu**, Shao-Kai Wang, Dong Yang, Yuan-Feng Hu, Shuo Jiang, Tao Yang, Hao Yin, Kai Chen, Cheng-Zhi Peng, and Jian-Wei Pan, *Experimental free-space quantum teleportation*, Nature Photonics 4, 376-381 (2010).

Acknowledgements

Every being that I have encountered deserves my deep gratitude, among whom I should like to include my supervisor, Prof. Jian-Wei Pan, for his continuous guidance and support through my studies. He has been teaching me the way to conduct scientific research with wisdom and encouragement. His physical insight, enthusiasm and curiosity for research make a strong impression and keep me motivated.

I would like to thank my dissertation committee, Prof. Matthias Weidemüller for graciously reviewing my thesis, and Prof. Luca Amendola and Prof. Klaus Pfeilsticker for taking the considerable effort to be examiners in the oral examination.

I would like to express my gratitude to my senior colleagues, Prof. Zhen-Sheng Yuan, Prof. Yu-Ao Chen, and Prof. Xiao-Hui Bao, for their patient instructions and generous assistance throughout the project.

I would also like to acknowledge all my workmates, Andreas Reingruber, Bing Yang, Han-Ning Dai, and Torsten Mandel, to whom I extend my heartfelt gratitude for the excellent team work and complete dedication. A special thank to Andreas for translating the abstract and correcting the grammar.

Many thanks to former members of the group, Alexander Goebel, Bo Zhao, Chao-Yang Lu, Claudia Wagenknecht, Che-Ming Li, Christian Lutz, Fan Yang, Huan Nguyen, Peter Dietrich, Shuai Chen, Thorsten Strassel, Xing-Can Yao, and Yong Zhao, as well as all members of the center for quantum dynamics. They have given me valuable experience and advice which ensure the project is progressing well.

I would additionally like to thank the people of the workshop, the secretaries of the institute, and the members of the graduate school, without whose strong support, this work would not have been possible.

Notably, I must thank my friends. It is my great pleasure to meet you, and life would not be easy without you. Especially, I appreciate the help of my friend Lu-Shuai Cao, a theoretical physicist, for his careful examination of the ring-exchange calculation.

I must also take the time to lovingly thank my parents, Fan Yang and Qi-Jian Xu, who raised me with love. Thank you for teaching me the value of faith, which builds my confidence. Thank you for teaching me the value of being honest, which helps me build strength of character. Thank you for teaching me the value of charity, which makes me enjoy the pleasure of helping others.

Finally, and above all, I should take the opportunity to express my love to my wife, Hui-Wen Tan. You are a good listener with spirit of optimism, and a fountain of happiness that never will run dry. I feel peaceful when you by my side. You have clear thinking and logical mind, from which my thesis benefit a lot. Thank you for every meal you cooked for me. Thank you for all the concessions you made for me. Holding you in my hand, all things will work out, and our sky grows bright.

Bibliography

[1] P.J. Mohr, B.N. Taylor, and D.B. Newell. CODATA internationally recommended values of the fundamental physical constants. `http://physics.nist.gov/cuu/Constants/index.html`, 2010. xxi

[2] P.J. Mohr, B.N. Taylor, and D.B. Newell. CODATA recommended values of the fundamental physical constants: 2010. *Reviews of Modern Physics*, 84(4):1527–1605, 2012. xxi

[3] D.A. Steck. Rubidium 87 D line data. `http://steck.us/alkalidata/`, 2001. xxi, 15, 81, 147

[4] N. Gisin, G. Ribordy, W. Tittel, and H. Zbinden. Quantum cryptography. *Reviews of Modern Physics*, 74(1):145–195, 2002. 1, 3, 50

[5] M.A. Nielsen and I.L. Chuang. *Quantum Computation and Quantum Information*. Cambridge University Press, 2000. 1, 149, 152

[6] C.H. Bennett, G. Brassard, C. Crépeau, R. Jozsa, A. Peres, and W.K. Wootters. Teleporting an unknown quantum state via dual classical and Einstein-Podolsky-Rosen channels. *Physical Review Letters*, 70(13):1895–1899, 1993. 2, 33

[7] D. Bouwmeester, J.-W. Pan, K. Mattle, M. Eibl, H. Weinfurter, and A. Zeilinger. Experimental quantum teleportation. *Nature*, 390(6660):575–579, 1997. 2, 33, 42

[8] A. Zeilinger. The quantum centennial. *Nature*, 408(6813):639–641, 2000. 2

[9] A. Einstein, B. Podolsky, and N. Rosen. Can quantum-mechanical description of physical reality be considered complete? *Physical Review*, 47(10):777–780, 1935. 2

[10] E. Schrödinger. Die gegenwartige Situation in der Quantenmechanik. *Naturwissenschaften*, 23(48):807–812, 1935. 2

[11] E. Schrödinger. Discussion of probability relations between separated systems. *Mathematical Proceedings of the Cambridge Philosophical Society*, 31(4):555–563, 1935. 2

[12] J.S. Bell. On the Einstein Podolsky Rosen paradox. *Physics*, 1(3):195–200, 1964. 2, 48

[13] J.F. Clauser and A. Shimony. Bell's theorem. Experimental tests and implications. *Reports on Progress in Physics*, 41(12):1881–1927, 1978. 2

[14] A. Aspect, P. Grangier, and G. Roger. Experimental realization of Einstein-Podolsky-Rosen-Bohm gedankenexperiment: A new violation of Bell's inequalities. *Physical Review Letters*, 49(2):91–94, 1982. 2

[15] T.E. Kiess, Y.H. Shih, A.V. Sergienko, and C.O. Alley. Einstein-Podolsky-Rosen-Bohm experiment using pairs of light quanta produced by type-II parametric down-conversion. *Physical Review Letters*, 71(24):3893–3897, 1993. 2

[16] G. Weihs, T. Jennewein, C. Simon, H. Weinfurter, and A. Zeilinger. Violation of Bell's inequality under strict Einstein locality conditions. *Physical Review Letters*, 81(23):5039–5043, 1998. 2

[17] A. Aspect. Bell's inequality test: more ideal than ever. *Nature*, 398(6724):189–190, 1999. 2

[18] M.A. Rowe, D. Kielpinski, V. Meyer, C.A. Sackett, W.M. Itano, C. Monroe, and D.J. Wineland. Experimental violation of a Bell's inequality with efficient detection. *Nature*, 409(6822):791–794, 2001. 2

[19] P.G. Kwiat, S. Barraza-Lopez, A. Stefanov, and N. Gisin. Experimental entanglement distillation and 'hidden' non-locality. *Nature*, 409(6823):1014–1017, 2001. 2

[20] J.-W. Pan. *Quantum Teleportation and Multi-photon Entanglement*. PhD thesis, Vienna University, 1999. 2

[21] M. Riebe, H. Häffner, C.F. Roos, W. Hänsel, J. Benhelm, G.P.T. Lancaster, T.W. Körber, C. Becher, F. Schmidt-Kaler, D.F.V. James, and R. Blatt. Deterministic quantum teleportation with atoms. *Nature*, 429(6993):734–737, 2004. 3, 33

[22] M.D. Barrett, J. Chiaverini, T. Schaetz, J. Britton, W.M. Itano, J.D. Jost, E. Knill, C. Langer, D. Leibfried, R. Ozeri, and D.J. Wineland. Deterministic quantum teleportation of atomic qubits. *Nature*, 429(6993):737–739, 2004. 3, 33

[23] S. Olmschenk, D.N. Matsukevich, P. Maunz, D. Hayes, L.M. Duan, and C. Monroe. Quantum teleportation between distant matter qubits. *Science*, 323(5913):486–489, 2009. 3, 33, 40, 42

[24] R.L. Rivest, A. Shamir, and L. Adleman. A method for obtaining digital signatures and public-key cryptosystems. *Communications of the ACM*, 21(2):120–126, 1978. 3

[25] P.W. Shor. Polynomial-time algorithms for prime factorization and discrete logarithms on a quantum computer. In *Proceedings 35th Annual Symposium on Foundations of Computer Science*, pages 124–134. IEEE, Los Alamitos, California, 1994. 3, 4, 51

[26] S. Wiesner. Conjugate coding. *ACM SIGACT News*, 15(1):78–88, 1983. 3

[27] C.H. Bennett and G. Brassard. Quantum cryptography: Public key distribution and coin tossing. In *Proceedings of the IEEE International Conference on Computers, Systems and Signal Processing*, pages 175–179. IEEE, New York, 1984. 3

[28] W.K. Wootters and W.H. Zurek. A single quantum cannot be cloned. *Nature*, 299(5886):802–803, 1982. 3

[29] C.H. Bennett, F. Bessette, G. Brassard, L. Salvail, and J. Smolin. Experimental quantum cryptography. *Journal of Cryptology*, 5(1):3–28, 1992. 3

[30] X.-B. Wang. Beating the photon-number-splitting attack in practical quantum cryptography. *Physical Review Letters*, 94(23):230503, 2005. 3

[31] H.-K. Lo, X. Ma, and K. Chen. Decoy state quantum key distribution. *Physical Review Letters*, 94(23):230504, 2005. 3

[32] A.K. Ekert. Quantum cryptography based on Bell's theorem. *Physical Review Letters*, 67(6):661–663, 1991. 3, 46

[33] T. Schmitt-Manderbach, H. Weier, M. Fürst, R. Ursin, F. Tiefenbacher, T. Scheidl, J. Perdigues, Z. Sodnik, C. Kurtsiefer, J.G. Rarity, A. Zeilinger, and H. Weinfurter. Experimental demonstration of free-space decoy-state quantum key distribution over 144 km. *Physical Review Letters*, 98(1):010504–10508, 2007. 3

[34] R. Ursin, F. Tiefenbacher, T. Schmitt-Manderbach, H. Weier, T. Scheidl, M. Lindenthal, B. Blauensteiner, T. Jennewein, J. Perdigues, P. Trojek, B. Ömer, M. Fürst, M. Meyenburg, J. Rarity, Z. Sodnik, C. Barbieri, H. Weinfurter, and A. Zeilinger. Entanglement-based quantum communication over 144km. *Nature Physics*, 3(7):481–486, 2007. 3

[35] H.J. Briegel, W. Dür, J.I. Cirac, and P. Zoller. Quantum repeaters: The role of imperfect local operations in quantum communication. *Physical Review Letters*, 81(26):5932–5935, 1998. 4, 45

[36] M. Żukowski, A. Zeilinger, M.A. Horne, and A.K. Ekert. “Event-ready-detectors” Bell experiment via entanglement swapping. *Physical Review Letters*, 71(26):4287–4290, 1993. 4, 23, 45

[37] C.H. Bennett, G. Brassard, S. Popescu, B. Schumacher, J.A. Smolin, and W.K. Wootters. Purification of noisy entanglement and faithful teleportation via noisy channels. *Physical Review Letters*, 76(5):722–725, 1996. 4

[38] J.I. Cirac, P. Zoller, H.J. Kimble, and H. Mabuchi. Quantum state transfer and entanglement distribution among distant nodes in a quantum network. *Physical Review Letters*, 78(16):3221–3224, 1997. 4

[39] L.M. Duan, M.D. Lukin, J.I. Cirac, and P. Zoller. Long-distance quantum communication with atomic ensembles and linear optics. *Nature*, 414(6862):413–418, 2001. 4, 10, 23, 40

[40] Z.-B. Chen, B. Zhao, Y.-A. Chen, J. Schmiedmayer, and J.-W. Pan. Fault-tolerant quantum repeater with atomic ensembles and linear optics. *Physical Review A*, 76(2):022329–22341, 2007. 4

[41] N. Sangouard, C. Simon, B. Zhao, Y.-A. Chen, H. de Riedmatten, J.-W. Pan, and N. Gisin. Robust and efficient quantum repeaters with atomic ensembles and linear optics. *Physical Review A*, 77(6):062301–062307, 2008. 4

[42] Z.-S. Yuan, Y.-A. Chen, B. Zhao, S. Chen, J. Schmiedmayer, and J.-W. Pan. Experimental demonstration of a BDCZ quantum repeater node. *Nature*, 454(7208):1098–1101, 2008. 4, 43, 45

[43] R. Feynman. Simulating physics with computers. *International Journal of Theoretical Physics*, 21(6):467–488, 1982. 4, 51

[44] D. Deutsch. Quantum theory, the Church-Turing principle and the universal quantum computer. *Proceedings of the Royal Society of London. A. Mathematical and Physical Sciences*, 400(1818):97–117, 1985. 4

[45] D. Deutsch. Quantum computational networks. *Proceedings of the Royal Society of London. A. Mathematical and Physical Sciences*, 425(1868):73–90, 1989. 4

[46] L.K. Grover. Quantum mechanics helps in searching for a needle in a haystack. *Physical Review Letters*, 79(2):325–328, 1997. 4, 51

[47] T.D. Ladd, F. Jelezko, R. Laflamme, Y. Nakamura, C. Monroe, and J.L. O'Brien. Quantum computers. *Nature*, 464(7285):45–53, 2010. 5

[48] P. Walther, K.J. Resch, T. Rudolph, E. Schenck, H. Weinfurter, V. Vedral, M. Aspelmeyer, and A. Zeilinger. Experimental one-way quantum computing. *Nature*, 434(7030):169–176, 2005. 5, 51, 53

[49] H.J. Briegel and R. Raussendorf. Persistent entanglement in arrays of interacting particles. *Physical Review Letters*, 86(5):910–913, 2001. 5, 51, 52

[50] R. Raussendorf and H.J. Briegel. A one-way quantum computer. *Physical Review Letters*, 86(22):5188–5191, 2001. 5, 51, 52

[51] K. Chen, C.-M. Li, Q. Zhang, Y.-A. Chen, A. Goebel, S. Chen, A. Mair, and J.-W. Pan. Experimental realization of one-way quantum computing with two-photon four-qubit cluster states. *Physical Review Letters*, 99(12):120503–120504, 2007. 5, 51

[52] M.S. Tame, R. Prevedel, M. Paternostro, P. Bohi, M.S. Kim, and A. Zeilinger. Experimental realization of Deutsch's algorithm in a one-way quantum computer. *Physical Review Letters*, 98(14):140501–140504, 2007. 5, 51

[53] R. Prevedel, P. Walther, F. Tiefenbacher, P. Böhi, R. Kaltenbaek, T. Jennewein, and A. Zeilinger. High-speed linear optics quantum computing using active feed-forward. *Nature*, 445(7123):65–69, 2007. 5, 51, 67

[54] G. Vallone, Pomarico, De Martini, and Mataloni. Active one-way quantum computation with two-photon four-qubit cluster states. *Physical Review Letters*, 100(16):160502, 2008. 5, 51

[55] Y. Tokunaga, S. Kuwashiro, T. Yamamoto, M. Koashi, and N. Imoto. Generation of high-fidelity four-photon cluster state and quantum-domain demonstration of one-way quantum computing. *Physical Review Letters*, 100:210501, 2008. 5, 51

[56] R. Kaltenbaek, J. Lavoie, B. Zeng, S.D. Bartlett, and K.J. Resch. Optical one-way quantum computing with a simulated valence-bond solid. *Nature Physics*, 6(11):850–854, 2010. 5, 51

[57] C. Chin, R. Grimm, P. Julienne, and E. Tiesinga. Feshbach resonances in ultracold gases. *Reviews of Modern Physics*, 82(2):1225–1286, 2010. 5

[58] M.H. Anderson, J.R. Ensher, M.R. Matthews, C.E. Wieman, and E.A. Cornell. Observation of Bose-Einstein condensation in a dilute atomic vapor. *Science*, 269(5221):198–201, 1995. 6, 70, 77

[59] D. Jaksch, C. Bruder, J.I. Cirac, C.W. Gardiner, and P. Zoller. Cold bosonic atoms in optical lattices. *Physical Review Letters*, 81:3108–3111, 1998. 6, 100, 101

[60] S. Chen, Y.-A. Chen, B. Zhao, Z.-S. Yuan, J. Schmiedmayer, and J.-W. Pan. Demonstration of a stable atom-photon entanglement source for quantum rfepeaters. *Physical Review Letters*, 99(18):180505–180509, 2007. 6, 9, 23, 26, 28, 53

[61] P. Treutlein, T. Steinmetz, Y. Colombe, B. Lev, P. Hommelhoff, J. Reichel, M. Greiner, O. Mandel, A. Widera, T. Rom, I. Bloch, and T.W. Hänsch. Quantum information processing in optical lattices and magnetic microtraps. *Elements of Quantum Information*, pages 121–144, 2007. 6

[62] O. Mandel, M. Greiner, A. Widera, T. Rom, T.W. Hänsch, and I. Bloch. Controlled collisions for multi-particle entanglement of optically trapped atoms. *Nature*, 425(6961):937–940, 2003. 6, 69

[63] M. Anderlini, P.J. Lee, B.L. Brown, J. Sebby-Strabley, W.D. Phillips, and J.V. Porto. Controlled exchange interaction between pairs of neutral atoms in an optical lattice. *Nature*, 448(7152):452–456, 2007. 6

[64] S. Trotzky, P. Cheinet, S. Fölling, M. Feld, U. Schnorrberger, A.M. Rey, A. Polkovnikov, E.A. Demler, M.D. Lukin, and I. Bloch. Time-resolved observation and control of superexchange interactions with ultracold atoms in optical lattices. *Science*, 319(5861):295–299, 2008. 6, 117, 123, 124

[65] Z. Hadzibabic and J. Dalibard. *Two-dimensional Bose fluids: An atomic physics perspective*, volume 173 of *Proceedings of the International School of Physics "Enrico Fermi"*. IOS Press, 2011. 6, 74, 75, 81, 90, 95

[66] P.G. Kwiat, K. Mattle, H. Weinfurter, A. Zeilinger, A.V. Sergienko, and Y. Shih. New high-intensity source of polarization-entangled photon pairs. *Physical Review Letters*, 75:4337–4341, 1995. 9, 45, 50

[67] J.I. Cirac and P. Zoller. Quantum computations with cold trapped ions. *Physical Review Letters*, 74(20):4091–4094, 1995. 9

[68] R. Blatt and D. Wineland. Entangled states of trapped atomic ions. *Nature*, 453(7198):1008–1015, 2008. 9

[69] J.M. Raimond, M. Brune, and S. Haroche. Manipulating quantum entanglement with atoms and photons in a cavity. *Reviews of Modern Physics*, 73:565–582, 2001. 9

[70] C. Emary, B. Trauzettel, and C.W.J. Beenakker. Emission of polarization-entangled microwave photons from a pair of quantum dots. *Physical Review Letters*, 95:127401, 2005. 9

[71] J.F. Sherson, H. Krauter, R.K. Olsson, B. Julsgaard, K. Hammerer, I. Cirac, and E.S. Polzik. Quantum teleportation between light and matter. *Nature*, 443(7111):557–560, 2006. 9, 33

[72] B. Julsgaard, J. Sherson, J.I. Cirac, J. Fiurášek, and E.S. Polzik. Experimental demonstration of quantum memory for light. *Nature*, 432(7016):482–486, 2004. 9

[73] K. Hammerer, K. Mølmer, E.S. Polzik, and J.I. Cirac. Light-matter quantum interface. *Physical Review A*, 70(4):044304, 2004. 9

[74] M.D. Lukin, S.F. Yelin, and M. Fleischhauer. Entanglement of atomic ensembles by trapping correlated photon states. *Physical Review Letters*, 84(18):4232–4235, 2000. 10

[75] A. Kuzmich, W.P. Bowen, A.D. Boozer, A. Boca, C.W. Chou, L.M. Duan, and H.J. Kimble. Generation of nonclassical photon pairs for scalable quantum communication with atomic ensembles. *Nature*, 423(6941):731–734, 2003. 10

[76] S.A. Moiseev and S. Kröll. Complete reconstruction of the quantum state of a single-photon wave packet absorbed by a Doppler-broadened transition. *Physical Review Letters*, 87(17):173601, 2001. 10

[77] B. Kraus, W. Tittel, N. Gisin, M. Nilsson, S. Kröll, and J.I. Cirac. Quantum memory for nonstationary light fields based on controlled reversible inhomogeneous broadening. *Physical Review A*, 73(2):020302, 2006. 10

[78] G. Hétet, J.J. Longdell, A.L. Alexander, P.K. Lam, and M.J. Sellars. Electro-optic quantum memory for light using two-level atoms. *Physical Review Letters*, 100(2):023601, 2008. 10

[79] L.M. Duan, J.I. Cirac, and P. Zoller. Three-dimensional theory for interaction between atomic ensembles and free-space light. *Physical Review A*, 66(2):023818, 2002. 10, 12

[80] B. Zhao. *Robust and Efficient Quantum Repeater with Atomic Ensembles and Linear Optics*. PhD thesis, University of Heidelberg, 2008. 10

[81] X.-H. Bao. *Quantum Information with Entangled Photons and Cold Atomic Ensembles*. PhD thesis, University of Heidelberg, 2010. 10

[82] M.G. Raymer and J. Mostowski. Stimulated Raman scattering: Unified treatment of spontaneous initiation and spatial propagation. *Physical Review A*, 24(4):1980–1993, 1981. 12, 14

[83] J.C. Englund and C.M. Bowden. Spontaneous generation of phase waves and solitons in stimulated Raman scattering: Quantum-mechanical models of stimulated Raman scattering. *Physical Review A*, 42(5):2870–2889, 1990. 12

[84] M. Scully and M. Zubairy. *Quantum Optics*. Cambridge University Press, 1997. 12

[85] M.D. Lukin. Colloquium: Trapping and manipulating photon states in atomic ensembles. *Reviews of Modern Physics*, 75(2):457–472, 2003. 14

[86] M.G. Raymer, I.A. Walmsley, J. Mostowski, and B. Sobolewska. Quantum theory of spatial and temporal coherence properties of stimulated Raman scattering. *Physical Review A*, 32(1):332–344, 1985. 14

[87] M. Fleischhauer, A. Imamoglu, and J.P. Marangos. Electromagnetically induced transparency: Optics in coherent media. *Reviews of Modern Physics*, 77(2):633–673, 2005. 14

[88] A.V. Gorshkov, A. Andre, M.D. Lukin, and A.S. Sørensen. Photon storage in Λ-type optically dense atomic media. II. free-space model. *Physical Review A*, 76(3):033805, 2007. 16

[89] S.D. Jenkins. *Theory of Light-Atomic Ensemble Interactions: Entanglement, Storage, and Retrieval*. PhD thesis, Georgia Institute of Technology, 2006. 16, 29

[90] R. Loudon. Non-classical effects in the statistical properties of light. *Reports on Progress in Physics*, 43(7):913–949, 1980. 16

[91] D.F. Walls and G.J. Milburn. *Quantum Optics*. Springer, 2nd edition, 2008. 16

[92] X.-F. Xu, X.-H. Bao, and J.-W. Pan. Demonstration of active feedforward one-way quantum computing with photon-matter hyperentanglement. *Physical Review A*, 86(5):050304, 2012. 17, 19, 21, 51

[93] Y.O. Dudin, L. Li, and A. Kuzmich. Light storage on the time scale of a minute. *Physical Review A*, 87(3):031801, 2013. 17, 43, 67, 144

[94] G. Breit and I.I. Rabi. Measurement of nuclear spin. *Physical Review*, 38(11):2082–2083, 1931. 19

[95] H.H. Ku. Notes on the use of propagation of error formulas. *Journal of Research of the National Bureau of Standards–C*, 70C(4):263, 1966. 19

[96] R. Zhao, Y.O. Dudin, S.D. Jenkins, C.J. Campbell, D.N. Matsukevich, T.A.B. Kennedy, and A. Kuzmich. Long-lived quantum memory. *Nature Physics*, 5(2):100–104, 2009. 21, 29

[97] B. Zhao, Z.-B. Chen, Y.-A. Chen, J. Schmiedmayer, and J.-W. Pan. Robust creation of entanglement between remote memory qubits. *Physical Review Letters*, 98(24):240502–240504, 2007. 24, 25

[98] E.L. Raab, M. Prentiss, A. Cable, S. Chu, and D.E. Pritchard. Trapping of neutral sodium atoms with radiation pressure. *Physical Review Letters*, 59(23):2631–2634, 1987. 26

[99] H. Metcalf and P. van der Straten. Cooling and trapping of neutral atoms. *Physics Reports*, 244(4-5):203–286, 1994. 27

[100] W.D. Phillips. Nobel lecture: Laser cooling and trapping of neutral atoms. *Reviews of Modern Physics*, 70(3):721–741, 1998. 27

[101] D.J. Wineland and W.M. Itano. Laser cooling of atoms. *Physical Review A*, 20(4):1521–1540, 1979. 27, 137

[102] E.D. Black. An introduction to Pound–Drever–Hall laser frequency stabilization. *American Journal of Physics*, 69(1):79–87, 2001. 27

[103] X.-F. Xu. *Efficient Entanglement Swapping with Long-Lived Quantum Memory*. Thesis of preparatory doctoral study, University of Heidelberg, 2009. 27, 30, 39

[104] D.N. Matsukevich, T. Chanelière, M. Bhattacharya, S.-Y. Lan, S.D. Jenkins, T.A.B. Kennedy, and A. Kuzmich. Entanglement of a photon and a collective atomic excitation. *Physical Review Letters*, 95(4):040405, 2005. 28, 53

[105] H. de Riedmatten, J. Laurat, C.W. Chou, E.W. Schomburg, D. Felinto, and H.J. Kimble. Direct measurement of decoherence for entanglement between a photon and stored atomic excitation. *Physical Review Letters*, 97(11):113603, 2006. 28

[106] S.-Y. Lan, S.D. Jenkins, T. Chaneliere, D.N. Matsukevich, C.J. Campbell, R. Zhao, T.A.B. Kennedy, and A. Kuzmich. Dual-species matter qubit entangled with light. *Physical Review Letters*, 98(12):123602, 2007. 28

[107] C.K. Hong, Z.Y. Ou, and L. Mandel. Measurement of subpicosecond time intervals between two photons by interference. *Physical Review Letters*, 59(18):2044–2046, 1987. 31

[108] P.G. Kwiat and H. Weinfurter. Embedded Bell-state analysis. *Physical Review A*, 58(4):R2623–R2626, 1998. 31

[109] S.D. Barrett, P. Kok, K. Nemoto, R.G. Beausoleil, W.J. Munro, and T.P. Spiller. Symmetry analyzer for nondestructive Bell-state detection using weak nonlinearities. *Physical Review A*, 71(6):060302, 2005. 31

[110] D. Boschi, S. Branca, F. De Martini, L. Hardy, and S. Popescu. Experimental realization of teleporting an unknown pure quantum state via dual classical and Einstein-Podolsky-Rosen channels. *Physical Review Letters*, 80(6):1121–1125, 1998. 33

[111] A. Furusawa, J.L. Sørensen, S.L. Braunstein, C.A. Fuchs, H.J. Kimble, and E.S. Polzik. Unconditional quantum teleportation. *Science*, 282(5389):706–709, 1998. 33

[112] Y.-A. Chen, S. Chen, Z.-S. Yuan, B. Zhao, C.-S. Chuu, J. Schmiedmayer, and J.-W. Pan. Memory-built-in quantum teleportation with photonic and atomic qubits. *Nature Physics*, 4(2):103–107, 2008. 33

[113] X.-H. Bao, X.-F. Xu, C.-M. Li, Z.-S. Yuan, C.-Y. Lu, and J.-W. Pan. Quantum teleportation between remote atomic-ensemble quantum memories. *Proceedings of the National Academy of Sciences*, 109(50):20347–20351, 2012. 33

[114] C.H. Bennett, D.P. DiVincenzo, P.W. Shor, J.A. Smolin, B.M. Terhal, and W.K. Wootters. Remote state preparation. *Physical Review Letters*, 87:077902, 2001. 36

[115] D.F.V. James, P.G. Kwiat, W.J. Munro, and A.G. White. Measurement of qubits. *Physical Review A*, 64(5):052312, 2001. 37, 56, 150

[116] R. Jozsa. Fidelity for mixed quantum states. *Journal of Modern Optics*, 41(12):2315– 2323, 1994. 37, 151

[117] S. Massar and S. Popescu. Optimal extraction of information from finite quantum ensembles. *Physical Review Letters*, 74(8):1259–1263, 1995. 38

[118] I.L. Chuang and M.A. Nielsen. Prescription for experimental determination of the dynamics of a quantum black box. *Journal of Modern Optics*, 44(11):2455–2467, 1997. 38, 152, 153

[119] J.F. Poyatos, J.I. Cirac, and P. Zoller. Complete characterization of a quantum process: The two-bit quantum gate. *Physical Review Letters*, 78(2):390–393, 1997. 38

[120] J.L. O'Brien, G.J. Pryde, A. Gilchrist, D.F.V. James, N.K. Langford, T.C. Ralph, and A.G. White. Quantum process tomography of a controlled-NOT gate. *Physical Review Letters*, 93(8):080502, 2004. 38, 61, 153

[121] N. Sangouard, C. Simon, H. de Riedmatten, and N. Gisin. Quantum repeaters based on atomic ensembles and linear optics. *Reviews of Modern Physics*, 83(1):33–80, 2011. 40

[122] H.J. Kimble. The quantum internet. *Nature*, 453(7198):1023–1030, 2008. 40, 66

[123] S.D. Barrett, P.P. Rohde, and T.M. Stace. Scalable quantum computing with atomic ensembles. *New Journal of Physics*, 12(9):093032, 2010. 40, 67

[124] Y. Han, B. He, K. Heshami, C.-Z. Li, and C. Simon. Quantum repeaters based on Rydberg-blockade-coupled atomic ensembles. *Physical Review A*, 81(5):052311, 2010. 42

[125] B. Zhao, M. Müller, K. Hammerer, and P. Zoller. Efficient quantum repeater based on deterministic Rydberg gates. *Physical Review A*, 81(5):052329, 2010. 42

[126] B. Julsgaard, A. Kozhekin, and E.S. Polzik. Experimental long-lived entanglement of two macroscopic objects. *Nature*, 413(6854):400–403, 2001. 42

[127] J. Simon, H. Tanji, J.K. Thompson, and V. Vuletić. Interfacing collective atomic excitations and single photons. *Physical Review Letters*, 98(18):183601, 2007. 43

[128] C.W. Chou, J. Laurat, H. Deng, K.S. Choi, H. de Riedmatten, D. Felinto, and H.J. Kimble. Functional quantum nodes for entanglement distribution over scalable quantum networks. *Science*, 316(5829):1316–1320, 2007. 43

[129] B.C. Jacobs, T.B. Pittman, and J.D. Franson. Quantum relays and noise suppression using linear optics. *Physical Review A*, 66(5):052307, 2002. 45

[130] D. Collins, N. Gisin, and H. De Riedmatten. Quantum relays for long distance quantum cryptography. *Journal of Modern Optics*, 52(5):735–753, 2005. 45

[131] J.-W. Pan, D. Bouwmeester, H. Weinfurter, and A. Zeilinger. Experimental entanglement swapping: Entangling photons that never interacted. *Physical Review Letters*, 80(18):3891–3894, 1998. 45

[132] A. Peres. Delayed choice for entanglement swapping. *Journal of Modern Optics*, 47(2):139–143, 2000. 45, 46

[133] D.N. Matsukevich, T. Chaneliere, S.D. Jenkins, S.-Y. Lan, T.A.B. Kennedy, and A. Kuzmich. Deterministic single photons via conditional quantum evolution. *Physical Review Letters*, 97(1):013601–013604, 2006. 45

[134] J.F. Clauser, M.A. Horne, A. Shimony, and R.A. Holt. Proposed experiment to test local hidden-variable theories. *Physical Review Letters*, 23(15):880–884, 1969. 48

[135] R.F. Werner. Quantum states with Einstein-Podolsky-Rosen correlations admitting a hidden-variable model. *Physical Review A*, 40(8):4277–4281, 1989. 48, 139

[136] P. Aravind. To what extent do mixed states violate the Bell inequalities? *Physics Letters A*, 200(5):345–349, 1995. 48

[137] A.M. Goebel, C. Wagenknecht, Q. Zhang, Y.-A. Chen, K. Chen, J. Schmiedmayer, and J.-W. Pan. Multistage entanglement swapping. *Physical Review Letters*, 101(8):080403, 2008. 50

[138] I. Buluta and F. Nori. Quantum simulators. *Science*, 326(5949):108–111, 2009. 51

[139] P. Kok, W.J. Munro, K. Nemoto, T.C. Ralph, J.P. Dowling, and G.J. Milburn. Linear optical quantum computing with photonic qubits. *Reviews of Modern Physics*, 79(1):135–174, 2007. 51

[140] J.L. O'Brien, A. Furusawa, and J. Vučković. Photonic quantum technologies. *Nature Photonics*, 3(12):687–695, 2009. 51

[141] S. Scheel. Single-photon sources-an introduction. *Journal of Modern Optics*, 56(2-3):141–160, 2009. 51

[142] A.J. Shields. Semiconductor quantum light sources. *Nature Photonics*, 1(4):215–223, 2007. 51

[143] A.I. Lvovsky, B.C. Sanders, and W. Tittel. Optical quantum memory. *Nature Photonics*, 3(12):706–714, 2009. 51

[144] C. Simon and et al. Quantum memories. *The European Physical Journal D*, 58(1):1–22, 2010. 51

[145] H.J. Briegel, D.E. Browne, W. Dür, R. Raussendorf, and M. Van den Nest. Measurement-based quantum computation. *Nature Physics*, 5(1):19–26, 2009. 51, 69

[146] D.E. Browne and H.J. Briegel. One-way quantum computation. *arXiv:quant-ph/0603226v2*, 2006. 52

[147] M. Hein, J. Eisert, and H.J. Briegel. Multiparty entanglement in graph states. *Physical Review A*, 69(6):062311, 2004. 52

[148] N. Kiesel, C. Schmid, U. Weber, G. Tóth, O. Gühne, R. Ursin, and H. Weinfurter. Experimental analysis of a four-qubit photon cluster state. *Physical Review Letters*, 95(21):210502, 2005. 55

[149] G. Tóth and O. Gühne. Entanglement detection in the stabilizer formalism. *Physical Review A*, 72(2):022340, 2005. 55, 56

[150] D.N. Matsukevich, T. Chanelière, S.D. Jenkins, S.-Y. Lan, T.A.B. Kennedy, and A. Kuzmich. Observation of dark state polariton collapses and revivals. *Physical Review Letters*, 96(3):033601, 2006. 56

[151] Z.-S. Yuan, Y.-A. Chen, S. Chen, B. Zhao, M. Koch, T. Strassel, Y. Zhao, G.-J. Zhu, J. Schmiedmayer, and J.-W. Pan. Synchronized independent narrow-band single photons and efficient generation of photonic entanglement. *Physical Review Letters*, 98(18):180503, 2007. 66

[152] X.-H. Bao, A. Reingruber, P. Dietrich, J. Rui, A. Dück, T. Strassel, L Li, N.-L. Liu, B. Zhao, and J.-W. Pan. Efficient and long-lived quantum memory with cold atoms inside a ring cavity. *Nature Physics*, 8(7):517–521, 2012. 66, 144

[153] A. Rossi, G. Vallone, A. Chiuri, F. De Martini, and P. Mataloni. Multipath entanglement of two photons. *Physical Review Letters*, 102(15):153902, 2009. 67

[154] R. Inoue, T. Yonehara, Y. Miyamoto, M. Koashi, and M. Kozuma. Measuring qutrit-qutrit entanglement of orbital angular momentum states of an atomic ensemble and a photon. *Physical Review Letters*, 103(11):110503, 2009. 67

[155] E. Martín-López, A. Laing, T. Lawson, R. Alvarez, X.-Q. Zhou, and J.L. O'Brien. Experimental realization of Shor's quantum factoring algorithm using qubit recycling. *Nature Photonics*, 6(11):773–776, 2012. 69

[156] B. Vaucher, A. Nunnenkamp, and D. Jaksch. Creation of resilient entangled states and a resource for measurement-based quantum computation with optical superlattices. *New Journal of Physics*, 10(2):023005, 2008. 69, 144

[157] L. Jiang, A.M. Rey, O. Romero-Isart, J.J. Garcia-Ripoll, A. Sanpera, and M.D. Lukin. Preparation of decoherence-free cluster states with optical superlattices. *Physical Review A*, 79(2):022309, 2009. 69, 144

[158] S. Bose. Plancks Gesetz und Lichtquantenhypothese. *Zeitschrift für Physik*, 26(1):178–181, 1924. 70

[159] A. Einstein. Quantentheorie des einatomigen idealen Gases. *Sitzungsberichte der Preussischen Akademie der Wissenschaften*, pages 261–267, 1924. 70

[160] A. Einstein. Quantentheorie des einatomigen idealen Gases–Zweite Abhandlung. *Sitzungsberichte der Preussischen Akademie der Wissenschaften*, pages 3–14, 1925. 70

[161] K.B. Davis, M.O. Mewes, M.R. Andrews, N.J. van Druten, D.S. Durfee, D.M. Kurn, and W. Ketterle. Bose-Einstein condensation in a gas of Sodium atoms. *Physical Review Letters*, 75(22):3969–3973, 1995. 70

[162] W. Ketterle. Nobel lecture: When atoms behave as waves: Bose-Einstein condensation and the atom laser. *Reviews of Modern Physics*, 74(4):1131–1151, 2002. 70

[163] F. Dalfovo, S. Giorgini, L.P. Pitaevskii, and S. Stringari. Theory of Bose-Einstein condensation in trapped gases. *Reviews of Modern Physics*, 71(3):463–512, 1999. 70

[164] C. Pethick and H. Smith. *Bose-Einstein Condensation in Dilute Gases*. Cambridge University Press, 2002. 70, 71, 77

[165] T.D. Lee and C.N. Yang. Low-temperature behavior of a dilute Bose system of hard spheres. I. equilibrium properties. *Physical Review*, 112(5):1419–1429, 1958. 71

[166] N. Bogoliubov. On the theory of superfluidity. *Journal of Physics (USSR)*, 11(1):23–32, 1947. 72

[167] E.P. Gross. Structure of a quantized vortex in boson systems. *Il Nuovo Cimento Series 10*, 20(3):454–477, 1961. 72

[168] L.P. Pitaevsk. Vortex lines in an imperfect Bose gas. *Soviet Physics JETP (USSR)*, 13(2):451–454, 1961. 72

[169] P.S. Julienne, F.H. Mies, E. Tiesinga, and C.J. Williams. Collisional stability of double Bose condensates. *Physical Review Letters*, 78(10):1880–1883, 1997. 73

[170] N.D. Mermin and H. Wagner. Absence of ferromagnetism or antiferromagnetism in one- or two-dimensional isotropic Heisenberg models. *Physical Review Letters*, 17(22):1133–1136, 1966. 73

[171] P.C. Hohenberg. Existence of long-range order in one and two dimensions. *Physical Review*, 158(2):383–386, 1967. 73

[172] S. Coleman. There are no Goldstone bosons in two dimensions. *Communications in Mathematical Physics*, 31(4):259–264, 1973. 73

[173] V. Berezinskii. Destruction of long-range order in one-dimensional and two-dimensional systems having a continuous symmetry group II. quantum systems. *Soviet Physics JETP (USSR)*, 34(3):610–616, 1972. 74

[174] J.M. Kosterlitz and D.J. Thouless. Ordering, metastability and phase transitions in two-dimensional systems. *Journal of Physics C: Solid State Physics*, 6(7):1181, 1973. 74, 75

[175] D.S. Fisher and P.C. Hohenberg. Dilute Bose gas in two dimensions. *Physical Review B*, 37(10):4936–4943, 1988. 75

[176] N. Prokof'ev, O. Ruebenacker, and B. Svistunov. Critical point of a weakly interacting two-dimensional Bose gas. *Physical Review Letters*, 87(27):270402, 2001. 75

[177] N. Prokof'ev and B. Svistunov. Two-dimensional weakly interacting Bose gas in the fluctuation region. *Physical Review A*, 66(4):043608, 2002. 75

[178] K.B. Davis, M.-O. Mewes, M.A. Joffe, M.R. Andrews, and W. Ketterle. Evaporative cooling of Sodium atoms. *Physical Review Letters*, 74(26):5202–5205, 1995. 77

[179] M.D. Barrett, J.A. Sauer, and M.S. Chapman. All-optical formation of an atomic Bose-Einstein condensate. *Physical Review Letters*, 87(1):010404, 2001. 77

[180] W. Ketterle, K.B. Davis, M.A. Joffe, A. Martin, and D.E. Pritchard. High densities of cold atoms in a dark spontaneous-force optical trap. *Physical Review Letters*, 70(15):2253–2256, 1993. 80, 84

[181] W. Ketterle, D. Durfee, and D. Stamper-Kurn. Making, probing and understanding Bose-Einstein condensates. *arXiv:cond-mat/9904034v2*, 1999. 81

[182] G. Reinaudi, T. Lahaye, Z. Wang, and D. Guéry-Odelin. Strong saturation absorption imaging of dense clouds of ultracold atoms. *Optics Letters*, 32(21):3143–3145, 2007. 82

[183] T. Yefsah, R. Desbuquois, L. Chomaz, K.J. Günter, and J. Dalibard. Exploring the thermodynamics of a two-dimensional Bose gas. *Physical Review Letters*, 107(13):130401, 2011. 82, 95

[184] S.P. Rath, T. Yefsah, K.J. Günter, M. Cheneau, R. Desbuquois, M. Holzmann, W. Krauth, and J. Dalibard. Equilibrium state of a trapped two-dimensional Bose gas. *Physical Review A*, 82(1):013609, 2010. 82, 95

[185] C.-L. Hung. *In Situ Probing of Two-Dimensional Quantum Gases.* PhD thesis, University of Chicago, 2011. 82, 110, 140

[186] J. Dalibard and C. Cohen-Tannoudji. Laser cooling below the Doppler limit by polarization gradients: simple theoretical models. *Journal of the Optical Society of America B*, 6(11):2023–2045, 1989. 84

[187] C. Lutz. *Design and Implementation of a Magnetic Transfer System for Bose-Einstein Condensation.* Projektpraktikum, University of Heidelberg, 2011. 86

[188] M. Greiner, I. Bloch, T.W. Hänsch, and T. Esslinger. Magnetic transport of trapped cold atoms over a large distance. *Physical Review A*, 63(3):031401, 2001. 86

[189] J.E. Bjorkholm, R.R. Freeman, A. Ashkin, and D.B. Pearson. Observation of focusing of neutral atoms by the dipole forces of resonance-radiation pressure. *Physical Review Letters*, 41(20):1361–1364, 1978. 87

[190] S. Chu, J.E. Bjorkholm, A. Ashkin, and A. Cable. Experimental observation of optically trapped atoms. *Physical Review Letters*, 57(3):314–317, 1986. 87

[191] R. Grimm and M. Weidemüller. Optical dipole traps for neutral atoms. *Advances In Atomic, Molecular, and Optical Physics*, 42:95–170, 2000. 88, 141

[192] J. Jackson. *Classical Electrodynamics.* John Willey & Sons, Inc., 3rd edition, 1998. 88

[193] C. Cohen-Tannoudji, J. Dupont-Roc, and G. Grynberg. *Atom - Photon Interactions: Basic Process and Appilcations.* Wiley-VCH Verlag GmbH & Co. KGaA, 2004. 88

[194] Y.J. Lin, A.R. Perry, R.L. Compton, I.B. Spielman, and J.V. Porto. Rapid production of ^{87}Rb Bose-Einstein condensates in a combined magnetic and optical potential. *Physical Review A*, 79(6):063631, 2009. 89

[195] J.F. Sherson, C. Weitenberg, M. Endres, M. Cheneau, I. Bloch, and S. Kuhr. Single-atom-resolved fluorescence imaging of an atomic Mott insulator. *Nature*, 467(7311):68–72, 2010. 90

[196] N. Gemelke, X.-B. Zhang, C.-L. Hung, and C. Chin. *In situ* observation of incompressible Mott-insulating domains in ultracold atomic gases. *Nature*, 460(7258):995–998, 2009. 90, 105

[197] M.R. Andrews, C.G. Townsend, H.J. Miesner, D.S. Durfee, D.M. Kurn, and W. Ketterle. Observation of interference between two Bose condensates. *Science*, 275(5300):637–641, 1997. 93

[198] M. Greiner, O. Mandel, T. Esslinger, T.W. Hänsch, and I. Bloch. Quantum phase transition from a superfluid to a Mott insulator in a gas of ultracold atoms. *Nature*, 415(6867):39–44, 2002. 97, 103

[199] C. Kittel. *Introduction to Solid State Physics*. John Willey & Sons, Inc., 8th edition, 2005. 97, 99

[200] N.W. Ashcroft and N.D. Mermin. *Solid State Physics*. Harcourt College Publishers, 1976. 98, 117

[201] M. Greiner. *Ultracold quantum gases in three-dimensional optical lattice potentials*. PhD thesis, Ludwig-Maximilians-Universität München, 2003. 98, 111, 114

[202] A.M. Rey. *Ultracold bosonic atoms in optical lattices*. PhD thesis, University of Maryland at College Park, 2004. 98, 100

[203] O. Morsch and M. Oberthaler. Dynamics of Bose-Einstein condensates in optical lattices. *Reviews of Modern Physics*, 78(1):179–215, 2006. 99

[204] D. Jaksch. *Bose-Einstein Condensation and Applications*. PhD thesis, Leopold-Franzens-Universitaet Innsbruck, 1999. 100

[205] I. Bloch, J. Dalibard, and W. Zwerger. Many-body physics with ultracold gases. *Reviews of Modern Physics*, 80(3):885–964, 2008. 101, 103, 117

[206] M.P.A. Fisher, P.B. Weichman, G. Grinstein, and D.S. Fisher. Boson localization and the superfluid-insulator transition. *Physical Review B*, 40(1):546–570, 1989. 104

[207] J.K. Freericks and H. Monien. Strong-coupling expansions for the pure and disordered Bose-Hubbard model. *Physical Review B*, 53(5):2691–2700, 1996. 104

[208] B. Capogrosso-Sansone, S.G. Söyler, N. Prokof'ev, and B. Svistunov. Monte Carlo study of the two-dimensional Bose-Hubbard model. *Physical Review A*, 77(1):015602, 2008. 104

[209] M. Rigol, G.G. Batrouni, V.G. Rousseau, and R.T. Scalettar. State diagrams for harmonically trapped bosons in optical lattices. *Physical Review A*, 79(5):053605, 2009. 105

[210] W.S. Bakr, A. Peng, M.E. Tai, R. Ma, J. Simon, J.I. Gillen, S. Fölling, L. Pollet, and M. Greiner. Probing the superfluid-to-Mott insulator transition at the single-atom level. *Science*, 329(5991):547–550, 2010. 105

[211] F. Gerbier. Boson Mott insulators at finite temperatures. *Physical Review Letters*, 99(12):120405, 2007. 105

[212] P.L. Kapitza and P.A.M. Dirac. The reflection of electrons from standing light waves. *Mathematical Proceedings of the Cambridge Philosophical Society*, 29(2):297–300, 1933. 107

[213] H. Batelaan. The Kapitza-Dirac effect. *Contemporary Physics*, 41(6):369–381, 2000. 107

[214] B. Gadway, D. Pertot, Reimann, M.G. Cohen, and D. Schneble. Analysis of Kapitza-Dirac diffraction patterns beyond the Raman-Nath regime. *Optics Express*, 17(21):19173–19180, 2009. 107

[215] J.H. Denschlag, J.E. Simsarian, H. Häffner, C. McKenzie, A. Browaeys, D. Cho, K. Helmerson, S.L. Rolston, and W.D. Phillips. A Bose-Einstein condensate in an optical lattice. *Journal of Physics B: Atomic, Molecular and Optical Physics*, 35(14):3095, 2002. 109

[216] S.R. Clark and D. Jaksch. Dynamics of the superfluid to Mott-insulator transition in one dimension. *Physical Review A*, 70(4):043612, 2004. 110

[217] T. Gericke, F. Gerbier, A. Widera, S. Fölling, O. Mandel, and I. Bloch. Adiabatic loading of a Bose-Einstein condensate in a 3D optical lattice. *Journal of Modern Optics*, 54(5):735–743, 2007. 110

[218] A. Kastberg, W.D. Phillips, S.L. Rolston, R.J.C. Spreeuw, and P.S. Jessen. Adiabatic cooling of Cesium to 700 nK in an optical lattice. *Physical Review Letters*, 74(9):1542–1545, 1995. 110

[219] M. Greiner, I. Bloch, O. Mandel, T.W. Hänsch, and T. Esslinger. Exploring phase coherence in a 2D lattice of Bose-Einstein condensates. *Physical Review Letters*, 87(16):160405, 2001. 110

[220] F. Gerbier, A. Widera, S. Fölling, O. Mandel, T. Gericke, and I. Bloch. Phase coherence of an atomic Mott insulator. *Physical Review Letters*, 95(5):050404, 2005. 111, 112, 115

[221] T.A. Zaleski and T.K. Kopeć. Atom-atom correlations in time-of-flight imaging of ultracold bosons in optical lattices. *Physical Review A*, 84(5):053613, 2011. 111

[222] M. Greiner, O. Mandel, T.W. Hänsch, and I. Bloch. Collapse and revival of the matter wave field of a Bose-Einstein condensate. *Nature*, 419(6902):51–54, 2002. 112

[223] E.M. Wright, D.F. Walls, and J.C. Garrison. Collapses and revivals of Bose-Einstein condensates formed in small atomic samples. *Physical Review Letters*, 77(11):2158–2161, 1996. 113

[224] A. Imamoḡlu, M. Lewenstein, and L. You. Inhibition of coherence in trapped Bose-Einstein condensates. *Physical Review Letters*, 78(13):2511–2514, 1997. 113

[225] S. Will, T. Best, U. Schneider, L. Hackermüller, D.-S. Lühmann, and I. Bloch. Time-resolved observation of coherent multi-body interactions in quantum phase revivals. *Nature*, 465(7295):197–201, 2010. 114

[226] P. Sengupta, M. Rigol, G.G. Batrouni, P.J.H. Denteneer, and R.T. Scalettar. Phase coherence, visibility, and the superfluid-Mott-insulator transition on one-dimensional optical lattices. *Physical Review Letters*, 95(22):220402, 2005. 115, 116

[227] S. Fölling, S. Trotzky, P. Cheinet, M. Feld, R. Saers, A. Widera, T. Müller, and I. Bloch. Direct observation of second-order atom tunnelling. *Nature*, 448(7157):1029–1032, 2007. 117

[228] S. Nascimbène, Y.-A. Chen, M. Atala, M. Aidelsburger, S. Trotzky, B. Paredes, and I. Bloch. Experimental realization of plaquette resonating valence-bond states with ultracold atoms in optical superlattices. *Physical Review Letters*, 108(20):205301, 2012. 117, 124, 133

[229] B. Paredes and I. Bloch. Minimum instances of topological matter in an optical plaquette. *Physical Review A*, 77(2):023603, 2008. 117, 124, 125, 126

[230] S. Fölling. *Probing Strongly Correlated States of Ultracold Atoms in Optical Lattices*. PhD thesis, Johannes Gutenberg-Universität in Mainz, 2008. 120, 123

[231] B. Josephson. Possible new effects in superconductive tunnelling. *Physics Letters*, 1(7):251–253, 1962. 121

[232] A.J. Leggett. Bose-Einstein condensation in the alkali gases: Some fundamental concepts. *Reviews of Modern Physics*, 73(2):307–356, 2001. 121

[233] P.W. Anderson. The resonating valence bond state in La_2CuO_4 and superconductivity. *Science*, 235(4793):1196–1198, 1987. 124

[234] S.A. Kivelson, D.S. Rokhsar, and J.P. Sethna. Topology of the resonating valence-bond state: Solitons and high-T_c superconductivity. *Physical Review B*, 35(16):8865–8868, 1987. 124

[235] J.B. Kogut. An introduction to lattice gauge theory and spin systems. *Reviews of Modern Physics*, 51(4):659–713, 1979. 125

[236] M.A. Levin and X.-G. Wen. String-net condensation: A physical mechanism for topological phases. *Physical Review B*, 71(4):045110, 2005. 125, 126

[237] M. Levin and X.-G. Wen. Colloquium: Photons and electrons as emergent phenomena. *Reviews of Modern Physics*, 77(3):871–879, 2005. 125, 126

[238] X. Jiang. *The Laser Frequency Stabilizing and Phase Locking on Quantum Memory Based on Cold Atoms*. PhD thesis, University of Science and Technology of China, 2009. 128

[239] J.A. Stone and H. Zimmerman. Index of refraction of air. `http://emtoolbox.nist.gov/Wavelength/Documentation.asp`, 2001. 129, 159

[240] A. Abragam. *The Principles of Nuclear Magnetism*. Oxford University Press, 1961. 133

[241] A. Widera, F. Gerbier, S. Fölling, T. Gericke, O. Mandel, and I. Bloch. Coherent collisional spin dynamics in optical lattices. *Physical Review Letters*, 95(19):190405, 2005. 133

[242] T. Müller, S. Fölling, A. Widera, and I. Bloch. State preparation and dynamics of ultracold atoms in higher lattice orbitals. *Physical Review Letters*, 99(20):200405, 2007. 134

[243] M. Horodecki, P. Horodecki, and R. Horodecki. General teleportation channel, singlet fraction, and quasidistillation. *Physical Review A*, 60(3):1888–1898, 1999. 139

[244] O. Mandel, M. Greiner, A. Widera, T. Rom, T.W. Hänsch, and I. Bloch. Coherent transport of neutral atoms in spin-dependent optical lattice potentials. *Physical Review Letters*, 91(1):010407, 2003. 141

[245] P.J. Lee, M. Anderlini, B.L. Brown, J. Sebby-Strabley, W.D. Phillips, and J.V. Porto. Sublattice addressing and spin-dependent motion of atoms in a double-well lattice. *Physical Review Letters*, 99(2):020402, 2007. 141

[246] P. Windpassinger and K. Sengstock. Engineering novel optical lattices. *Reports on Progress in Physics*, 76(8):086401, 2013. 141

[247] P. Soltan-Panahi, J. Struck, P. Hauke, A. Bick, W. Plenkers, G. Meineke, C. Becker, P. Windpassinger, M. Lewenstein, and K. Sengstock. Multi-component quantum gases in spin-dependent hexagonal lattices. *Nature Physics*, 7(5):434–440, 2011. 141

[248] B. Antonio and S. Bose. Two-qubit gates for decoherence-free qubits using a ring exchange interaction. *Physical Review A*, 88(4):042306, 2013. 144

[249] K. Inaba, Y. Tokunaga, K. Tamaki, K. Igeta, and M. Yamashita. High-fidelity cluster state generation for ultracold atoms in an optical lattice. *Physical Review Letters*, 112(11):110501, 2014. 144

[250] C. Weitenberg, M. Endres, J.F. Sherson, M. Cheneau, P. Schauss, T. Fukuhara, I. Bloch, and S. Kuhr. Single-spin addressing in an atomic Mott insulator. *Nature*, 471(7338):319–324, 2011. 145

[251] M. Levitt. *Spin Dynamics: Basics of Nuclear magnetic Resonance*. John Willey & Sons, Ltd, 2nd edition, 2008. 145

[252] E. Jané, G. Vidal, W. Dür, P. Zoller, and J.I. Cirac. Simulation of quantum dynamics with quantum optical systems. *Quantum Information and Computation*, 3(1):15–37, 2003. 145

[253] I. Bloch, J. Dalibard, and S. Nascimbène. Quantum simulations with ultracold quantum gases. *Nature Physics*, 8(4):267–276, 2012. 145

[254] A. Uhlmann. The transition probability in the state space of a *-algebra. *Reports on Mathematical Physics*, 9(2):273– 279, 1976. 151

[255] M. Hübner. Explicit computation of the Bures distance for density matrices. *Physics Letters A*, 163(4):239– 242, 1992. 152

[256] B. Edlén. The refractive index of air. *Metrologia*, 2(2):71, 1966. 159

[257] K.P. Birch and M.J. Downs. An updated Edlén equation for the refractive index of air. *Metrologia*, 30(3):155, 1993. 159

[258] K.P. Birch and M.J. Downs. Correction to the updated Edlén equation for the refractive index of air. *Metrologia*, 31(4):315, 1994. 159